DEPARTMENT OF PHYSICS
UNIVERSITY OF JYVÄSKYLÄ
RESEARCH REPORT No. 6/2018

CHARACTERISTIC *Kα* EMISSION OF ELECTRON CYCLOTRON RESONANCE ION SOURCE PLASMAS

BY

MOENIR SAKIELDIEN

Academic Dissertation
for the Degree of
Doctor of Philosophy

To be presented, by permission of the
Faculty of Mathematics and Science
of the University of Jyväskylä,
for public examination in Auditorium FYS1 of the
University of Jyväskylä on August 31st, 2018
at 12 o'clock noon

Jyväskylä, Finland
August 2018

ABSTRACT

Sakieldien, Moenir
Characteristic $K\alpha$ emission of Electron Cyclotron Resonance Ion Source plasmas
Jyväskylä: University of Jyväskylä, 2018, 116 p. (+included articles)
Department of Physics Research Report No. 6/2018
ISSN 0075-465X
ISBN 978-951-39-7491-6 (paper copy)
ISBN 978-951-39-7492-3 (PDF)
Diss.

This thesis presents the results of an investigation of the volumetric $K\alpha$ emission rate/inner shell ionization rate from an Electron Cyclotron Resonance Ion Source (ECRIS) plasma tuned predominantly for high charge state ion production. The experimental work include four complimentary studies covering the influence of a parametric sweep of the four source tune parameters i.e microwave power, neutral gas flow, biased disc voltage and magnetic field on the volumetric $K\alpha$ emission rate, an investigation into the gas mixing effect, an investigation into the effectiveness of double-frequency heating mode and finally an investigation into microwave induced electron losses (relative and direct) from the ECRIS plasma.

The parametric sweeps revealed that only the microwave power and neutral gas flow has a significant impact on the volumetric $K\alpha$ emission rate. From the study it was concluded that this observation is presumably dictated by the plasma energy content. It is also argued that this novel plasma parameter i.e. the volumetric inner shell ionization rate can be used to benchmark numerical simulations on ECRIS plasmas as this plasma parameter can easily be reproduced by most simulation codes. The investigation into the gas mixing concluded that the ion cooling effect is in all likelihood the mechanism responsible for the favourable influence of the gas mixing. One of the mechanism responsible for the favourable influence of double-frequency heating was found to be due to the increasing electron density, based on the results of the various diagnostic probes. The latter two investigations were combined with optical emission spectroscopy to directly probe the ion density of different charge states. Finally, the electron losses from an ECRIS plasma were shown to correlate with the microwave power in both CW and pulsed operations. This investigation combined a number of diagnostic methods to develop the current understanding of this scarcely studied plasma process which predominantly affects the heated electron populations of the plasma.

Keywords: ECRIS, plasma diagnostics, electron losses, volumetric Kα emission

Author

Moenir Sakieldien
Department of Physics
University of Jyväskylä
Finland

Supervisors

Dr. Hannu Koivisto
Department of Physics
University of Jyväskylä
Finland

Dr. Olli Tarvainen
Department of Physics
University of Jyväskylä
Finland

Dr. Pete Jones
Subatomic Physics Department
iThemba Laboratory for Accelerator Based Sciences
South Africa

Reviewers

Dr. Sándor Biri
Hungarian Academy of Sciences (HAS)
Accelerator Centre
Budapest

Prof. Osvaldo Daniel Cortázar
University of Castilla-La Mancha
Spain

Opponent

Dr. Laurent Maunoury
Grand Accélérator National d'Ions Lourds (GANIL)
SDA/GPI
Caen

PREFACE

The work reported in this thesis has been carried out during the years 2013-2017 at the accelerator laboratory of the Department of Physics, University of Jyväskylä and at iThemba LABS in Cape Town, South Africa.

Firstly I wish to express my sincere gratitude to my supervisor Dr. Hannu Koivisto for all the support and guidance received over the course of this research work. Dr. Koivisto welcomed me into his prestigious group and was absolutely instrumental in the successful completion of the research study. Additionally he was always available and keen to share his vast knowledge and expertise on the various aspects of ion sources. The kind hospitality of Dr. Koivisto and his family is also acknowledged. I also wish to extend my heartfelt gratitude to Dr. Olli Tarvainen for firstly suggesting the research topic and secondly for always being available to answer my many questions regarding the finer detail of ion source plasma physics. Dr. Tarvainen has throughout the course of this research study been a constant source of information and invaluable guidance and I feel absolutely privileged to have worked with him. I would also like to thank Dr. Pete Jones for invaluable assistance with the analysis tools and for his expertise with spectroscopy related issues. Dr. Jones has also been absolutely instrumental in the completion of this research study. I would also like to express my gratitude to Dr. Sándor Biri and Prof. Osvaldo Daniel Cortázar for reviewing my thesis and providing me with valuable comments which helped to improve the thesis.

I wish to also express my sincere gratitude to my colleague and friend Mr. Risto Kronholm for the many discussions we had on ion source physics and the many hours spent together collecting data. The kind hospitality of Risto and his family (Hanna, Martti and Siiri) is also fondly acknowledged. I would also like to gratefully acknowledge Dr. Taneli Kalvas for his assistance with the simulations. The contributions of Dr. Vadim Skalyga and Dr. Ivan Izotov is also acknowledged especially for their assistance with the electron losses investigations. Dr. Janne Laulainen is also acknowledged for his assistance. I would also like to express my sincere gratitude to Ms. Minttu Haapaniemi and Ms. Marjut Hilska for logistical support provided during my many visits to Jyväskylä.

At my home institute, iThemba LABS, I would like to acknowledge the support received from the iThemba LABS Management. A big word of thanks also needs to be given to the Ion Source Group at iThemba LABS (Dr. Joele Mira, Dr. Rainer Thomae and Dr. Fhumulani Nemulodi) for many hours of measurements and valuable discussions. I also wish to express my sincere gratitude to Ms. Vanessa de Jongh for logistical support with the many travel arrangements over the course of this research study. I also wish to thank Ms. Audrey Sauls for her invaluable

assistance with sourcing the many research articles required for this work. A huge word of thanks also needs to be extended to the Education Training and Development Committee, specifically Dr. Rudzani Nemutudi for believing in me and supporting my studies. My friends Abduraghmaan Phillips, Chris Antonie, Amien Crombie, Mark Herbert and Melanie Robertson also deserves my thanks for their support given throughout this difficult journey.

Finally I wish to thank my brothers, Shaheed and Abubaker, and sister, Wadeedah, for their encouragement as well as my parents, Jamieriem Sakildien and the late Fatima Sakildien. My biggest debt of gratitude has to go to my wife Rachmat and our two sons Ziyaad and Ameer. Without their support and encouragement none of this would have been possible.

This work is dedicated to the memory of my late mother-in-law Amiena Albertyn who sadly passed away on the 5th of July 2018.

Cape Town, August 2018

Moenir Sakieldien

ACKNOWLEDGEMENTS

The work presented in this thesis was supported by Academy of Finland under the Finnish Center of Excellence Program (Contract No 213503) and mobility grant (No 290390). The work is also based on research supported in part by iThemba LABS and the National Research Foundation of South Africa (Grant Nos 90741, 109887 and 110072).

LIST OF INCLUDED ARTICLES

PI Muneer Sakildien, Risto Kronholm, Olli Tarvainen, Taneli Kalvas, Pete Jones, Rainer Thomae and Hannu Koivisto. Inner shell ionization of argon in ECRIS plasma. *Nuclear Inst. and Methods in Physics Research, A* ***900*** *(2018) 40-52*.

PII Muneer Sakildien, Olli Tarvainen, Taneli Kalvas, Hannu Koivisto, Risto Kronholm, Rainer Thomae, Joele Mira, Fhumulani Nemulodi and Pete Jones. Investigation into the gas mixing effect in ECRIS plasma using Kα and optical diagnostics. *Accepted for publication in AIP Conference Proceedings (2018)*.

PIII Muneer Sakildien, Olli Tarvainen, Risto Kronholm, Taneli Kalvas, Pete Jones and Hannu Koivisto. Studying the double-frequency heating mode in ECRIS plasma using Kα diagnostics. *Accepted for publication in AIP Conference Proceedings (2018)*.

PIV Muneer Sakildien, Olli Tarvainen, Risto Kronholm, Ivan Izotov, Vadim Skalyga, Taneli Kalvas, Pete Jones and Hannu Koivisto. Experimental evidence on microwave induced electron losses from ECRIS plasma. *Physics of Plasmas* ***25****, 062502 (2018)*.

The author of this thesis has performed most of the experimental work and the data analysis and has written the manuscripts in all the publications. The publications listed above are included in the appendices of the thesis.

CONTENTS

1 INTRODUCTION

The majority of ion sources are plasma devices [1] from which ion beams are extracted and frequently further accelerated using one or more particle accelerators. The ion beam, extracted from the plasma reservoir of the ion source, can be used in a wide variety of research fields and industrial applications [2] including nuclear fusion experiments [3], atomic physics research [4], radiation hardness testing of space electronics [5], radiation therapy [6], radionuclide production [7] and fundamental nuclear [8] and particle physics research [9]. Depending on the polarity of the required ion species, the operating principle of the ion source vary greatly. Positive ions are produced by using photons, electrons or thermal ionization to provide the ionization energy required to dislodge a bound electron from one of the shells surrounding the nucleus. Negative ions are produced by attachment of an electron to a neutral atom. Similarly the operating principle of the ion source differs greatly depending on the type of ion species required, the desired charge state of the ion species and the required beam intensity.

Highly charged positive ions are produced using mainly two different types of ion sources: the Electron Beam Ion Source (EBIS) [10] and the Electron Cyclotron Resonance Ion Source (ECRIS) [11]. The EBIS confines positive ions radially in a potential well created by an electron beam and axially by electrostatic potential barriers. During confinement the ions are bombarded with energetic electrons knocking out bound electrons from the confined ions. While the EBIS is capable of producing very high charge state (HCS) ions by tuning the so-called charge breeding time and the energy of the electron beam, it is preferentially operated in pulsed mode. The ECRIS on the other hand, which is in the focus of this work, can be operated in both pulsed and continuous wave (CW) mode, but is inferior to the EBIS in delivering very HCS ions. However, the charge storage capacity of an EBIS is limited by factors such as the length of the confinement trap and the electron current, while the ECRIS (in principle) has unlimited charge storage

capacity. The choice of ion source is also dependent on the type of accelerator, with ECRISs mostly used on cyclotrons utilizing ion beams of stable elements and EBISs mostly reserved for synchrotrons, both being viable options for linear accelerators. Currently both ion sources are actively studied in an attempt to meet the diverse technical challenges posed by charge breeding of radioactive ions [12], for example.

The specific interest of this study is the production of highly charged, heavy-ion beam species of stable elements delivered from an ECRIS coupled to a fixed K-value cyclotron. Typical applications of such cyclotrons include nuclear fission studies, studying the excitation energies within the nucleus as well as the decay modes of nuclei populated in nuclear reactions. To study particle interactions with the atomic nucleus, the projectile particle needs to have sufficient energy to overcome the repulsive Coulomb force between the positively charged particle and the atomic nucleus. In addition to this, extra energy is required to excite the nucleus to study the states of interest. Typically energies on the order of > 5 MeV per nucleon for a specific nucleus are required. To increase the maximum particle energy requires either increasing the K-value of the cyclotron or increasing the charge state delivered from the ion source. Increasing the K-value of a cyclotron requires an enormous capital investment as the maximum energy delivered from the cyclotron only scales linearly with the K-value. Alternatively increasing the charge state of the ions requires less capital investment and the maximum energy delivered by a cyclotron scales with the square of the charge state, which makes this option more efficient and viable. By increasing the maximum deliverable beam energy, the experimental nuclear physicists can study novel applications and low cross section processes which could not be accessed previously due to the energy limitation from the cyclotron. This gives huge impetus to increase the charge state delivered by an ECRIS coupled to such a fixed K-value cyclotron. Additionally by increasing the extracted ion beam current from the plasma reservoir of the ion source, the possibility to study new areas of scientific research, such as the production of previously unknown elements and nuclear spectroscopy of super-heavy elements [13], becomes viable. All these factors strongly dictate greater understanding of the plasma processes occurring inside the ECRIS plasma to meet the continuously increasing demands set by experimentalists.

The ECRIS in its most basic form (see Fig. 1) consist of a cylindrical metallic structure surrounded by a complex magnetic field. This magnetic field is produced by a set of solenoidal coils and a multipolar field, with all modern ECRISs utilizing a hexapole field. The superposition of the solenoid and hexapole fields serves for three purposes; (1) it provides a closed resonance zone for energy transfer from the microwaves to the plasma electrons in the ECR, (2) it provides axial and radial confinement allowing for the production of HCS ions and (3) it suppresses

magnetohydrodynamic (MHD) instabilities [14]. The metallic structure also consist of a number of ports, one of which is used to introduce gas atoms into the source. Using a different port, high frequency microwaves of 6.4 - 45 GHz are launched into the source chamber via wave coupling structures. The microwaves have an electric field component polarized in the same direction as the electron gyromotion. If there exists a favourable phase relation between the gyrating electrons and the electric field component of the microwaves, then an energy transfer between the electrons and the microwaves becomes possible. As a result of this energy transfer the electrons are heated in a process called Electron Cyclotron Resonance Heating (ECRH). The heated electrons subsequently have sufficient energy to remove even the inner shell electrons surrounding the nucleus of an atom. If the ions remained confined for a sufficiently long time, along with the heated electrons, the source is able to produce HCS ions via the process of stepwise electron-impact ionization.

The plasma processes contributing to HCS ion production are many and immensely complex, largely due to the huge number of participating particles. This results in a system governed by many inter-particle forces as well as plasma waves generated as a result of the plasma dynamics. Such systems are frequently numerically modelled to advance the current understanding of the various competing processes. To simplify such simulations, a number of assumptions are usually build into the numerical models. This makes the results of the simulations sensitive to these assumptions. To benchmark numerical simulations, it is often required to compare the results of the simulations to a direct plasma parameter, hence the need for plasma diagnostics. Additionally it is often required for the plasma diagnostic to be non-invasive so as not to disturb the plasma conditions, which is especially important in the case of plasmas containing HCS ions. In previous years, ECRH plasmas were mostly studied non-invasively using bremsstrahlung diagnostics [15, 16, 17]. While this diagnostic tool gives extremely valuable information, it does not say much about the actual process of ionization or more specifically HCS production. To study this process $K\alpha$ diagnostics probing the rate of inner shell ionization is an excellent tool, as discussed thoroughly in this thesis.

This thesis is outlined as follows. Chapter 2 deals with the fundamental aspects of ECR ion sources and the related plasma physics concepts as it pertains to HCS production. This chapter also deals with the underlying physical processes which results in emission of a broad spectrum of plasma radiation. Chapter 3 presents the experimental arrangement and analysis techniques employed on the two different ECR ion sources used in this work. Chapter 4 presents the experimental results obtained during the work described in this thesis. The chapter is subdivided into four sections. The first section deals with the volumetric $K\alpha$ emission. The second section deals with the investigation into the gas mixing effect. The third

section deals with the investigation into the double-frequency heating mode. The fourth section deals with the microwave induced electron losses from the magnetic confinement system of an ECRIS. Finally, chapter 5 presents a summary of the most pertinent experimental observations, as well as suggestions for future investigations using $K\alpha$ diagnostics.

2 FUNDAMENTAL ASPECTS OF ECRIS PLASMA

To create positively charged particles, the electrons orbiting the nucleus of an atom or ion (hereinafter atom will imply both neutral atom and ion) are removed in a process called ionization. This creates an ensemble of positively charged ions, electrons and neutral gas atoms, from the initial gas distribution. As the fractional ionization [3] or ionization degree of the neutral gas exceeds a certain (often ambiguous) limit, the collection of charged and neutral particles can be described as a plasma. Positive ions can be extracted from the plasma by appending the reservoir with an extraction system i.e. applying a potential difference between the vessel containing the plasma and the surrounding environment (beamline). This creates a device known as an ion source. The ECRIS, invented by Geller in May 1965 [11], have become one of the most widespread ion sources used for the production of HCS heavy ions.

The plasma of an ECRIS and any other ion source can be described by a number of macroscopic plasma parameters such as the particle density and temperature. The statistical description of the plasmas is typically based on the energy or velocity distribution function of the particle species and its temporal evolution. These plasma parameters are of great importance in deciphering the underlying physical processes occurring in ECRIS plasmas. To measure or at least estimate such plasma parameters, a remarkable amount of resources is currently being invested in devising and proving techniques for diagnosing the properties of an ECRIS plasma. This leads to the ever expanding field of ECRIS plasma diagnostics. Two plasma diagnostic techniques of particular interest to this study are performed by measuring the characteristic X-rays and bremsstrahlung radiation emitted from the ECRIS plasma. These diagnostic tools are excellent for directly probing the various plasma processes non-invasively. However probing the ECRIS plasma is challenging due to the fact that the electron population is far from equilibrium. Another important aspect of ECRIS plasmas is electron

losses. The electron losses from an ECRIS plasma are largely influenced by four processes i.e. Coulomb collisions, microwave induced losses, inelastic (ionizing) losses and plasma instabilities [18, 19] and will also be studied. In the following subsections the fundamental aspects of ECRIS plasma physics such as electron heating, electron losses and plasma confinement (unique to minimum-B devices) as well as the ideal properties of an ECRIS plasma for optimal HCS production are discussed. In addition to this, the fundamental radiation physics processes required to understand the diagnostics described in this thesis are also discussed.

2.1 Electron Cyclotron Resonance Heating in ECRIS

The basic reaction equation for ionization of a target atom A by a projectile electron e^- (as described above) is as follows:

$$e^- + A \rightarrow A^+ + 2e^- \tag{2.1}$$

As a result of the ionizing interaction, a second free electron is released. The projectile electron must have sufficient kinetic energy W for the ionizing reaction to occur. The threshold energy required for ionization is given by:

$$W \geq eV_i \tag{2.2}$$

where eV_i is the ionization potential or binding energy of the bound electron. The threshold energy required increases with increasing charge state and in order to produce HCS ions, electrons of several keV (kiloelectron volt) energy are required. Ionization potentials are listed for example in Ref. [20]. To ensure that a sufficient number of plasma electrons of an ECRIS attain this minimum kinetic energy, an electron heating mechanism is needed. The heating mechanism used in ECR ion sources is based on an energy exchange between microwaves and the plasma electrons.

The plasma electrons spiral in a clockwise direction (when viewed along the direction of the magnetic field) around the magnetic field lines, as dictated by the Lorentz force. By balancing the centripetal and centrifugal forces acting on such an electron, an orbital electron cyclotron frequency ω_{ce} can be defined to be:

$$\omega_{ce} = \frac{eB}{\gamma m_e} \tag{2.3}$$

where e is the charge of the electron, B is the strength of the imposed magnetic field, γ is the relativistic factor and γm_e is the relativistic mass of the electron[1]. A resonance condition can occur if the orbital electron cyclotron frequency matches the angular frequency of an electric field component of the microwaves. This

[1] $\gamma = 1 + \frac{E_k}{511\ \mathrm{keV}}$ where E_k is the kinetic energy in keV units

condition is given by the following expression:

$$\omega_{ce} = \omega_{rf} = \frac{eB_{ECR}}{\gamma m_e} = 2\pi f_{rf} \tag{2.4}$$

where B_{ECR} is the magnetic field strength at the resonance 'point' and f_{rf} is the frequency of the microwaves. Since the plasma electrons residing inside the ECRIS plasma have a broad distribution in energy, the resonance condition can be satisfied at a range of magnetic field strengths. The resonance condition is therefore not confined to a single point in space but over a closed surface (shown in Fig. 1) with a finite thickness affected by the gradient of the magnetic field as well [21]. The fact that the resonance surface is closed is due to the magnetic field topology i.e. minimum-B as discussed thoroughly later.

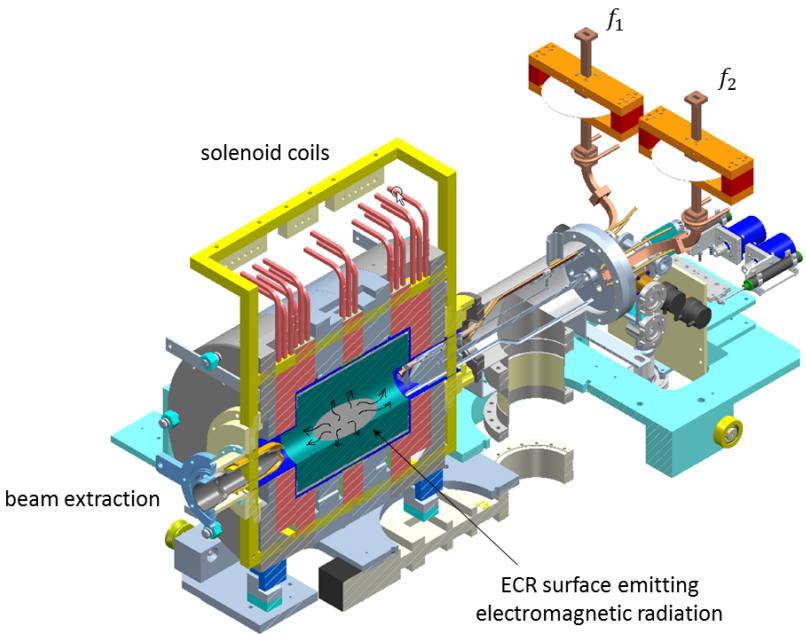

FIGURE 1 Cross-sectional cut of a typical ECRIS displaying the microwave coupling schemes for two heating frequencies, f_1 and f_2, the magnetic confinement (three solenoid coils plus a hexapole which is not visible), a schematic representation of the ECR surface and the beam extraction system.

During the resonant interaction, the velocity of the plasma electrons can either be increased or decreased. This depends on the phase difference between the velocity vector of the gyrating electron and the perpendicular (relative to the imposed B-field) electric field component of the microwaves, as well as the relation between the phase velocity of the heating microwave and the average velocity of the electron distribution [22]. As a result of reflection at the mirror points (as discussed in section 2.3.1) of the magnetic confinement system of an ECRIS, the electrons pass through the resonance zone multiple times. On average electrons will increase their energy in moving through the resonance zone and absorb energy from the microwave electric field thus damping the wave. The average energy

gained by the electron in passing through the resonance zone can be estimated from the following expression [2]:

$$\langle E_{ECR} \rangle = \frac{\pi e^2 E_r^2}{m_e \omega_{ce} |\alpha| v_{\parallel}} \tag{2.5}$$

where E_r is the magnitude of electric field component of the microwave, $v_{\parallel}$ is the parallel velocity component of the electron at the resonance zone and α is given by the following expression:

$$\alpha = \frac{1}{\omega_{ce}} \left(\frac{\partial \omega_{ce}}{\partial z'} \right)_{res} = \frac{e}{\gamma m_e \omega_{ce}} \left(\frac{\partial B}{\partial z'} \right)_{res} \tag{2.6}$$

i.e. the energy gain is inversely proportional to the gradient of the magnetic field at the resonance. This implies that a flatter magnetic field gradient at the resonance is more advantageous for electron heating. However, if the gradient becomes too flat the plasma becomes prone for kinetic instabilities driven by the anisotropy of the electron velocity distribution (as discussed below) due to the more efficient heating. Equation (2.5) assumes that the initial electron velocity is much smaller than the phase velocity of the microwave. In this case, the resonance interaction preferentially increases the perpendicular (relative to the magnetic field) velocity component of the electron $v_{\perp}$ with $v_{\parallel}$ remaining largely unperturbed [23]. The resulting electron velocity and energy distributions are therefore strongly anisotropic i.e. $v_{\perp} \gg v_{\parallel}$ and $E_{\perp} \gg E_{\parallel}$, where $E_{\perp}$ and $E_{\parallel}$ are the perpendicular and parallel energy components (with respect to the magnetic field vector), respectively. This makes the ECRIS plasma prone to instabilities [24], as will be discussed later. Taking into account the phase velocity of the microwave, the increment in the perpendicular and parallel velocity components acquired during a crossing of the ECR zone have been calculated by Girard *et al.* and are given by the following expressions [23]:

$$\Delta v_{\parallel} = \frac{eE_r}{m_e} \frac{v_{\perp}}{v_{\phi}} \sqrt{\frac{\pi}{\omega' v_{\parallel}}} \tag{2.7}$$

$$\Delta v_{\perp} = \frac{eE_r}{m_e} \left(1 - \frac{v_{\parallel}}{v_{\phi}} \right) \sqrt{\frac{\pi}{\omega' v_{\parallel}}} \tag{2.8}$$

where v_{ϕ} is the phase velocity of the microwaves and ω' is the derivative of the local electron cyclotron frequency along the magnetic field line.

As long as the bounce period τ_b between the two reflection points of the magnetic confinement system of the ECRIS is long i.e. $f_{rf} \gg 1/\tau_b$, the net energy gain is positive and the heating is stochastic. As the electrons are heated by the interaction with the electromagnetic (EM) wave, the kinetic energy of the electrons increases and beyond some point stochastic heating is lost together with the loss of phase randomisation. The phase randomisation is lost because the time between successive heatings decreases with increasing energy. At this point the heating mechanism moves into a different heating domain and the electron is 'locked'

onto a specific phase. The interaction between the heated electron and the EM-wave can now be described as superadiabatic [25]. In this new heating domain the electron energies are high i.e. $f_{rf} \sim 1/\tau_b$ and the interaction between the fast electron and the resonance zone becomes periodic. This is due to the change in the relativistic mass of the electron breaking the resonance condition as given by Eq. (2.4). As a result of this interaction the energy of the electron oscillates in time and is limited to the so-called adiabatic heating limit by the ECRH process. The expressions for stochastic W_s and adiabatic energy limits W_a are estimated by [26]:

$$W_s = 0.2 \left[m_e L \left(1 + \frac{l^2}{L^2} \right) \right]^{\frac{1}{4}} l \omega^{\frac{1}{2}} (eE)^{\frac{3}{4}} \tag{2.9}$$

$$W_a = 5 W_s \tag{2.10}$$

where L can be approximated from the axial magnetic field profile (discussed in section 2.3.1) i.e. $B = B_0 \left(1 + z^2/L^2\right)$ and $z = \pm l$ i.e. the axial location of the resonance.

From the discussion above it can be inferred that the plasma electrons of an ECRIS consist of a number of different electron populations. Based on qualitative arguments [27] and experimental investigations [28] it is assumed three different electron populations reside inside an ECRIS plasma. It is well established that the plasma of an ECRIS never achieve a Maxwellian distribution due to long equilibration times of the hot electrons [29]. It has recently been verified experimentally that the Electron Energy Distribution Function (EEDF) of the electrons escaping the confinement is strongly non-Maxwellian [30]. Despite all of this, the distribution of the plasma electrons of an ECRIS is frequently described as a tri-Maxwellian EEDF [28], which alleviates the statistical description of electron interactions and calculation of rate coefficients and process rates. In terms of this assumption, the plasma electrons consist of a cold electron population with a typical energy range of tens of electron volts [31]. The ECRIS plasma also has a warm electron population, mainly responsible for ionization processes of HCS ions, with typical energies ranging from few keV to tens of keV also observed experimentally [30]. Finally the EEDF of an ECRIS has a hot electron population (> 100 keV) which is well confined by the magnetic field configuration as discussed below. The maximum energy of this electron population could be close to the adiabatic energy limit [32]. The hot electron population causes most of the bremsstrahlung radiation and, thus, poses problems especially for superconducting ion sources where the cryostat is heated by the flux of energetic photons [33]. Furthermore, the hot electrons are responsible for kinetic instabilities which can limit the ECRIS performance [24].

2.2 Collisions in ECRIS plasmas

In addition to resonant microwave heating, the energy distribution of the electrons is affected by collisions (elastic and inelastic) and electron losses, both discussed hereafter. The plasma electrons of an ECRIS have a certain probability of undergoing collisions with other electrons, ions, neutral atoms and molecules. The collisions between neutral particles (and ions) mostly result in so-called charge exchange as fully discussed in section 2.4. Henceforth only interactions between charged particles are considered here. The time τ between two collisions is determined from the mean-free path between the collisions and the velocity of the projectile particle. In this model the common assumption is that the heavier particle species is stationary. This however does not hold for electron-electron collisions causing small angle scattering in velocity space. Using the afore-mentioned model enables a definition of a collision frequency i.e $\nu = 1/\tau$. For a distribution of particle velocities the most common approach adopted is to define a collision frequency over a Maxwellian distribution [34]. Using this approach the average electron-electron and electron-ion collision frequencies are given by the following expressions [34]:

$$\langle \nu_{ei} \rangle = \frac{2^{1/2} n_i Z^2 e^4 \ln \Lambda}{12\pi^{3/2} \epsilon_0^2 m_e^{1/2} T_e^{3/2}} \tag{2.11}$$

$$\langle \nu_{ee} \rangle \approx \frac{\langle \nu_{ei} \rangle}{n_i Z^2 / n_e} \approx \frac{n_e e^4 \ln \Lambda}{\epsilon_0^2 m_e^{1/2} T_e^{3/2}} \tag{2.12}$$

where ϵ_0 is the permittivity of vacuum, n_i is the ion density, n_e is the electron density, T_e is the electron temperature, T_i is the ion temperature, Z is the charge state of the ion and $\ln \Lambda \approx 10$ is the so-called Coulomb logarithm. The expression for the ion-ion collision frequency is given by [34]:

$$\langle \nu_{ii} \rangle = \frac{n_i Z^4 e^4 \ln \Lambda}{12\pi^{3/2} \epsilon_0^2 M^{1/2} T_i^{3/2}} \tag{2.13}$$

Equations (2.11 - 2.13) allow for an estimation of the various collision frequencies occurring inside an ECRIS plasma. As an example, for an argon plasma with average charge state $\langle Z \rangle \approx \Sigma_i n_i Z_i / n_e = 8$ and typical electron and ion temperatures and densities of $T_e = 1$ keV, $T_i = 1$ eV and $n_i \approx n_e = 10^{11}$ cm^{-3} the various collision frequencies are estimated to be:

$$\langle \nu_{ii} \rangle \approx 31 \text{ MHz} \quad \langle \nu_{ei} \rangle \approx 5.9 \text{ kHz} \quad \langle \nu_{ee} \rangle \approx 90 \text{ Hz} \tag{2.14}$$

The numerical example demonstrates that ion-ion collisions are more frequent than other types of collisions. The ion-ion and electron-ion collision frequencies can be compared to the gyrofrequencies of ions (of different charge states) and electrons in the magnetic field of an ECRIS. For example, for a typical magnetic field range of 0.3 - 2 T and argon charge state of 8+ with an ion temperature of 1 - 10 eV, the estimated ion gyrofrequency range is 0.9 - 6 MHz. Similarly for (cold)

electrons in the same B-field range the electron gyrofrequency is in the range 8.4 - 56 GHz. Since ion-ion collision frequency of the HCS ions is higher than their gyrofrequency, HCS ions cannot be considered to be magnetically confined. The opposite holds for electrons. Also, it can be shown that the frequency of electron-ion collisions decreases with T_e [34]. Since there is a significant mass difference between ions and electrons, the energy transfer from the hot electron population to the ion population is inefficient with the ions remaining relatively cold i.e. the equilibration time between the hot electron and ion populations is longer than the ion confinement time discussed later [35].

2.3 Plasma confinement

An important aspect of ECR ion sources is the confinement of the plasma constituents. The confinement scheme of electrons and ions differs greatly due to the collision processes described above. Electrons are well confined by the magnetic field, especially in the plasma core, with HCS ions thought to be confined electrostatically in the local potential dip [36] created by the magnetically confined electrons. The neutral atoms are unaffected by the plasma confinement schemes.

2.3.1 Magnetic confinement of the plasma

The magnetic confinement scheme used in most modern ECR ion sources is based on the superposition of the solenoid and hexapole fields, forming the so-called minimum-B configuration. The solenoidal field is produced by winding two (or more) coils around the plasma chamber of the source, at different axial positions. This arrangement is commonly known as the magnetic bottle or simple mirror configuration [11]. The coils, which can be either room temperature or superconducting, provide axial confinement of the charged particles. Soft magnetic materials with saturation fields 2.2 - 2.5 T are often used for reducing the number of ampere turns required for achieving sufficient axial field strength. This confinement scheme is based on the invariance of the magnetic moment μ of the gyrating charged particle q. The magnetic moment is given by the following expression:

$$\mu = IA = \left(\frac{|q|\omega_{cq}}{2\pi}\right)\left(\pi r_q^2\right) = \frac{W_\perp}{B} \tag{2.15}$$

$$\omega_{cq} = \frac{v_\perp}{r_q} = \frac{|q|B}{m} \tag{2.16}$$

where I is the current produced by the gyromotion of the charged particle q (where q can be either an ion i or an electron e), A is the area inscribed by the

charged particle in gyrating around the magnetic field line and $W_\perp$ is the perpendicular kinetic energy component of the charged particle. The invariance of the magnetic moment is violated by the ECR heating but the assumption is required here to establish the foundation of magnetic confinement.

As a result of the magnetic bottle, a strong axial magnetic field exists at the axial position of the solenoid coils, with a weaker magnetic field in-between. When the charged particle gyrates around the magnetic field lines, in the absence of collisions, the invariance of μ needs to be preserved. To achieve this, the parallel and perpendicular kinetic energy components change to compensate for the changing magnetic field, while concurrently preserving energy conservation i.e. $W_0 = W_\parallel + W_\perp = \text{constant}$, where W_0 is the total kinetic energy of the charged particle and $W_\parallel$ and $W_\perp$ are the parallel and perpendicular kinetic energy components, respectively. As the gyrating particle approaches the magnetic field maximum coinciding with the axial position of the coil, the perpendicular kinetic energy increases to preserve the invariance of the magnetic moment. To ensure energy conservation the parallel component of the kinetic energy decreases i.e. $v_\parallel$ decreases. Depending on the initial velocity components of the electron a point can be subsequently reached where $v_\parallel = 0$ and the charged particle is reflected in the magnetic bottle due to the $F = -\mu\nabla B$ force. This axial position is commonly referred to as the reflection point. The value of the magnetic field strength at the reflection point depends on the ratio of the electron velocity components. Increasing the strength of the magnetic field maximum causes a larger fraction of the electrons to become confined in the magnetic bottle.

To confine the ECRIS plasma (electrons) radially, a hexapole field is most commonly used, though other multipole fields have been experimented with [37]. As a result of the hexapole, the radial magnetic field increases with increasing radius resulting in a radial mirroring effect similar to that observed with the axial mirrors. The electrons are therefore reflected in both axial and radial directions resulting in enhanced plasma confinement. Additionally this structure completes the minimum-B configuration and makes the resonance surface closed. Hexapole fields can be generated using either a permanent magnet array or a superconducting magnet winding. Due to demagnetization issues the strength of the radial field achievable with permanent magnets is limited to 1.4 - 1.5 T at the wall of the plasma chamber. Additionally the permanent magnet hexapole can be constructed with either an open structure or closed Halbach structure [38]. The latter provides a higher magnetic field strength as the volume between the poles are filled with a magnetic material. It has however one distinct disadvantage in that it allows no radial access to the plasma chamber. In the overwhelming majority of magnetic field configurations currently used, the hexapole is positioned closer to the plasma chamber, with the solenoid coils wound around the hexapole. To date only for SECRAL (Superconducting ECR ion source with Advanced design

in Lanzhou) has this configuration been reversed [39].

The superposition of solenoidal and hexapolar fields results in a minimum magnetic field B_{min} in the center of the plasma chamber, with the magnetic field strength increasing in all directions from B_{min} outwards. It therefore becomes possible to define a closed surface i.e. ECR surface where the resonance condition is satisfied. The magnetic field configuration is depicted in Fig. 2 showing the magnetic field lines and the resonance surface of the JYFL 14 GHz ECRIS.

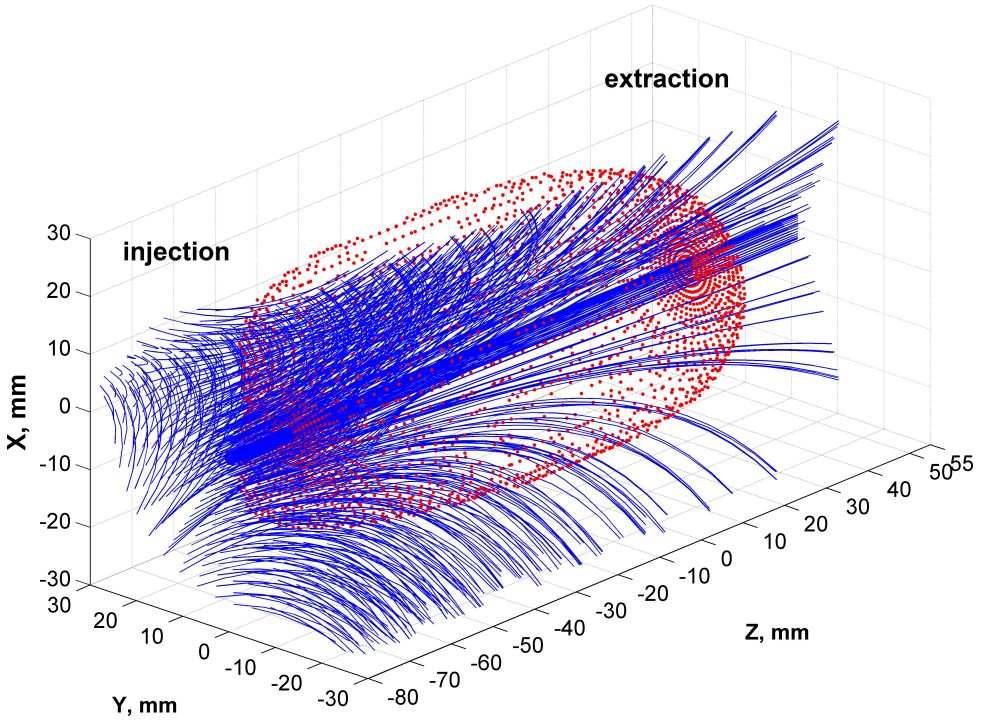

FIGURE 2 A schematic representation of the magnetic field lines (blue solid lines) and ECR resonance surface (red dots) of the JYFL 14 GHz ECRIS. This figure is adapted from Ref. [24].

Much of the improved performance of ECR ion sources over the years has come as a result of improving the magnetic confinement [40]. Based on experimental results the optimum fields should have the following characteristics [41]:

$$\frac{B_{inj}}{B_{ECR}} \geq 4 \qquad \frac{B_{ext}}{B_{ECR}} \geq 2 \qquad \frac{B_{rad}}{B_{ECR}} \geq 2 \qquad \frac{B_{min}}{B_{ECR}} \approx 0.8 \qquad \frac{B_{ext}}{B_{rad}} \approx 0.9 \tag{2.17}$$

where B_{inj} and B_{ext} are the maximum axial magnetic field strengths at injection and extraction, respectively, B_{rad} is the maximum radial magnetic field strength, B_{min} and B_{ECR} are as defined earlier. It is worth noting that increasing the operating frequency of an ECRIS, which is the common path towards better performance for HCS production, requires scaling the magnetic field which is perceived as the greatest challenge in ECRIS development.

Another important function of the minimum-B configuration is to reduce electron losses due to MHD instabilities. The minimum-B configuration suppresses MHD-driven electron losses by ensuring that the magnetic field pressure induced by the external magnetic field greatly exceeds the outward particle pressure. The particle pressure is mostly generated by the heated electrons. The criteria for suppressing MHD instability is given by $\beta \ll 1$, with β given by:

$$\beta = \frac{\text{particle pressure}}{\text{magnetic field pressure}} \approx \frac{n_e \Sigma k T}{B^2/2\mu_0} \tag{2.18}$$

where k is the Boltzmann's constant and μ_0 is the vacuum permeability. The summation in Eq. (2.18) is meant to be performed over all the different electron populations residing inside the ECRIS plasma. It is, however, emphasized that the majority of the plasma energy content (kinetic pressure) is carried by the warm and hot electron populations.

2.3.2 The loss cone in velocity space

From the discussion of the magnetic mirrors it is known that the electron loss rate is a strong function of the magnetic confinement field of the ECRIS. The B-field can be related to the velocity components $(v_\perp, v_\parallel)$ of the plasma electrons at every point along their trajectories inside the magnetic bottle. This relation is based on the conservation of the magnetic moment in Eq. (2.15), assuming no electric fields are encountered during the electron trajectories inside the magnetic bottle i.e. the electron's kinetic energy is conserved. From the description of the electron motion inside the magnetic bottle in section 2.3.1 it is known that the electron's perpendicular and parallel velocity components determine whether or not the electron remains confined or is lost. The velocity components can be plotted in the $v_\perp, v_\parallel$ plane to give a depiction of the electron behaviour in the so-called velocity space. This enables the definition of a conical boundary surface, in velocity space, with a pitch angle θ at any point z along the electron's trajectory inside the magnetic bottle. The pitch angle of the plasma electrons are defined by [11]:

$$\tan\theta = \frac{v_\perp(z)}{v_\parallel(z)} = \sqrt{\frac{W_\perp(z)}{W_\parallel(z)}} \tag{2.19}$$

Denoting B_{min} as the magnetic field strength at the center of the magnetic bottle (as defined earlier) and $B(z)$ as the magnetic field strength at an arbitrary point z inside the magnetic bottle. The pitch angles corresponding to the above-mentioned magnetic field strengths are θ_0 and θ, respectively. The invariance of μ, given by Eq. (2.15), leads to the following expressions:

$$\frac{\frac{1}{2}m_e v^2 \left(\sin^2\theta\right)}{B(z)} = \frac{\frac{1}{2}m_e v^2 \left(\sin^2\theta_0\right)}{B_{min}} \tag{2.20}$$

$$\frac{\sin^2\theta}{B(z)} = \frac{\sin^2\theta_0}{B_{min}} \tag{2.21}$$

where v is the speed of the plasma electron. The electron is reflected at $\theta = 90^\circ$ [42] corresponding to $B(z) = B_{max}$. This leads to the following expression for the pitch angle of a trapped electron:

$$\theta_0 = \sin^{-1}\sqrt{\frac{B_{min}}{B_{max}}} = \sin^{-1}\sqrt{\frac{1}{R_m}} \tag{2.22}$$

where R_m is known as the mirror ratio [11]. For an ECRIS with a fixed R_m, electrons with a pitch angle at B_{min} greater than θ_0 will be reflected before reaching B_{max}. Similarly plasma electrons with a pitch angle at B_{min} less than θ_0 will escape the confinement system of the ECRIS i.e. it will have a non-zero $v_{\parallel}$ at B_{max}. For an ECRIS B_{min} is typically replaced by B_{ECR} as the magnetic moment invariance is violated each time the electron passes through the resonance. Additionally collisions, which can alter the velocity components, are also explicitly ignored in the current discussion. Based on the argument developed above it becomes evident that a loss cone in three dimensional velocity space can be defined, as shown in Fig. 3. The fraction ξ of electron losses can be estimated by integrating over the defined loss cone in velocity space and is given by:

$$\xi = \frac{\int_0^v \int_0^{\theta_c} \int_0^{2\pi} v^2 \sin\theta dv d\theta d\phi}{\int_0^v \int_0^{\pi/2} \int_0^{2\pi} v^2 \sin\theta dv d\theta d\phi} = 1 - \cos\theta_c \tag{2.23}$$

where θ_c defines the boundary of the loss cone in velocity space. However the electron losses discussed thus far only apply when no ambipolar field is present inside the ECRIS plasma. As a result of the positive plasma potential build-up, as discussed in section 2.3.4, cold electron losses are reduced altering the boundary of the loss cone in velocity space [43]. Plasma electrons with kinetic energies below the plasma potential are electrostatically confined and only electrons with kinetic energies above the plasma potential can potentially be expelled into the loss cone. This results in a loss hyperboloid, as oppose to a loss cone, as shown in Fig. 4 and given by the following expression:

$$\theta_c = \sin^{-1}\left[\left(\frac{1}{R_m}\left(1 - \frac{v_{pe}^2}{v^2}\right)\right)^{\frac{1}{2}}\right] \tag{2.24}$$

where $v_{pe} = \sqrt{2eV_p/m_e}$ and V_p is the plasma potential [43]. Due to the plasma potential Eq. (2.23) is modified by replacing the 0 (lower boundary of the integral) with v_{pe}. The plasma electrons of an ECRIS which fall within the loss cone (or loss hyperboloid) are lost from the magnetic confinement system of the ECRIS, typically within a few micro-seconds of populating the loss cone [18]. For ions, especially for HCS ions, such loss cones are not relevant as they are confined electrostatically.

2.3.3 Electron loss processes

The electron losses from the magnetic bottle of an ECRIS are largely influenced by four processes, namely Coulomb collisions, microwave induced losses, inelas-

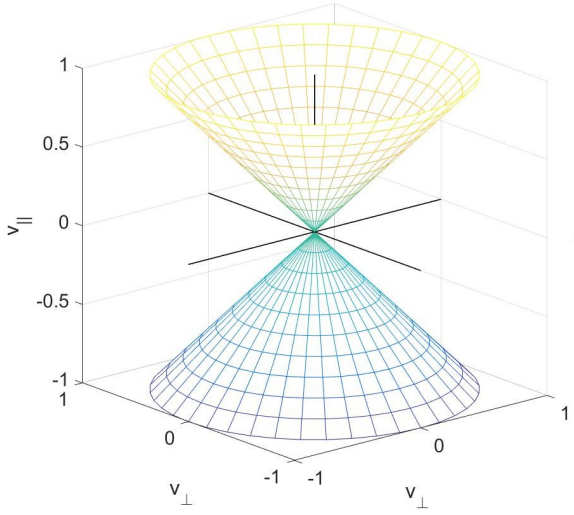

FIGURE 3 Loss cone for electrons.

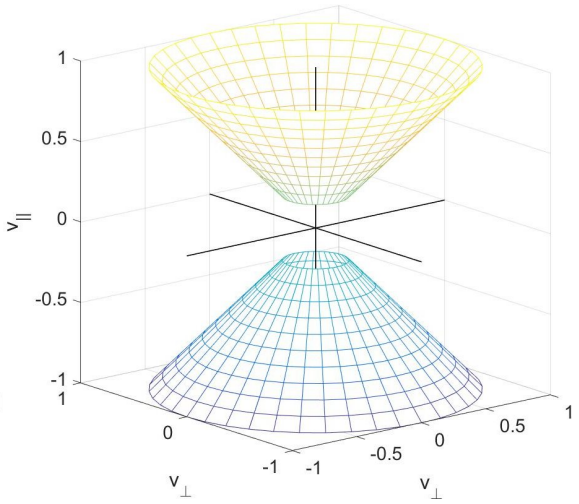

FIGURE 4 Loss hyperboloid for electrons.

tic (ionizing) losses and plasma instabilities. As a result of each of these loss processes, a fraction ξ of the plasma electrons can populate the loss cone. Upon entering the loss cone the plasma electrons drift azimuthally around the magnetic field lines, at the end of the magnetic bottle, until they find a region of weakest magnetic field and are subsequently lost from the ECRIS [18].

2.3.3.1 Collisional losses

Various types of collisions are possible in ECRIS plasmas as discussed in section 2.2. These collisions can be subdivided into inelastic and elastic collisions. The inelastic collisions result in ionization and excitation. The elastic collisions only change the trajectories of the colliding particles due to momentum transfer, leaving the internal energy state of the colliding particles unchanged. As a result of the collisions (elastic and inelastic) the pitch angles of the plasma electrons are altered, which results in collisional diffusion and electron losses from the magnetic confinement. The electron collision frequencies, as can be seen from Eq. (2.11) and Eq. (2.12), depend strongly on the temperature of the electron population with cold electrons suffering from collisional losses more than the hot electrons.

The fraction of electron losses as a result of elastic Coulomb collisions is actively being investigated, using various plasma diagnostics and numerical simulations [19]. When an electron approaches a charged particle it will be deflected, through a small angle, by the Coulomb field of the particle. The magnitude of the deflection is a strong function of the distance of approach and the energy of the plasma electrons. In ECRIS plasmas many so-called small angle deflections are required to result in a large angle of scattering [11]. As a result of these cumu-

lative Coulomb collisions the velocity components of the plasma electrons are altered. In so doing Coulomb collisions induce electron losses.

Inelastic ionizing collisions can influence electron losses from the magnetic confinement system of an ECRIS in at least two different ways. Firstly electron-impact ionization is mainly responsible for the production of the cold electron population of the ECRIS plasma. Given that the Coulomb collision frequencies scale with $T_e^{-\frac{3}{2}}$, see Eq. (2.11) and Eq. (2.12), the cold electron population with isotropic velocity distribution can easily be expelled from the ECRIS via any of the loss mechanisms assuming that the electron energies are sufficient to overcome the positive plasma potential. Hence the electron losses can be enhanced by electron-impact ionization. Secondly, the projectile electron which results in the removal of a bound electron loses energy during the ionizing interaction. As a result of this energy loss and redistribution of its velocity components, the incident electron might populate the loss cone and in so doing be expelled from the magnetic confinement of the ECRIS.

2.3.3.2 Radiofrequency (rf)-induced losses

Similar to Coulomb collisions, the injected microwave power into the ECRIS plasma can also induce electron losses. The main loss mechanism associated with the microwave power is pitch angle scattering due to the interaction with the magnetic field component of the injected EM-waves, given by:

$$B_{EM} = \frac{E_{EM}}{v_\phi} \tag{2.25}$$

where E_{EM} is the electric field component of the EM-wave. This interaction has first been studied theoretically by Kennel *et al.* [22][2]. Considering energy conservation in the frame moving with the wave, it can be shown that the electrons interacting with the right-hand circularly polarized (RHCP) electric field component of the EM-wave, of phase velocity v_ϕ, move in the velocity space along a circle defined by:

$$v_\perp^2 + \left(v_\parallel - v_\phi\right)^2 = a^2 \tag{2.26}$$

where a is a constant [22]. It is convenient to express Eq. (2.26) in spherical polar coordinate system (v, ψ, ϕ) in the velocity space, where v is the electron speed, $\arccos\psi$ is the pitch angle, i.e. $\psi = \frac{v_\parallel}{v}$, and ϕ is the angle about the axial magnetic field [44]. Equation (2.22) then becomes

$$v^2 - 2v\psi v_\phi = b^2 \tag{2.27}$$

[2] To the author's best knowledge, the rf-induced pitch angle scattering has also been studied independently in the Soviet Union. However, the work has been published in Russian journals and never translated to English.

where b is yet another constant [44]. Differentiating Eq. (2.27) yields the increments $(\Delta v, \Delta\psi)$ in velocity and pitch angle during the interaction, i.e. [44]

$$\Delta v \left(\frac{v}{v_\phi} - \psi \right) - v\Delta\psi = 0 \tag{2.28}$$

In order to understand microwave induced loss processes we need to consider two cases defined by the phase difference between the electron gyromotion and the electric field of the microwaves i.e. (a) $\Delta v > 0$ and (b) $\Delta v < 0$ corresponding to acceleration or deceleration of electrons at the resonance, respectively.

1. Electron energy gain $(\Delta v > 0)$: It follows from Eq. (2.28) that if $\left(\frac{v}{v_\phi} - \psi \right) < 0$, then $\Delta\psi < 0$, similarly if $\left(\frac{v}{v_\phi} - \psi \right) > 0$, then $\Delta\psi > 0$. We may rewrite this condition as $\frac{v}{v_\phi} \lessgtr \frac{v_\parallel}{v}$. It is evident from $v^2 = v_\parallel^2 + v_\perp^2$ that $\frac{v_\parallel}{v} \leqslant 1$ and hence the condition for microwave heating improving electron confinement (decrease of ψ) becomes $\frac{v}{v_\phi} < 1$ i.e. $v < v_\phi$. On the contrary, microwave heating induces electron losses (increase of ψ) if $\frac{v}{v_\phi} > 1$ i.e. $v > v_\phi$. Since electrons with velocities above the phase velocity are mainly pitch-angle scattered, the maximum mean velocity of the electron distribution function is the phase velocity at the resonance.
2. Electron energy loss $(\Delta v < 0)$: Applying similar reasoning as above, it follows from Eq. (2.28) that $\Delta\psi \lessgtr 0$ when $v \gtrless v_\phi$ i.e. for electron velocities less than the phase velocity of the EM-wave, the electron confinement is weakened by the interaction between electrons and the microwave electric field in decelerating phase. On the other hand, electrons whose velocity exceeds the phase velocity become better confined as a result of interacting with the magnetic field of the EM-wave despite of their energy loss.

All of the interaction mechanisms identified above play a role in ECRIS plasmas. However, improvement of electron confinement due to pitch angle scattering $(\Delta v, \Delta\psi < 0)$ is of negligible importance since, due to the nature of the interaction between the electrons and the microwave EM-field the loss cone can be considered to be empty at high electron energies (as discussed in Ref. [PIV]) and is populated by pitch angle scattering when $\Delta v > 0$. This results to a stochastic diffusion coefficient $D_{\mu\mu}$ in pitch angle which can be defined as [43]:

$$D_{\mu\mu} = \pi \left(\frac{eE}{2m_e} \right)^2 \frac{d}{L\omega} \left(\frac{v}{v_p} \right)^2 = D_{vv} \left(\frac{v}{v_p} \right)^2 \tag{2.29}$$

where d is the characteristic length for the magnetic field gradient, L the characteristic plasma length and ω the microwave (angular) frequency. D_{vv} corresponds to the velocity diffusion coefficient. In ECR-heated plasmas the phase velocity of the wave becomes smaller and smaller as the wave approaches resonance and thus pitch angle scattering by the magnetic field of the EM-wave presumably limits the plasma energy density [44].

The phase velocity of the EM-wave can be estimated from the following expression [45]:

$$\frac{v_p}{c} = \frac{1}{\pi^{\frac{1}{6}}} \left(\frac{\omega}{\omega_{pe}} \right)^{\frac{2}{3}} \left(\frac{\langle v \rangle}{c} \right)^{\frac{1}{3}} \tag{2.30}$$

where ω_{pe} is the plasma oscillation frequency, c is the speed of light in vacuum and $\langle v \rangle$ is the mean velocity of the Maxwellian electron distribution. The plasma oscillation frequency is given by the following expression:

$$\omega_{pe}^2 = \frac{n_e e^2}{m_e \epsilon_0} \tag{2.31}$$

From this expression it is clear that the electron losses is influenced by the electron density with pitch angle scattering becoming increasingly effective at high plasma densities approaching the critical density, which could be reached in the plasma core [46]. The critical density is defined as the electron density at which the natural plasma oscillation frequency exceeds the frequency of the microwaves sustaining the plasma, thus ceasing the wave propagation. This density scales with the square of the microwave frequency and is approximately 2.4×10^{12} cm^{-3} for 14 GHz microwaves. However, the estimate of the phase velocity given by Eq. (2.30) does not take into account the fact that the phase velocity is reduced from the value given Eq. (2.30) as the wave approaches the resonance. This is thoroughly discussed in Refs. [21, 47]. The actual phase velocity at resonance is estimated to be reduced by at least an order of magnitude [47] from the value given by Eq. (2.30). The role of rf-induced electron losses is studied and discussed in Ref. [PIV].

2.3.3.3 Plasma instabilities

Finally electron losses can also be caused by plasma instabilities. A prime example of such instabilities is the kinetic electron cyclotron instability driven by the hot electron population of an ECRIS [24]. As a result of the strong anisotropy of the EEDF, plasma waves that periodically expel hot electrons from the magnetic confinement are excited. The electron losses as a result of kinetic instabilities were found to be largely influenced by the B_{min}/B_{ECR}-ratio [24], which controls the transition from stable to unstable plasma regime.

2.3.4 Ambipolar confinement

As suggested earlier, the collisional ion component (specifically HCS ions) of an ECRIS plasma is poorly confined by the magnetic field. This emphasizes the need for an alternative confinement scheme for ions, first suggested by Canobbio *et al.* for fusion research purposes [11]. The confinement scheme is driven by the plasma requirement to sustain charge-neutrality, given by the following expres-

sion:

$$n_e = \Sigma_Z Z \cdot n_i \tag{2.32}$$

In the plasma core, the hot electrons are very well confined by the magnetic field and are practically collisionless. This results in an increased density of hot electrons in the inner region of the plasma as indirectly detected by Ropponen *et al.* [48]. The hot electrons generate a potential dip $\Delta\phi$ in the plasma core as formulated by Shirkov [36]. To preserve charge-neutrality, the hot electron population confines ions via its so-called ambipolar field. It is this confinement scheme which traps the ions and is suggested to lead to enhanced ion confinement in the plasma core. The resulting expression for the ion confinement time in terms of this model is given by [49]:

$$\tau_q = R\frac{\sqrt{\pi}L}{v_{T_i}} \exp\left(\frac{|qe\Delta\phi|}{kT_i}\right) \tag{2.33}$$

where L is the half-length of the plasma and v_{T_i} is the ion thermal velocity. This expression however becomes questionable at high densities [27] which has led to an alternative expression for the ion confinement time. The parallel (relative to the magnetic field vector) confinement time of an ion with charge state q can be estimated with the following expressions [27]: (units: τ, s; L, cm; n_e, cm^{-3}; T_i, eV; E, V/m)

$$\tau_q = 7.1 \times 10^{-20} Lq \ln\Lambda\sqrt{A}\frac{n_e Z_{\text{eff}}}{T_i^{3/2}E} \tag{2.34}$$

$$\tau_q = 7.1 \times 10^{-20} L^2q^2 \ln\Lambda\sqrt{A}\frac{n_e Z_{\text{eff}}}{T_i^{5/2}} \tag{2.35}$$

where A is the atomic mass number, $Z_{\text{eff}} = \Sigma_q n_q q^2/n_e$ is the effective charge of the plasma.

Given that the cold electron population of an ECRIS plasma is highly collisional i.e. $\nu_{ee}, \nu_{ei} \sim T_e^{-\frac{3}{2}}$, cold electrons are most easily expelled from the magnetic confinement system of an ECRIS, with warm and hot electrons remaining well confined. The enhanced cold electron losses and the higher mobility of electrons in comparison to ions perturbs the charge-neutrality condition. To maintain charge-neutrality, the plasma builds up a positive 10 - 60 V [50] ambipolar plasma potential, with respect to the plasma chamber walls, which regulates the cold electron losses mostly from the peripheral plasma outside the core plasma surrounded by the resonance zone. The positive plasma potential enhances ion losses from the ECRIS plasma and in so doing ensures charge-neutrality. It is thus beneficial for ion confinement and HCS production to minimize the plasma potential. Finally, the existence of the potential dip implies that HCS ions reside near the source axis, which is consistent with emittance measurements [51].

2.4 The properties of ECRIS plasma for high charge state production

To produce HCS ions, the plasma of an ECRIS needs to have certain desirable properties. These properties have been articulated by Shirkov *et al.* in formulating a set of non-linear differential equations. The equations describe the time evolution of ion densities of the different charge states present inside an ECRIS plasma and are given by the following expression [52]:

$$\sum_{q=1}^{Z} \frac{dn_i^q}{dt} = n_e n_i^{q-1} \langle \sigma_{ion}^{q-1 \to q} v \rangle - n_e n_i^q \langle \sigma_{ion}^{q \to q+1} v \rangle + n_0 n_i^{q+1} \langle \sigma_{cx}^{q+1 \to q} v \rangle - n_0 n_i^q \langle \sigma_{cx}^{q \to q-1} v \rangle - \frac{n_i^q}{\tau_i^q} \quad (2.36)$$

where n_i^{q-1} is the ion density of ions with charge state $q-1$, n_i^q is the ion density of ions with charge state q, n_i^{q+1} is the ion density of ions with charge state $q+1$, n_0 is the neutral density, $\langle \sigma_{ion}^{q-1 \to q} v \rangle$ is the ionization rate coefficient from charge state $q-1$ to q, $\langle \sigma_{ion}^{q \to q+1} v \rangle$ is the ionization rate coefficient from charge state q to $q+1$, $\langle \sigma_{cx}^{q \to q-1} v \rangle$ is the charge exchange rate coefficient from charge state q to $q-1$, $\langle \sigma_{cx}^{q+1 \to q} v \rangle$ is the charge exchange rate coefficient from charge state $q+1$ to q, τ_i^q is the confinement time of ions with charge state q and Z is the number of electrons of the neutral gas atom. When all the processes described by Eq. (2.36) have reached a state of equilibrium, the set of equations relaxes to a set of stationary balance equations i.e. $\sum_{q=1}^{Z} \frac{dn_i^q}{dt} = 0$. From this set of stationary balance equations, three conditions can be listed that should prevail inside the ECRIS plasma for optimal HCS ion production.

The first condition to maximize HCS ion production, is an optimum ionization rate. Figure 5 shows a typical charge state distribution (CSD) measured with the source optimized for Ar^{13+} production. The peak of the distribution ($\sim Ar^{10+}$) is defined by two plasma parameters i.e. plasma energy content $n_e kT$ and the ion confinement time. The plasma energy content is defined by the electron energy distribution which affects the rate coefficients for each ionization process.

Figure 6 presents the cross section for electron-impact ionization of Ar^{4+} and Ar^{12+}, as a function of the electron energy leading to Ar^{5+} and Ar^{13+}, respectively. From this figure it is apparent that the optimum ionization rate of an ECRIS plasma for a specific charge state is a strong function of the electron energy (or kT of the commonly assumed Maxwellian distribution). The cross section (and rate coefficient) for Ar^{5+} production is approximately an order of magnitude larger than that for Ar^{13+} production. Similarly it can be seen that a threshold energy is required to produce both ion species, with the threshold energy for Ar^{13+} production being significantly higher. Both these observations imply

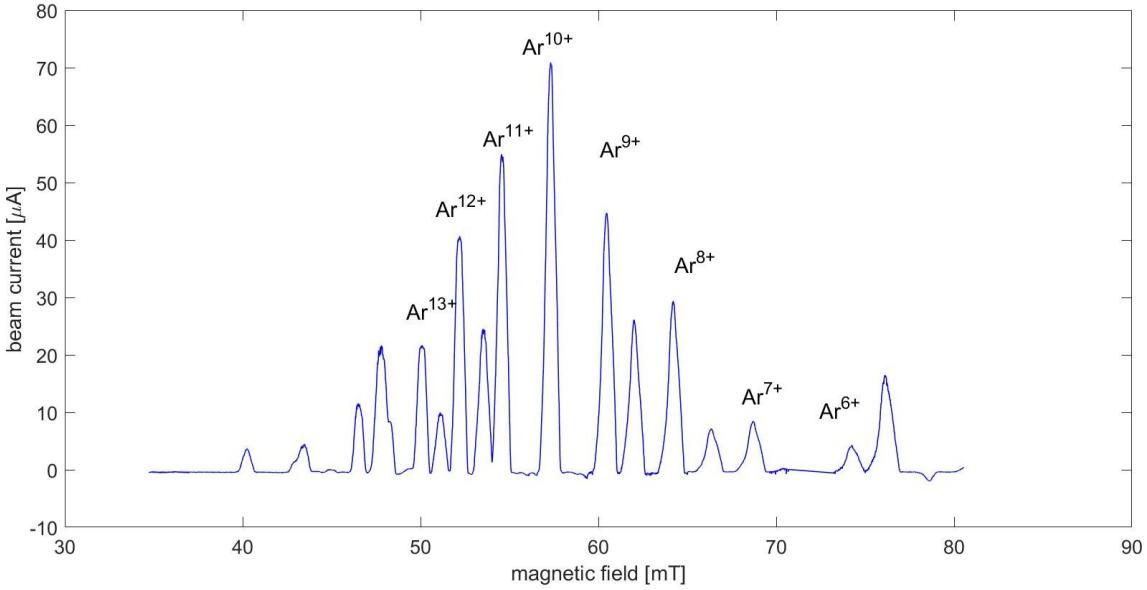

FIGURE 5 A typical extracted charge state distribution measured from the JYFL 14 GHz ECRIS with the source optimized for Ar^{13+} production.

that the EEDF of the ECRIS plasma should be tailored to the specific optimum charge state required. To accomplish this difficult task it becomes necessary to obtain knowledge on the parameters affecting the EEDF. To achieve this feat numerous attempts have been made in the past to measure the EEDF using the bremsstrahlung radiation [15] and more recently by measuring the electron losses from the ECRIS plasma [30]. Another important plasma parameter which can significantly influence the ionization rate is the warm electron density. To measure this important plasma parameter, plasma diagnostics such as diamagnetic loops and microwave interferometry are commonly used [17]. The typical electron density in ECRIS plasma is believed to be on the order of 10^{11} cm^{-3} i.e. below the critical density, which is approximately 2.4×10^{12} cm^{-3} for second generation 14 GHz sources.

The second condition that should prevail inside an ECRIS plasma to facilitate increased HCS ion production through stepwise ionization is increased ion confinement time τ_i. This requirement however needs to be balanced against beam extraction as ion losses via diffusion and other transport processes into the extraction aperture constitutes a favourable loss process. This implies that by increasing the ion confinement time, the ion losses from the plasma will decrease resulting in reduced beam extraction. Thus, optimizing the ion confinement time for the production of ion beam of a specific charge state is all about finding a balance between the production and loss rates of the ions, which needs to be done experimentally by changing the microwave power, gas feed rate and magnetic field strength. This process, based on trial and error, is often referred to as ion source tuning.

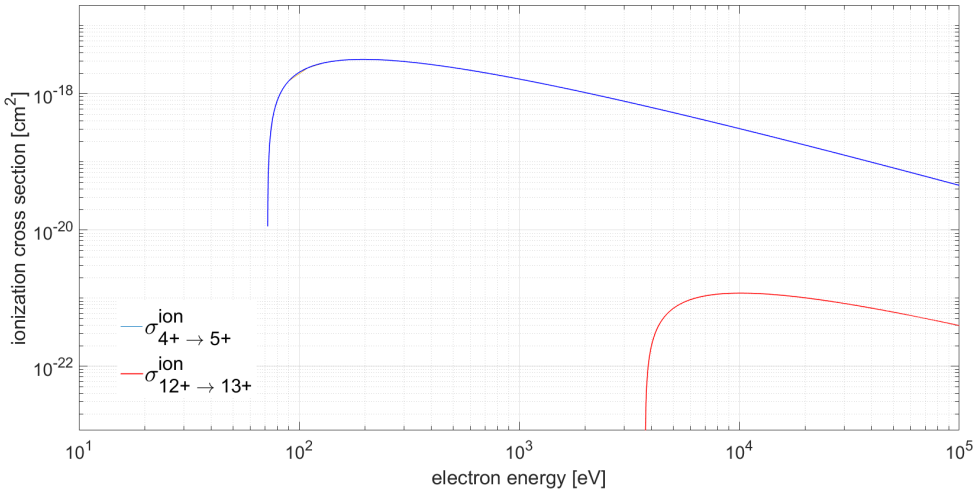

FIGURE 6 Comparison of the electron-impact ionization cross sections of argon $\sigma^{\text{ion}}_{4+\rightarrow 5+}$ and $\sigma^{\text{ion}}_{12+\rightarrow 13+}$, as a function of the electron energy.

The third condition required for optimal HCS ion production is minimal neutral pressure. The high charge state tail seen in Fig. 5 (i.e. Ar^{11+} - Ar^{14+}) is dictated by the neutral pressure through charge exchange processes. This refers to the interaction between a HCS ion and a neutral atom or lower charge state ion, in which an electron is exchanged between the two participants. As a result of this interaction, HCS ions are destroyed decreasing the mean charge state of the ECRIS plasma. The cross section for charge exchange (in units of cm^2) can be estimated with the following expression [53, 54]:

$$\sigma_{cx} \approx 1.43 \times 10^{-12} \cdot q^{1.17} \cdot P^{-2.76} \tag{2.37}$$

where q is the initial charge state of the ion species and P is the first ionization potential of the ion in eV. From this expression it is clear that the cross section for charge exchange increases if the charge state of the ion increase and as the ionization potential decreases. Charge exchange between the highest charge state ion species present inside the ECRIS plasma and neutral gas atoms therefore account for the bulk of the loss processes of HCS ions through charge exchange. This condition dictates excellent base pressure in the plasma chamber of the ion source. Typical base pressure of most modern ECRISs are in the region of 10^{-8} mbar. This requires very efficient pumping systems and conditioning the plasma chamber for many hours after exposing the plasma chamber to atmospheric pressure.

2.5 The main tuning parameters of an ECRIS

Arguably the greatest challenge to accurately predicting the performance of an ECRIS comes from the tenuous relationship between the internal plasma parameters and the external variables. Most high-performance ECR ion sources operational today have a minimum of three externally adjustable variables i.e. magnetic field, gas flow and microwave power with which the source performance can be optimized. The precise quantitative influence of each of these so-called tuning parameters on the ECRIS performance is actively being studied using a variety of experimental and computational tools. While these investigations have significantly advanced the current understanding of the field, the total influence of each tuning parameter remains incomplete. This has resulted in a number of semi-empirical ECRIS scaling laws being proposed for improved HCS ion production, which can be summarized as follows [11, 55]:

$$I^q \propto \omega_{\mathrm{RF}}^2 m_i^{-1} \tag{2.38}$$

$$n_e v_e \tau \propto \begin{cases} B_{\mathrm{ave}}^{\frac{3}{2}} \\ \omega_{\mathrm{RF}}^{\frac{7}{2}} \end{cases} \tag{2.39}$$

$$q_{\mathrm{opt}} \propto \begin{cases} \log B_{\mathrm{ave}}^{\frac{3}{2}} \\ \log \omega_{\mathrm{RF}}^{\frac{7}{2}} \\ P_{\mathrm{RF}}^{\frac{1}{3}} \end{cases} \tag{2.40}$$

where q^{opt} is the charge state yielding the highest output current, I^q is the value of the current of charge state q, v_e is the electron velocity, τ is the confinement time, ω_{RF} is the angular microwave heating frequency, m_i is the mass of the ion, P_{RF} is the incident microwave power and $B_{\mathrm{ave}} = \frac{1}{2}(B_{max} + B_{min})$ is the average magnetic field. In the following section the qualitative influence of each of the three tuning parameters, as well as the influence of the microwave heating frequency, will be briefly discussed.

The most influential parameter which impacts the beam current of a particular charge state is the microwave heating frequency, as shown by Eq. (2.38). However, increasing the microwave frequency has implications on the other tune parameters. For example, the maximum solenoid and hexapole fields at the plasma chamber wall, which fulfils the scaling law on microwave frequency is beyond the practical limit set by room temperature magnets [14]. This makes the use of superconducting technology for the magnetic confinement field of an ECRIS mandatory for 3$^{\mathrm{rd}}$ and 4$^{\mathrm{th}}$ generation sources which complies with the scaling laws. Additionally the emittance of the ion beam scales with the magnetic field at extraction which poses problems at strong B-field. Several explanations have been proposed for the effectiveness of frequency scaling. These include reduced damping of the microwave electric field at resonance and reduced electron losses

due to rf-pitch angle scattering, both of which scale with the square of the microwave frequency [14]. Modern ECRISs operate at frequencies of 18 – 45 GHz.

The magnetic field, as discussed earlier, is known to confine charge particles, particularly warm and hot electrons. For room temperature ECR ion sources the magnetic field is adjusted by varying the current flowing through the solenoid coils of the magnetic confinement system. For superconducting ion sources it is also possible to adjust the hexapole field. Most modern ECR ion sources operational today employ the minimum-B configuration. By adjusting the solenoid coil current (or the hexapole field in the case of superconducting ion sources) the B_{min}-field is indirectly adjusted. Additionally such an adjustment also influences the magnetic field gradient on the resonance surface which impacts plasma heating. Finally this adjustment could also affect the plasma stability as defined by β. The magnetic field scaling is thoroughly discussed in Ref. [56].

The gas flow controls the amount of gas atoms or molecules injected into the plasma chamber. The influence of this tuning parameter on ion beam production is described by the rate coefficients for the various processes impacting ion production. By comparing the cross section for each of these processes it can be seen that HCS ion production is predominately affected by electron-impact ionization and charge exchange. To minimize the impact of charge exchange on HCS ion production, the neutral gas flow should be minimized yet supplying a sufficient number of atoms to reach the desired beam current. As an example, the peak cross section for charge exchange of Ar^{8+} with a neutral gas atom is approximately 2000 greater than the ionization cross section of Ar^{8+} [57], highlighting the need for minimal gas flow rates. It must be emphasized though that the actual process rates also depend on the particle densities. Additionally it is also extremely difficult, if not impossible, to relate the amount of gas injected into the plasma chamber to the pressure at the resonance zone. This strengthens the need and significance of numerical simulations [58]. Given that the pressure at the resonance zone is unknown, the optimum gas flow is usually deduced from other measurable quantities such as the extracted ion beam current [59]. If the gas flow is more than the required optimum, charge exchange will reduce the density of the HCS ions. If the gas flow is below the optimum, the ion density and extracted current of HCS ions are low due to the low ionization rate of HCS ions.

The influence of the microwave power on ion production is arguably the most complex of all the tuning parameters. As a start not all of the microwave power launched from the external power source is injected into the plasma chamber. A fraction of the power is lost in the transmission system and reflected back from the waveguide transitions and the imperfect load of the plasma. In addition to this the microwaves propagate undisturbed outside the plasma volume, however inside the plasma volume the wave propagation is strongly disturbed by the plasma electrons. Due to their huge mass, relative to the electrons, the ions do not

respond to the microwave fields. Additionally only the electric field component of the injected microwaves interact with the electrons, with the magnetic field component being negligible in comparison to the imposed magnetic field. The effect of the microwave magnetic field component only becomes important as the phase velocity of the waves decreases, leading to electron losses as discussed in section 2.3.3.2. To estimate the effect of the electric field at the resonance on electron heating, the plasma chamber of the ECRIS can be considered as a resonating cavity [47], filled by a medium (plasma) with a certain dielectric constant. As a result of the microwave power introduced into the cavity, a wave structure is excited inside the cavity. For a plasma chamber quality factor Q, the relation between the electric field at the resonance E_{ECR} and the absorbed microwave power P is given by the following expression:

$$E_{ECR} \propto Q\sqrt{P} \tag{2.41}$$

where the Q-value is affected by the plasma properties and distribution as discussed in Ref. [60].

From the frequency scaling discussed above it is known that the maximum beam current extracted from an ECRIS plasma scales with the square of the microwave frequency. However, this scaling should be accompanied by a corresponding increase in microwave power. The scaling of the microwave power with ion beam current was determined to be linear over a significant range of powers [61]. From such power scaling estimates and operational experience it is known that for a 28 GHz ECRIS (such as VENUS) 10 kW of power is required, whereas 26 kW of power is required for a 45 GHz ECRIS and 40 kW of power for a 56 GHz ECRIS [40]. Such power and frequency scaling also has implications on the source extraction voltage (V_{ext}) to control space charge effects [40] resulting in the following proposed scaling:

$$V_{\text{ext}} \propto \omega_{\text{RF}}^{4/3} \tag{2.42}$$

This scaling ensures that the extracted ion beam maintains the same transverse dimensions [40]. Lyneis suggests that the VENUS source requires 30 kV to transport 20 mA of extracted ion beam current, with 56 kV required for 45 GHz ECRIS and 75 kV required at 56 GHz [40].

2.6 Techniques to improve ECRIS performance

To further improve the performance of an ECRIS it becomes mandatory to increase the number of tune parameters with which the source performance can be optimized, in addition to those given by the scaling laws (power, B-field, frequency, etc.). This requirement has led to a number of techniques devised over the years which alter the fundamental plasma parameters for example electron density, ion confinement time and plasma potential, resulting in enhanced HCS

production. While many of these techniques are commonly practised on various ECRISs, the underlying physics governing them remain not completely understood. With the advent of improved plasma diagnostics and computational tools, these techniques can now be studied to resolve the complex plasma interactions leading to its success. In the following section three of these techniques are briefly discussed. This discussion aides in understanding the experimental results presented in section 4.

2.6.1 Multiple frequency heating

From the discussion of the minimum-B field it is known that the surface over which ECR heating occurs is closed, with a thickness partly defined by the spread of electron energies. For a single heating frequency, an egg-shaped ECR heating surface is generated over which the average electron energies are successively increased upon crossing the resonance zone. This creates the warm and hot electron populations of the EEDF. If two or more heating frequencies are simultaneously launched into the plasma chamber and the resonance condition is satisfied for each injected frequency, multiple ECR heating surfaces can be generated. This situation is illustrated for two heating frequencies by the schematic presented in Fig. 7. If the secondary heating frequency is below the primary and the corresponding resonance field exceeds the minimum field at the trap center, the resulting secondary resonance zone is enclosed by the primary resonance zone , due to the minimum-B topology, as illustrated in Fig. 7. This could in principal increase the number of heated electrons and has been demonstrated to increase HCS production by up to an order of magnitude [62]. The effect of the secondary (or multiple) heating frequency becomes increasingly evident with increasing charge state of the ion. It has been observed for example that O^{6+} and O^{7+} ion current increased by a factor of ~ 2 when the secondary frequency was applied [63]. In addition to this, multiple frequency heating operation improves the source efficiency [63] and suppresses plasma instabilities [64].

Heating the plasma electrons of an ECRIS with multiple heating frequencies has first been realized and demonstrated on the Lawrence Berkeley National Laboratory (LBNL) Advanced ECR (AECR) ion source [65]. The technique is most commonly implemented by heating the plasma electrons simultaneously with two power sources. This is largely driven by certain experimental investigations which report minimal or no increased source performance with the addition of a third heating frequency [62, 63] . With so-called double-frequency heating the primary power is usually delivered from a fixed frequency amplifier such as a klystron or a gyrotron and the second heating frequency is provided by a variable frequency power generator such as a broadband traveling wave tube amplifier (TWTA). Apart from the power delivered from the TWTA, this heating scheme

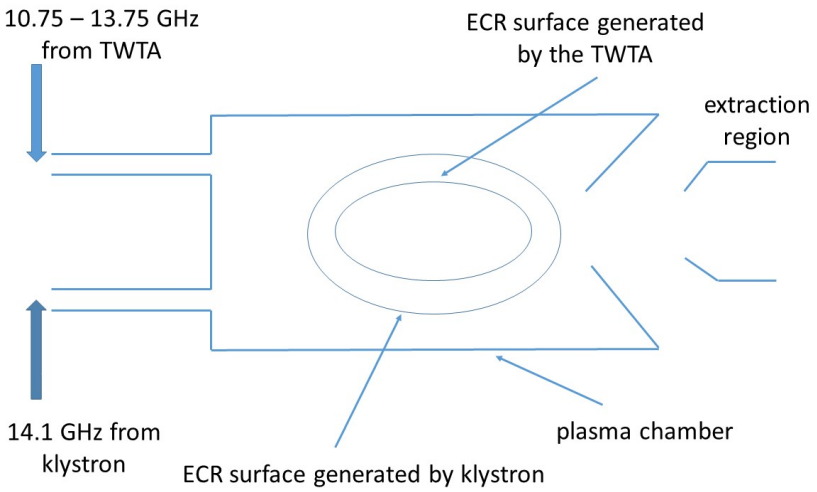

FIGURE 7 Schematic view of the ECR surfaces with two heating frequencies. The frequencies correspond to those used in the JYFL 14 GHz ECRIS.

provides an additional tune parameter, i.e. frequency tuning of the TWTA, with which the source can be tuned. The coupling efficiency between the microwave power and the plasma is however usually different for the two power sources [66]. Multiple explanations have been proposed for the effectiveness of double-frequency heating. This includes efficient heating resulting to modified plasma parameters (n_e and T_e) [63], lowering of the plasma potential [50], modifying the plasma (potential) structure [63] and improving plasma stability [64, 66].

2.6.2 Gas mixing

The gas mixing effect, discovered in 1983, entails mixing a lighter gas species into the plasma of an ECRIS, resulting in enhanced HCS production of the heavier element [67]. The technique is widely practiced, but similar to multiple frequency heating, is not entirely understood. Based on systematic investigations, it has been shown that the mass of the mixing gas A_{mix} should be less than the mass of the working gas species to be ionized A_{beam}, where A is the isotopic mass number. It has however been observed that this requirement is not sufficient for improved source performance. As an example, it has been found that nitrogen in some instances (despite its relative light mass) is a poor mixing gas [68]. This abnormality has recently been studied with numerical simulations by Mironov *et al*. Based on this investigation it was suggested that the spatial distribution of the ion density could account for the abnormality observed experimentally with this mixing gas [58].

Various explanations have been advanced to explain the beneficial influence of the gas mixing on HCS production. One of the first plausible explanations ad-

vanced for the beneficial effect of the gas mixing was proposed by Geller *et al.* In terms of this explanation it was suggested that the increase of energy lifetime of the ions was the mechanism responsible for the favourable effect [55]. The energy lifetime of the ions is inversely proportional to the average charge state inside the ECRIS plasma. Hence, by reducing the average charge state by introducing the lighter gas with lower Z, the ion confinement is increased resulting in enhanced HCS production. Antaya *et al.* proposed a different explanation accounting for the beneficial effect of the gas mixing [69]. In terms of their explanation the heavier energetic HCS ions collide with the lighter mixing gas ion species. During this encounter energy is exchanged between the two ion species with the lighter ion species being heated and the heavier ion species being cooled. In the elastic limit, the maximum energy transferred in a single collision increases with increasing mass of the lighter gas species, given by [69]:

$$\frac{E_2^{\max}}{E_1} = \frac{2A_1A_2}{(A_1 + A_2)^2} \tag{2.43}$$

where $E_2^{\max}$ is the maximum energy transferred to the mixing gas, A_2 is the mass of the mixing gas, A_1 is the mass of the working gas and E_1 is the initial energy of the working gas. The reduction in energy of the heavier gas species implies better confinement resulting in enhanced HCS production. This explanation has become known as the ion cooling effect. The ion cooling process was also studied with the numerical code of Jongen [70], showing a reduction in energy spread, which strengthens the argument for ion cooling. Evidence for the ion cooling effect were also presented by Tarvainen *et al.* who measured the energy spread of different charge state ion beams and concluded that gas mixing affects predominantly the effective temperatures of the low charge state ions of the lighter element [71]. It should be mentioned that 'heating' the light ion species should deteriorate their confinement. The important role of the low charge state ions has also been emphasized by Drentje *et al.* [72]. Yet another explanation for the favourable influence of the gas mixing credits the increase in electron density, resulting in increased ionization rate [73]. A final explanation stems from plasma potential measurements performed on AECR at LBNL. In terms of this explanation it is suggested that an improvement in plasma stability leads to enhanced HCS production [74].

2.6.3 Biased disc

The biased disc is a probe which is insulated from the plasma chamber and installed at the tip of the injection plug of the ion source. It can be negatively biased up to a few hundred volts and has been proven to have a positive effect on the source performance [35]. The exact reason for the positive influence remains unclear. A plausible explanation is based on the idea of emission of cold secondary electrons as a result of impact with positive ions accelerated into the biased disc. The plasma flux impinging on the biased disc is dictated by the magnetic field

lines. This process has been studied with the TrapCAD code [75] which led to the conclusion that the shape of the biased disc is not of significant importance [76]. The optimal shape should presumably coincide with the plasma flux. Another plausible explanation for the effectiveness of the biased disc relates to the so-called Simon short-circuit currents [77]. As a result of the plasma dynamics, a fraction of the electron and ion fluxes bombard the various surfaces surrounding the plasma e.g. the biased disc and plasma chamber walls. The sum of all of these currents including the drain current has to equate to zero to retain the quasi-neutrality of the plasma [78] and to maintain temporal equilibrium. As a result of the 'current perturbation' introduced by the applied voltage of the biased disc, the overall balance between radial ion losses and axial electron losses is altered. This results in a suggested increase in electron density as well as an increase in ion confinement, both due to the reduced ion and electron losses. The biased disc can also be used as a primitive Langmuir probe to study the ECRIS plasma [79, 80]. However the main drawback of this approach is that the biased disc alters the plasma conditions, distorting the results if the voltage is swept similar to traditional probe measurements. In charge breeder ECRIS there is no biased disc as the 1+ injection is realized through the injection iron plug leaving no space for the electrode, thus prohibiting the use of the method in that case.

2.7 Characteristic X-ray emission and inner shell ionization

To describe the various properties of an atom consisting of a nucleus of protons and neutrons orbited by Z electrons, the atomic system needs to be considered as a collective. In such a system, the electron motion can be approximated in an electrostatic field of the (stationary) nucleus and the Z electrons of the atom. This description of the atomic system is commonly known as the central-field approximation [81]. The orbitals of the Z electrons around the nucleus are called electron shells, depicted in Fig. 8 for argon. The electron shells of an atom are denoted by either the principal quantum number n or a capital letter. In this nomenclature the shell closest to the nucleus is termed the K-shell or $n = 1$. This is followed by the L-shell or $n = 2$ and the M-shell or $n = 3$, etc. Each of the electron shells can at most be occupied by a fixed number of electrons as stipulated by the Pauli exclusion principle for fermions, with electrons of the same principal quantum number termed equivalent electrons. The distribution of electrons amongst the different shells and subshells of the atom is known as the electron configuration. From Fig. 8 it can be seen that argon, similar to all noble gases, have a closed outer subshell which makes such gases chemically inert. In the central-field approximation, the energy of an electron is completely described by specifying the electron configuration nl, where l is the orbital angular momentum. If however the magnetic interactions between the orbital angular momentum and the elec-

tron spin are taken into consideration, the energy of the electron is specified by nlj where $j = l + s$ is the total angular momentum [20]. The resulting discrete electron energies of the atom are called energy levels. The possible energy levels of an atom can be conveniently depicted by means of an energy level diagram or so-called Grotrian diagram [82].

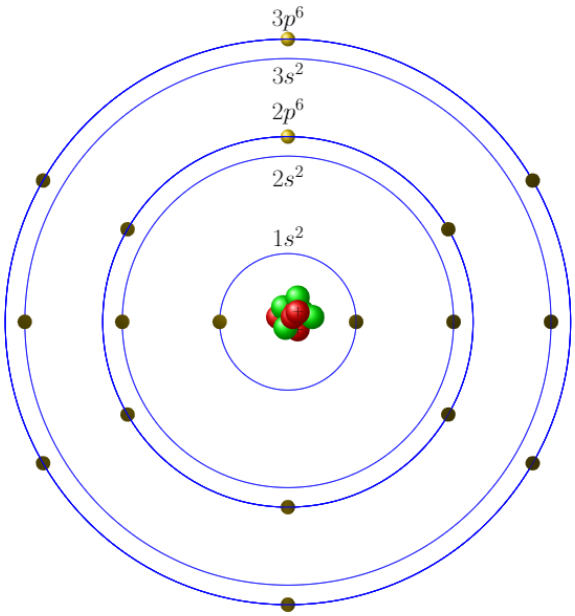

FIGURE 8 Schematic of the electron shell structure of a neutral argon atom, with electron configuration $1s^2 2s^2 2p^6 3s^2 3p^6$.

When a vacancy exists in one of the inner shells of an atom (with bound outer shell electrons), the atom is in an excited state and the inner shell vacancy must be filled for the atom to return to the ground state or lowest energy state. As stated earlier, in this context atom refers to both a neutral atom and an ion. Such a vacancy can be filled by either a radiative or a radiationless transition. In filling the vacancy an electron moves from a higher energy level E_2 to a lower energy level E_1. If the vacancy is filled by a radiative transition, the electron transition (from $E_2 \rightarrow E_1$) is accompanied by emission of a photon of energy $\Delta E = E_2 - E_1$. Similarly, if the vacancy is filled by a radiationless transition, the electron transition is accompanied by either ejection of a second Auger electron [83, 84] or by an electron transition between subshells having the same principal quantum number [85]. The former radiationless transition is called an Auger transition and the latter Coster-Kronig transition. During the Auger process the energy released in filling the vacancy is transferred to another electron, commonly an outer shell electron. If the transferred energy ΔE is greater than the binding energy of the second electron, this electron i.e. Auger electron is ejected from the atom with a certain kinetic energy. The Coster-Kronig transition is considered as a special case of the Auger process. The total rate S at which vacancies are filled is given

by the sum of the partial filling rates [86]:

$$S = S_R + S_A + S_C \tag{2.44}$$

where the subscripts denote the radiative, Auger and Coster-Kronig filling rates. This leads to the definition of a transition yield which gives the ratio of the rate of the respective transitions i.e. radiative, Auger and Coster-Kronig to the total rate of transitions. If the initial vacancy is created in the K-shell of the atom, the K-shell radiative or fluorescence yield can be defined as the ratio of the total number of K X-rays emitted I_K to the total number of primary K-shell vacancies n_K [86].

$$\omega_K = \frac{I_K}{n_K} \tag{2.45}$$

From theoretical calculations and published experimental data it is known that the K-shell fluorescence yield generally increases with increasing atomic number Z of the atom, while the radiationless yield decreases in this case [87]. A commonly used semi-empirical formula for ω_K is given by the following expression [88]:

$$\omega_K = \frac{\left[\sum_{i=0}^{3} C_i Z^i\right]^4}{1 + \left[\sum_{i=0}^{3} C_i Z^i\right]^4} \tag{2.46}$$

with $C_0 = 0.0370 \pm 0.0052$, $C_1 = 0.03112 \pm 0.00044$, $C_2 = (5.44 \pm 0.11) \times 10^{-5}$ and $C_3 = -(1.250 \pm 0.070) \times 10^{-6}$ [86]. Table 1 presents a listing of the two possible K-shell vacancy filling mechanisms for selected noble gases, oxygen, nitrogen and iron [87], which are the elements discussed in subsequent sections. Since Coster-Kronig transitions are between subshells having the same principal quantum number, a primary K-shell vacancy cannot be filled by them.

TABLE 1 Fluorescence and Auger yields for filling a K-shell vacancy of various atom species. The $K\alpha$ and $K\beta$ energies of the various atom species are also shown.

	K-shell fluorescence yield ω_K	Auger yield a_K	$K\alpha$ [eV]	$K\beta$ [eV]
nitrogen	5.2×10^{-3}	0.995	392	-
oxygen	8.3×10^{-3}	0.992	525	-
neon	0.016	0.982	849	-
argon	0.118	0.882	2958	3191
iron	0.340	0.660	6404	7058
krypton	0.643	0.357	12649	14112
xenon	0.891	0.109	29779	33624

During a radiative transition, the energy of the emitted radiation is given by the energy difference between the two energy levels involved in the transition. If the

initial vacancy is therefore in the K-shell and an electron from the L-shell fills the vacancy, the active electron makes a $2p \rightarrow 1s$ transition. Employing the so-called Siegbahn notation, such an electron would result in the emission of a $K\alpha$ photon, whereas an electron transition from $3p \rightarrow 1s$ results in $K\beta$ emission. The energy of the emitted characteristic X-rays in the case of $K\alpha$ and $K\beta$ transitions is given by:

$$E_{K\alpha} = E_{2p} - E_{1s} \tag{2.47}$$

$$E_{K\beta} = E_{3p} - E_{1s} \tag{2.48}$$

The $K\alpha$ and $K\beta$ energies of neutral atoms are listed in Table 1. From the stipulated energies it can be seen that the $K\alpha$ and $K\beta$ energies increase with increasing mass number A of the atom species. Due to the effective central potential produced by the nucleus and the Z electrons of the atom, the energy levels of the atom are influenced by its charge state. As a result of this effective potential difference, the energy of a $K\alpha$ transition in a neutral atom differs from that of an ion. A common nomenclature used in referring to a transition formed by filling an inner shell vacancy in a neutral atom is a diagram line. If such a transition occurs in ions, it is referred to as a satellite line. The general observation is for X-ray energies to shift to higher values with increasing charge state, a phenomenon known as X-ray energy shift [20]. Table 2 presents the energy of the argon $K\alpha$ diagram (neutral) line as well as the energies of selected argon $K\alpha$ satellite lines [20]. The table illustrates the typical magnitude of a $K\alpha$ X-ray energy shift relative to the diagram line. In an ECRIS plasma all charge states exist hence the effective shift and observed line width depend on the CSD.

TABLE 2 $K\alpha$ and $K\beta$ energies of a neutral argon atom and selected argon ions.

	$K\alpha$ energy (eV)	$K\beta$ energy (eV)
Ar^{0}	2958	3191
Ar^{5+}	2964	3217
Ar^{8+}	2971	-
Ar^{13+}	3075	-

In an ECRIS, K-shell vacancies are largely generated by two processes i.e. electron-impact ionization and electron-impact excitation. The total cross section for electron-impact ionization of a K-shell electron can be estimated from the Lotz equation given by [89]:

$$\sigma_{ion} = a_i q_i \frac{\ln(\varepsilon / I_i)}{\varepsilon I_i} \left(1 - b_i \exp[-c_i (\varepsilon / I_i - 1)]\right) \tag{2.49}$$

where q_i is the number of equivalent electrons in the i-th subshell, ε is the kinetic energy of the projectile electron relative to the target atom, I_i is the minimum energy required to remove an electron from the i-th subshell and a_i, b_i and c_i are constants which do not strongly depend on the charge state of the ion. The cross

section for K-shell electron-impact excitation can be estimated from the Van Regemorter formula [90]:

$$\sigma_{exc} = \pi a_0^2 \frac{8\pi f_{2p\to 1s}}{\sqrt{3}} \frac{R^2}{E_{2p\to 1s}^2} \frac{G_{2p\to 1s}(x)}{x} \tag{2.50}$$

where a_0 is the Bohr radius, $f_{2p\to 1s}$ is the absorption oscillator strength, R is the Rydberg energy unit, $G_{2p\to 1s}$ is the Gaunt factor and $x = \varepsilon / E_{2p\to 1s}$. The relative number of K-shell vacancies generated by each of the above processes can be calculated if the relevant properties of the ECRIS plasma are known. In an ECRIS plasma the densities of HCS ions with vacancies in the $2p$-subshell are small in comparison to low charge state ions. Additionally from Fig. 9 it can be seen that the rate coefficient for inner shell ionization is significantly larger than the rate coefficient for inner shell excitation. It is therefore much more likely for inner shell ionization to occur as oppose to inner shell excitation. As a result of this assumption henceforth only electron-impact ionization is considered as a means of generating inner shell vacancies in ECRIS plasmas. The error in this assumption is much smaller than the error in the cross section which justifies this approach.

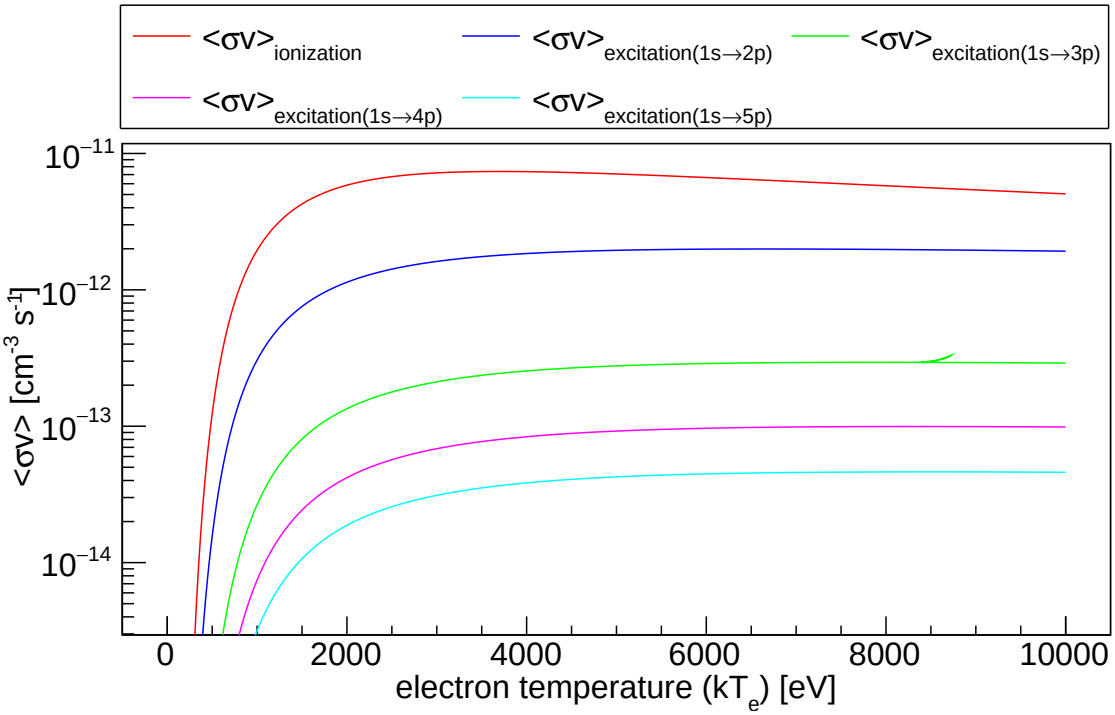

FIGURE 9 Comparison of the rate coefficients for ionization and excitation to various excited states. This figure is reproduced from Ref. [PI].

The total number of K-shell vacancies created per unit volume, per unit time as a result of electron-impact ionization is given by:

$$R = n_e n_i \langle \sigma_{ion} v \rangle \tag{2.51}$$

where $\langle \sigma_{ion} v \rangle$ is the ionization rate coefficient. The rate coefficient for inner shell ionization is given by the expression:

$$\langle \sigma v \rangle = \int f(E) \sigma_{ion}(E) v_e(E) dE \tag{2.52}$$

where $f(E)$ is the prevailing EEDF in the ECRIS plasma and $v_e(E)$ is the speed of the projectile electron. For removal of a K-shell electron i.e. inner shell ionization in an ECRIS, the cold Maxwellian electron population has a too low average energy. The temperature of the warm electron population overlaps with the peak of the rate coefficient and thus this population is often considered the most important one for inner shell ionization. This can also be seen from Fig. 9.

From the discussion above, it becomes apparent that the emitted $K\alpha$ characteristic X-rays can be used as a measure of the volumetric inner shell ionization rate occurring inside the ECRIS plasma, if a correction is made for the non-radiative transitions occurring as a result of K-shell vacancies and the emitting plasma volume can be determined. This is the topic of the experimental research reported in the following sections.

2.8 Bremsstrahlung radiation

Another important source of X-ray radiation emitted from the plasma of an ECRIS is bremsstrahlung (or 'braking radiation' translated to English from the original German expression). This radiation is emitted when a free electron moves through the plasma or the material of its containment vessel and can be of great importance for plasma diagnostics [91]. There are several ways in which free electrons can result in X-ray emission, but the process of prime interest for the current discussion is the radiation emitted when a free electron is decelerated (or accelerated) in the Coulomb field of a charged particle. Generally electron-electron collisions are ignored as their contribution to the emitted radiation is small [91]. When an electron moves in the Coulomb field of an ion, the kinetic energy of the electron can be reduced by emission of radiation. The energy of the emitted photon is proportional to the reduction in kinetic energy of the electron. Since the electron can lose any amount of energy during such a collision, the energy spectrum of the emitted radiation is continuous. The continuum radiation spectrum is known to scale with square of the atomic number of the target material [20]. If the radiation is generated as a result of a collision with the atoms of the containment vessel or any other structure outside the so-called plasma volume then the radiation is termed wall or thick-target bremsstrahlung. Similarly, if the radiation originates in the plasma volume it is referred to as thin-target or plasma bremsstrahlung. The distinction between the two types of bremsstrahlung is of particular importance for determining the EEDF by deconvolution of the mea-

sured bremsstrahlung spectra.

In the plasma volume the electron trajectories are effectively randomized although the spatial distribution of the plasma is determined largely by the *B*-field. The intensity distribution of plasma bremsstrahlung emission from an ECRIS can be considered to be evenly distributed [92]. However, due to the directionality of the escaping electron flux [93], this is not the case for the intensity distribution of thick-target bremsstrahlung [92]. Figure 10 illustrates the normalized angular distribution of bremsstrahlung emitted by electrons (of energy E) incident on aluminium target atoms. The presented results is normalized with respect to the intensity of the bremsstrahlung emission at 0° i.e. I_{0°, with $\theta = 0^\circ$ corresponding to the initial direction in which the projectile electron moves. The results is based on the theoretical work of Kissel *et al.* [94]. From this results it can be observed that the thick-target bremsstrahlung emission is strongly anisotropic. Finally since bremsstrahlung is emitted as a result of loss processes suffered by the electrons, the radiation can be used to gain information (such as the EEDF) of this electron population of the ECRIS plasma. However, despite of several notable efforts (for example Refs. [95, 96, 97, 98]), deconvolution of the EEDF of electrons escaping the ECRIS plasma from the measured bremsstrahlung spectrum is deemed practically impossible. The bremsstrahlung diagnostics can be used for detecting the effects of different source parameters on the electron population in qualitative terms.

2.9 Radiation from an ECRIS plasma

The X-ray radiation (100 eV to 100 keV) emanating from an ECRIS plasma is largely caused by three plasma processes namely, electron-impact ionization (characteristic X-rays), electron losses (bremsstrahlung) and ECR heating (cyclotron emission). Depending on the electron shell of the initial vacancy created during electron-impact ionization a spectrum of 'mono-energetic X-rays' are emitted. Two typical X-ray spectra measured from the plasmas of the JYFL 14 GHz ECRIS and the GTS at iThemba LABS are presented in Figs. 11 and 12, respectively. In both these cases the sources were operated with argon as working gas hence the most prominent feature is the Ar $K\alpha$ characteristic X-ray line. In addition to the Ar $K\alpha$ line, characteristic emission also occurs on the surface of the containment vessel of the plasma. The electrons expelled from the magnetic confinement system of the ECRIS interact with the metallic surface surrounding the plasma and in so doing lead to radiative transitions resulting in the characteristic line emission. Hence the spectra in the figures also show other characteristic lines for e.g. iron which are direct evidence of plasma-wall interactions. The fact that the characteristics lines are different and their ratios differ is due to the

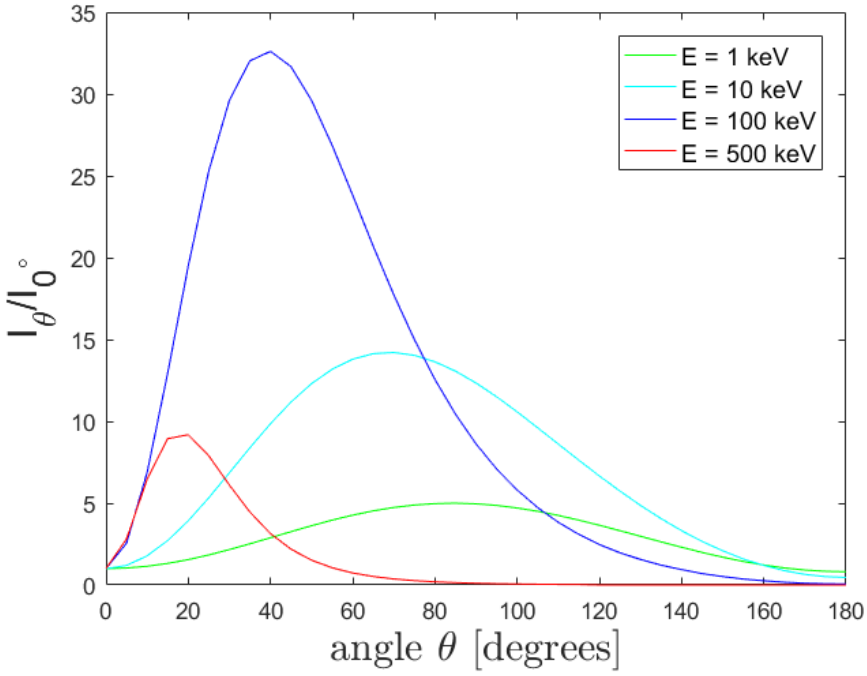

FIGURE 10 Normalized angular distribution of bremsstrahlung produced by electrons of energy E incident on aluminium target. The presented results is normalized with respect to the bremsstrahlung intensity at $\theta = 0^\circ$.

different chamber materials used in the two sources. In addition to the discrete energy lines described above, Figs. 11 and 12 also shows a continuum energy spectrum. The continuum bremsstrahlung spectrum consists of both plasma and wall bremsstrahlung and constitutes a sizeable fraction of the radiation emitted in an ECRIS. Finally, due to ECRH, electrons spiral around the magnetic fields lines resulting in cyclotron emission, but its intensity is insignificant in comparison to the two afore-mentioned processes. The radiation emitted by a single electron is discrete but since the ECRIS plasma consist of a distribution of electrons, the emitted spectrum transforms into a continuum spectrum. Additionally the magnetic field is inhomogeneous and relativistic effects also plays a role. The figures show a superposition of all the emitted radiation. It is worth noting that the relative importance of each radiation type in the measured spectra depends on the measurement geometry and collimation.

2.10 Detection of radiation

Depending on the energy of the emitted radiation, different instruments are required to detect the emitted photons. The energy range of particular interest

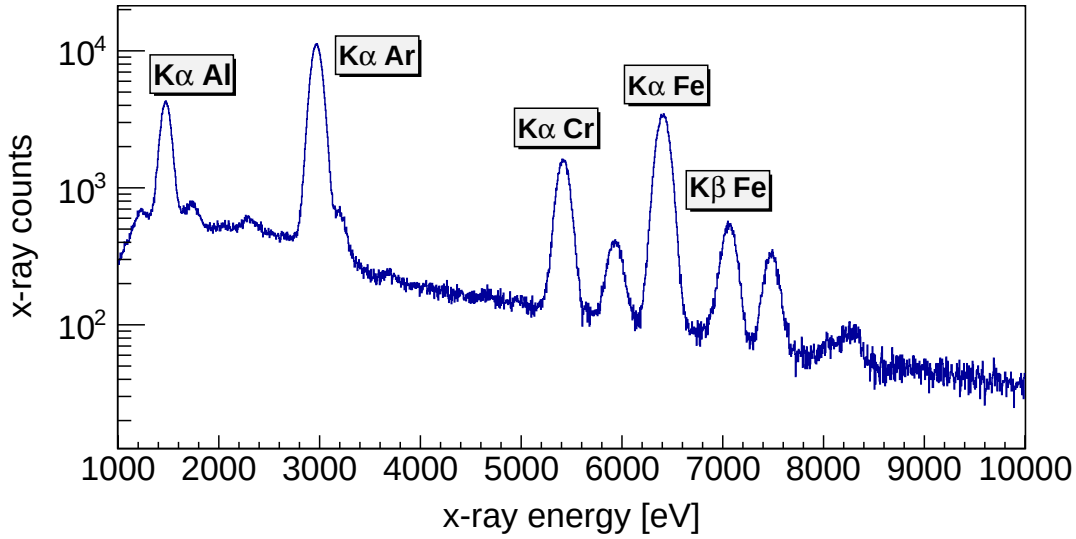

FIGURE 11 A typical X-ray spectrum measured from the plasma of JYFL 14 GHz ECRIS. The most prominent lines measured in the spectrum (and discussed in Ref. [PI]) are as follows: Al $K\alpha$ (1.5 keV), Ar $K\alpha$ (3.0 keV), Cr $K\alpha$ (5.4 keV), Mn $K\alpha$ (5.9 keV), Fe $K\alpha$ (6.4 keV), Fe $K\beta$ (7.1 keV) and Ni $K\alpha$ (7.5 keV). The bremsstrahlung background has not been subtracted in this spectrum. This figure is reproduced from Ref. [PI].

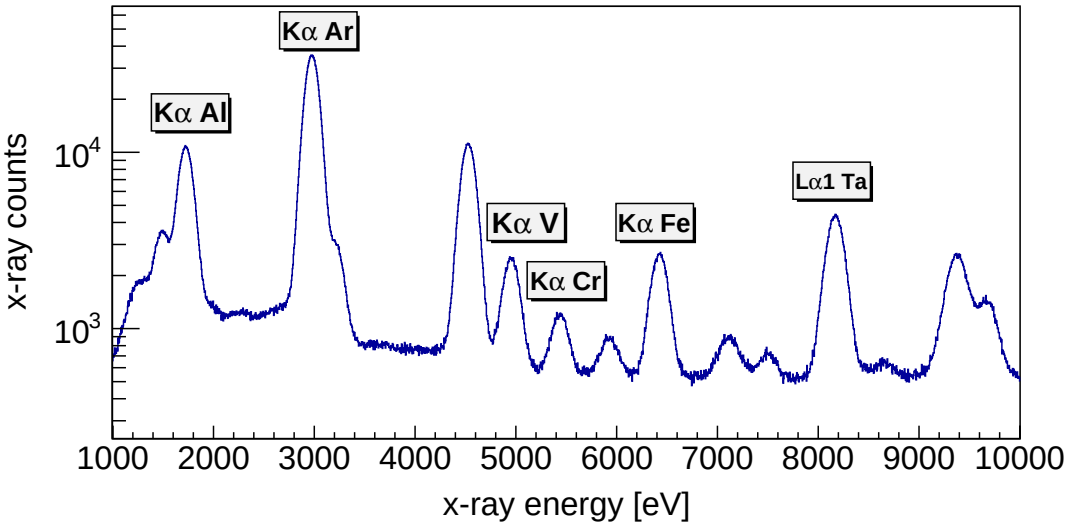

FIGURE 12 A typical X-ray spectrum measured from the ECRIS plasma of the GTS at iThemba LABS. The most prominent lines measured in the spectrum (and discussed in Ref. [PI]) are as follows: Al $K\alpha$ (1.5 keV), Ta $M\alpha 1$ (1.7 keV), Ar $K\alpha$ (3.0 keV), Ti $K\alpha$ (4.5 keV), V $K\alpha$ (4.9 keV), Cr $K\alpha$ (5.4 keV), Mn $K\alpha$ (5.9 keV), Fe $K\alpha$ (6.4 keV), Fe $K\beta$ (7.1 keV), Ta $L\alpha$ (8.1 keV) and Ta $L\beta$ (9.4 keV). The bremsstrahlung background has not been subtracted in this spectrum. This figure is reproduced from Ref. [PI].

for HCS ion production is 1 keV to 1 MeV, covering X-rays and γ-rays. In the following section the most commonly used detectors to measure ECRIS plasma radiation are briefly discussed including some of their benefits and drawbacks.

To measure plasma radiation, solid-state detectors are arguably the most commonly applied instruments. In these detectors, the incoming photon interacts with the semiconductor material (typically silicon, germanium or cadmium telluride) of the detector in the so-called depletion region. As a result of the interaction electron-hole pairs are created and collected by the electrodes owing to an applied bias voltage as illustrated in Fig. 13. The number of electron-hole pairs generated is directly proportional to the energy of the incoming photon. With certain solid-state detectors for e.g. high purity germanium crystals, the detector needs to be operated at liquid nitrogen temperatures to prevent excessive leakage current. This requires bulky liquid nitrogen dewars and constant refilling of the liquid nitrogen reservoir which can make these detectors tedious to operate over extended measurement periods. An important feature of X-ray and γ-ray detectors is the efficiency of the detector. This parameter, as thoroughly discussed in section 3.3, relates to the fraction of incoming photons detected by the instrument. The efficiency is intimately linked to the energy of the incoming photon and the physical size of the detector crystal. As a result of the applied bias voltage the charge collected by the electrodes of the detector (resulting in a current pulse) are converted to a voltage pulse and preamplified. Certain state-of-the-art detectors have improved electrode structures which results in improved energy resolution of the detector. The amplified voltage pulse is sent to a data acquisition system for post-processing of the measured signal. The voltage pulse generated is directly proportional to the energy of the incoming photon. Two properties of the measurement system is of prime importance namely the energy resolution of the detector and the deadtime of the acquisition system. Both these properties place a limitation on the plasma processes which can be studied. A major drawback of solid-state detectors are the maximum depletion depth and active volume that can be achieved, making these devices only applicable to short-range radiation [99]. A common approach in recent years have been to use silicon detectors for low energy X-ray applications, typically 1 keV - 20 keV, and use germanium detectors for measuring higher energy radiation.

Another common scheme employed to measure X- and γ-ray photons is by using scintillation material. With a scintillation detector, the incident radiation interacts with the scintillation material and the electrons (of the scintillation material) are raised to an excited state. As a result of transitions from the upper excited state to the lower ground state, photons in the visible wavelength range are emitted. The process of photon emission is usually very prompt which makes these detectors ideally suited for studying very fast processes. The scintillation photons are converted into an electronic signal usually with the aid of a photomultiplier

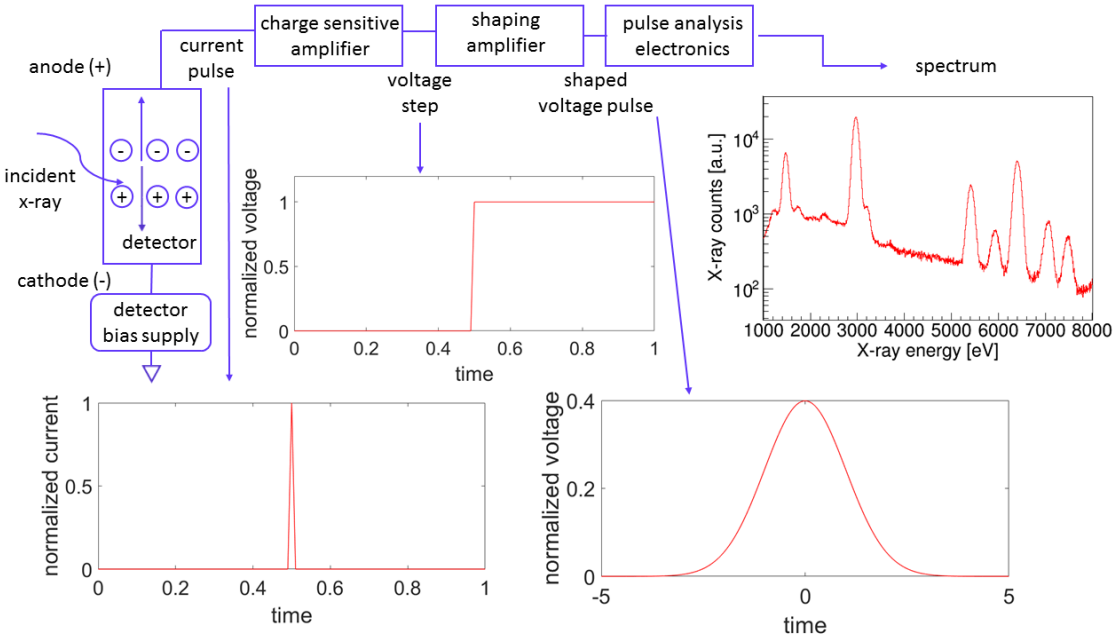

FIGURE 13 Schematic illustration of electron-hole pair generation and the typical outputs at each stage of the processing electronics.

tube (PMT). The photocathode of the PMT converts the scintillation photons to electrons. Following this stage a series of dynodes multiply, at each stage, the electrons into a measurable electronic signal. The major drawback of these detectors is the poor energy resolution which is thought to be the worst of any commonly used detector [99], in comparison to detector technology discussed above. A major advantage however is high scintillation efficiency.

2.11 Summary of previous works on radiation emitted by ECRIS

The radiation emitted from the magnetically confined plasma of an ECRIS have in the past been studied using various diagnostic techniques. Some of the earliest of these investigations focused on the bremsstrahlung radiation [15]. These early investigations highlighted the importance of proper collimation. Some even proposed deconvolution methods to extract the EEDF from the measured volume bremsstrahlung spectrum [95, 96]. Over the years many improvements on these deconvolution methods have been proposed to determine the EEDF from both thin-target as well as thick-target bremsstrahlung spectra [97, 98]. As a result of the many factors involved in deconvoluting the measured bremsstrahlung spectrum, it is deemed virtually impossible to extract the EEDF. Instead of the EEDF, the measurement of bremsstrahlung radiation can be used to yield the spectral temperature T_s [100], allowing to probe the effects of different source parameters

on T_s, most importantly the magnetic field. For example, a recent investigation by Benitez *et al.* used the spectral temperature of the bremsstrahlung spectrum to describe the importance of B_{min} on the hot plasma electron population [101].

Another recent investigation performed Hohl *et al.* used bremsstrahlung spectra to estimate the electron density and temperature of an assumed two temperature electron population, both being assumed Maxwellian [102]. This method however becomes questionable for 14 GHz ECRISs studied in this work. Some of the more recent bremsstrahlung measurements were performed in so-called time-resolved mode and were combined with the time evolution of ion currents of different charge states. This investigation was aimed to shed more light on the time required to reach the equilibrium EEDF and on the production time of different charge states [16]. The investigation was also one of the first to probe the time evolution of bremsstrahlung radiation as a function of source parameters like the neutral gas pressure and the microwave power. As the diagnostic techniques and instruments have improved over the years many investigations were initiated probing the ECRIS plasma simultaneously with multiple diagnostics [27, 28, 103]. This allowed for example a determination of the ECRH electron population properties, as well as its influence on ion production.

To closer relate ECRH to ion production, spectroscopy of characteristic X-rays emitted from an ECRIS plasma were performed. The first of these measurements were performed in the early 1990s [103, 104]. By installing the detector inside the vacuum, X-ray spectroscopy of low energy X-rays became possible. This allowed for the first time to relate the measured X-rays counts to the ion density inside the ECRIS plasma [103]

$$n_i = \Phi_r \left[C \int_{E_b}^{\infty} f(E)\sigma(E)v_e(E) \right] \tag{2.53}$$

where n_i is the ion density, Φ_r is the measured X-ray counts of the characteristic line, C is a constant that depends on the detector geometry and efficiency, $f(E)$ is the EEDF, σ is the cross section for ionization and $v_e(E)$ is the electron velocity. This characteristic X-ray diagnostic was later combined with bremsstrahlung diagnostics to gain a better understanding of the ion confinement mechanism inside ECRIS plasmas [27]. The latter investigation highlighted again the broadening of the $K\alpha$ lines as the extracted highly charged ion production increased. This observation was attributed to the energy shift of the $K\alpha$ line and the inferior resolution of the detector which could not resolve the individual lines. These observations led to improved plasma diagnostic instruments and signalled the start of wavelength dispersive measurements on ECR ion sources [103, 105]. Continuing from this early work Martins *et al.* performed detailed investigations into $K\alpha$ emission from an Ar plasma [106]. While this investigation only took into consideration single-ionization processes a later analysis took multi-ionization processes

into consideration [107]. With this investigation many of the low intensity peaks could be accounted for. Guerra *et al.* recently measured the CSD in an ECRIS plasma using high-resolution X-ray spectra and compared this to the extracted CSD [108]. This investigation like that of Santos *et al.* (see Ref. [107]) also took into consideration multi-ionization processes. In this analysis the EEDF inside the ECRIS plasma is simulated by an 'almost Maxwellian' distribution function. This assumption can result in changes in the ionic densities of up to 20% [108]. The influence of metastable states however needs to be better understood.

With the more recent investigations X-ray spectroscopy are combined with CCD (charge-coupled device) cameras viewing the plasma through a pinhole [109]. These studies are spatially resolved and also probe the electron distribution in space and energy. Such investigations are largely geared towards investigating plasma heating and the wave-plasma interaction. This allowed for a better understanding of the influence of tuning parameters used for HCS production. Another recent investigation combined X-ray spectroscopy with X-ray imaging to investigate the influence of tuning the heating frequency and the B-field profile to gain deeper understanding of the plasma heating processes [46].

The work performed in this thesis combines a number of different plasma diagnostics for e.g. $K\alpha$ emission, optical emission and electron losses (relative and direct) to gain a deeper understanding of the underlying plasma processes. The $K\alpha$ emission yields two plasma parameter i.e. the volumetric inner shell ionization rate and the relative electron losses which enables the influence of the source tune parameters on these plasma parameters to be probed. The optical emission allows the study of ion production inside the plasma excluding the influence of beam losses in the transfer beam line. To date none of the investigations mentioned probed the relative influence of electron losses on HCS production. In addition to enabling development of a more complete picture, the investigation discussed in the thesis could also be of importance to the ECRIS simulation community as discussed earlier.

3 EXPERIMENTAL SETUP

The experimental results presented in this thesis were obtained with two ECR ion sources, in which the plasma is sustained with 14.1 - 14.5 GHz frequencies. One of the ion sources is operated at the Accelerator Laboratory in the department of Physics at the University of Jyväskylä, Finland (JYFL). The second ECRIS is operated at iThemba LABS (Laboratory for Accelerator Based Sciences) in Cape Town, South Africa. Both sources are second generation, room temperature ECR ion sources with only minor differences in microwave heating frequency, magnetic confinement field and pumping arrangement. One of the important results presented in this work entails proposing a novel plasma parameter, i.e. the volumetric rate of inner shell ionization against which the results of numerical simulations can be benchmarked. To cross-check the order-of-magnitude of this parameter, it was deemed important to obtain measured results on two independent ECRISs.

3.1 JYFL 14 GHz ECRIS

The JYFL 14 GHz ECRIS [110] is one of three ECR ion sources currently operated at JYFL for medium to HCS heavy ion production. A schematic of the source is presented in Fig. 14. The aluminium plasma chamber of the source has a length of 28 cm and a diameter of 7.8 cm. The microwave heating frequency is supplied by two power sources i.e. a 14.1 GHz klystron and a TWTA in the frequency range of 10.75 - 12.75 GHz. The maximum power delivered by the klystron is 2.5 kW, but limited to 700 - 800 W for practical purposes (cooling of the plasma chamber which restricts the temperature rise of the permanent magnets), while the maximum for the TWTA is 400 W, limited to 150 W in nominal operation. Two microwave injection ports enable the source to be operated in double-frequency

heating mode and also provide an additional tune parameter with which the source can be optimized. The source has a stainless steel biased disc with a 21 mm diameter mounted at the tip of the injection iron plug. The magnetic field is provided by two solenoid coils and a permanent magnet hexapole, resulting in maximum magnetic field strengths at injection and extraction of 2.1 T and 0.95 T, respectively within the range of nominal coil currents. The radial magnetic field strength on the magnetic pole is 1.07 T, when the coils are not energized. The magnetic confinement field of the JYFL 14 GHz ECRIS is presented in Figs. 15 and 16. The radial magnetic field profile presented in Fig. 16 is produced by permanent magnets without energizing the solenoid coils. The base pressure in the source is approximately 1×10^{-7} mbar. The NdFeB permanent magnet hexapole has an open structure which enables radial pumping of the plasma chamber of the source. Additionally the radial pumping ports enable installation of radial diagnostics and the radial injection of material to be ionized e.g. by sputtering. The extraction aperture of the source is 8 mm in diameter. In the present configuration the source has one einzel lens to focus the extracted beam. The typical extraction voltages (source potentials) range from 9 to 14 kV and are determined by the required final beam energy of the cyclotron.

3.2 Grenoble Test Source at iThemba LABS

The Grenoble Test Source (GTS) at iThemba LABS, is an identical copy of the GTS currently operated at CERN (the European Organization for Nuclear Research) for the injection of lead ion beams into the Large Hadron Collider (LHC) [111]. A schematic of the source is shown in Fig. 17. The source is equipped with two 2.3 kW klystrons, operating at 14.5 GHz and 18 GHz heating frequencies. For practical purposes the injected power is typically limited to 600 W as a maximum. For the results described in this work, only the 14.5 GHz klystron was coupled to the ECRIS. The plasma chamber has an active length of 30 cm and a diameter of 7.8 cm. The radial confinement field is provided by a permanent magnet hexapole with a magnetic field strength of 1.27 T, at the plasma chamber wall. To reach this high magnetic field strength, the permanent magnet employs the so-called closed Halbach hexapole structure filling the entire volume of the hexapole with magnet material [38]. This implies that the source has no radial access ports. The source is equipped with three solenoidal coils used for longitudinal plasma confinement. The third solenoid or so-called center coil gives an additional tune parameter which allows adjusting the B-minimum (almost) independently from the axial mirror fields. Like the JYFL 14 GHz ECRIS, the GTS was initially fitted with an aluminium plasma chamber but due to erosion effects [112] after operation observed with the GTS at CERN, the plasma chamber was exchanged for a stainless steel plasma chamber. The GTS has an asymmetric tantalum biased disc

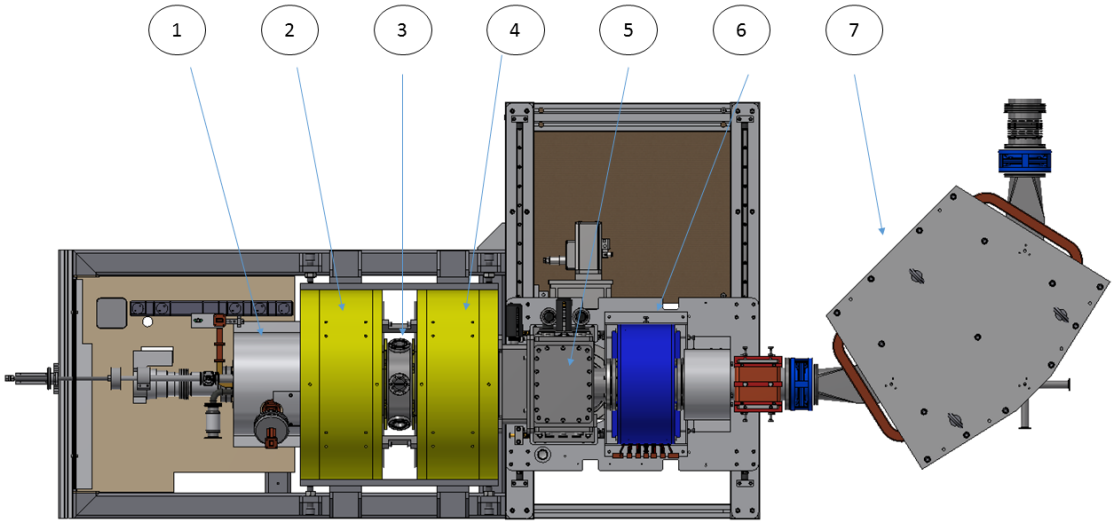

FIGURE 14 Schematic of the JYFL 14 GHz ECRIS. The injection chamber (1) includes the gas injection ports, a port for the oven or MIVOC (Metal Ions from VOlatile Compounds) and two waveguides for the primary klystron and secondary TWTA heating frequencies. The magnetic system consists of the injection (2) and extraction (4) coils and a permanent magnet hexapole wound around the plasma chamber. As a result of the open hexapole structure, the source has radial access ports (3) for pumping, radial diagnostics and a pressure gauge. The extraction chamber (5) houses the extraction electrodes, i.e. the puller and an Einzel lens for electrostatic focusing. The first focusing solenoid (6) and 90° analyzing magnet (7) of the transfer beamline are also shown in the schematic. This figure is reproduced from Ref. [PI].

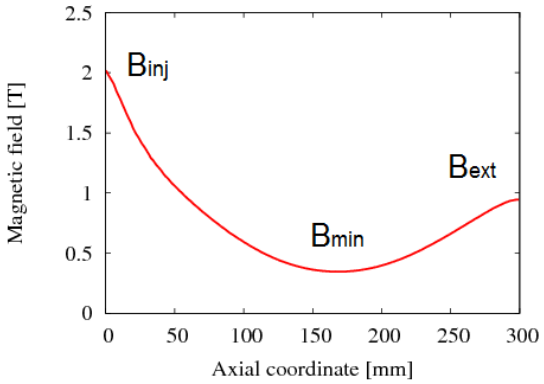

FIGURE 15 Axial magnetic field.

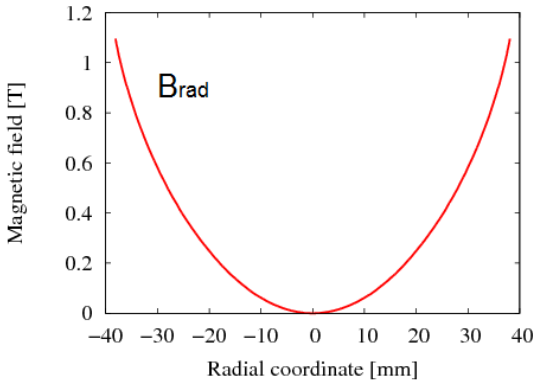

FIGURE 16 Radial magnetic field.

with a surface area of 12 cm^2. The extraction aperture of the source is 12 mm in diameter. The typical extraction voltage used is 10 kV.

3.3 Plasma diagnostic tools

3.3.1 Kα diagnostics

Figure 18 shows the experimental arrangement used at iThemba LABS to measure the characteristic $K\alpha$ X-rays. The $K\alpha$ emission from an ECR ion source can be measured in either the axial or radial direction, if an access port is available to install the diagnostic instrument. In both experimental arrangements used at JYFL and iThemba LABS, the X-ray detector measuring the $K\alpha$ X-rays was installed in an open (alignment) port on the vacuum chamber of the analyzing magnet in the transfer beamline (shown on the far right in Fig. 25(a) in the case of the JYFL 14 GHz ECRIS). This enabled the X-ray detector to view the plasma volume through the extraction aperture of the source and in so doing measure the axially emitted $K\alpha$ X-rays. To ensure that the detector predominantly measures X-ray emission emanating from the plasma volume, strict collimation was introduced. Additionally the collimator also limits the X-ray flux to the detector preventing possible saturation of the processing electronics leading to increased deadtime of the detection system. For the results obtained on the JYFL 14 GHz ECRIS, the diameter of the aperture of the collimator used was 900 μm while 500 μm aperture was used with the GTS. The distance D from the extraction aperture to the front of the collimator, for both experimental arrangements, is given in table 3. The geometric solid angle defined by both collimators allowed for the ECRIS plasma to be viewed through the extraction aperture of the source, without observing direct thick-target radiation from the plasma electrode. This however does not exclude the possibility of Compton scattered X-rays from entering the detector. Since the

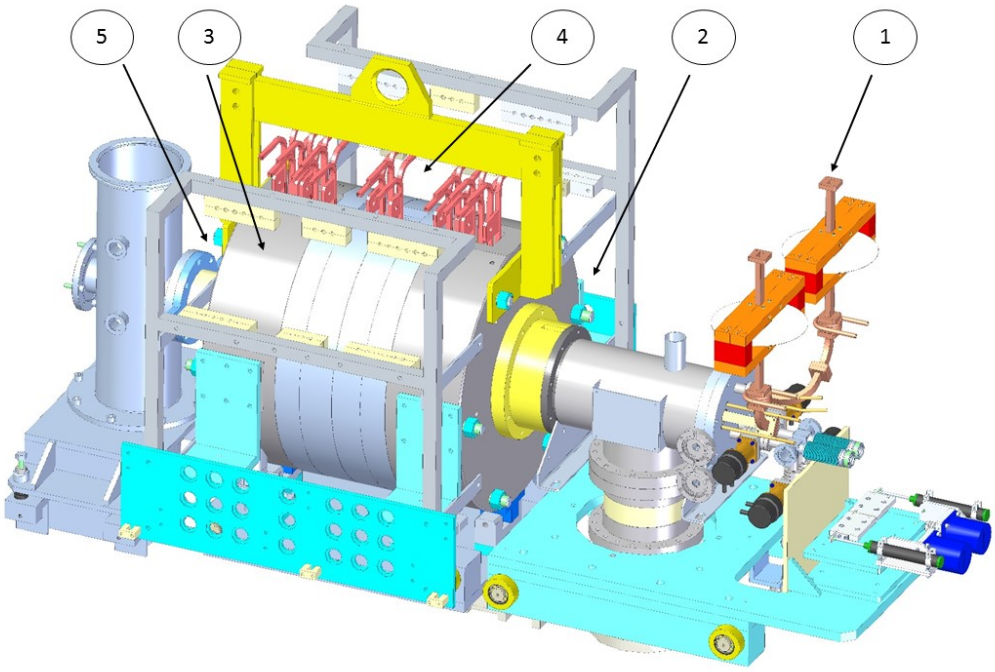

FIGURE 17 Schematic of the Grenoble Test Source at iThemba LABS. The injection chamber includes the gas injection ports, two ports for the ovens, two waveguides (1) for the 14.5 and 18 GHz heating frequencies and a pressure gauge for measuring the pressure at injection. The injection region (2) houses the biased disc and iron plug. The stainless steel plasma chamber (3) is evacuated by four 700 l/s turbomolecular pumps. The magnetic system consists of three solenoid coils (4) and a permanent magnet hexapole. The extraction chamber (5) houses the extraction electrodes.

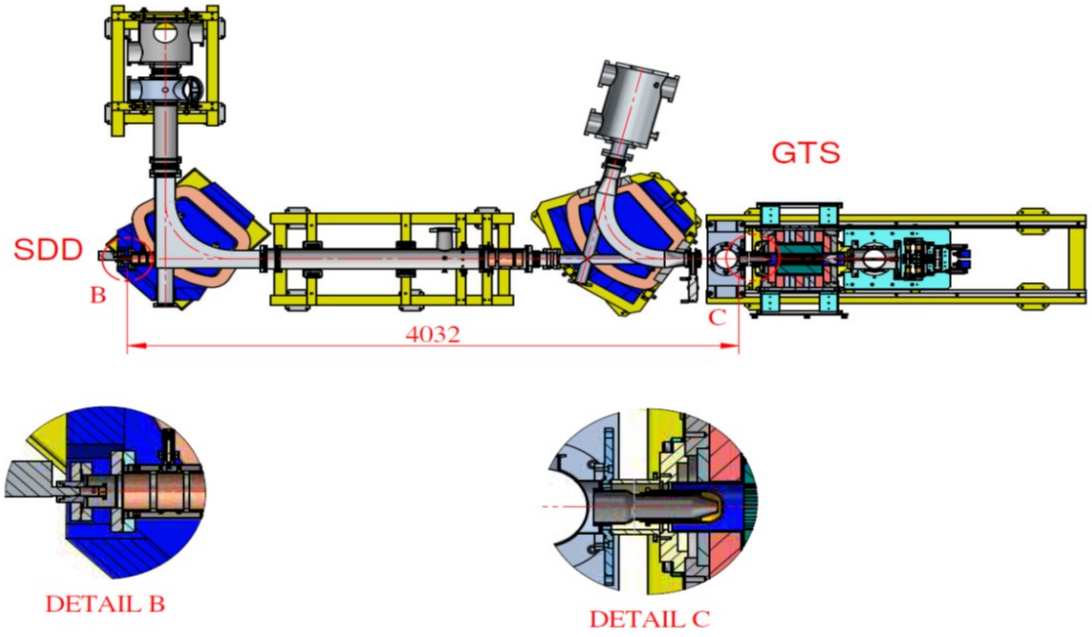

FIGURE 18 Schematic of the $K\alpha$ experimental arrangement used at iThemba LABS. The schematic (reproduced from Ref. [PI]) shows the position of the X-ray detector (SDD) as well as the layout of the connecting transfer beamlines.

detector views the plasma volume through the plasma electrode aperture, it is also able to observe thick-target radiation emanating to backward angles from the biased disc located at the injection region. This potential annoyance turned out to be a blessing in disguise as it allowed for an estimation of the relative electron losses as discussed later.

The number of $K\alpha$ X-rays emitted from the ECRIS plasma, visible to the detector, per unit volume, per unit time i.e. the observed volumetric emission rate is given by the following expression [113]:

$$\frac{d\Phi_t}{dVdt} = \frac{4\pi\left(D+\frac{L}{2}\right)^2}{A_e A_d L\left(1+\frac{L}{D}+\frac{1}{3}\frac{L^2}{D^2}\right)}\Phi_e \tag{3.1}$$

where L is the length of the plasma chamber, A_d is the area of the collimator aperture in front of the detector, A_e is the area of the plasma electrode aperture and Φ_e is the $K\alpha$ counts measured by the detector. This expression assumes that the $K\alpha$ emission is isotropic. Additionally the volumetric emission rate defined by Eq. (3.1) assumes that the plasma volume visible to the detector can be defined by a truncated slightly conical cylinder and that the $K\alpha$ emission is uniformly distributed inside the plasma chamber volume visible to the detector [113]. The measured $K\alpha$ emission rate can be used for determining the inner shell ionization rate by taking into account the detector efficiencies, pile-up events, fluorescence

yields, bremsstrahlung background and the estimated number of inner shell ionizations resulting from excitation. Finally the assumption is made that the inner shell vacancy generated is filled promptly i.e there is practically no delay between inner shell ionization and $K\alpha$ emission.

TABLE 3 Geometric dimensions of the different experimental arrangements used at JYFL and iThemba LABS. D is the distance from the extraction aperture to the front of the collimator, L is the length of the plasma chamber and A_d and A_e are the areas of the collimator and plasma electrode apertures, respectively.

	D	L	A_d	A_e
14.1 GHz JYFL ECRIS	2627 mm	280 mm	$\pi(0.45\text{ mm})^2$	$\pi(4\text{ mm})^2$
14.5 GHz GTS	4032 mm	300 mm	$\pi(0.25\text{ mm})^2$	$\pi(6\text{ mm})^2$

The instrument used for all the $K\alpha$ X-ray measurements described in this work was the Amptek X-123 X-ray spectrometer [114]. This compact device includes the silicon drift detector (SDD), preamplifier, digital pulse processor (DP5) and power supplies all in one package. When electromagnetic radiation is emitted from the ECRIS plasma, it has a certain probability of entering the X-ray detector through the 12.5 μm (0.5 mil) beryllium window. Upon entering the so-called depletion region or active volume of the detector, the radiation creates a number of electron-hole pairs along its trajectory. The number of electron-hole pairs generated is directly proportional to the energy of the incoming photon which enables the detector to distinguish between radiation of different energies. Due to the finite width of the depletion region i.e 450 μm, high energy photons might pass through the detector undetected. Similarly, low energy photons may not have sufficient energy to pass through the Be window and dead layers in front of the active detector volume resulting in their attenuation. In total these two effects lead to the definition of an efficiency which gives the fraction of incoming photons undergoing some interaction in the active volume of the detector. Figure 19 present a typical plot of the efficiency versus the photon energy of X-rays and γ-rays [114]. Due to an applied high voltage, the electron-hole pairs generated as a result of the incoming electromagnetic radiation drift towards opposite electrodes generating a current pulse. This current pulse is converted to a output voltage pulse and relayed to the processing electronics.

The processing electronics of the X-123 X-ray spectrometer consist of the shaping amplifier and the pulse analysis electronics. The shaping amplifier has two parallel signal processing paths i.e. the fast and slow channels. The slow channel is optimized for accurate pulse height information and the fast channel is optimized for accurate timing information. Additionally the shaping amplifier also filters out noise and ensures that the voltage output from the preamplifier is in

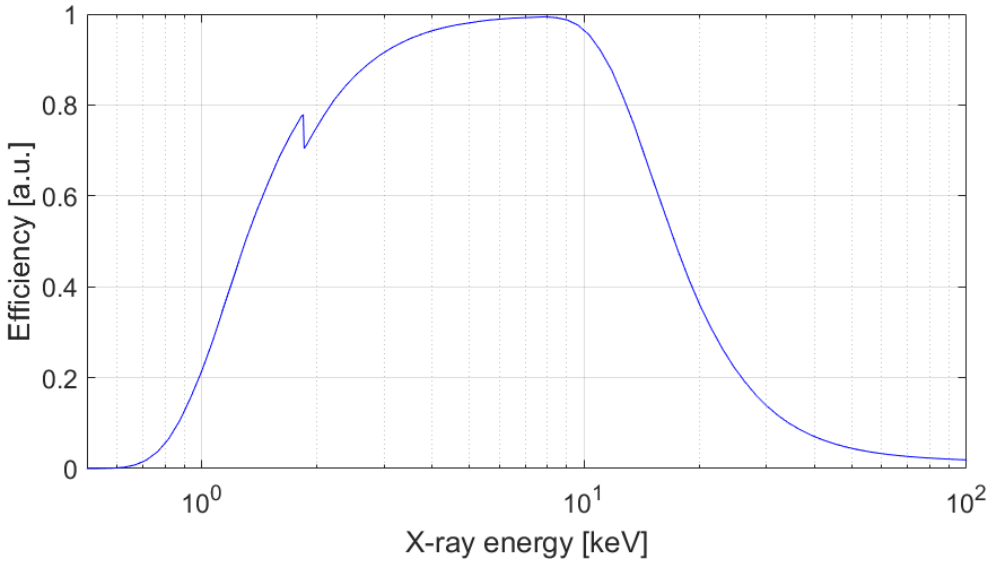

FIGURE 19 The efficiency versus energy for the Amptek SDD with 12.5 μm (1/2 mil) Be window [114].

the correct range to be digitized accurately at a high rate (20 - 80 MHz) [114]. The pulse analysis electronics produces a histogram (multichannel analyzer) of the measured peak heights. When the peak height, as given by the slow channel output, meets a set of criteria, a corresponding counter is increased in the histogram ultimately resulting in the measured spectrum. These criteria include pile-up rejection and gating of certain signals based on an external logic signal. During pile-up, two photons arrive at the entry of the detector in a very short time. If these peaks can be separated by the fast channel, the two photons are registered by the fast channel as separate photons. If subsequently pile-up rejection is enabled, both photons are ignored which assures that their combined energy (E_1 and E_2) are not inaccurately interpreted as a single high-energy photon ($E = E1 + E2$), which can distort the spectrum. The raw digital data (photon energy, arrival time of the photon, pile-up information, etc.) of the incoming radiation is stored in the FIFO (First In First Out) memory of the spectrometer. This information is subsequently readout to a host computer (via the USB port) for post-processing. A typical example of a raw X-ray spectrum measured on the JYFL 14 GHz ECRIS is presented in Fig. 20. During post-processing of the measured spectra, the spectra is corrected for the efficiency of the detector. An example of such an efficiency correction is presented in Fig. 21. Additionally the bremsstrahlung background is removed from the measured spectrum as shown in Fig. 22. Finally a Gaussian peak is fitted to the $K\alpha$ line of interest and the number of counts obtained by integrating between the two 10 % thresholds of the fitted Gaussian peak. An example of such a Gaussian fit is shown in Fig. 23.

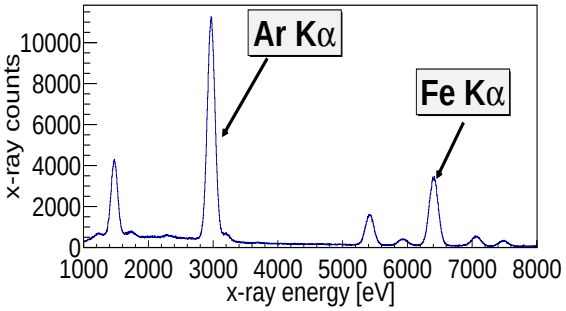

FIGURE 20 Raw X-ray spectrum.

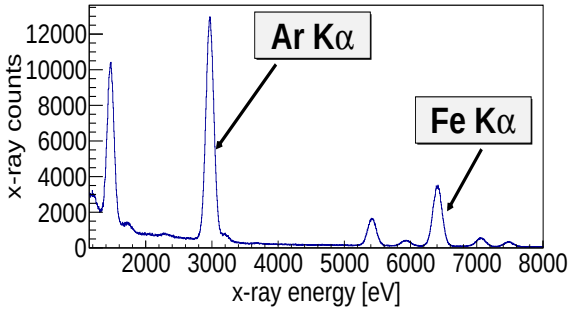

FIGURE 21 Efficiency corrected spectrum.

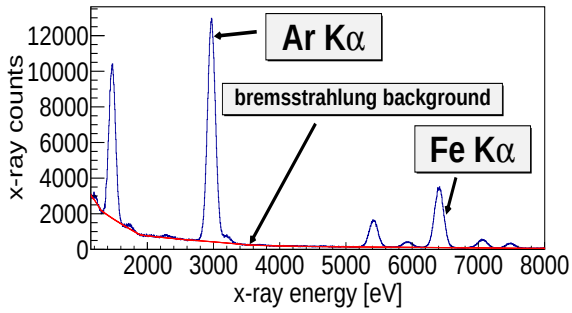

FIGURE 22 Background removal.

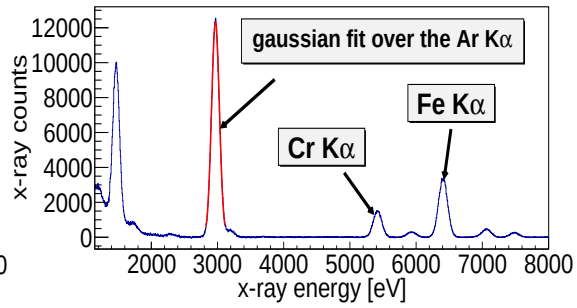

FIGURE 23 Gaussian fit of Ar $K\alpha$.

3.3.2 Optical emission spectroscopy setup

The experimental setup used to obtain the optical emission spectroscopy (OES) data has been thoroughly described in Ref. [31] and here only the most pertinent features of the arrangement will be mentioned. Figure 24[1] illustrates the major components of the OES setup. The setup consist of the following three functional parts: the optical interface, the spectrometer and the data acquisition and control system. To maximize the detected photon flux, the optical emission was measured from one of the radial pumping ports of the JYFL 14 GHz ECRIS. The emission is subsequently focused by a single lens into the optical fiber which transports the light over a distance of three meters to a chopper. The chopper pulses the light signals in time, which is required by the lock-in amplifier. The lock-in amplifier forms part of the acquisition system. In addition to pulsing the light signal, the chopper also supplies a reference signal to the lock-in amplifier. The spectrometer of the OES setup consist of the monochromator and the photomultipler tube detector. To separate the different emission lines a Fastie-Ebert type monochromator nicknamed POSSU (Plasma Optical SpectroScopy Unit, piglet in Finnish) is used. The intensities of different emission lines are measured by rotating the diffraction grating of the monochromator by using a stepper motor. This

[1] This figure is by courtesy of Risto Kronholm.

enables emission lines in the wavelength range 350 - 700 nm (with gain higher than 20 %) to be measured. The resolution of the monochromator is determined by a number of factors as discussed in Ref. [31]. For the results discussed in this work the spectrometer had a typical wavelength resolution of 31 pm. The light passing through the exit of the monochromator is coupled to the PMT detector which converts the light signal to a current signal. The current signal is converted to a voltage signal by a transimpedance amplifier and conveyed to the phase sensitive frequency lock-in amplifier. The lock-in amplifier eventually yields a DC-output signal which is proportional to the amplitude of the voltage signal from the PMT.

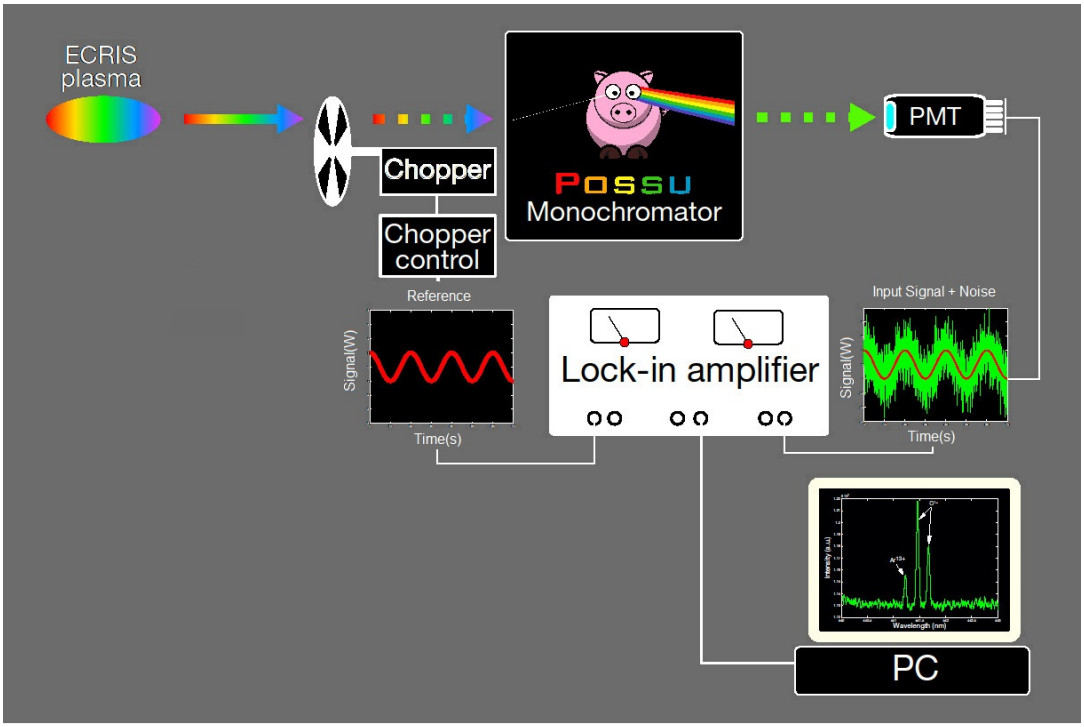

FIGURE 24 Experimental setup used for the optical emission spectroscopy.

3.3.3 Electron losses detection system

Figure 25 presents the experimental setup used at JYFL for measuring the relative electron losses as well as the setup used for measuring the escaping electron losses. The relative electron losses were determined from the measured $K\alpha$ emission of argon and iron. The details of the experimental arrangement used for measuring the $K\alpha$ emission has been described in some detail earlier. Figure 25(a) shows the position of the X-ray detector used to study the relative electron losses. To quantify the relative electron losses, the ratio of the $K\alpha$ of iron to the $K\alpha$ of argon (hereinafter denoted by r) were used. As thoroughly discussed in Ref.

[PIV], the Ar $K\alpha$ emission emanates mostly from the plasma volume whereas the Fe $K\alpha$ mostly emanate from the stainless steel biased disc located at the injection side of the plasma chamber. The ratio r is therefore proportional to the number of warm and hot electrons which escape the magnetic confinement system of the ECRIS plasma and interacts with the biased disc. The investigation probing the relative electron losses were performed with the source operated in CW mode.

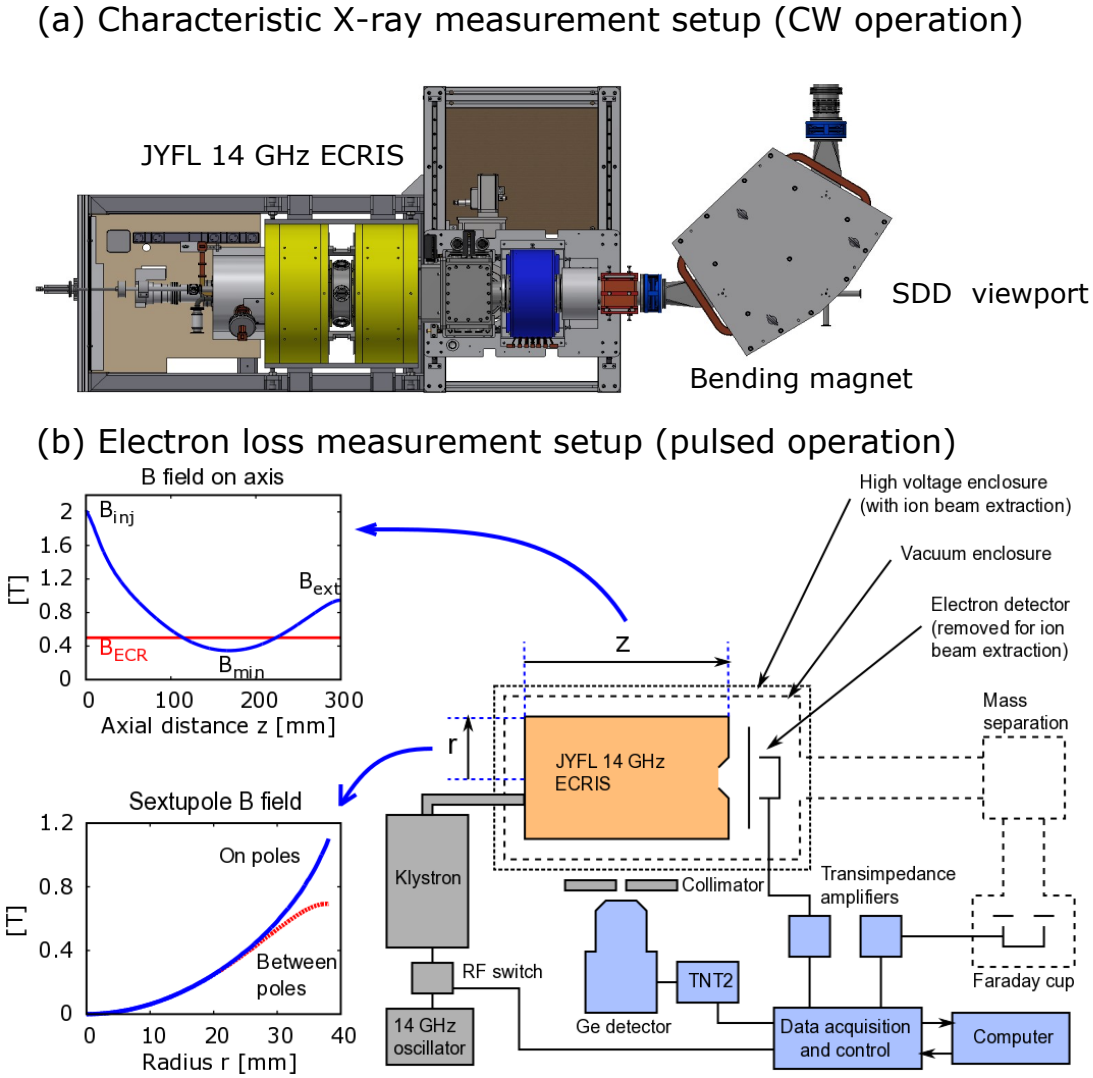

FIGURE 25 Experimental setup used for measuring the relative electron losses in CW operation (a) and the setup used for measuring the escaping electrons in pulsed operation (b). This figure is reproduced from Ref. [PIV].

Figure 25(b) presents the details of the experimental arrangement used to study the escaping electron losses. The device used to measure the escaping electrons has first been described by Izotov *et al.* [115]. With the current description only the main features of the experimental setup are highlighted. The investigation was performed with the source operated in pulsed mode. Three complimentary diagnostics were combined for this investigation. The first diagnostic used was a

detector for measuring the escaping electron current through the extraction aperture of the ECRIS. This device consisted of an array of aluminium foils, a suppression electrode and a Faraday cup. Table 4 presents the foil thickness and the approximate energy threshold for each foil. The aluminium foils provided only a crude determination of the energy resolution of the escaping electrons. In addition to the direct losses, the bremsstrahlung radiation and visible light emission (total light signal across the visible light range) from the ECRIS plasma were also measured during this study. Both these diagnostics were mounted in radial ports of the source. The diagnostics were purely used to compare the temporal evolution of the bremsstrahlung radiation and the light emission with the temporal evolution of the escaping electron signal. The diagnostics are discussed in greater detail in Ref. [PIV].

TABLE 4 Foil thickness and corresponding (approximate) energy thresholds assuming perpendicular angle of incidence.

Foil number	Thickness [mg/cm^2]	Energy threshold [keV]
1	no foil	0
2	1.0	20
3	6.8	55
4	18.4	100
5	88.1	270
6	270 (1 mm plate)	570

4 EXPERIMENTAL RESULTS

This chapter presents a summary of the main experimental results obtained during this study. For more details on the experimental results, plasma diagnostics and analysis tools used, the experimental work is documented as four peer-reviewed articles attached as appendices to the thesis. The attached articles are hereafter referred to as Ref. [PI]-[PIV].

The goal of the work presented in this thesis is to develop the current understanding of the physical processes occurring in ECRIS plasmas underlying the main purpose of the device, ion beam production. To achieve this difficult feat, a novel plasma parameter i.e. volumetric $K\alpha$ emission rate (absolute and/or relative) is proposed against which the results of numerical simulations on ECRIS plasmas can be benchmarked. The first section of this chapter focuses on studying the variation of this plasma parameter during a parametric sweep of the main source tune parameters. The second and third sections of the chapter focus on using the $K\alpha$ diagnostic to gain a deeper understanding of the gas mixing and double-frequency heating techniques commonly applied to enhance HCS ion production in ECR ion source plasmas. The fourth section is dedicated to studying the microwave induced electron losses from the ECRIS plasma using both relative (derived from the $K\alpha$ measurements) and direct electron losses from the magnetic confinement system of the ECRIS.

4.1 Volumetric $K\alpha$ emission rate and absolute inner shell ionization rate

To advance ECRIS development, a number of numerical codes have been developed over the years (see for e.g. Refs. [47, 70, 75, 116, 117, 118, 119]) and can

be crudely categorized as electron heating codes, codes modeling ion dynamics and beam extraction codes. While many of these codes can adequately replicate a number of experimentally obtained results, the simulations remain sensitive to the assumptions build into the underlying theoretical models or plasma parameters used in the code. A classic example of this difficulty is illustrated by the numerous codes simulating the electron heating process in ECRIS plasmas. To aid the development of numerical codes, the volumetric $K\alpha$ emission rate is proposed as a novel plasma parameter which can easily be produced as an intermediate output by most simulation codes and used for benchmarking. This motivated the study of this plasma parameter as a function of the parametric sweeps of the four main source tune parameters, namely absorbed microwave power, neutral gas flow, biased disc voltage and magnetic field.

To calculate the volumetric emission rate using Eq. (3.1), it was assumed that the whole plasma volume visible to the detector has a uniform plasma density. From recent simulations into the plasma density distribution, it has been shown that the plasma core housing the ECR zone is more dense implying more $K\alpha$ emission should emanate from this region [120]. As a consequence of the assumptions made in Eq. (3.1), the results reported in this work corresponds to the lower limit of the volumetric $K\alpha$ emission rate in the plasma core. This implies that the absolute inner shell ionization rate determined from the volumetric emission rate corresponds to the *minimum* ionization rate. The upper limit of the volumetric $K\alpha$ emission rate can be estimated by considering that the $K\alpha$ photons are only emitted from a homogeneous plasma inside the volume defined by the ECR zone and using this reduced volume to calculate the volumetric $K\alpha$ emission rate. The actual situation prevailing inside the ECRIS is in all likelihood in-between these two extremes.

4.1.1 Biased disc voltage and magnetic field sweeps

The investigation of the minimum volumetric $K\alpha$ emission rate and resulting minimum absolute inner shell ionization rate of argon as a function of the parametric sweeps revealed that both plasma parameters are strongly influenced by only two of the four source tune parameters i.e. absorbed microwave power and neutral gas flow. This led to the conclusion that the two remaining tune parameters i.e. biased disc voltage and magnetic field influence the HCS production and resulting beam current indirectly for e.g. through increased ion confinement time. The influence of the biased disc voltage on both parameters was probed by varying the negative biased disc voltage between -300 V and -20 V, while keeping all other source tune parameters constant at the baseline source settings shown in table 5.

The results of this investigation, presented in Fig. 26 (see also Ref. [PI]), along

TABLE 5 The baseline ion source settings for each parametric sweep. The pressure reading is given without igniting the plasma as this distorts the gas flow into the ionization gauge.

calibrated pressure at injection (0 W)	4.3×10^{-7} mbar
B_{inj} (magnetic field strength at injection)	2.02 T
B_{min} (B minimum)	0.35 T
B_{ext} (magnetic field strength at extraction)	0.95 T
microwave power	400 W
biased disc voltage	-170 V

with the earlier plasma potential results obtained on the 6.4 GHz ECRIS at JYFL [50] allowed to identify a plausible explanation of the underlying physical process at work. From those earlier results it is known that the plasma potential decreases with increasing biased disc voltage. This implies that less electrons are diffusing from the confinement system of the ECRIS. Given the typical voltage applied to the biased disc, this tune parameter acts exclusively on the cold electron population of the ECRIS EEDF and, thus, affects predominantly their loss rate (in comparison to warm and hot electrons). This could result to a different equilibrium of charged particle losses (particularly axial particle losses) and thereby affect the ion currents in a favorable manner [78]. The results of the biased disc voltage sweep and measured CSD revealed a significant decrease in the extracted ion beam current of Ar^{13+} if the applied biased disc voltage is reduced below a threshold value. This suggest that the cold electron losses are significantly enhanced below the threshold voltage. Altogether the experimental results seems to support the claim that the biased disc voltage indirectly influences the HCS ion production by altering the dynamics of cold electrons and ions while the impact of the biased disc voltage on the warm electron population is minute as witnessed by the insensitivity of the $K\alpha$ emission rate to this parametric sweep.

The variation of the volumetric $K\alpha$ emission and inner shell ionization rates with magnetic field configuration was determined from two figures characteristic of the ECRIS magnetic field i.e the average magnetic field gradient parallel to the field lines across the entire ECR surface i.e. $\langle \frac{\vec{B}}{|\vec{B}|} \cdot \nabla \vec{B} \rangle$ and the B_{min}/B_{ECR}-ratio. During this parametric sweep presented in Fig. 27 (fully discussed in Ref. [PI]), the average parallel magnetic field gradient was varied from 7.53 T/m to 4.03 T/m corresponding to a variation from 0.688 to 0.832 of the B_{min}/B_{ECR}-ratio, with all other source parameters kept constant at the values shown in Table 5. At these source settings the stability threshold is crossed at $B_{min}/B_{ECR} \approx 0.8$. The results of this parametric sweep indicated that the measured rates are within the experimental error of the measurement (fully discussed in Ref. [PI]), hence this tune parameter appears to have minimal influence on the emission and ionization

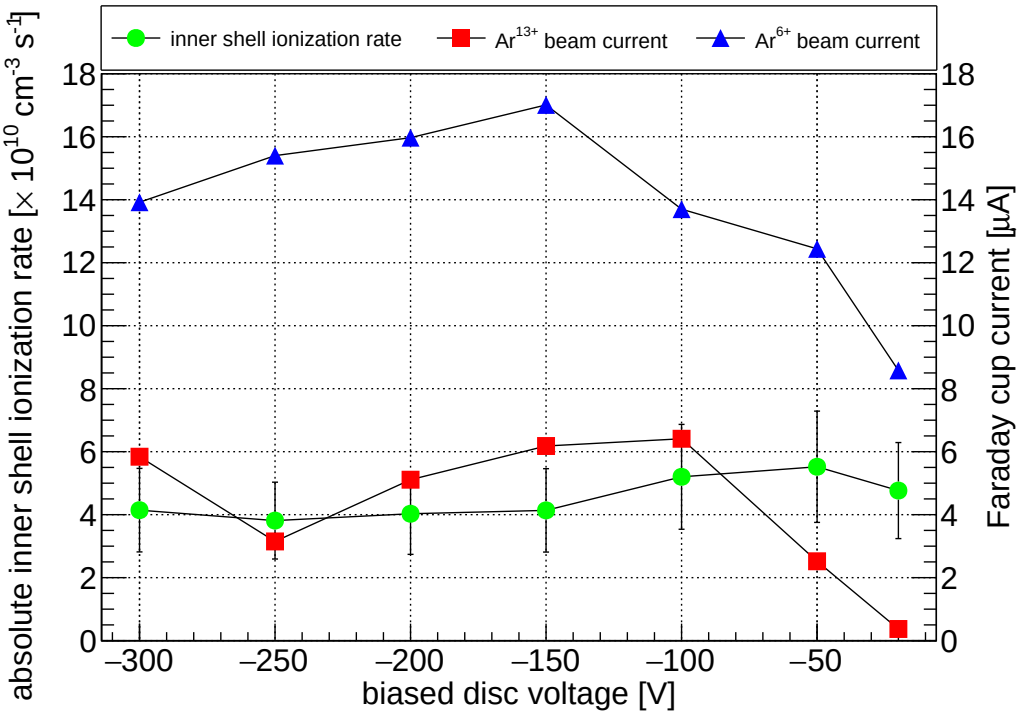

FIGURE 26 Variation of the (minimum) absolute inner shell ionization rate as a function of biased disc voltage as well as the Faraday cup current of Ar^{13+} and Ar^{6+}. This figure is reproduced from Ref. [PI].

rates. Contrary to the emission and ionization rates, the extracted ion beam current of Ar^{13+} (also measured during this investigation) seemed to increase with increasing *B*-field/decreasing gradient as long as the threshold of kinetic instabilities is not crossed [24]. From a previous investigation measuring the plasma bremsstrahlung emanating from an ECRIS plasma it was noted that the magnetic field largely impacts the hot electron population [17]. Another investigation also showed higher average electron energies with decreasing average parallel magnetic field gradient [121]. The latter effect is suggested to be caused by the more efficient heating at the resonance zone. Based on the previous investigations and the results obtained in the current investigation, it was concluded that the magnetic field sweep influences largely the hot electron population, increasing the average electron energy with stronger B-field (lower gradient) while also reducing the electron losses [30]. By increasing the number density of the hot electron population of the EEDF, residing in the core of the plasma, the confinement time of the trapped ions can be increased. This assertion is based on the assumed plasma potential structure along the axial and radial directions of minimum-*B* traps. Due to the well confined hot electrons inside the plasma core a small negative potential dip is created. This negative potential dip is suggested to trap cold ions via the ambipolar field of the well confined hot electrons, increasing the ion confinement time. This in turn results in increased HCS production presumably accounting for the experimental observation.

From the behaviour of the inner shell ionization rate as a function of the magnetic field strength and biased disc voltage it can be observed that the inner shell ionization rate remains largely constant, within the experimental uncertainty, during the parameter sweeps. In stark contrast to this, the beam currents of low and high charge state ions can change drastically over the course of the parameter sweeps. This highlights the fact that the changes in the plasma behaviour, induced during the parameter sweeps manifests differently in the $K\alpha$ emission rate and the extracted ion beam currents of the different charge states. This underlines the importance of using $K\alpha$ emission as a plasma diagnostic and benchmarking tool for ECRIS simulations.

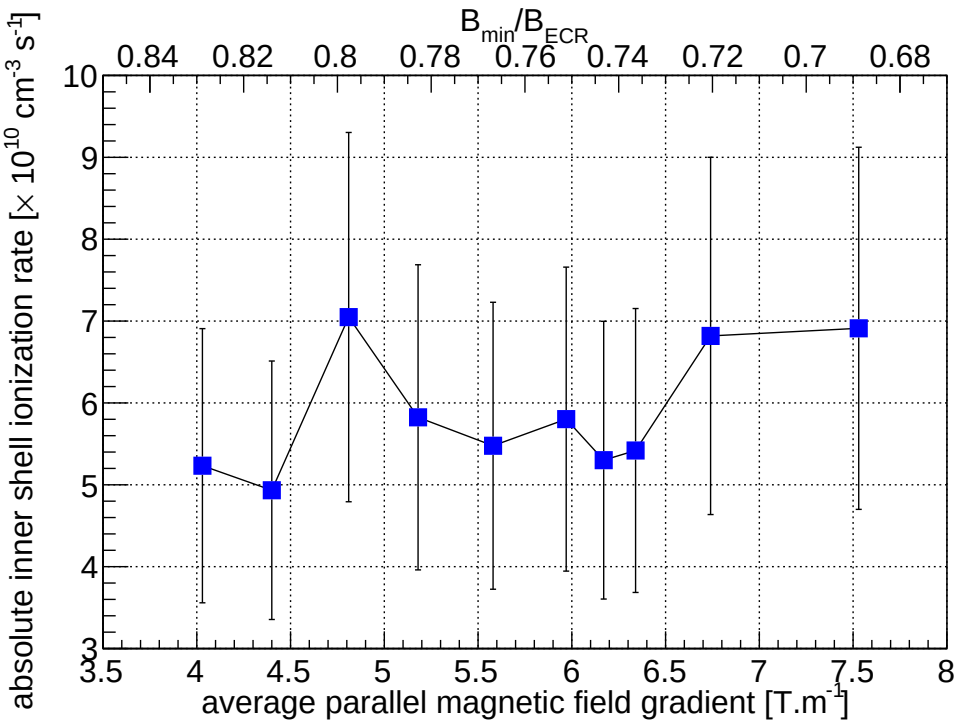

FIGURE 27 Variation of the (minimum) absolute inner shell ionization rate as a function of average parallel magnetic field gradient and B_{min}/B_{ECR}-ratio. This figure is reproduced from Ref. [PI].

4.1.2 Absorbed microwave power and neutral gas flow sweeps

The investigation into the influence of the microwave power on the volumetric $K\alpha$ emission rate (thoroughly discussed in Ref. [PI]) was initiated by correcting for the microwave power losses in the transmission line. The variation of the minimum absolute inner shell ionization rate as a function of absorbed microwave power, at different neutral gas pressures, is presented in Fig. 28. For this investigation the incident microwave power was varied between 100 W and 600 W. The

propagated error on the absolute inner shell ionization rate shown in Fig. 28 (and all other parameter sweeps) is thoroughly discussed in Ref. [PI].

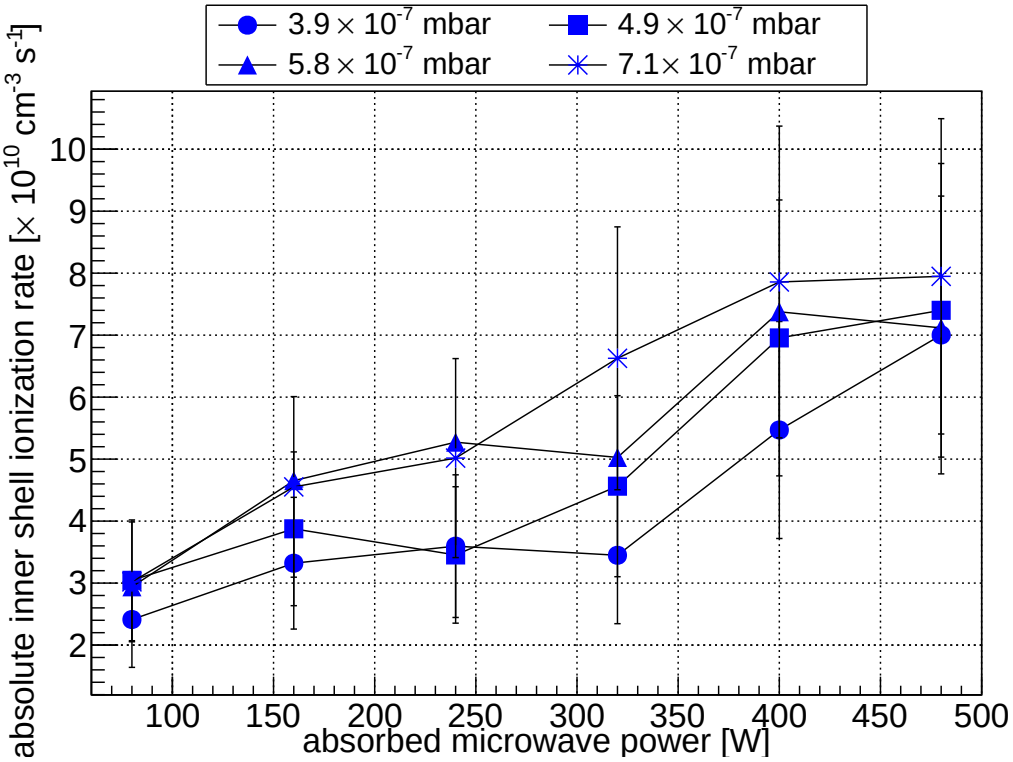

FIGURE 28 Variation of the (minimum) absolute inner shell ionization rate as a function of absorbed microwave power, at different neutral gas pressures. This figure is reproduced from Ref. [PI].

From the discussion in Ref. [PI] it is known that the observable $K\alpha$ emission rate depends on the average charge state ($\langle Z \rangle = \sum_i n_i Z_i / n_e$) and ionization degree of the plasma ($\delta = n_i / n_n$), as well as on the electron energy and density (through the rate coefficient). From the CSD results reported in Ref. [PI] it is clear that $\langle Z \rangle$ can not completely account for the variation observed in Fig. 28. This assertion is premised on the observation that the average extracted charge state (used to estimate the average charge state in the plasma core) was observed to change from 7.98 to 10.45, while the absolute inner shell ionization rate was determined to be between 8.80×10^9 cm^{-3} s^{-1} and 3.00×10^{10} cm^{-3} s^{-1}, during the same parameter sweep (see Ref. [PI]). It is commonly assumed that the CSD of the plasma core differs from the extracted CSD [122], but in the current investigation the extracted CSD was used to purely gain insight into the changing plasma core CSD during the parametric sweep. The relative variation of the absolute inner shell ionization rate (during the parameter sweep) is at least three times more than the variation in the estimated average charge state of the plasma core which supports the assertion that average charge state of the plasma core probably plays

a lesser role in comparison to the other plasma parameters which affect the inner shell ionization rate.

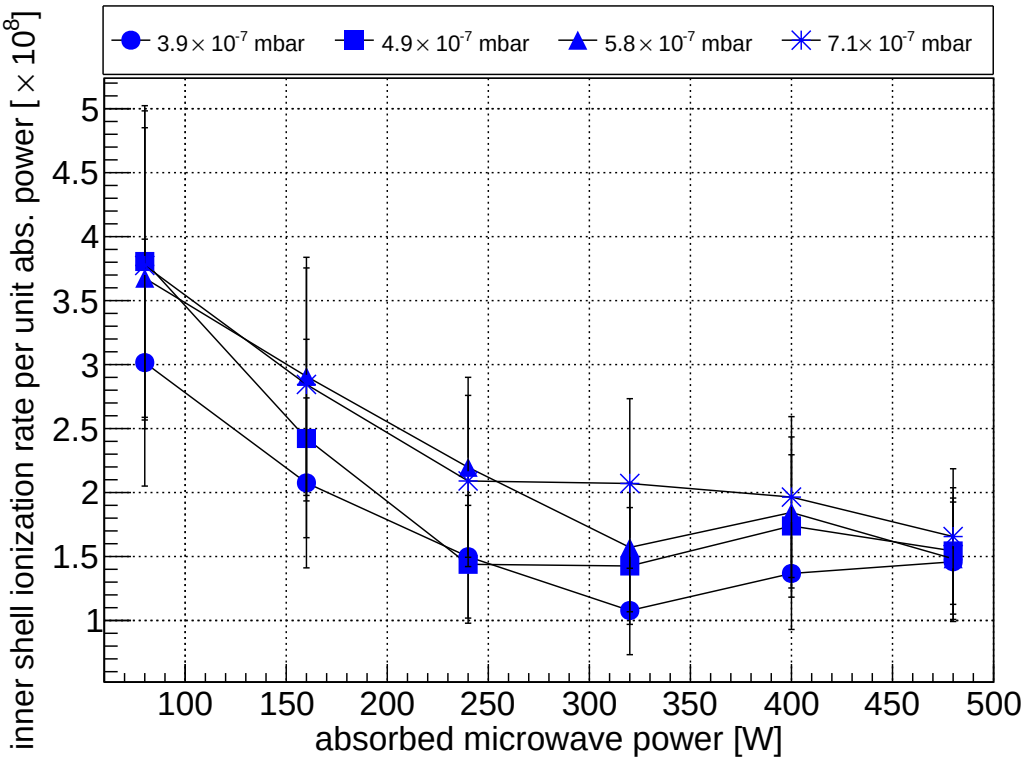

FIGURE 29 Variation of the (minimum) absolute inner shell ionization rate per unit absorbed microwave power as a function of absorbed microwave power, at different neutral gas pressures. This figure is reproduced from Ref. [PI].

The influence of the ionization degree on the absolute inner shell ionization rate can be established by determining the efficiency of producing inner shell ionization, per unit of absorbed microwave power. The implicit assumption made is that the ionization degree of the plasma increases as the absorbed microwave power increases. Such behaviour has been deduced from studies of the total production efficiency [123], comparing the flux of injected gas to the extracted ion beam currents, summed over the CSD. The ratio of the absolute inner shell ionization rate to the absorbed microwave power, as a function of absorbed microwave power, at different neutral pressures is presented in Fig. 29. The figure shows that the rate of producing inner shell ionization, per unit of absorbed microwave power, is highest at the lowest absorbed microwave power. This implies that inner shell ionization is most effectively produced at low degree of ionization of the plasma. Since this result is different to the behavior of the absolute inner shell ionization rate as a function of absorbed microwave presented in Fig. 28 it is concluded that the ionization degree of the plasma does not alone dictate the behavior presented in Fig. 28.

The dominant mechanism at work which could account for the experimental observation presented in Fig. 28 is the plasma energy content i.e. $n_e kT$. Initially the electron density is low due to the low absorbed microwave power. As the absorbed microwave power increases, the ionization rate increases resulting in higher electron densities. Additionally it is also known that the electric field strength E for a given cavity of quality factor Q scales with square root of the applied microwave power P i.e. $E \propto Q\sqrt{P}$. It can therefore be reasonably assumed the electrons are heated to higher energies. Both of these factors favour an increase of the plasma energy content with increasing microwave power driving the experimental observation presented in Fig. 28. Eventually the plasma energy content saturates due to the increase in electron density with increasing microwave power, as a point is reached where the absorbed microwave power becomes insufficient to sustain further heating of the plasma electrons. This leads to the saturation observed in Fig. 28, at high absorbed microwave power.

The variation of the minimum absolute inner shell ionization rate as a function of the neutral gas pressure, at different incident microwave powers, is presented in Fig. 30. With this parametric sweep, the neutral gas flow was varied such that the neutral gas pressure at injection is changed between 2.5×10^{-7} mbar and 1.1×10^{-6} mbar. It is worth noting that the pressure measured by the gauge differs from the actual plasma chamber pressure. The pressure reading by the gauge depends on factors like the position of the gauge in the vacuum system i.e. the pumping speed at the gauge position, the total gas composition in the plasma chamber and the type of gas species that needs to be measured. All these factors imply an error in the measured neutral gas pressure. Additionally the neutral pressure needs to be measured without igniting the plasma as this also hugely affects the pressure reading due to the so-called ion pumping effect.

With the current investigation it was found that the behaviour of the volumetric $K\alpha$ emission rate with increasing neutral gas pressure, and by implication also the absolute inner shell ionization rate with increasing gas pressure, behaves very similar to the results obtained in the Ref. [17]. The inner shell ionization rate was found to initially increase rapidly with increasing neutral gas pressure. The rapid increase in absolute inner shell ionization rate is most likely due to the increase in the target densities (atoms and ions), as well as the electron density. As a result of this situation the plasma energy content experience a rapid increase as the flow rate is increased. This assertion is premised on the notion that the plasma energy content is somewhat limited at low flow rates due to enhanced electron losses, as shown experimentally in section 4.4.1. The rate of increase of the plasma energy content becomes larger as the microwave power is increased. This most likely points to the increased contribution to inner shell ionization due to the increasing plasma energy content, with increasing microwave power. With further increase in pressure, the inner shell ionization rate reaches a saturation

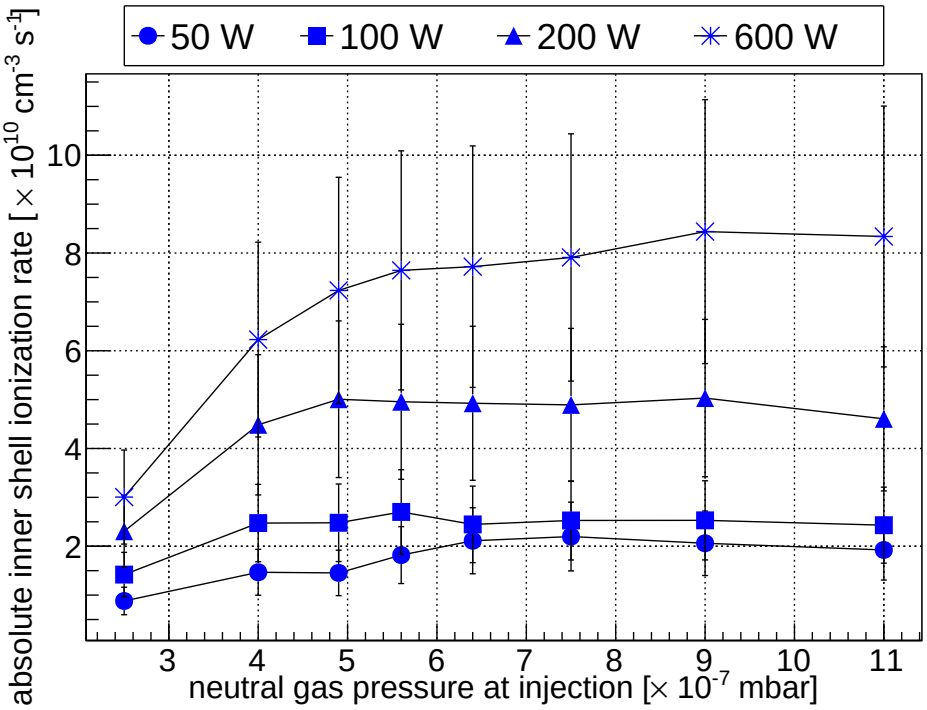

FIGURE 30 Variation of the (minimum) absolute inner shell ionization rate as a function of neutral gas pressure, at different incident microwave powers. This figure is reproduced from Ref. [PI].

point. At this point the energy content of the plasma is considered insufficient to sustain any further growth in the ionization degree of the plasma. This assertion is supported by the saturation in the production rate of HCS ions observed in the results obtained in Ref. [PI]. This transition is characterized by a plateau as seen in Fig. 30. With further increase in neutral gas pressure a point is reached at which charge exchange starts to significantly impact HCS production. This interpretation is based on two facts: (i) the volumetric inner shell ionization rate remains constant with increasing pressure and (ii) the HCS beam currents drop as a function of pressure. These two points considered together imply charge exchange.

4.1.3 Comparison of the absolute inner shell ionization rate

To gain confidence on the order of magnitude of the volumetric $K\alpha$ emission rate and the absolute inner shell ionization rate it was important to measure the emission rate on two independent ECR ion sources. Additionally such an exercise would indicate if the observed trends are unique to a specific ECR ion source or the same for both sources. A typical result of such a measurement performed on the JYFL 14 GHz ECRIS and the GTS at iThemba LABS is presented in Fig. 31. The presented results show the calculated absolute inner shell ionization rates as

a function of the microwave power sweep obtained on the two sources. The results highlight two important points. Firstly, the calculated absolute inner shell ionization rate is similar for both ECR ion sources. This result is expected as both sources are second generation ECR ion sources with only minor differences as highlighted earlier. This gives confidence that the order of magnitude is correct within the assumptions made in defining the line-of-sight volume and the plasma distribution. Secondly, the observed trends of the various source tune parameters match very well. This suggests that the observed trends are presumably universal to all 14 GHz ECR ion sources. The absolute values, saturation points, rate of increase, etc. though most likely depend on the source design (power, frequency, plasma volume, etc.) This further strengthens the argument to use the $K\alpha$ volumetric emission rate as a plasma parameter for benchmarking numerical codes since the trends observed are in all likelihood the same for all 14 GHz ECR ion sources.

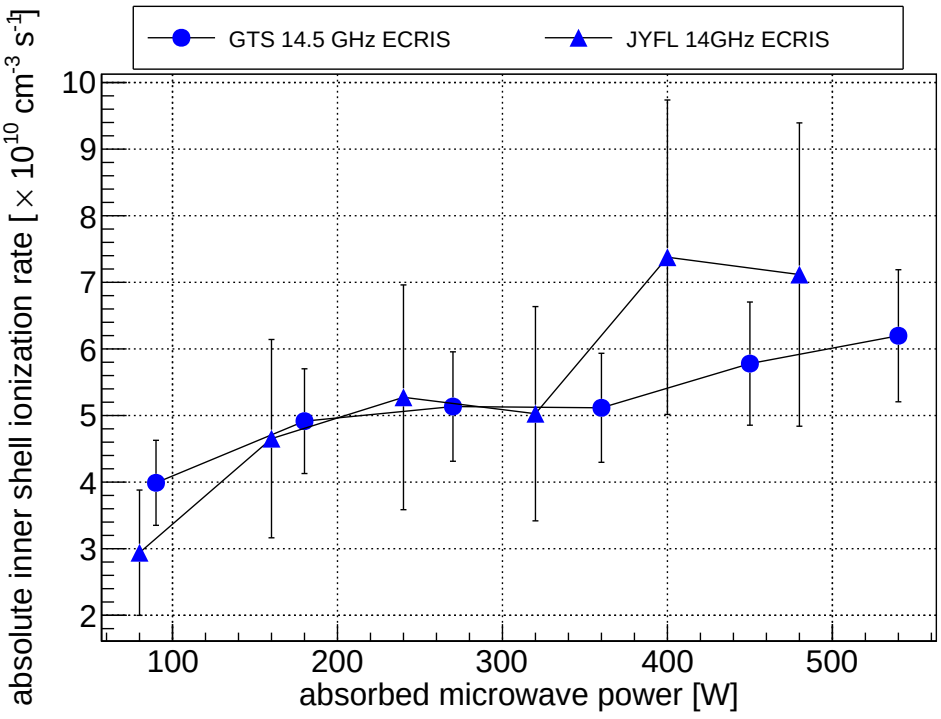

FIGURE 31 Comparison of the (minimum) absolute inner shell ionization rates. Variation of the (minimum) absolute inner shell ionization rate as a function of absorbed microwave power for the GTS at iThemba LABS and the JYFL 14 GHz ECRIS. This figure is reproduced from Ref. [PI].

4.2 Investigation into the gas mixing effect using $K\alpha$ and optical diagnostics

Over the years numerous techniques have been developed to enhance HCS production in ECR ion sources, as discussed in section 2.6. The gas mixing is one of those techniques which has proven to be very successful in terms of HCS production, but remains not completely understood. To contribute towards the current understanding of this technique, two non-invasive plasma diagnostics were combined to study HCS production using different mixing gases. The investigation was performed on both the JYFL 14 GHz ECRIS and the GTS at iThemba LABS. In both cases argon was used as working gas, with helium, neon and krypton used as mixing gases on the JYFL 14 GHz ECRIS. With the gas mixing experiments performed on the GTS, data were also recorded with oxygen and xenon. The pumping speed at the plasma chamber is completely different between the two sources due to the different pumping arrangements i.e. radial pumping ports on the JYFL 14 GHz ECRIS versus no radial pumping on the GTS, which impacts the amount of gas injected into the source at seemingly identical pressure range. Additionally the total pressure measured by the ionization gauge is a strong function of the gas composition which changed with each mixing gas. Both these factors complicate the analysis and make direct comparison of results between the two sources intricate. Nevertheless, the comparison of the results obtained with two ion sources assists with establishing certain trends that can be used for deducing the physics of gas mixing.

Although it is clear that the gas mixing enhances HCS production, the key to unraveling the physics potentially lies with the low charge state ions. This assertion is premised on the notion that with ion cooling, the low charge state ions of the lighter gas species are heated which limits their confinement [72]. Another point to consider is the broad pressure sweep performed during this investigation. At the upper limit of the pressure sweep the production of HCS ions is limited by charge exchange. To address this difficulty the Ar^{9+} beam current was used as an indication of HCS ion production. This choice is justified as this ion is produced by removal of an electron from the L-shell resulting in a significant increase in ionization potential in comparison to low charge state ions. The gas mixing investigation also posed an additional difficulty as both sources had ion optical limitations. At JYFL the m/q range was limited to ≤ 8 with 10 kV extraction voltage due to the maximum current of the bending magnet and at iThemba LABS the transport efficiency of the extracted beams was limited due to losses in the beamline section between the ion source and the bending magnet. To address the m/q limitation due to the analyzing magnet in the transfer beamline at JYFL the optical emission from the transition $3s^2 3p^4(^3P)4p\ ^4D^\circ_{5/2} \rightarrow 3s^2 3p^4(^3P)4s\ ^4P^\circ_{3/2}$ of Ar^{1+} was also measured. This enabled the behaviour of the low charge state ions

i.e. Ar^{1+} to be tracked from measurement of the optical emission.

The results of the gas mixing investigation are fully discussed in Ref. [PII]. The investigation was started by keeping the flow rate of the argon working gas constant and varying the flow rate of the mixing gas while simultaneously measuring the Ar $K\alpha$ emission, the optical emission and the extracted ion beam charge state distribution. The results of the $K\alpha$ investigation for the two ion sources are presented in Figs. 32 and 33. As a result of the difficulties (described earlier) in measuring the actual neutral gas pressure in the plasma chamber, it was decided to present the results as a function of the valve setting of the mixing gas. This choice is supported by the fact that both the bias disc current and the source drain current (total particle current exiting the plasma) were observed to not follow the gas flow rate monotonically. Additionally only the results obtained with the noble gases are presented. The results obtained with oxygen were omitted as the energy released in molecular dissociation affect the ion dynamics, which complicates interpretation of the results. From the results presented in Figs. 32

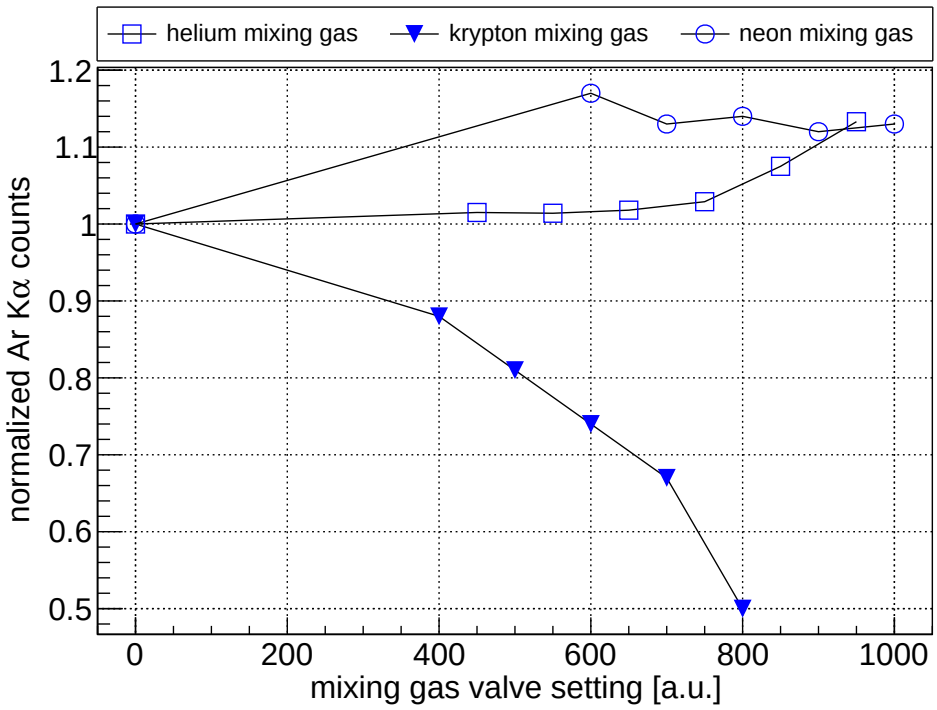

FIGURE 32 Normalized Ar $K\alpha$ emission/inner shell ionization rates as a function of the mixing gas flow for the 14 GHz ECRIS at JYFL. The neutral gas pressure at injection without adding mixing gas was 4.9×10^{-7} mbar. This figure is reproduced from Ref. [PII].

and 33 it appears as if the Ar $K\alpha$ emission rate increase if the mass of the mixing gas species is lighter than that of argon. The only notable exception to this result is observed with neon. With neon mixing gas, the Ar $K\alpha$ emission rate dis-

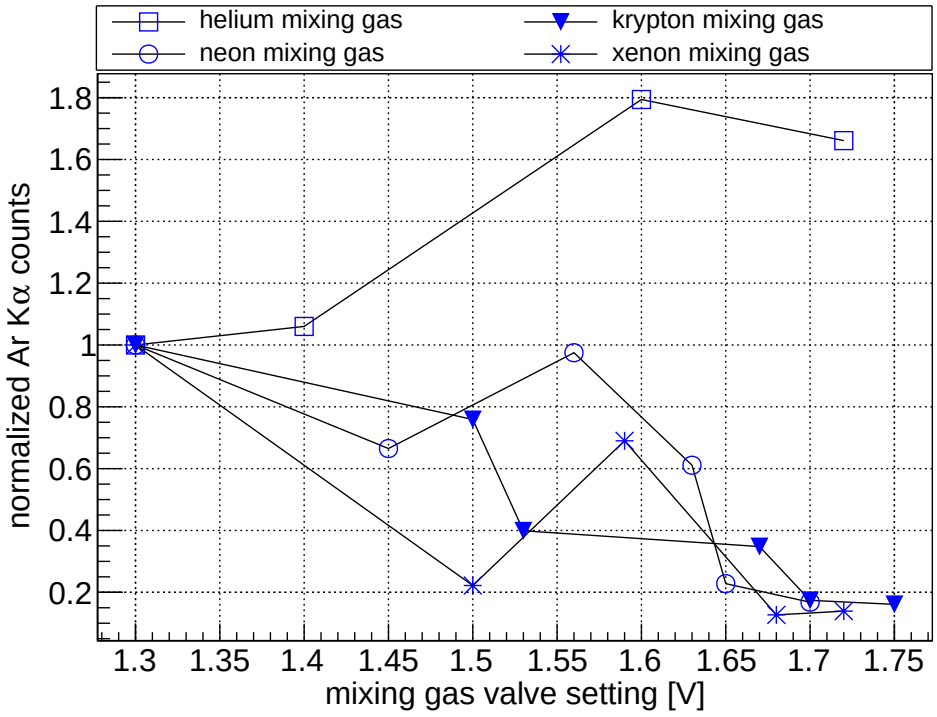

FIGURE 33 Normalized Ar $K\alpha$ emission/inner shell ionization rates as a function of the mixing gas flow for the GTS at iThemba LABS. This figure is reproduced from Ref. [PII].

plays different behaviours on the two sources. The Ar $K\alpha$ emission rate increased when adding neon as a mixing gas in the case of the JYFL 14 GHz ECRIS, while the Ar $K\alpha$ emission rate decreased with increasing neon flow rate on the GTS at iThemba LABS. The exact reason for this observation remains unclear. Explaining the 'neon abnormality' would require further experiments but this was omitted here as it is a minor detail when viewed against the scope of the whole thesis. Hence the results obtained with neon mixing gas are omitted from the following discussion.

From Eq. (2.51) it is known that the Ar $K\alpha$ emission rate (and inner shell ionization rate) is a function of the electron density, argon density and the rate coefficient for ionization. The increase in Ar $K\alpha$ emission rate with lighter mixing gas species can therefore be due to two scenarios i.e. the electron density increases and/or the argon density increases. This assessment is based on the assumption that the rate coefficient for inner shell ionization, at different charge states, remains quasi-constant. This assumption has two components: (1) the binding energy of the K-shell electrons does not change significantly as the charge state of the ion changes and (2) the relative number of radiative versus radiationless transitions does not change significantly with the charge state of the ion. The increase in binding energy of the $1s$ electrons of the K-shell is estimated to be $\approx$ 700 eV, from neutral argon to Ar^{15+} [20], which justifies the first part of the

assumption. The second part of the assumption i.e. $\omega_K \approx$ constant at different charge states of the ion is supported by Ref. [124]. This discussion gives the basis for the assumption of a quasi-constant rate coefficient at different charge states.

The speculated increase in electron density (which could partly/wholly account for the experimental observation in Figs. 32 and 33) with increasing mixing gas pressure is suggested to be caused by ionization of the mixing gas and argon species. Assuming ionization of the mixing gas species occurs predominately as a result of the removal of the outermost electrons, xenon and krypton should result in the fastest growth in electron density as the binding energy of their outermost electron is 11 eV and 13 eV, respectively. Additionally the heavier noble gases have more electrons which have lower ionization cross sections. The growth in electron density should be slowest with the helium mixing gas as the binding energy of its outermost electron is 23 eV and only two electrons can be removed before reaching fully ionized state of the atom. The fact that Ar $K\alpha$ emission rate monotonically decreases with heavier mixing gas species leads to the conclusion that the Ar $K\alpha$ emission rate is dominated by a different process i.e. the argon density decreases with the addition of the heavier mixing gas, with the electron density playing a lesser role.

The proposed reason for the change of argon density can best be discussed by considering high and low charge state production, measured simultaneously with the Ar $K\alpha$ emission. Figures 34 and 35 presents the normalized Ar^{9+} beam current and the normalized Ar^{1+} optical emission, respectively. From Fig. 34 it can be seen that the Ar^{9+} beam current increases with helium as mixing gas and decreases with krypton as mixing gas. Simultaneously from Fig. 35 it can be seen that the Ar^{1+} ion production (as estimated from the optical emission) decreases with helium and increases with krypton. Both these results indicate a strong mass dependence on the Ar $K\alpha$ emission rate. In total the results presented suggest that argon becomes better confined with lighter mixing gas leading to the increased $K\alpha$ emission. In addition to this Fig. 35 further suggests enhanced losses of the lighter ion species. Hence when krypton is used as a mixing gas, argon is preferentially lost and when helium is used as a mixing gas, helium ions are preferentially lost. The results appear to favour ion cooling [69] as the mechanism leading to enhanced HCS production during gas mixing. The lowering of the average charge state of the plasma [55] can however not be excluded from causing the observation.

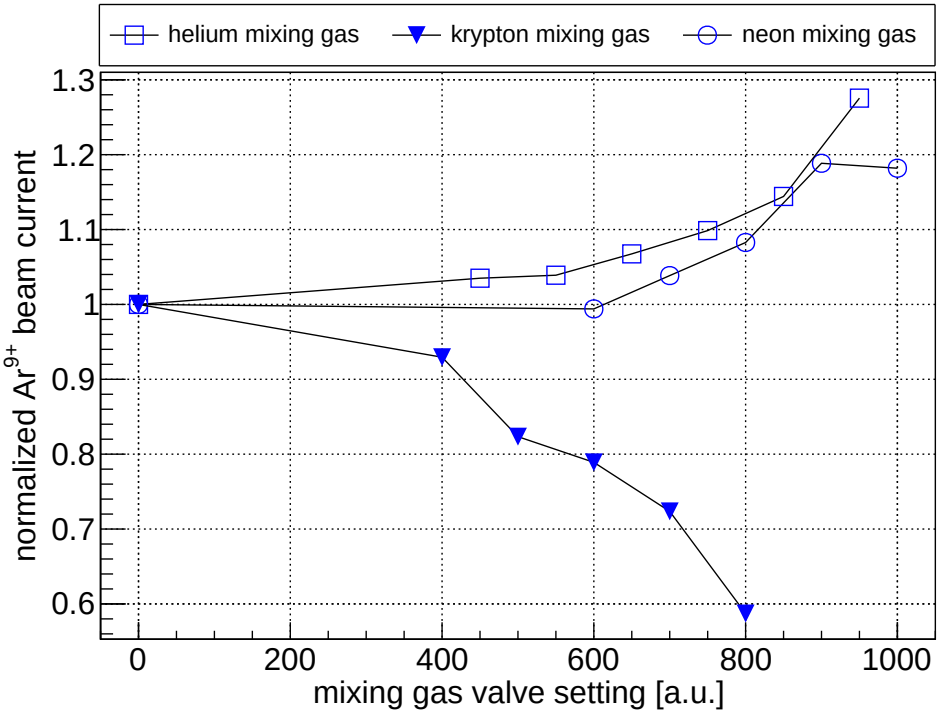

FIGURE 34 Normalized Ar^{9+} beam current as a function of the mixing gas flow for the 14 GHz ECRIS at JYFL. This figure is reproduced from Ref. [PII].

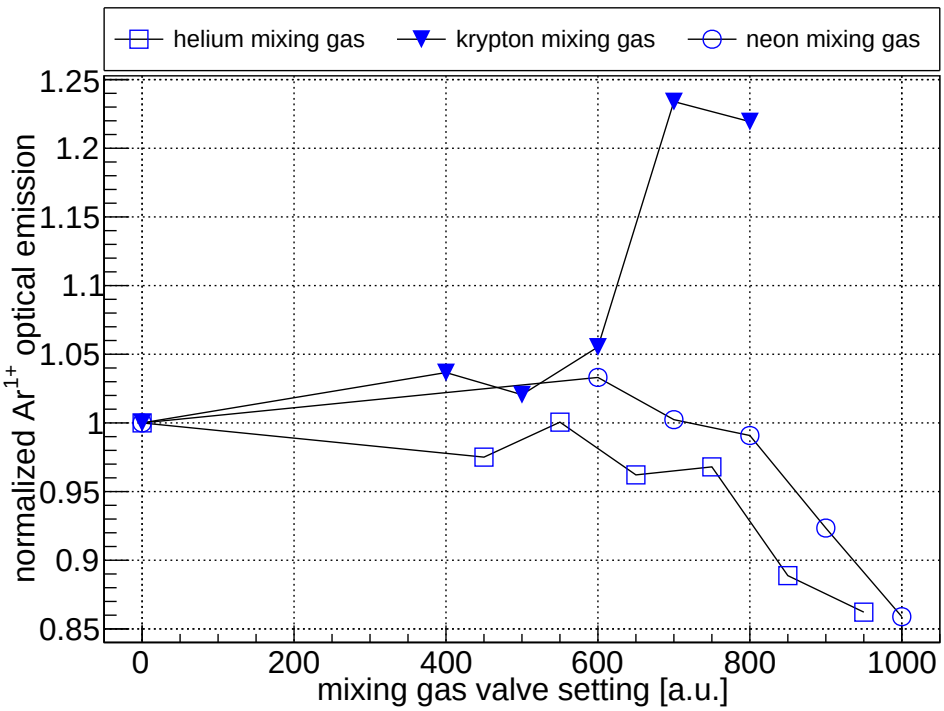

FIGURE 35 Normalized Ar^{1+} optical emission as a function of the mixing gas flow for the 14 GHz ECRIS at JYFL. This figure is reproduced from Ref. [PII].

4.3 Studying the double-frequency heating mode using $K\alpha$ diagnostics

To shed more light on the underlying mechanism resulting in favourable plasma conditions for HCS production with double-frequency heating, this plasma heating mode was investigated using a combination of three different diagnostic techniques i.e. $K\alpha$ emission, optical emission and the extracted ion beam charge state distribution. In addition to estimating the volumetric inner shell ionization rate, the $K\alpha$ emission (as fully discussed in section 4.4) also enabled an estimation of the relative electron losses from the confinement system of the ECRIS. To study the evolution of two different charge states during the investigation, the optical emission of two transitions were acquired radially. To follow the Ar^{9+} ion production rate the $2s^2 2p^5\ P^{\circ}_{1/2} \rightarrow 2s^2 2p^5\ P^{\circ}_{3/2}$ transition was measured and to follow the Ar^{13+} ion production rate the $2s^2 2p^2\ P^{\circ}_{3/2} \rightarrow 2s^2 2p^2\ P^{\circ}_{1/2}$ transition was measured. The investigation was only performed on the JYFL 14 GHz ECRIS, as this source is equipped with two power sources as discussed in section 3.1. Additionally the JYFL 14 GHz ECRIS also has radial ports for optical diagnostics.

The investigation (fully discussed in Ref. [PIII]) was started by operating the source in single-frequency mode and varying the heating frequency and power delivered from the TWTA. The heating frequency from the TWTA was varied between 11.100 GHz and 12.450 GHz, with the power varied between 50 W and 150 W, in 50 W steps. From operational experience at JYFL certain microwave heating frequencies delivered from the TWTA are known to be effective in enhancing HCS ion production and they do not deposit power on the waveguide elements such as the high voltage break. As a result of this the frequencies were chosen so that the microwave-plasma coupling is known to be effective. The first part of the investigation enabled a determination of the relative sensitivity of the various diagnostics signals as shown in Table 6. As expected, the Ar $K\alpha$ emission rate (and the relative electron losses) increased with increasing microwave power. This result is consistent with those obtained in section 4.1. The reason for the increased relative electron losses with microwave power is fully discussed in section 4.4. The influence of varying the heating frequency, also known as frequency tuning, on the various diagnostics signals indicates that the Ar $K\alpha$ emission rate and extracted Ar^{9+} beam current increase with the heating frequency which is indicative of increasing electron density as suggested by the $I_q \propto \omega_{RF}^2$ scaling law. In addition to this the injection mirror ratio $R_{\mathrm{inj}} = B_{\mathrm{inj}}/B_{\mathrm{ECR}}$ was also varied. This investigation revealed that the relative electron losses (towards the biased disc) is not exclusively determined by R_{inj} but perhaps also by the absolute magnitude of the magnetic field, which underlines the difficulty of determining the effective mirror ratio in ECRIS plasmas.

With the second part of this investigation the source was operated in single- and

TABLE 6 Ar and Fe $K\alpha$ counts, Fe-to-Ar $K\alpha$ ratio (r), Ar $K\alpha$ volumetric inner shell ionization rate and extracted Ar^{9+} beam current as a function of the microwave frequency at constant 150 W power and $R_{inj} = 3.87$. The volumetric rate is calculated for the plasma volume visible to the X-ray detector.

Frequency [GHz]	Ar $K\alpha$ counts [cps]	Fe $K\alpha$ counts [cps]	Fe-to-Ar $K\alpha$-ratio (r)	Ar $K\alpha$ volumetric rate [counts/ cm^3]	Ar^{9+} current [μA]
11.100	110	720	6.4	9.9×10^9	17
11.560	200	1010	5.1	1.7×10^{10}	35
12.450	290	860	2.9	2.6×10^{10}	50
14.056	600	160	0.3	5.2×10^{10}	81

double-frequency modes with the heating frequency of the TWTA set to 11.56 GHz, which is the experimentally found optimum secondary frequency for the JYFL 14 GHz ECRIS. The source was optimized for Ar^{9+} and Ar^{13+} ion production, respectively. With the source optimized for Ar^{9+} ion production, 320 W of microwave power was injected into the plasma chamber and 520 W for the Ar^{13+} optimized setting. The microwave power was increased from the optimized setting in 10 W steps by adding power respectively from the TWTA (double-frequency mode) and klystron (single-frequency mode) while acquiring the various diagnostics signals. In double-frequency mode the TWTA power was ramped up to 19% (Ar^{13+}) and 31% (Ar^{9+}) of the klystron power in the two cases. Figures 36 and 37 present the normalized Ar $K\alpha$ counts on the primary axis and the Fe-to-Ar $K\alpha$ ratio (used to estimate the relative electron losses) on the secondary axis with the source optimized for Ar^{13+} and Ar^{9+} ion production, respectively. This result highlights two important points, firstly the performance of the source in terms of Ar $K\alpha$ emission rate remains the same whether the additional power is added from the TWTA (double-frequency mode) or the klystron (single-frequency mode) with the source optimized for Ar^{9+} ion production. This result is illustrated on the primary axis of Fig. 37. Additionally the figure also indicates that the relative electron losses (as given by r on the secondary axis) remains constant for both heating modes with the source optimized for Ar^{9+} ion production. Secondly, the favourable influence of double-frequency heating only becomes prevalent if the source is optimized for Ar^{13+} ion production as seen on the primary axis of Fig. 36. The latter observation is consistent with Refs. [63, 125] reporting that the effect of the secondary frequency is only observed for very HCS ions both in CW and pulsed operation modes. The relative electron losses, as seen from the secondary axis of Fig. 36 decreases in double-frequency mode and remains practically constant in single-frequency mode with the source optimized for Ar^{13+} ion production.

Figures 38 and 39 present the normalized optical emission for the $2s^22p^2\ P^\circ_{3/2} \rightarrow 2s^22p^2\ P^\circ_{1/2}$ transition of Ar^{13+} and $2s^22p^5\ P^\circ_{1/2} \rightarrow 2s^22p^5\ P^\circ_{3/2}$ transition of Ar^{9+}.

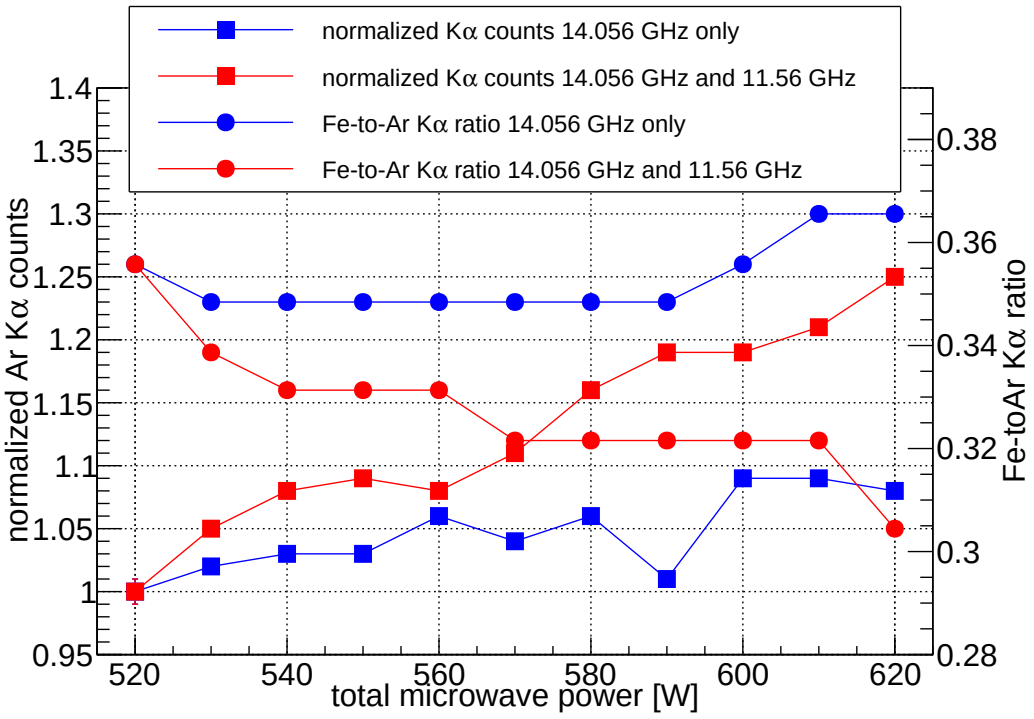

FIGURE 36 Normalized Ar *Kα* counts and the Fe-to-Ar *Kα* ratio with the source optimized for Ar^{13+} ion production. This figure is reproduced from Ref. [PIII].

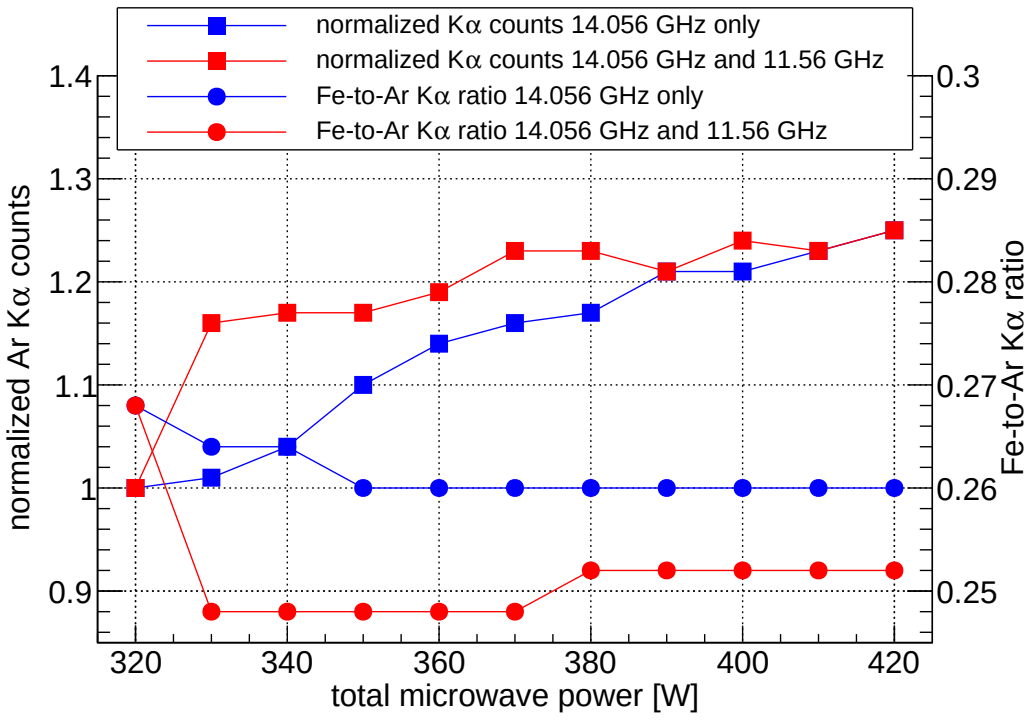

FIGURE 37 Normalized Ar *Kα* counts and the Fe-to-Ar *Kα* ratio with the source optimized for Ar^{9+} ion production. This figure is reproduced from Ref. [PIII].

These figures show a similar observation made with the normalized Ar $K\alpha$ emission. Figure 38 indicates (with the source optimized for Ar^{13+}) that there is a clear difference between power added from the TWTA versus power added from the klystron i.e. the additional power added with the TWTA improves Ar^{13+} production. The difference between the normalized optical emission with the source optimized for Ar^{9+} production is less pronounced as presented in Fig. 39.

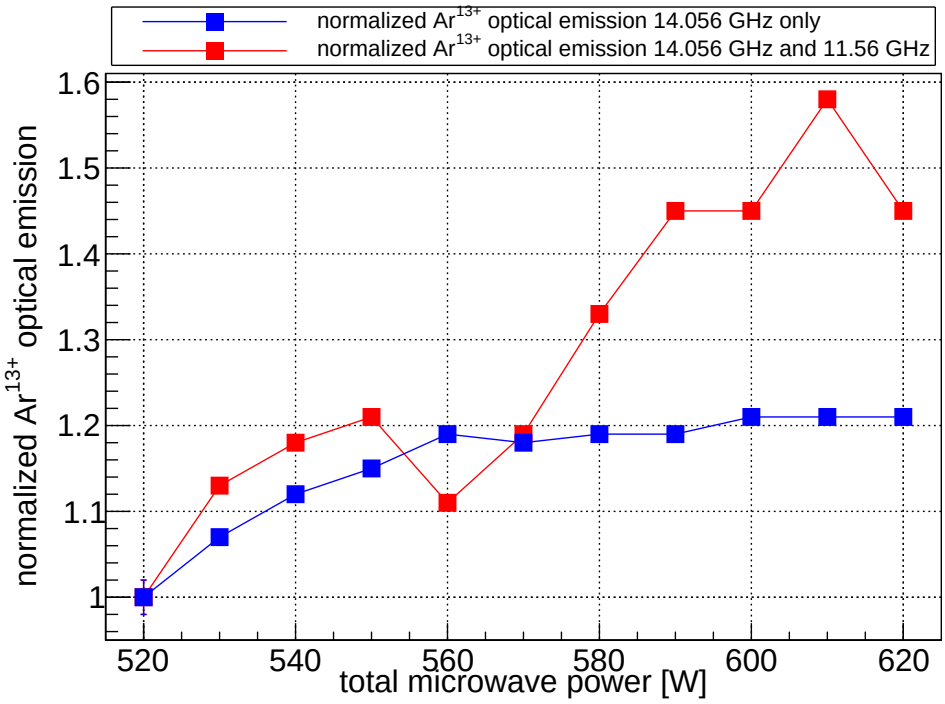

FIGURE 38 Normalized optical emission for $2s^22p^2\ P^{\circ}_{3/2} \rightarrow 2s^22p^2\ P^{\circ}_{1/2}$ transition of Ar^{13+} with the source optimized for Ar^{13+} ion production. This figure is reproduced from Ref. [PIII].

Figures 40 and 41 present the extracted beam currents of Ar^{13+} and Ar^{9+}, respectively. Figure 40 shows similar trends observed with the optical emission and the Ar $K\alpha$ emission. With the source optimized for Ar^{13+} there is a clear difference between the extracted Ar^{13+} beam with the source operated in single- and double-frequency mode. As observed earlier with the other diagnostic signals, the difference between single- and double-frequency heating modes are minimal for Ar^{9+} extracted beam as shown in Fig. 41. An interesting observation can be made by comparing Fig. 39 with Fig. 41. From this comparison it can be seen that the Ar^{9+} ion density increases with increasing microwave power as shown in Fig. 39. The extracted ion beam current of Ar^{9+} in contradiction to the ion density decreases with increasing microwave power as shown in Fig. 41. This abnormality has been investigated by Kronholm *et al.* and the observation was attributed to the diffusion transport of the argon ion species from the plasma core

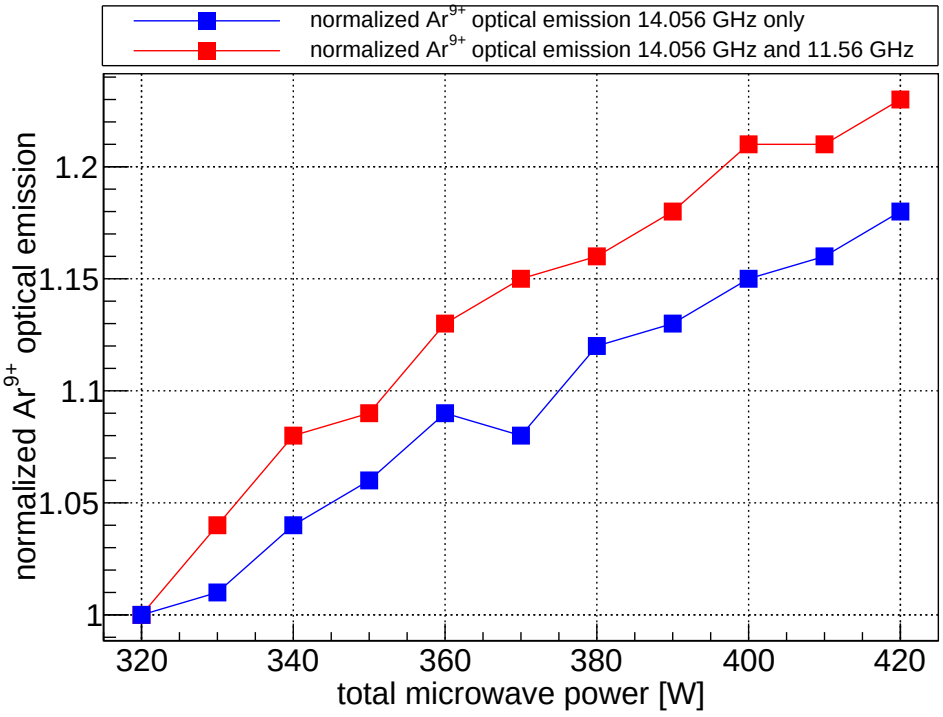

FIGURE 39 Normalized optical emission for $2s^2 2p^5\ P^{\circ}_{1/2} \rightarrow 2s^2 2p^5\ P^{\circ}_{3/2}$ transition of Ar^{9+} with the source optimized for Ar^{9+} ion production. This figure is reproduced from Ref. [PIII].

to the extraction aperture of the source as well as the ion extraction [126].

In total the conclusion drawn from the combined diagnostic investigation into the effectiveness of double-frequency heating indicates the increase in warm electron density in double-frequency mode as oppose to single-frequency mode in all likelihood accounts for the favourable effect. Additionally the Fe-to-Ar $K\alpha$ emission ratio (secondary axis of Figs. 36 and 37) seems to indicate less warm electrons are expelled or the electrons expelled in double-frequency mode are preferentially those belonging to the high energy tail of the distribution in double-frequency mode compared to single-frequency mode. This leads to the conclusion that the power distribution between the two resonance surfaces affects the microwave induced pitch angle scattering (as discussed in section 2.3.3.2) improving the plasma stability. The possibility that double-frequency heating affects the electrostatic confinement of ions and hence the production of HCS ions can however not be excluded based on the diagnostics used in this investigation.

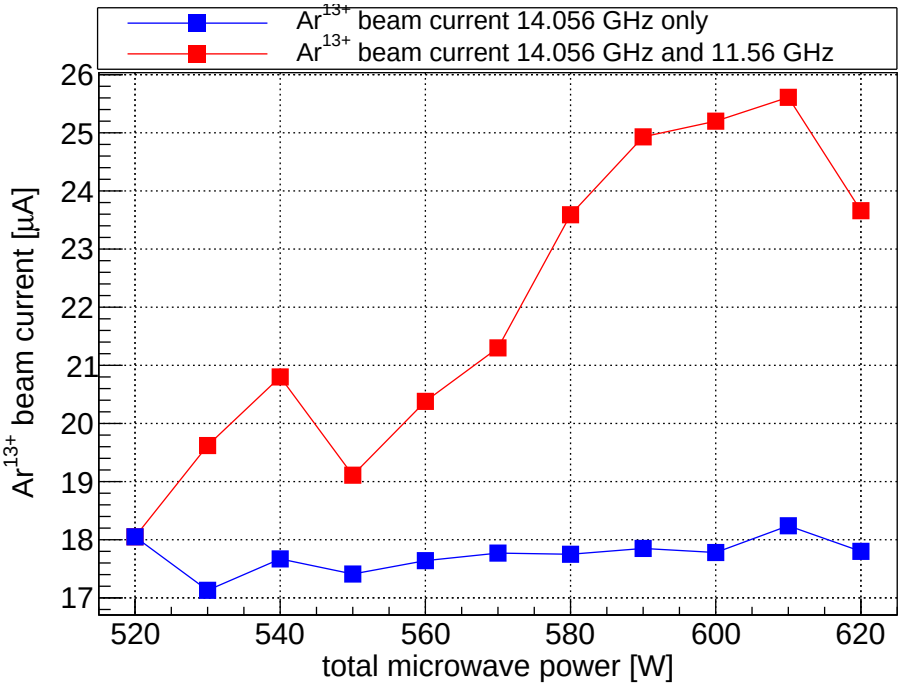

FIGURE 40 Ar^{13+} beam current with the source optimized for Ar^{13+} ion production. This figure is reproduced from Ref. [PIII].

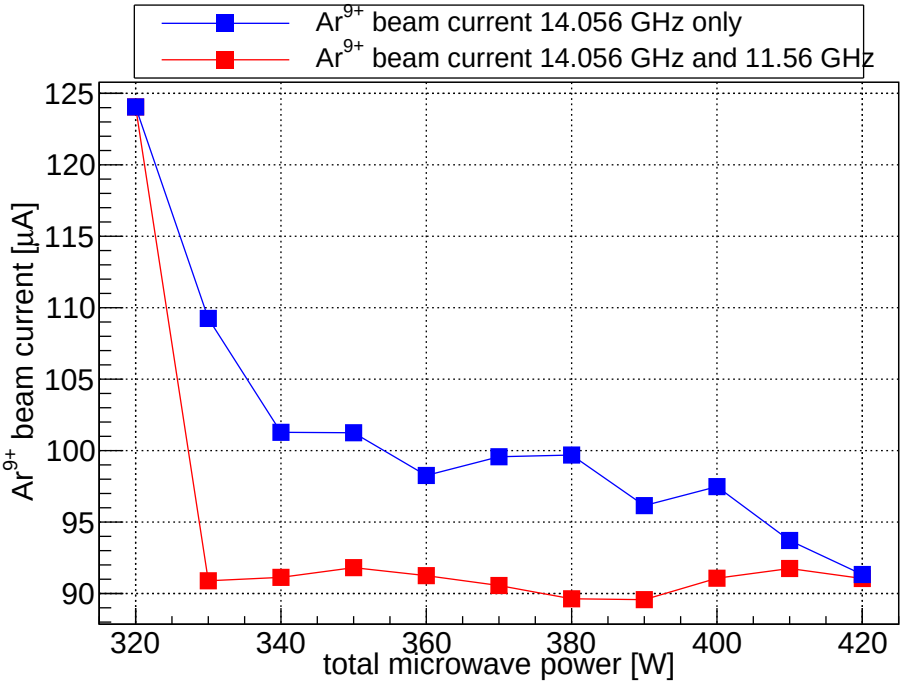

FIGURE 41 Ar^{9+} beam current with the source optimized for Ar^{9+} ion production. This figure is reproduced from Ref. [PIII].

4.4 Experimental investigation into microwave induced electron losses from an ECRIS plasma

It has been suggested that the observed saturation in ECRIS performance in terms of ion charge state production is due to saturation of the electron density by enhanced electron losses [44]. From the discussion in section 2.3.3 it is known that a number of interactions can result in electron losses. The interaction of prime interest for the current discussion is the microwave induced electron loss, due to the magnetic field component of the microwave radiation. For the work described in this section the microwave induced electron losses have been studied using four plasma diagnostic techniques i.e. the Fe-to-Ar $K\alpha$ emission ratio, detection of the electrons escaping from the magnetic confinement system of the ECRIS, bremsstrahlung radiation and visible light emission. The first diagnostic technique was applied with the source operated in CW mode with argon while the latter three techniques were applied with the source operated in pulsed mode with oxygen. Both investigations, thoroughly discussed in Ref. [PIV], were performed on the JYFL 14 GHz ECRIS.

4.4.1 Relative electron losses in CW mode of operation

The relative (or fractional) electron losses can be estimated by measuring the Fe-to-Ar $K\alpha$ emission ratio, hereinafter referred to as r. This assertion is premised on the fact that the respective $K\alpha$ emission lines originate from different regions inside the source. The Fe $K\alpha$ emission is largely due to warm and hot electrons escaping the magnetic confinement system of the ECRIS. Consequently the lost electrons interact with the biased disc located at the tip of the injection plug i.e. the iron characteristic radiation is predominantly emitted from the surface of the biased disc. The Ar $K\alpha$ emission is due to inner shell ionization of the argon. Additionally it should be emphasized that argon, as a noble gas, does not accumulate to the walls of the containment vessel and therefore the emitted Ar $K\alpha$ emission predominately emanates from the confined plasma volume. Given that the Fe $K\alpha$ emission is proportional to the electron losses towards the biased disc and the Ar $K\alpha$ emission is proportional to the density of the confined electrons, the ratio r can be used to estimate the relative electron losses as a function of the ion source operating parameters.

To establish the influence of the four source tune parameters i.e. biased disc voltage, B-field, microwave power and neutral gas pressure on r, a parametric sweep of the four tune parameters were performed. The parametric sweep of the biased disc voltage revealed that this tune parameter has practically no influence on the relative electron losses. This observation is thought to be due to the fact that the biased disc voltage exclusively operates on the cold electron population of the

ECRIS having only indirect impact on the other electron populations. As a result of this observation the investigation and discussion into the relative electron losses was limited to the remaining three parameters.

Figure 42 presents the variation of r as a function of the magnetic field strength which was altered by adjusting the currents of both coils simultaneously and hence preserving the relative strength of the axial magnetic mirrors. The magnetic field strength is again characterized by the same two numbers as was used in section 4.1.1. The general trend observed is for r to decrease monotonically as the B_{min}/B_{ECR}-ratio increases or as the average parallel magnetic field gradient decreases. As extensively discussed in Ref. [PI] and given by Eq. (2.51), the inner shell ionization rate is a function of electron density, ion density and inner shell ionization rate coefficient. The average parallel magnetic field gradient decreases with increasing B-field, which presumably results in more efficient heating as suggested by Eq. (2.5). A recent investigation performed by Izotov *et al.* showed that the EEDF of the electrons escaping through the extraction mirror (plasma electrode) has a number of local maxima at energies 7-15 keV, shifting towards higher energies as the B_{min}/B_{ECR}-ratio is increased [30]. This should favour Fe $K\alpha$ emission over Ar $K\alpha$ emission as the rate coefficient for inner shell ionization of iron peaks at higher energy in comparison to argon. It can be expected that the parametric dependence of the EEDF of the escaping electrons reflects the parametric dependence of the EEDF of the confined electrons [30]. Altogether these observations imply that the decrease of r as a function of B_{min}/B_{ECR}-ratio is not explained by the change of the EEDF with the field strength. The only plausible explanation which fits the experimental result presented in Fig. 42, as well as the results of Izotov *et al.* [30] is:

- the electron density in the plasma volume visible to the detector increases with increasing magnetic field strength and/or
- the electron loss rate towards the injection region (biased disc) decreases with increasing magnetic field strength

The first scenario is consistent with improved source performance in terms of HCS production. In both Ref. [PI] and Ref. [24] it was shown that the HCS production is enhanced with increasing B-field as long as the instability threshold is not exceeded. The instability threshold for the JYFL 14 GHz ECRIS is located at approximately $B_{min}/B_{ECR} = 0.8$ (at a neutral gas pressure of 4.3×10^{-7} mbar). Beyond this point the source becomes prone to kinetic instabilities resulting in periodic bursts of electrons [24] and fluctuations of the plasma potential, decreasing the ion confinement time. Such electron losses can not be detected with the X-ray detector used to obtain the results presented in Fig. 42. The focus of the current investigation was however on electron losses in stable operation, neglecting electron losses due to plasma instabilities. The implicit assumption is that the

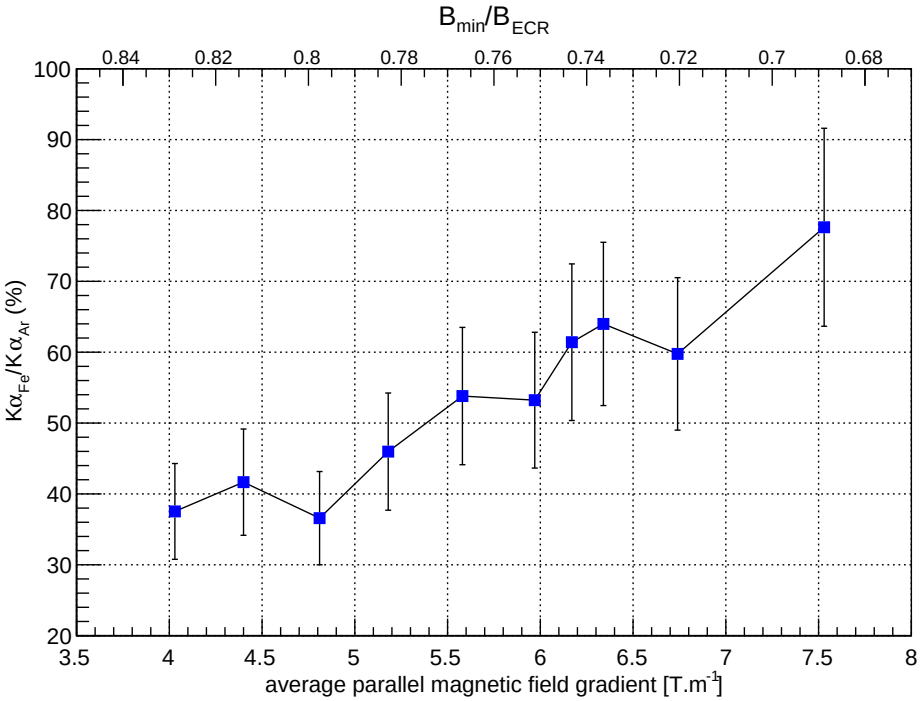

FIGURE 42 Variation of r as a function of the magnetic field strength with 400 W microwave power and 4.3×10^{-7} mbar neutral pressure. This figure is reproduced from Ref. [PIV].

electron losses due to plasma instabilities are minimal in stable operation making their detection irrelevant. However, the result of increased electron density with increasing B-field is inconsistent with those obtained in Ref. [PI]. In the cited investigation it was found that the electron density remains virtually constant with varying the B-field in the range discussed here. This strengthens the case for the axial B-field affecting the electron loss rate and their spatial distribution i.e. axial versus radial losses further supported by the fact that the radially emitted flux of the bremsstrahlung emission is observed to increase with increasing axial (mirror) field.

The second (and most probable) scenario is consistent with Eqs. (2.22) - (2.24) which indicates that the rate of axial electron losses is a strong function of the injection (and extraction) mirror ratio. The higher the mirror ratio, the smaller will be the electron loss rate. The reduction of the electron flux impinging the biased disc is consistent with the observation that the electron flux escaping through the extraction aperture is also reduced by the increase of the axial magnetic field strength [30]. It is also worth noting that the measurement here probes only axial losses. Ropponen *et al*. have shown that the radially emitted bremsstrahlung flux increases with increasing axial field strength, which leads to the conclusion that adjustments of the axial field strength redistribute the electron losses with higher field favouring radial losses [127]. In total the experimental result presented in

Fig. 42 along with the result obtained in Ref. [PI] suggests that the reduced electron losses with increasing B-field account for the observation. This investigation does not directly probe microwave induced electron losses but merely emphasizes the critical role of the magnetic field in determining the particle losses, which is not always obvious in the case of ECR ion sources. To study microwave induced electron losses the B-field should therefore be kept constant as was done for the remainder of the relative electron losses investigation.

Figure 43 presents the variation of r as a function of neutral gas pressure with $B_{min}/B_{ECR} = 0.706$, at selected microwave powers. From auxiliary diagnostics such as the biased disc and drain currents it is known that the electron density scales with the neutral gas pressure. This assertion assumes that the applied microwave power is sufficient to sustain or increase the ionization degree of the plasma. At low neutral pressure, the electron density can also be assumed to be low resulting in more efficient heating at fixed microwave power as compared to higher neutral pressure/higher electron density. This argument is reinforced by Ref. [16] reporting the results of bremsstrahlung emission measurements with the JYFL 14 GHz ECRIS at various neutral gas pressures. The microwave power absorbed at low neutral pressure can therefore easily result in high mean electron velocities which can exceed the phase velocity of the EM-wave. This would lead to enhanced electron losses at low neutral pressure as discussed in section 2.3.3.2. Figure 43 indicates a strong increase in r with increasing microwave power at low neutral pressure. This observation suggests an electron loss mechanism which depends on the plasma density and is coupled to the microwave power. As the neutral pressure is increased, both the electron density and argon density increase. This could impact r in two ways: (1) the increasing argon density leads to increased argon inner shell ionization decreasing r, (2) the increasing electron density results in increased damping of the EM-wave at resonance reducing r due to reduced rate of microwave induced pitch angle scattering. Although the data in Fig. 43 indicate that the relative $K\alpha$ emission depends on the plasma density the result does not unambiguously support the conclusion that rf-induced losses dominate the observed behaviour at low pressure. The conclusion drawn from the current parametric sweep is that the best way to probe microwave induced losses is to conduct a power sweep at several different neutral pressures keeping the magnetic field constant.

Figure 44 presents the influence of the absorbed microwave power on r with $B_{min}/B_{ECR} = 0.706$, at different neutral pressures. This result indicates two distinct domains: (1) r initially increases with absorbed microwave power and (2) r saturates with increasing absorbed microwave power. The increasing absorbed microwave power could impact the ECRIS plasma in at least three distinct ways:

– changing the EEDF leading to higher average electron energies

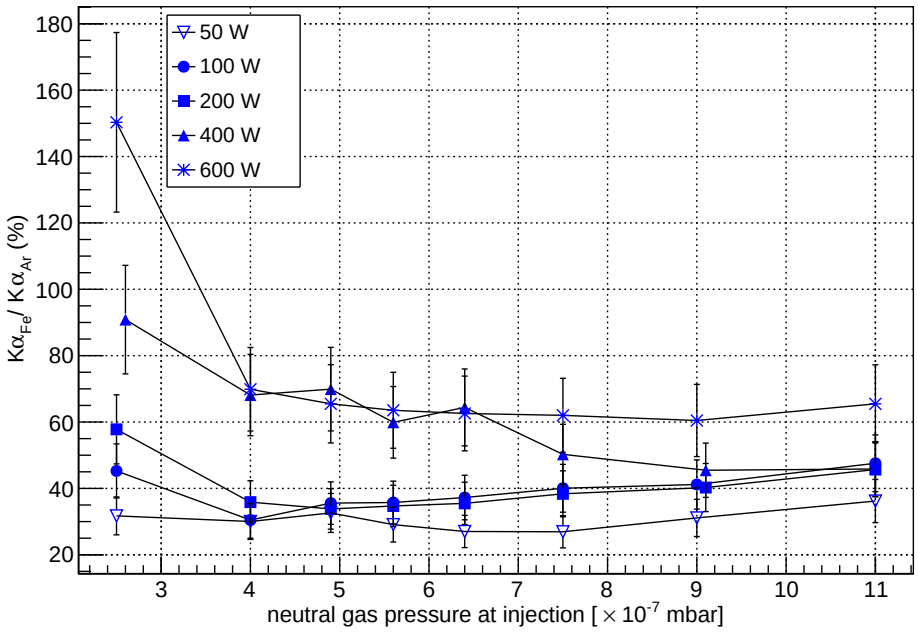

FIGURE 43 Variation of r as a function of neutral gas pressure with $B_{min}/B_{ECR} = 0.706$ at different microwave powers. This figure is reproduced from Ref. [PIV].

– increasing the electron density
– increasing the electron loss rate

Assessing the results presented in Fig. 44 against each of these possibilities excludes the increasing electron density from causing the first domain observed in Fig. 44. This is due to the fact that the increasing electron density would impact both Fe and Ar $K\alpha$ emission in a similar fashion, assuming the electron loss rate remains unchanged. The changing EEDF could account for the first domain as the increase in mean electron velocity could increase $\langle v \rangle$ in excess of the phase velocity which would favour microwave induced losses as discussed in section 2.3.3.2. However, the changing EEDF with increasing microwave power is in contradiction with the recent experimental observation by Izotov *et al.* [30] demonstrating that the microwave power has a minimal effect on the EEDF of the axially escaping electrons. This leads to the conclusion that the first domain observed in Fig. 44 indicates enhanced electron losses induced by the microwave power. It is emphasized that the conclusion cannot be drawn from merely monitoring the flux of escaping electrons but instead the measurement of the $K\alpha$ emission proportional to the electron loss rate (iron) and the density of confined electrons (argon) is required to make the conclusion. The saturation of r with microwave power is suggested to be dictated by the plasma energy content i.e. $n_e kT$. As the absorbed microwave power increases, the plasma density also increases up

until a point is reached at which the absorbed microwave power becomes insufficient to heat the plasma electrons released during ionization. This presumably causes the saturation observed in the second domain of Fig. 44. The saturation of the plasma energy content with injected microwave power has also been demonstrated by Noland *et al.* conducting experiments on the plasma diamagnetism [17] and (also) concluding that the effect is most likely dictated by rf-induced pitch angle scattering.

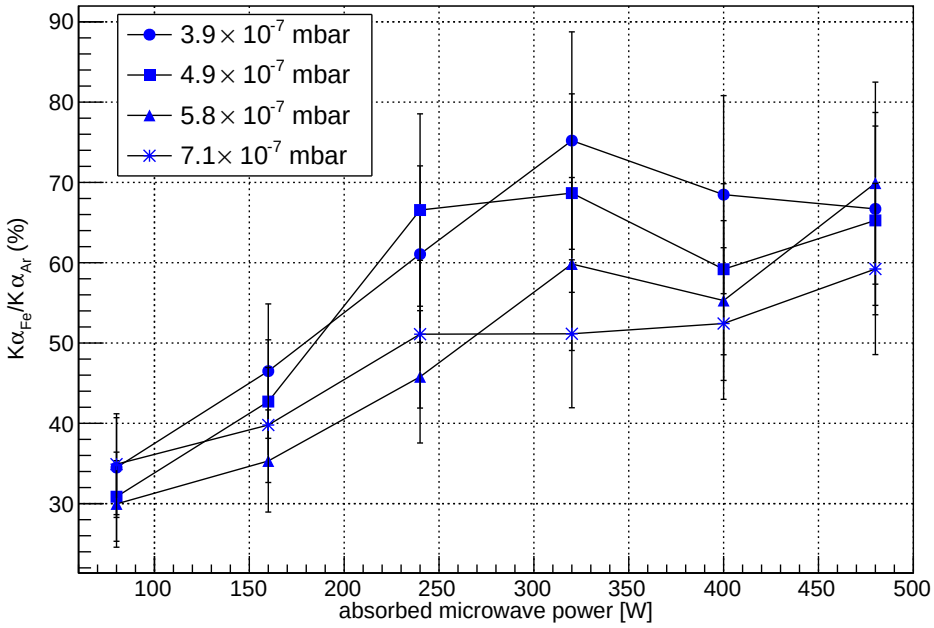

FIGURE 44 Variation of r as a function of the absorbed microwave power with $B_{min}/B_{ECR} = 0.706$ at different neutral pressures. This figure is reproduced from Ref. [PIV].

4.4.2 Electron losses in pulsed mode operation

The results presented above indicate the importance of rf-scattering for highly charged ECRIS plasmas only indirectly. Hence it was deemed mandatory to directly probe the electron losses as well. Thus, the microwave induced electron losses were investigated in pulsed operation to gain confidence for the arguments presented above. The experimental setup used for this investigation is presented in Fig. 25(b) in section 3.3.3. With this investigation aluminium foils of different thicknesses were inserted in front of the Faraday cup (see Ref. [115] for more details on the detector) and the electron signals measured with different source settings. The aluminium foils allowed for a crude determination of the threshold energies of the escaping electrons, as given by Table 4. The results of the

experiments are thoroughly discussed in Ref. [PIV] with a short summary given hereafter. This enabled the influence of the source settings on the various crude electron energy ranges to also be probed. With a future investigation the energy resolution of the measurement arrangement will be improved by using the dipole magnet in the transfer beamline as a spectrometer to separate the escaping electrons in more accurately defined energy ranges.

Figure 45 presents an example of a typical electron signal (in μA) measured with 25 ms / 200 W (14 GHz) microwave pulses with a repetition rate of 2 Hz, with different foils inserted. The magnetic field for this example had the following profile: $B_{\text{inj}} = 2.11$ T / $B_{\text{min}} = 0.39$ T / $B_{\text{ext}} = 1.02$ T. The presented example reveals a burst of electrons shortly after the microwave power is launched into the plasma chamber. The electron burst observed with all foils (cut-off energies) is caused by the so-called seed electrons [128] remaining trapped for the entire time between consecutive microwave pulses and finally escaping the confinement following the switch-on of the microwave power, thus providing direct evidence of microwave induced electron losses. The characteristics i.e. duration and magnitude of the electron bursts were found to be influenced by the source settings.

Figure 46 presents the variation of the electron signal with 25 ms / 700 W microwave pulses at different repetition rates, measured with the 1 mg/cm^2 foil inserted i.e. the signal corresponds to the (integrated) current of electrons with energies > 20 keV. The data was obtained with the following magnetic field profile: $B_{\text{inj}} = 2.01$ T / $B_{\text{min}} = 0.35$ T / $B_{\text{ext}} = 0.95$ T. The presented results highlight the fact that the characteristics of the electron burst associated with switching on the microwave power is influenced by the repetition rate of the incident power pulses. Fig. 46 indicates that the electron bursts becomes more pronounced as the repetition rate increases. The fact that the repetition rate influences the magnitude of the electron bursts strengthens the argument that the expelled electrons consist of the well-confined seed electrons. The effect of the seed electrons is observed down to 0.5 Hz repetition rate, which corresponds to a confinement time on the order of a few seconds matching the observations reported earlier in Ref. [80]. The behaviour observed with the 1 mg/cm^2 foil was replicated with foils of different thicknesses which indicate that the electron bursts have a broad energy range.

To gain a more complete understanding of the underlying mechanism at work, the electron signals were combined with visible light emission spectroscopy and bremsstrahlung diagnostics. The latter two diagnostic signals were integrated over the corresponding energy ranges and were acquired via the radial ports of the source. Figure 47 presents the electron signal measured with selected foil thicknesses, as well as the visible light signal and bremsstrahlung count rate. By comparing the maximum magnitude of the transient electron burst with the saturation electron signal, at the various foil thicknesses, it can be observed that

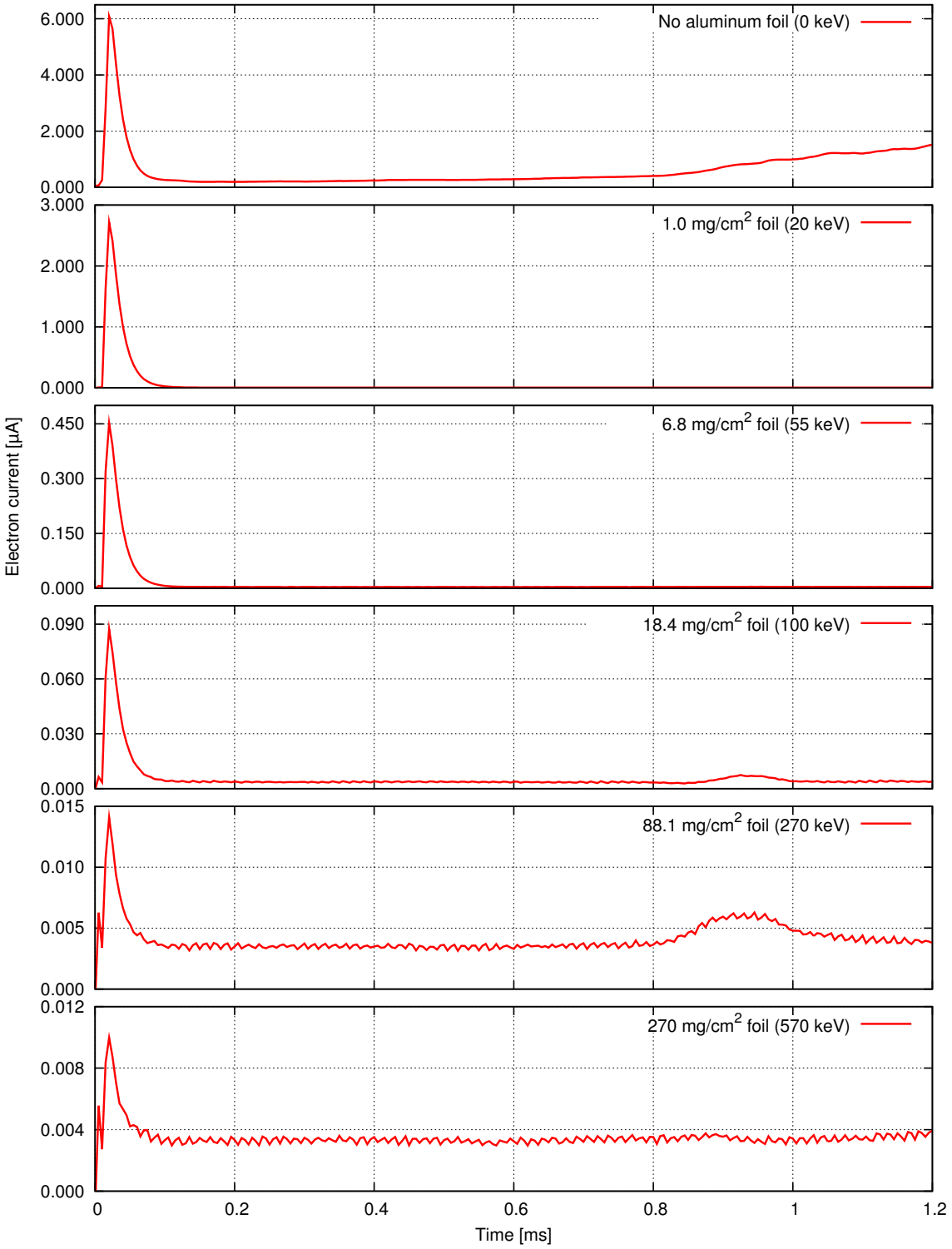

FIGURE 45 Variation of the electron signal with 25 ms / 200 W microwave pulse at a repetition rate of 2 Hz with different foils inserted. This figure is reproduced from Ref. [PIV].

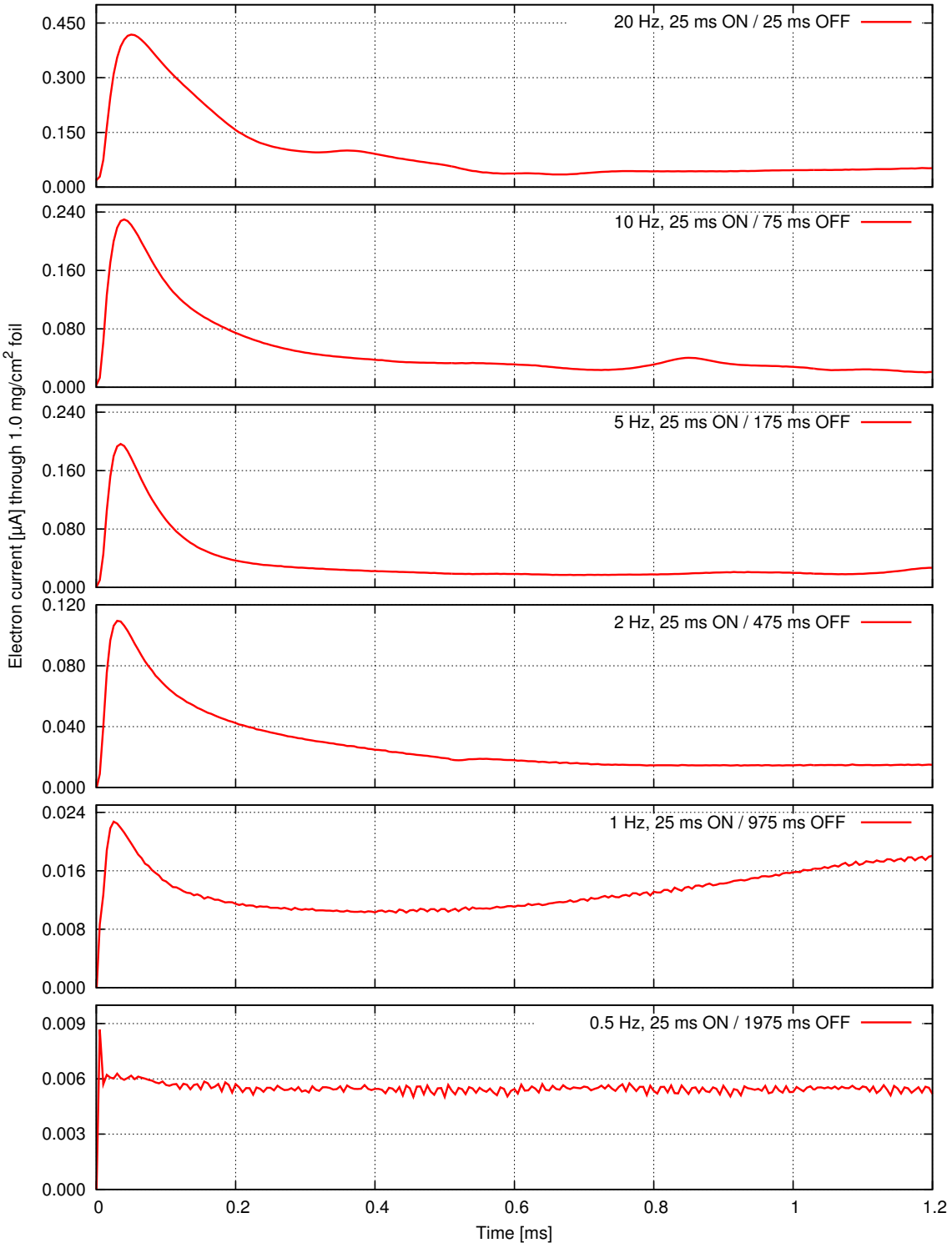

FIGURE 46 Variation of the electron signal with 25 ms / 700 W microwave pulse at different repetition rates with the 1 mg/cm^2 foil inserted. This figure is reproduced from Ref. [PIV].

the electron bursts becomes more pronounced with increasing electron energy. Meanwhile the visible light signal emitted predominantly by neutral atoms and low charge state ions is proportional to the cold $(10^2 - 10^3$ eV) electron density of the plasma. From this signal it can be deduced that the electron density is low during the transient electron bursts. At low plasma density, the electric field strength is high due to the reduced damping of the EM-wave. The plasma electrons subsequently attain a high mean electron velocity (as demonstrated in Ref. [48]) which favours microwave induced pitch angle scattering as discussed in section 2.3.3.2. The result presented in Fig. 47 therefore favours the suggestion of enhanced microwave induced losses. The bremsstrahlung count rate, measured via a radial port, indicates that the electron bursts is also observed in the radial direction. Additionally, as the ionization cascade proceeds the electric field strength at resonance and the mean electron velocity is decreased due to enhanced damping of the EM-wave. This presumably leads to the saturation of the high energy electron signal to a level below the initial transient as observed in Fig. 47.

Figure 48 presents the electron signal measured with selected foils, the visible light signal, the total bremsstrahlung count rate and the microwave power signal associated with the trailing edge of the microwave pulse at 24.85 ms. The electron signal is observed to decrease to less than 50% of its saturation value in about 20 μs after the microwave power is switched off. This is followed by a slower decay lasting some tens of milliseconds. The bremsstrahlung count rate also decays rapidly, followed by a smoother exponential decay. In contrast the decay of the visible light signal exhibits a smoother curve throughout the transient. The visible light signal however mostly probes the neutral atoms and low charge state ions so a different tendency is expected. The initial decay of the electron signals and the bremsstrahlung count rate is in excess of electron losses by Coulomb collisions only. This suggests a different loss mechanism i.e. microwave induced pitch angle scattering. The data associated with the trailing edge of the pulse offers the best direct evidence of microwave induced scattering of electrons into the loss cone.

The fractional contribution to electron losses due to the three loss mechanisms discussed in section 2.3.3 have been numerically investigated [19]. From the results of this simulation it is concluded that Coulomb collision losses account for between 20 – 35% of the total electron losses under stable plasma conditions. The drop of the electron signal at the end of the microwave pulse to less than 50 % of the rf ON signal suggests that the Coulomb collisions account for this fraction of the total losses. This result suggests that the simulation by Cluggish *et al.* (see Ref. [19]) is in good agreement with the experiment.

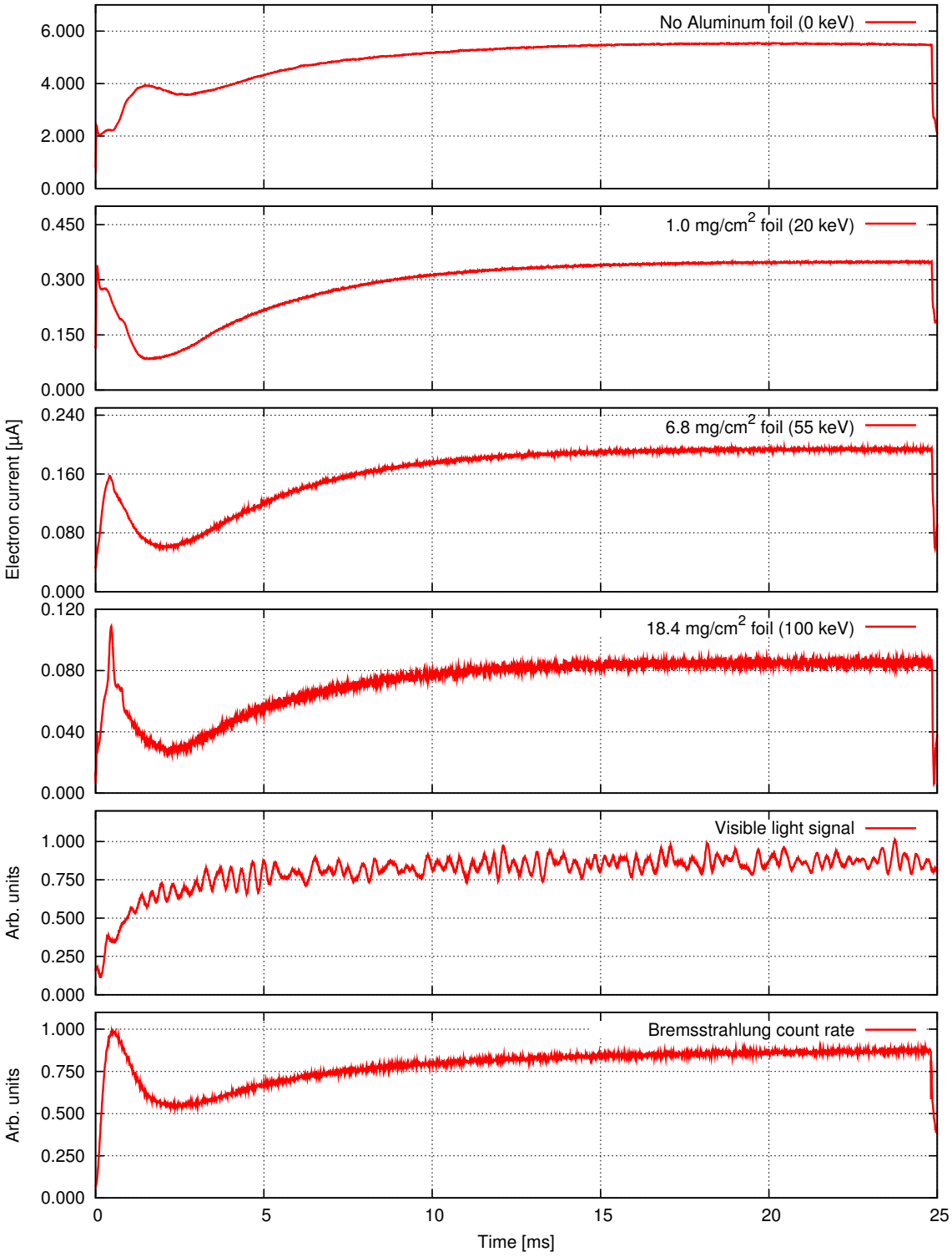

FIGURE 47 Variation of the electron signal, visible light signal and bremsstrahlung count rate with 25 ms / 200 W microwave pulse at a 20 Hz repetition rate. This figure is reproduced from Ref. [PIV].

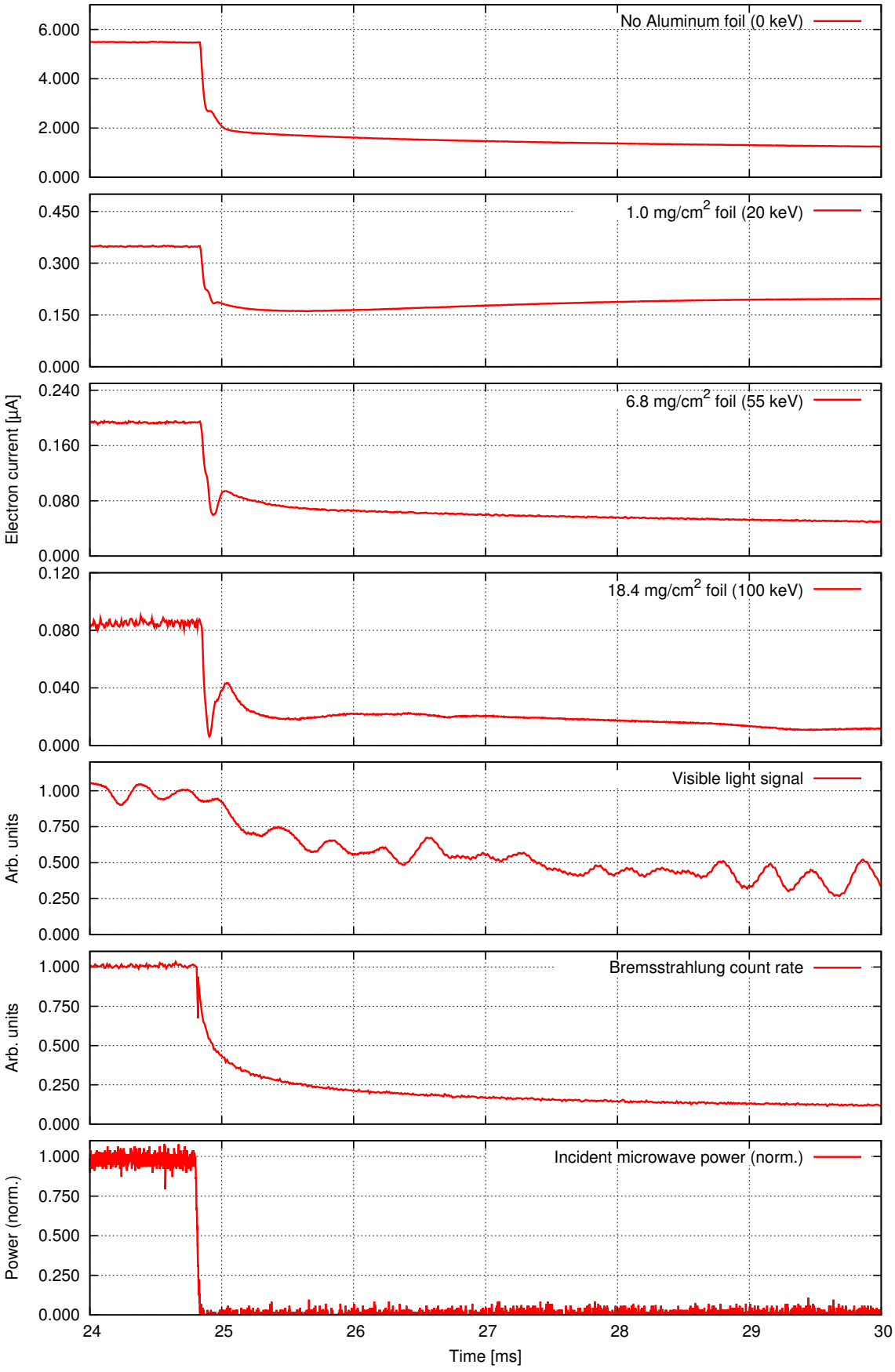

FIGURE 48 Variation of the electron signal, visible light signal, bremsstrahlung count rate and microwave power signal associated with the trailing edge of the microwave pulse at 24.85 ms. This figure is reproduced from Ref. [PIV].

5 DISCUSSION AND CONCLUSIONS

The continual request for increased production of highly charged, heavy-ion beam species of both stable and radioactive elements is demanding greater understanding of the fundamental plasma processes occurring in ECR ion sources. To study ECRIS plasmas, $K\alpha$ diagnostics have proven to be a versatile and valuable tool which can be used in isolation or combined with other plasma diagnostics to develop a more complete understanding of the various plasma processes. Additionally, $K\alpha$ diagnostics allow for the definition of an intermediate plasma parameter i.e. the volumetric inner shell ionization rate (absolute and/or relative) against which the results of numerical simulations on ECRIS plasmas can be benchmarked. The need for such a direct plasma parameter has long been identified by the community [122]. In this thesis work the different source tune parameters affecting $K\alpha$ emission have been studied. To develop a more complete understanding of ECRIS processes leading to HCS production, this plasma diagnostic was combined with bremsstrahlung diagnostics, optical emission spectroscopy and visible light spectroscopy to probe the ECRIS plasma non-invasively. Additionally the (relative and direct) electron losses from the magnetic confinement system of an ECRIS were also studied to shed more light on microwave induced electron losses, which is thought to impede ultimate source performance [44].

The investigation into the influence of the parametric sweep of the four source tune parameters on the volumetric $K\alpha$ emission rate/inner shell ionization rate revealed that only two of the tune parameters i.e. microwave power and neutral gas flow significantly impacted the volumetric $K\alpha$ emission rate. In both cases it was postulated that the $K\alpha$ emission rate is strongly coupled to the plasma energy content (Ref. [PI]). As a result of this 'coupled' behaviour it was observed that the measured volumetric $K\alpha$ emission rate increase with increasing microwave power. This behaviour is however expected to depend strongly on the range of the microwave power sweep. By increasing the microwave power beyond an

ambiguous threshold the plasma becomes prone to instabilities [24, 129] and numerous electron loss mechanisms [43], which in all likelihood would affect the plasma energy content and subsequently also the volumetric inner shell ionization rate. With the neutral gas flow sweep, it was observed that the volumetric $K\alpha$ emission rate initially increases rapidly followed by a saturation, with both features presumably being dictated by the plasma energy content (Ref. [PI]). It could be argued that the general trends observed during both parameter sweeps are universal to all ECRISs but certain characteristic features such as absolute values, rate of increase and saturation points depend on the design of a particular source. To interrogate this assertion, $K\alpha$ diagnostic investigations could be performed on modern superconducting sources operating at frequencies 18-45 GHz to verify how the volumetric inner shell ionization rate depends on the source design, in particular the volume of the plasma chamber versus injected microwave power and frequency. For example, it is proposed that the plasma chamber dimensions strongly influence frequency tuning due to the different modes excited inside the cavity. Probing the variation of the volumetric inner shell ionization rate as a function of multiple source design parameters for example B-field, heating frequency and plasma chamber material could yield a wealth of information and potentially inform future source design. Similarly it could be argued that the plasma chamber volume affects the ion confinement but larger plasma volumes require more power. These trends could be investigated with the volumetric $K\alpha$ emission rate.

The influence of the B-field and biased disc voltage sweeps on the volumetric $K\alpha$ emission rate was observed to be within the experimental error of the measurements (Ref. [PI]). In contrast to this, significant variations of both low and high charge state extracted ion beams were observed during both parametric sweeps. This highlights two important points: (1) both tune parameters influence HCS ion production indirectly for example through the ion confinement time (2) the important impact the volumetric inner shell ionization rate could have on benchmarking numerical simulations. The latter point is based on the fact that the plasma behaviour, induced during the parameter sweeps, manifests differently in the volumetric inner shell ionization rate and the extracted ion beam currents of the different charge states. The production of HCS ions for example is not only influenced by the plasma energy content but also by additional interactions occurring inside the ECRIS plasma such as charge exchange reactions. This implies that the evolution of HCS ion production during parametric sweeps could differ from the volumetric $K\alpha$ emission rate. The volumetric inner shell ionization rate could easily be reproduced as an intermediate output by most simulation codes.

With this thesis work the gas mixing effect was also investigated using $K\alpha$ diagnostics, with different mixing gases, on both the JYFL 14 GHz ECRIS and the GTS at iThemba LABS. It has been suggested that the key to unravelling

the physics governing this effect lies with the low charge state ions [72]. To estimate the ion density of the low charge state ions residing in the plasma, the $3s^2 3p^4(^3P)4p\ ^4D^\circ_{5/2} \rightarrow 3s^2 3p^4(^3P)4s\ ^4P^\circ_{3/2}$ transition of Ar^{1+} was measured through the radial diagnostics port of the JYFL 14 GHz ECRIS. Combining this diagnostic with *Kα* emission led to the suggestion that the ion cooling effect [69] most probably account for the favourable behavior observed with the gas mixing (Ref. [PII]). The investigation however could not exclude the lowering of the average charge state of the plasma as suggested by Geller *et al.* [55] from causing the beneficial effect. To conclusively address this issue, the ion temperatures of the different ion species (working and mixing gases) could be measured. Such an attempt has been made by Melin *et al.* [29] to determine the ion temperatures. The ion temperatures were however calculated from the extracted ion beam currents which introduce some uncertainty on the calculated result. Recently Kronholm *et al.* [31] have presented promising results obtained with an optical emission spectrometer which could directly measure the ion temperatures from the Doppler broadening of the emission lines. Given that the low charge state ions of the lighter gas species is proposed to be heated during ion cooling, see Eq. (2.43), measuring the ion temperatures directly from the plasma radiation could settle the debate.

During a measurement campaign with the JYFL 14 GHz ECRIS, conducted as part of this thesis work, the effectiveness of double-frequency heating over single-frequency heating was probed with both *Kα* diagnostics and optical emission spectroscopy. The optical emission allowed for two transitions (of Ar^{9+} and Ar^{13+}) to be measured simultaneously with the *Kα* emission. The *Kα* diagnostics enabled an estimation of the relative electron losses which led to the suggestion that the secondary heating frequency reduces the electron losses in the energy range most relevant for inner shell ionization (Ref. [PIII]). This does not imply that electron losses are reduced across the complete energy range of the EEDF. Additionally it was also observed that the second frequency only becomes effective if the source is tuned for HCS ion production, which is consistent with earlier investigations [63, 125]. A logical extension of this investigation would be to probe multiple-frequency heating. Additionally the frequency tuning effect could also be probed on multiple sources with different microwave coupling schemes as this is thought to significantly impact frequency tuning. Such investigations would yield more information on the crucial impact of frequency tuning and multiple-frequency heating. Probing the inner shell ionization rate would offer more direct evidence of frequency tuning in comparison to extracting HCS ions since there are numerous steps between electron heating (frequency dependent) and ion extraction.

The microwave induced electron loss rate from an ECRIS plasma is a subject which has been scantly studied. With this thesis work, this loss mechanism was

studied in both CW and pulsed operation modes. Some of the first direct experimental evidence of microwave induced electron losses on ECRIS plasmas were only demonstrated recently [17, 115]. With *Kα* diagnostics an attempt was made to gain a deeper understanding of the plasma conditions leading to pitch angle scattering by the magnetic field component of the microwaves. The *Kα* diagnostics, used in this investigation, allows for the relative electron losses to be estimated non-invasively which enabled an investigation into the influence of the source tune parameters on electron losses. This allows for a set of conditions to be defined which makes studying the microwave induced electron losses possible. The results obtained with the *Kα* diagnostics in this investigation are in good agreement with those obtained by Noland *et al.* [17] through diamagnetism diagnostics. To gain confidence on the results presented with this investigation, the direct electron losses were also measured as a function of various source settings in pulsed mode. Both investigations produced evidence of electron losses coupled to the microwave power (Ref. [PIV]). In the case of the pulsed investigation, the electron losses measured during the decay pulse presented the most compelling evidence of microwave induced electron losses. This subject still requires intensive investigations to develop a more complete understanding of the underlying mechanism which leads to electron losses by pitch angle scattering.

REFERENCES

[1] I. G. Brown, *The Physics and Technology of Ion Sources*. Weinheim, Germany: John Wiley & Sons Inc., 2004.

[2] M. A. Lieberman and A. J. Lichtenberg, *Principles of Plasma Discharges and Material Processing*. New Jersey, USA: John Wiley & Sons Inc., 2005.

[3] F. F. Francis, *Introduction to Plasma Physics*. New York, USA: Plenum Press, 1977.

[4] T. A. Littlefield and N. Thorley, *Atomic and Nuclear Physics*. Boston, MA: Springer-Verlag, 1979.

[5] A. Virtanen, J. Hyvönen, K. Ranttila, I. Rekikoski, and J. Tuppurainen, "Heavy ion and proton test site at JYFL-accelerator laboratory," *Nuclear Instruments and Methods in Physics Research Section A: Accelerators, Spectrometers, Detectors and Associated Equipment*, vol. 426, no. 1, pp. 68–71, 1999.

[6] D. T. L. Jones and A. N. Schreuder, "Magnetically scanned proton therapy beams: rationales and principles," *Radiation Physics and Chemistry*, vol. 61, no. 3, pp. 615–618, 2001.

[7] T. N. van der Walt and C. Naidoo, "Recovery of ^{201}Tl by ion exchange chromatography from proton bombarded thallium cyclotron targets," *Radiochimica Acta*, vol. 88, no. 3-4, pp. 185–188, 2001.

[8] P. E. Hodgson, E. Gadioli, and E. Gadioli Erba, *Introductory Nuclear Physics*. New York, USA: Oxford University Press, 1997.

[9] D. H. Perkins, *Introduction to High Energy Physics*. Massachusetts, USA: Addison-Wesley Publishing, 1982.

[10] E. D. Donets, *The Physics and Technology of Ion Sources*, p. 245. New York, USA: Wiley-VCH Verlag GmbH and Co. KGaA, 1989. edited by I.G. Brown.

[11] R. Geller, *Electron Cyclotron Resonance Ion Sources and ECR Plasmas*. Bristol, UK: Institute of Physics Publising, 1996.

[12] R. Vondrasek, A. Levand, R. Pardo, G. Savard, and R. Scott, "Charge breeding results and future prospects with electron cyclotron resonance ion source and electron beam ion source," *Review of Scientific Instruments*, vol. 83, no. 2, p. 02A913, 2012.

[13] G. T. Seaborg and W. D. Loveland, *The Elements beyond Uranium*. New York, USA: John Wiley & Sons, 1990.

[14] O. Tarvainen, T. Kalvas, H. Koivisto, V. Skalyga, I. Izotov, and D. Mansfeld, "Electron cyclotron resonance ion sources - physics, technology and future challenges," in *Proceedings of the 10th International Workshop 2017 "Strong Microwaves and Teraherts Waves: Sources and Applications"*, pp. 1–2, EDP Sciences, 08 2017.

[15] K. Bernhardi and K. Wiesemann, "X-ray bremsstrahlung measurements on an ECR-discharge in a magnetic mirror," *Plasma Physics*, vol. 24, no. 8, pp. 867–884, 1982.

[16] T. Ropponen, O. Tarvainen, P. Jones, P. Peura, T. Kalvas, P. Suominen, and H. A. Koivisto, "Time Evolution of High-Energy Bremsstrahlung and Argon Ion Production in Electron Cyclotron Resonance Ion-Source Plasma," *IEEE Transactions on Plasma Science*, vol. 37, no. 11, pp. 2146–2152, 2009.

[17] J. Noland, O. Tarvainen, D. Benitez, D. Leitner, C. Lyneis, and J. Verboncoeur, "Studies of electron heating on a 6.4 GHz ECR ion source through measurement of diamagnetic current and plasma bremsstrahlung," *Plasma Sources Science and Technologies*, vol. 20, no. 3, pp. 1–11, 2011.

[18] T. Thuillier, J. Angot, J. Y. Benitez, A. Hodgkinson, C. M. Lyneis, D. S. Todd, and D. Z. Xie, "Investigation on the electron flux to the wall in the VENUS ion source," *Review of Scientific Instruments*, vol. 87, no. 2, p. 02A736, 2016.

[19] B. P. Cluggish, L. Zhao, and J.-S. Kim, "Modeling of the stability of electron cyclotron resonance ion source plasmas," *Nuclear Instruments and Methods in Physics Research Section A*, vol. 631, no. 1, pp. 111–120, 2011.

[20] G. Zschornack, *Handbook of X-ray data*. New York, USA: Springer-Verlag, 2007.

[21] M. C. Williamson, A. J. Lichtenberg, and M. A. Liebermann, "Self-consistent electron cyclotron resonance absorption in a plasma with varying parameters," *Journal of Applied Physics*, vol. 72, no. 9, pp. 3924–3933, 1992.

[22] C. F. Kennel and F. Engelmann, "Velocity Space Diffusion from Weak Plasma Turbulence in a Magnetic Field," *The Physics of Fluids*, vol. 9, no. 12, pp. 2377–2388, 1966.

[23] A. Girard, C. Perret, and G. Melin, "Modeling of electron-cyclotron-resonance ion source and scaling laws," *Review of Scientific Instruments*, vol. 69, no. 2, pp. 1100–1102, 1998.

[24] O. Tarvainen, J. Laulainen, J. Komppula, R. Kronholm, T. Kalvas, H. Koivisto, I. Izotov, D. Mansfeld, and V. Skalyga, "Limitations of electron cyclotron resonance ion source performances set by kinetic plasma instabilities," *Review of Scientific Instruments*, vol. 86, no. 2, p. 023301, 2015.

[25] I. V. Izotov, T. Lamy, L. Latrasse, A. V. Sidorov, V. A. Skalyga, T. Thuillier, and V. G. Zorin, "Experimental and Theoretical Investigation of the Preglow in ECRIS," *IEEE Transactions on Plasma Science*, vol. 36, no. 4, pp. 1494–1501, 2008.

[26] N. C. Wyeth, A. J. Lichtenberg, and M. A. Lieberman, "Electron cyclotron resonance heating in a pulsed mirror experiment," *Plasma Physics*, vol. 17, no. 9, pp. 679–688, 1975.

[27] G. Douysset, H. Khodja, A. Girard, and J. P. Briand, "Highly charged ion densities and ion confinement properties in an electron-cyclotron-resonance ion source," *Physical Review E*, vol. 61, no. 3, pp. 3015–3022, 2000.

[28] C. Barué, M. Lamoureux, P. Briand, A. Girard, and G. Melin, "Investigation of hot electrons in electron-cyclotron resonance ion sources," *Journal of Applied Physics*, vol. 76, no. 5, pp. 2662–2670, 1994.

[29] G. Melin, A. G. Drentje, A. Girard, and D. Hitz, "Ion behavior and gas mixing in electron cyclotron resonance plasmas as sources of highly charged ions," *Journal of Applied Physics*, vol. 86, no. 9, pp. 4772–4779, 1999.

[30] I. Izotov, O. Tarvainen, V. Skalyga, D. Mansfeld, T. Kalvas, H. Koivisto, and R. Kronholm, "Measurement of the energy distribution of electrons escaping minimum-B ECR plasmas," *Plasma Sources Science and Technology*, vol. 27, no. 2, p. 025012, 2018.

[31] R. Kronholm, T. Kalvas, H. Koivisto, and O. Tarvainen, "Spectroscopic method to study low charge state ion and cold electron population in ECRIS plasma," *Review of Scientific Instruments*, vol. 89, no. 4, p. 043506, 2018.

[32] D. Leitner, J. Y. Benitez, C. M. Lyneis, D. S. Todd, T. Ropponen, J. Ropponen, H. Koivisto, and S. Gammino, "Measurement of the high energy component of the x-ray spectra in the VENUS electron cyclotron resonance ion source," *Review of Scientific Instruments*, vol. 79, no. 3, p. 033302, 2008.

[33] C. Lyneis, D. Leitner, D. Todd, S. Virostek, T. Loew, A. Heinen, and O. Tarvainen, "Measurement of bremsstrahlung production and x-ray cryostat heating in VENUS," *Review of Scientific Instruments*, vol. 77, no. 3, p. 03A342, 2006.

[34] R. J. Goldston and P. H. Rutherford, *Introduction to Plasma Physics*. Philadelphia, USA: Institute of Physics Publishing, 1995.

[35] G. Melin, C. Barué, F. Bourg, P. Briand, J. Debernardi, M. Delaunay, R. Geller, A. Girard, K. S. Golovanivsky, D. Hitz, B. Jacquot, P. Ludwig, J. M. Mathonnet, T. K. Nguyen, L. Pin, J. C. Pontonnier, M Rocco, and F. Zadworny, "Recent developments and future projects on ECR ion sources at

Grenoble," in *Proceedings of Tenth International Workshop on ECR Ion Sources*, pp. 1–16, Oak Ridge National Laboratory, November 1990.

[36] G. Shirkov, "Multicomponent consideration of electron fraction of electron-cyclotron resonance source plasma," *Review of Scientific Instruments*, vol. 71, no. 2, pp. 850–855, 2000.

[37] Y. Jongen and C. M. Lyneis, "Experimental results from an ECR source using an octupole," *Nuclear Instruments and Methods in Physics Research Section B: Beam Interactions with Materials and Atoms*, vol. 9, no. 4, pp. 529–531, 1985.

[38] K. Halbach, "Design of permanent multipole magnets with oriented rare earth cobalt material," *Nuclear Instruments and Methods*, vol. 169, no. 1, pp. 1–10, 1980.

[39] H. W. Zhoa, L. T. Sun, X. Z. Zhang, Z. M. Zhang, X. H. Guo, W. He, P. Yuan, M. T. Song, J. Y. Li, Y. C. Feng, Y. Cao, X. X. Li, W. L. Zhan, B. W. Wei, and D. Z. Xie, "Advanced superconducting electron cyclotron resonance ion source SECRAL: Design, construction and the first test result," *Review of Scientific Instruments*, vol. 77, no. 3, p. 03A333, 2006.

[40] C. Lyneis, "Scaling laws in electron cyclotron resonance ion sources," in *Proceedings of 22nd International Workshop on ECR Ion Sources*, pp. 1–4, Korea Basic Science Institute, August 2016.

[41] D. Hitz, A. Girard, G. Melin, S. Gammino, G. Ciavola, and L. Celona, "Results and interpretation of high frequency experiments at 28 GHz in ECR ion sources, future prospects.," *Review of Scientific Instruments*, vol. 73, no. 2, pp. 509–512, 2002.

[42] J. A. Bittencourt, *Fundamentals of Plasma Physics*. New York, USA: Springer-Verlag, 2004.

[43] A. Girard, C. Pernot, G. Melin, and C. Lécot, "Modeling of electron-cyclotron-resonance-heated plasmas," *Physical Review E*, vol. 62, no. 1, pp. 1182–1189, 2000.

[44] C. Perret, A. Girard, H. Khodja, and G. Melin, "Limitations to the plasma energy and density in electron cyclotron resonance ion sources," *Physics of Plasmas*, vol. 6, no. 8, pp. 3408–3415, 1999.

[45] T. H. Stix, *Waves in Plasmas*. New York, USA: Springer-Verlag, 1992.

[46] D. Mascali, L. Celona, F. Maimone, J. Maeder, G. Castro, F. P. Romano, A. Musumarra, C. Altana, C. Caliri, G. Torrisi, L. Neri, S. Gammino, K. Tinschert, K. P. Spaedtke, J. Rossbach, R. Lang, and G. Ciavola, "X-ray spectroscopy of warm and hot electron components in the CAPRICE source

plasma at EIS testbench at GSI," *Review of Scientific Instruments*, vol. 85, no. 2, p. 02A956, 2014.

[47] T. Ropponen, O. Tarvainen, P. Suominen, T. K. Koponen, T. Kalvas, and H. Koivisto, "Hybrid simulation of electron cyclotron resonance heating," *Nuclear Instruments and Methods in Physics Research A*, vol. 587, no. 1, pp. 115–124, 2008.

[48] T. Ropponen, O. Tarvainen, I. Izotov, J. Noland, V. Toivanen, G. Machicoane, D. Leitner, H. Koivisto, T. Kalvas, P. Peura, P. Jones, V. Skalyga, and V. Zorin, "Studies of plasma breakdown and electron heating on a 14 GHz ECR ion source through measurement of plasma bremsstrahlung," *Plasma Sources Science and Technology*, vol. 20, no. 5, p. 055007, 2011.

[49] T. D. Rognlien and T. A. Cutler, "Transition from Pastukhov to collisional confinement in a magnetic and electrostatic well," *Nuclear Fusion*, vol. 20, no. 8, p. 1003, 1980.

[50] O. Tarvainen, P. Suominen, and H. Koivisto, "A new plasma potential measurement instrument for plasma ion sources," *Review of Scientific Instruments*, vol. 75, no. 10, pp. 3138–3145, 2004.

[51] D. Winklehner, D. Todd, J. Benitez, M. Strohmeier, D. Grote, and D. Leitner, "Comparison of extraction and beam transport simulations with emittance measurements from the ECR ion source VENUS," *Journal of Instrumentation*, vol. 5, no. 12, p. P12001, 2010.

[52] G. D. Shirkov, C. Mühle, G. Musiol, and Zschornack, "Ionization and charge dispersion in electron cyclotron resonance ion sources," *Nuclear Instruments and Methods in Physics Research Section A: Accelerators, Spectrometers, Detectors and Associated Equipment*, vol. 302, no. 1, pp. 1–5, 1991.

[53] A. Müller and E. Salzborn, "Scaling of cross sections for multiple electron transfer to highly charged ions colliding with atoms and molecules," *Physics Letters A*, vol. 62, no. 6, pp. 391–394, 1977.

[54] E. Salzborn and A. Müller, "Electron Capture by Multi-Charged Ions Colliding with Multi-Electron Targets," in *Proceedings of Eleventh International Conference on Physics of Electronic and Atomic Collisions*, pp. 407–426, North-Holland, August 1979.

[55] R. Geller, F. Bourg, P. Briand, F. Debernardi, M. Delauny, B. Jaquot, P. Ludwig, R. Pauthenet, M. Pontonnier, and P. Sortais, "The Grenoble ECRIS status in 1987 and Proposals for ECRIS scaling," in *Proceedings of International Conference on ECR Ion Sources*, pp. 1–9, Michigan State University, November 1987.

[56] D. Hitz, "Recent Progress in High Frequency Electron Cyclotron Resonance Ion Sources," *Advances in Imaging and Electron Physics*, vol. 144, no. 1, pp. 1–163, 2006.

[57] H. Tawara and T. Kato, "Total and partial ionization cross sections of atoms and ions by electron impact," *Atomic Data and Nuclear Data Tables*, vol. 36, no. 2, pp. 167–353, 1987.

[58] V. Mironov, S. Bogomolov, A. Bondarchenko, A. Efremov, and V. Loginov, "Numerical simulations of gas mixing effect in electron cyclotron resonance ion sources," *Physical Review Accelerators and Beams*, vol. 20, no. 1, p. 013402, 2017.

[59] V. Mironov, S. Bogomolov, A. Bondarchenko, A. Efremov, and V. Loginov, "Numerical model of electron cyclotron resonance ion source," *Physical Review Accelerators and Beams*, vol. 18, no. 12, p. 123401, 2015.

[60] L. Celona, G. Ciavola, S. Gammino, N. Gambino, F. Maimone, D. Mascali, and R. Miracoli, "On the observation of standing waves in cylindrical cavities filled by microwave discharge plasmas," in *Proceedings of 18th International Workshop on ECR Ion Sources*, pp. 140–144, Argonne National Laboratory, September 2008.

[61] L. Sun, J. W. Guo, W. Lu, W. H. Zhang, Y. C. Feng, Y. Yang, C. Qian, X. Fang, H. Y. Ma, X. Z. Zhang, and H. W. Zhoa, "Advancement of highly charged ion beam production by superconducting ECR ion source SECRAL," *Review of Scientific Instruments*, vol. 87, no. 2, p. 02A707, 2016.

[62] H. Koivisto, P. Suominen, O. Tarvainen, A. Virtanen, and A. Parkkinen, "Electron cyclotron resonance ion source related development work for heavy-ion irradiation tests," *Review of Scientific Instruments*, vol. 77, no. 3, p. 03A316, 2006.

[63] R. C. Vondrasek, R. Scott, and R. C. Pardo, "ECRIS operation with multiple frequencies," *Review of Scientific Instruments*, vol. 77, no. 3, p. 03A337, 2006.

[64] V. Skalyga, I. Izotov, T. Kalvas, H. Koivisto, J. Komppula, R. Kronholm, J. Laulainen, D. Mansfeld, and O. Tarvainen, "Suppression of cyclotron instability in Electron Cyclotron Resonance ion sources by two-frequency heating," *Physics of Plasmas*, vol. 22, no. 8, p. 083509, 2015.

[65] Z. Q. Xie and C. M. Lyneis, "Two-frequency plasma heating in a high charge state electron cyclotron resonance ion source," *Review of Scientific Instruments*, vol. 66, no. 8, pp. 4281–4286, 1995.

[66] S. Biri, A. Kitagawa, M. Muramatsu, A. G. Drentje, R. Rácz, K. Yano, Y. Kato, N. Sasaki, and W. Takasugi, "Two-frequency heating technique at

the 18 GHz electron cyclotron resonance ion source of the National Institute of Radiological Sciences," *Review of Scientific Instruments*, vol. 85, no. 2, p. 02A931, 2014.

[67] A. G. Drentje, "The ECR ion source and associated equipment at the KVI," *Nuclear Instruments and Methods in Physics Research Section B: Beam Interactions with Materials and Atoms*, vol. 9, no. 4, pp. 526–528, 1985.

[68] A. G. Drentje, "Anomalous charge state distribution in ECRIS for oxygen isotopes," *Review of Scientific Instruments*, vol. 63, no. 4, pp. 2875–2877, 1992.

[69] T. A. Antaya, "A review of studies for the variable frequency superconducting ECR ion source project at MSU," in *Proceedings of International Conference on ECR Ion Sources*, pp. 707–726, Journal de Physique, January 1989.

[70] Y. Jongen, "Distributions d'Etats de Charge dans le Plasma d'une Source ECR." LC-8003, Laboratoire du Cyclotron, Université Catholique de Louvain, 1980.

[71] O. Tarvainen, P. Suominen, T. Ropponen, T. Kalvas, P. Heikkinen, and H. Koivisto, "Effect of the gas mixing technique on the plasma potential and emittance of the JYFL 14 GHz electron cyclotron resonance ion source," *Review of Scientific Instruments*, vol. 76, no. 9, p. 093304, 2005.

[72] A. G. Drentje, A. Girard, D. Hitz, and G. Melin, "Role of low charge state ions in electron cyclotron resonance ion source plasmas," *Review of Scientific Instruments*, vol. 71, no. 2, p. 623, 2000.

[73] M. Delaunay, "Influence of ionization cross sections on the gas mixing effect for the production of Ar^{9+} ions in a CAPRICE ECR source," *Review of Scientific Instruments*, vol. 63, no. 4, pp. 2861–2865, 1992.

[74] Z. Q. Xie and C. M. Lyneis, "Plasma potentials and performance of the advanced electron cyclotron resonance ion source," *Review of Scientific Instruments*, vol. 65, no. 9, pp. 2947–2950, 1994.

[75] J. Vámosi and S. Biri, "TrapCAD - A program to model magnetic traps of charged particles," *Computer Physics Communications*, vol. 98, no. 1-2, pp. 215–223, 1996.

[76] S. Biri, T. Nakagawa, M. Kidera, Y. Miyazawa, M. Hemmi, T. Chiba, N. Inabe, M. Kase, T. Kageyama, O. Kamigaito, A. Goto, and Y. Yano, "Production of highly charged ions in the RIKEN 18 GHz ECR ion source using an electrode in two modes," *Nuclear Instruments and Methods in Physics Research B: Beam Interactions with Materials and Atoms*, vol. 152, no. 2-3, pp. 386–396, 1999.

[77] A. Simon, "Ambipolar Diffusion in a Magnetic Field," *Physical Review*, vol. 98, no. 2, pp. 317–318, 1955.

[78] A. G. Drentje, U. Wolters, A. Nadzeyka, D. Meyer, and K. Wiesemann, "Simon short circuit effect in ECRIS," *Review of Scientific Instruments*, vol. 73, no. 2, pp. 516–520, 2002.

[79] V. Mironov, K. E. Stiebing, O. Hohn, L. Schmidt, H. Schmidt-Böcking, S. Runkel, A. Schempp, G. Shirkov, S. Biri, and L. Kenéz, "Influence of the biased electrode on the plasma potential in ECRIS," *Review of Scientific Instruments*, vol. 73, no. 2, pp. 623–625, 2002.

[80] O. Tarvainen, T. Ropponen, V. Toivanen, J. Ärje, and H. Koivisto, "Plasma breakdown diagnostics with the biased disc of electron cycltron resonance ion source," *Plasma Sources Science and Technology*, vol. 18, no. 3, p. 035018, 2009.

[81] R. D. Cowan, *The Theory of atomic structure and spectra*. New York, USA: Plenum Press, 1981.

[82] National Institute of Standards and Technology, "NIST atomic spectra database." http://www.nist.gov/pml/atomic-spectra-database, 2018.

[83] P. Auger, "Sur l'effet photoélectrique composé," *Journal de Physique et Le Radium*, vol. 6, no. 6, pp. 205–208, 1925.

[84] L. Meitner, "Über die Entstehung der β-Strahl-Spektren radioaktiver Substanzen," *Zeitschrift für Physik*, vol. 9, no. 1, pp. 131–144, 1922.

[85] Coster, D and Kronig, R de L, "New type of auger effect and its influence on the x-ray spectrum," *Physica*, vol. 2, no. 1-12, pp. 13–24, 1935.

[86] W. Bambynek, B. Crasemann, R. W. Fink, H. U. Freund, H. Mark, C. D. Swift, R. E. Price, and P. Venugopala Rao, "X-ray Fluorescence Yields, Auger and Coster-Kronig Transition Probabilities," *Reviews of Modern Physics*, vol. 44, no. 4, pp. 716–813, 1972.

[87] M. O. Krause, "Atomic Radiative and Radiationless Yields for K and L Shells," *Journal of Physical and Chemical Reference Data*, vol. 8, no. 2, pp. 307–327, 1979.

[88] E. H. S. Burhop, "Le rendement de fluorescence," *Journal de Physique Radium*, vol. 16, no. 7, pp. 625–629, 1955.

[89] W. Lotz, "Electron-impact ionization cross-sections and ionization rate coefficients for atoms and ions from hydrogen to calcium," *Zeitschrift für Physik*, vol. 216, no. 3, pp. 241–247, 1968.

[90] H. Van Regemorter, "Rate of Collisional Excitation in Stellar Atmospheres," *Astrophysical Journal*, vol. 136, pp. 906–915, 1962.

[91] I. H. Hutchinson, *Principles of Plasma Diagnostics*. Cambridge, Massachusetts: Cambridge University Press, 2001.

[92] H. W. Koch and J. W. Motz, "Bremsstrahlung Cross-Section Formulas and Related Data," *Reviews of Modern Physics*, vol. 31, no. 4, pp. 920–955, 1959.

[93] T. Kalvas, O. Tarvainen, H. Koivisto, and K. Ranttila, "Thermal Design of Refridgerated Hexapole 18 GHz ECRIS HIISI," in *Proceedings of Twenty-first International Workshop on ECR Ion Sources*, pp. 114–119, Institute of Applied Physics of the Russian Academy of Sciences, August 2014.

[94] L. Kissel, C. A. Quarles, and R. H. Pratt, "Shape functions for atomic-field bremsstrahlung from electrons of kinetic energy 1-500 keV on selected neutral atoms $1 \leq Z \leq 92$," *Atomic Data and Nuclear Data Tables*, vol. 28, no. 3, pp. 381–460, 1983.

[95] K. Bernhardi, "An improved deconvolution method for bremsstrahlung spectra from hot plasmas," *Computer Physics Communications*, vol. 19, no. 1, pp. 17–21, 1980.

[96] R. Friedlein and G. Zschornack, "Angle dispersive de-convolution of bremsstrahlung spectra from plasma," *Nuclear Instruments and Methods in Physics Research Section A: Accelerators, Spectrometers, Detectors and Associated Equipment*, vol. 349, no. 2-3, pp. 554–557, 1984.

[97] M. Lamoureux and P. Charles, "General deconvolution of thin-target and thick-target Bremsstrahlung spectra to determine electron energy distributions," *Radiation Physics and Chemistry*, vol. 75, no. 10, pp. 1220–1231, 2006.

[98] M. Lamoureux, P. Waller, P. Charles, and N. B. Avdonina, "Bremsstrahlung from thick targets and a diagnostic for electron energy distributions," *Physical Review E*, vol. 62, no. 3, pp. 4091–4095, 2000.

[99] G. F. Knoll, *Radiation Detection and Measurement*. New York, USA: John Wiley & Sons, 1979.

[100] J. Y. Benitez, J. D. Noland, D. Leitner, C. Lyneis, D. S. Todd, and J. Verboncoeur, "High Energy Component of X-ray Spectra in ECR Ion Sources," in *Proceedings of Eighteenth International Workshop on ECR Ion Sources*, pp. 77–84, Argonne National Laboratory, September 2008.

[101] J. Benitez, C. Lyneis, L. Phair, D. Todd, and D. Xie, "Dependence of the Bremsstrahlung Spectral Temperature in Minimum-*B* Electron Cyclotron Resonance Ion Sources," *IEEE Transactions on Plasma Science*, vol. 45, no. 7, pp. 1746–1754, 2017.

[102] M. Hohl, P. Wurz, and P. Bochsler, "Investigation of the density and temperature of electrons in a compact 2.45 GHz electron cyclotron resonance ion source plasma by x-ray measurements," *Plasma Sources Science and Technology*, vol. 14, no. 4, pp. 692–699, 2005.

[103] R. Friedlein, S. Herpich, U. Lehnert, H. Tyrroff, H. Wirth, C. Zippe, and G. Zschornack, "X-ray spectroscopy on ECR plasmas," *Nuclear Instruments and Methods in Physics Research B: Beam Interactions with Materials and Atoms*, vol. 98, no. 1-4, pp. 585–588, 1995.

[104] I. P. Vinogradov, B. Jettkant, D. Meyer, and K. Wiesemann, "Spectroscopic density determination of nitrogen species in an ECR discharge," *Journal of Physics D: Applied Physics*, vol. 27, no. 6, pp. 1207–1226, 1994.

[105] U. Lehnert, C. Zippe, and G. Zschornack, "High resolution wavelength dispersive X-ray spectroscopy for ECR plasma diagnostics," *Hyperfine Interactions*, vol. 99, no. 1, pp. 235–241, 1996.

[106] M. C. Martins, A. M. Costa, J. P. Santos, P. Indelicato, and F. Parente, "Interpretation of x-ray spectra emitted by Ar ions in an electron-cyclotron resonance ion source," *Journal of Physics B: Atomic, Molecular and Optical Physics*, vol. 34, no. 4, pp. 533–543, 2001.

[107] J. P. Santos, A. M. Costa, J. P. Marques, M. C. Martins, P. Indelicato, and F. Parente, "X-ray spectroscopy analysis of electron-cyclotron-resonance ion-source plasmas," *Physical Review A*, vol. 82, no. 6, p. 062516, 2010.

[108] M. Guerra, P. Amaro, C. I. Szabo, A. Gumberidze, P. Indelicato, and J. P. Santos, "Analysis of the charge state distribution in an ECRIS Ar plasma using high-resolution x-ray spectra," *Journal of Physics B: Atomic, Molecular and Optical Physics*, vol. 46, no. 6, p. 065701, 2013.

[109] S. Biri, A. Valek, T. Suta, E. Takács, C. Szabó, L. T. Hudson, B. Radics, J. Imrek, B. Juhász, and J. Pálinkás, "Imaging of ECR plasmas with a pinhole x-ray camera," *Review of Scientific Instruments*, vol. 75, no. 5, pp. 1420–1422, 2004.

[110] H. Koivisto, P. Heikkinen, V. Hänninen, A. Lassila, H. Leinonen, V. Nieminen, J. Pakarinen, K. Ranttila, J. Ärje, and E. Liukkonen, "The first results with the new JYFL 14 GHz ECR ion source," *Nuclear Instruments and Methods in Physics Research Section B: Beam Interactions with Materials and Atoms*, vol. 174, no. 3, pp. 379–384, 2001.

[111] R. Thomae, J. Conradie, D. Fourie, J. Mira, F. Nemulodi, D. Küchler, and V. Toivanen, "Beam experiments with the Grenoble test electron cyclotron resonance ion source at iThemba LABS," *Review of Scientific Instruments*, vol. 87, no. 2, p. 02A731, 2016.

[112] D. Küchler, A. Michet, J. Ferreira Somoza, and V. Toivanen, "Never Run Your ECR Ion Source with Argon in Afterglow for 6 Months," in *Proceedings of 22nd International Workshop on ECR Ion Sources*, pp. 89–91, JACoW, Geneva, Switzerland, August 2016.

[113] J. Komppula, O. Tarvainen, T. Kalvas, H. Koivisto, R. Kronholm, J. Laulainen, and P. Myllyperkiö, "VUV irradiance measurement of a 2.45 GHz microwave-driven hydrogen discharge," *Journal of Physics D: Applied Physics*, vol. 36, no. 48, pp. 1–12, 2015.

[114] Amptek, "X-123 Complete X-ray Spectrometer with Silicon Drift Detector (SDD)." http://amptek.com/products/x-123sdd-comlete-x-ray-spectrometer-with-silicon-drift-detector-sdd, 2017.

[115] I. Izotov, D. Mansfeld, V. Zorin, T. Grahn, T. Kalvas, H. Koivisto, J. Komppula, P. Peura, O. Tarvainen, and V. Toivanen, "Plasma instability in the afterglow of electron cyclotron resonance discharge sustained in a mirror trap," *Physics of Plasmas*, vol. 19, no. 12, p. 122501, 2012.

[116] H. I. West, "Calculation of ion charge-state distribution in ECR ion sources." Lawrence Livermore National Laboratory, UCRL-53391, 1982.

[117] V. Mironov and J. P. M. Beijers, "Three-dimensional simulations of ion dynamics in the plasma of an electron cyclotron resonance ion source," *Physical Review Special Topics - Accelerators and Beams*, vol. 12, no. 7, p. 073501, 2009.

[118] G. Shirkov and Nakagawa, "Numerical simulation of highly charged ion production in RIKEN 18 GHz electron cyclotron resonance ion source," *Review of Scientific Instruments*, vol. 69, no. 2, pp. 1141–1143, 1998.

[119] P. Spädtke, "KOBRA3-INP." www.inp-dme.com, 2017.

[120] D. Mascali, L. Neri, S. Gammino, L. Celona, G. Ciavola, N. Gambino, R. Miracoli, and S. Chikin, "Plasma ion dynamics and beam formation in electron cyclotron resonance ion sources," *Review of Scientific Instruments*, vol. 81, no. 2, p. 02A334, 2010.

[121] T. Ropponen, P. Jones, T. Kalvas, H. Koivisto, P. Peura, O. Tarvainen, and P. Suominen, "Time Evolution of Endpoint Energy of Bremsstrahlung Spectra and Ion Production from an Electron Cyclotron Resonance Ion Source," in *Proceedings of Eighteenth International Workshop on ECR Ion Sources*, pp. 160–167, Argonne National Laboratory, September 2008.

[122] D. H. Edgell, J. S. Kim, I. N. Bogatu, R. C. Pardo, and R. C. Vondrasek, "Modelling of electron cyclotron resonance ion source plasmas," in *Proceedings of 2001 Particle Accelerator Conference*, pp. 2135–2137, Argonne National Laboratory, June 2001.

[123] O. Tarvainen, *Studies of electron cyclotron resonance ion source plasma physics*. PhD thesis, University of Jyväskylä, 2005.

[124] A. M. Costa, M. C. Martins, F. Parente, J. P. Santos, and P. Indelicato, "Dirac-Fock Transition energies and Radiative and Radiationless Transition Probabilities for Ar^{9+} to Ar^{16+} Ion Levels with K-shell Holes," *Atomic Data and Nuclear Data Tables*, vol. 79, no. 2, pp. 223–239, 2001.

[125] V. Toivanen, G. Bellodi, D. Küchler, F. Wenander, and O. Tarvainen, "Effects of double frequency heating on the lead afterglow beam currents of an electron cyclotron resonance ion source," *Physical Review Accelerators and Beams*, vol. 20, no. 10, p. 103402, 2017.

[126] R. Kronholm, M. Sakildien, D. Neben, H. Koivisto, T. Kalvas, O. Tarvainen, J. Laulainen, and P. Jones, "The effect of micowave power on the Ar^{9+} and Ar^{13+} optical emission intensities and ion beam currents in ECRIS." Manuscript submitted for publication, 2017.

[127] T. Ropponen, O. Tarvainen, P. Jones, P. Peura, T. Kalvas, P. Suominen, H. Koivisto, and J. Ärje, "The effect of magnetic field strength on the time evolution of high energy bremsstrahlung radiation created by an electron cyclotron resonance ion source," *Nuclear Instruments and Methods in Physics Research Section A: Accelerators, Spectrometers, Detectors and Associated Equipment*, vol. 600, no. 3, pp. 525–533, 2009.

[128] O. Tarvainen, T. Ropponen, T. Thuillier, J. Noland, V. Toivanen, T. Kalvas, and H. Koivisto, "The role of seed electrons on the plasma breakdown and preglow of electron cyclotron resonance ion source," *Review of Scientific Instruments*, vol. 81, no. 2, p. 02A303, 2010.

[129] O. Tarvainen, J. Angot, I. Izotov, V. Skalyga, H. Koivisto, T. Thuillier, T. Kalvas, and T. Lamy, "Plasma instabilities of a charge breeder ECRIS," *Plasma Sources Science and Technology*, vol. 26, no. 10, p. 105002, 2017.

ORIGINAL PAPERS

PI

INNER SHELL IONIZATION OF ARGON IN ECRIS PLASMA

by

Muneer Sakildien, Risto Kronholm, Olli Tarvainen, Taneli Kalvas, Pete Jones,
Rainer Thomae and Hannu Koivisto

Nuclear Inst. and Methods in Physics Research, A **900** (2018) 40-52

Nuclear Inst. and Methods in Physics Research, A 900 (2018) 40–52

Contents lists available at ScienceDirect

Nuclear Inst. and Methods in Physics Research, A

journal homepage: www.elsevier.com/locate/nima

Inner shell ionization of argon in ECRIS plasma

M. Sakildien [a,b,*], R. Kronholm [b], O. Tarvainen [a], T. Kalvas [b], P. Jones [a], R. Thomae [a], H. Koivisto [b]

[a] iThemba LABS (Laboratory for Accelerator Based Sciences), PO Box 722, Somerset West, 7192, South Africa
[b] University of Jyväskylä, Department of Physics, 40500 Jyväskylä, Finland

ARTICLE INFO

Keywords:
ECRIS
Plasma
Volumetric emission rate
Inner shell ionization rate

ABSTRACT

The volumetric $K\alpha$ emission rate of argon emitted from the electron cyclotron resonance (ECR) heated plasmas of the JYFL (University of Jyväskylä, Department of Physics) 14 GHz ECR ion source (ECRIS) and the 14.5 GHz Grenoble Test Source (GTS) at iThemba Laboratory for Accelerator Based Sciences have been measured to gain an understanding of the influence of the ion source tune parameters on the absolute inner shell ionization rate. It was observed that the behaviour of the ionization rate and the extracted ion beam currents react differently, depending the parametric sweep performed. The neutral gas pressure and incident microwave power was found to have the strongest influence on the ionization rate. At high neutral gas pressure, the absolute inner shell ionization rate was found to saturate. This observation is as a result of the plasma energy content becoming insufficient to sustain the growth in ionization rate. It was also observed that the incident microwave power should be increased much more to counter the decrease in high charge state production as a result of the gas increase and subsequent increase in charge exchange. At low incident microwave, the ionization rate per unit absorbed microwave power was found to be high, which suggests that the inner shell ionization process is driven by the ion dynamics as opposed to the electron dynamics. The influence of the biased disc voltage and magnetic field configuration on the ionization rate was found to be minimal. This led to the suggestion that these two tune parameters does not directly impact the warm electron population of the ECRIS plasma during the parametric sweeps. The $K\alpha$ emission rate can be used as an additional tool for benchmarking the results of numerical simulation codes on ECRIS plasmas.

1. Introduction

Electron cyclotron resonance ion sources (ECRISs) are used to produce multiply charged ions, which are frequently further accelerated and transported, via a transfer beamline, to a target station. To produce multiply charged ions in an ECRIS, plasma electrons are confined by a complex magnetic field, consisting of a solenoidal mirror field and a multipolar field. The vector sum of these two fields is a minimum in the centre of the magnetic field configuration, forming the so-called minimum-B field [1]. As a result of the imposed magnetic field, the plasma electrons spiral around the magnetic flux lines at the cyclotron frequency. To sustain the ECRIS plasma, high-frequency electromagnetic (EM) waves are launched into the plasma chamber from the high magnetic field side of the magnetic confinement system resulting in an efficient energy transfer between the EM waves and the circulating plasma electrons. For wave-electron energy transfer to occur, the injected EM waves must have an electric field component polarized in the same direction as the electron gyromotion. Additionally, the relative phase between the electron gyromotion and rotating electric field needs to be favourable for acceleration of the plasma electrons. If both of these conditions are met, the plasma electrons are heated resonately.

These electrons heated in the resonance have a certain probability to collide with gas atoms injected through a different port on the plasma chamber. Such collisions may result in the removal of a single bound electron from any of the electron shells surrounding the nucleus of the atom. This process is referred to as electron impact single ionization. By confining the high energy electrons in the ECRIS, it will ionize atoms and ions in a 'step-by-step' fashion. Each successive ionization will remove a single electron and will eventually lead to a multiply charged ion. Removal of an electron from one of the inner shells of the atom or inner shell ionization, results in a vacancy in that shell. Such a vacancy can either be filled by a radiative or radiationless transition [2,3]. If the filling of the vacancy is radiative, a higher lying electron fills the

* Corresponding author at: iThemba LABS, PO Box 722, Somerset West, 7129, South Africa.
E-mail address: muneer@tlabs.ac.za (M. Sakildien).

https://doi.org/10.1016/j.nima.2018.05.045
Received 7 September 2017; Received in revised form 2 February 2018; Accepted 22 May 2018
Available online 25 May 2018

vacancy and a characteristic X-ray is emitted in the process. If the filling of the vacancy is radiationless, a higher lying electron fills the vacancy and a second electron is ejected. This electron is commonly referred to as an Auger electron [4]. An inner shell vacancy can also be filled by Coster-Kronig transitions which are radiationless transitions between subshells having the same principal quantum number [5]. For the purpose of the current discussion, Coster-Kronig transitions will be considered as a special case of the Auger process as the filling of the vacancy is radiationless in both cases.

Characteristic X-rays, emitted during radiative transitions, can be used as a non-invasive diagnostic tool to study the electron impact ionization process inside the ECRIS plasma. For the results described in this work, we were mostly concerned with transitions from the $2p$ to the $1s$ subshell resulting in $K\alpha$ X-rays, using the Siegbahn notation. Transitions from higher lying shells to the $1s$ subshell are much less probable, but were also included in the measured emission rate. For the rest of this manuscript we will refer to the measured K-emission rate as the $K\alpha$ emission rate with the implicit understanding that it includes $K\beta$ emission as well. The main reason for performing the experiments were to study the influence of the ion source tune parameters on the inner shell ionization rate. In addition, the extracted ion beam currents were also measured in the transfer beamline. This allowed for a comparison between the measured ion beam currents and the inner shell ionization rates, as a function of the source tune parameters. The study therefore allows for a determination of the influence of the changing electron and ion dynamics on the absolute inner shell ionization rate. The $K\alpha$ emission rate from the ECR heated plasma was used to determine the absolute inner shell ionization rate of two different ion sources. The main reason for measuring and comparing the emission rates from two sources were firstly to cross-check the order-of-magnitude of the absolute emission rate and by implication also the absolute inner shell ionization rate. Secondly the comparison also enabled us to determine if the parametric dependencies are unique to a specific source or the same for both sources. The sources used were the JYFL (University of Jyväskylä, Department of Physics) 14 GHz ECRIS [6] and the 14.5 GHz Grenoble Test Source (GTS) [7,8] at iThemba LABS (Laboratory for Accelerator Based Sciences). For both ion sources, argon was chosen as working gas, as it is a noble gas and does not get adsorbed on the walls of the plasma chamber. The measured emission rates therefore originate from the plasma and not from the plasma chamber walls. Additionally the efficiency of the X-ray detector, installed in the vacuum, is very close to unity at 2.96 keV ($K\alpha$ of argon) [9]. This made argon a logical choice as working gas from the pool of available noble gases.

This work could be of particular interest to groups performing numerical simulations on ECRIS plasmas. Modelling of the ECRIS plasma is an exceedingly challenging task, but one that could lead to a better understanding of the physics of the ion source and resulting improvement in its performance. To simulate the ECRIS plasma, ECRIS codes attempt to cover a wide range of phenomena. Some codes use a single particle approach to simulate the heating process inside the plasma [10,11]. While these codes can evaluate certain plasma parameters with great success it cannot account for others like the multiple electron populations present in the ECRIS plasma [11]. Other plasma processes, like collisional processes and ion and electron dynamics, are simulated using codes based on the Particle-In-Cell (PIC) model [11–13]. Some codes have even been developed to model the space-charge effects during beam extraction and transport [14]. All plasma simulation codes make a number of simplifying assumptions which makes the results of the simulation sensitive to such assumptions. To gauge the success of the simulation, the results of the codes is frequently compared to experimentally determined quantities like the extracted ion beam currents, the sputtering pattern on the plasma electrode and the beam widths. The current investigation proposes an additional parameter i.e. the $K\alpha$ emission rate against which simulation codes can be benchmarked, a need identified in the literature [15]. As an example, the $K\alpha$ emission rate of argon can be varied by sweeping one of the source tune parameters. This result could easily be simulated by most simulation codes which could output an intermediate parameter for benchmarking purposes.

2. Theoretical background

As a result of the wave-electron energy transfer and collisional processes occurring inside the ECRIS plasma, the plasma electrons develop into a quasi-continuous energy spectrum which can be described by an electron energy distribution function (EEDF). To determine this distribution function, the ECRIS plasma have in the past been studied using bremsstrahlung diagnostics [16]. From the measured bremsstrahlung spectra, a number of deconvolution schemes have been developed to determine the EEDF [17–19]. Despite all this effort the real EEDF inside an ECRIS plasma remains not well-known. To complicate matters, the EEDF of the high energy electrons is strongly anisotropic. ECR heating occurs in the plane perpendicular to the magnetic field lines which selectively heats the perpendicular component of the EEDF, not imparting any energy to its parallel component. The perpendicular component therefore has a larger energy than the parallel component. Despite of all the afore-mentioned complications, a multi-component Maxwellian EEDF is commonly assumed for the ECRIS plasma [1]. This is largely because for a Maxwellian EEDF it is convenient to define an electron temperature, kT_e, which is not well-defined for any other distribution function. As a result of the selective heating of the plasma electrons and confinement which strongly depends on the kinetic energy of the plasma electrons, in the absence of collisions, three different electron populations (cold, warm and hot) are thought to exist in an ECRIS plasma [20]. Each of the three electron populations are modelled as a Maxwellian distribution, with a different electron temperature. The warm, 1–10 keV, electron population of this tri-Maxwellian EEDF is most relevant for inner shell ionization.

To create a vacancy in the inner shell or K-shell of an ion, confined inside an ECRIS, two processes are of prime importance namely electron-impact excitation and inner shell ionization. Electron-impact excitation of inner shell electrons refers to the process where a target atom (or ion) has an impact with a projectile electron and in the process moves from a lower state ($1s$) to an upper state ($n'l'$), resulting in a vacancy in the K-shell of the atom (or ion). This vacancy can be filled by any of the allowed transitions between the nl-states of the atom (or ion), along with the emission of a characteristic X-ray of transition energy, $E_{1s\rightarrow n'l'}$. The total cross section for electron-impact excitation of inner shell electrons can be estimated using the Van Regemorter formula [21]

$$\sigma_{\mathrm{exe},1s\rightarrow\sum_{n=2}^{\infty}np}=\sum_{n=2}^{\infty}\pi a_0^2\frac{8\pi f_{1s\rightarrow np}}{\sqrt{3}}\frac{R^2}{E_{1s\rightarrow np}^2}\frac{G_{1s\rightarrow np}(x)}{x} \tag{1}$$

where a_0 is the Bohr radius, $f_{1s\rightarrow np}$ is the absorption oscillator strength, R is the Rydberg energy unit, $G_{1s\rightarrow np}(x)$ is the Gaunt factor, $x=\left(\varepsilon/E_{1s\rightarrow np}\right)$ and ε is the kinetic energy of the projectile electron relative to the target atom or ion. By comparing the results of the Van Regemorter formula with more accurate computations, the error using this formula was estimated to be as large as an order of magnitude [22]. However, by a proper choice of the Gaunt factor this error can be reduced to 50%, at high energies, for Ar^{17+} [23]. From the discussion above it is clear that excitation to any of the upper states requires a vacancy to exists in those states for the electron to occupy. Thus the number of possible excited states and therefore total excitation cross section depends on the charge state of the ion. Inner shell ionization is very similar to electron-impact excitation with the exception that the bound electron is expelled to the continuum as a result of the impact with the projectile electron. The cross section for inner shell ionization can be determined from the semi-empirical Lotz equation [24]

$$\sigma_{\mathrm{ion}}=a_iq_i\frac{\ln\varepsilon/I_i}{\varepsilon I_i}\{1-b_i\exp[-c_i(\varepsilon/I_i-1)]\} \tag{2}$$

where q_i is the number of equivalent electrons in the ith subshell (for the $1s$ subshell $q=2$), ε is as defined in Eq. (1), I_i is the minimum energy required to remove an electron from the ith subshell (3.21 keV for the K-shell electrons of Ar) and a_i, b_i and c_i are constants which do not strongly depend on the charge state of the ion. It is worth

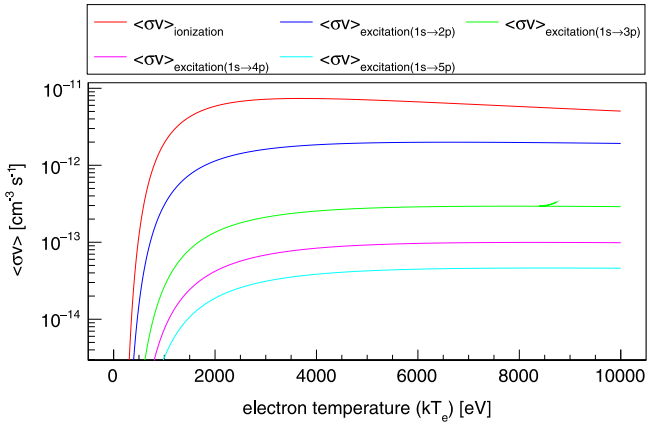

Fig. 1. Comparison of the rate coefficients for ionization and excitation to various excited states.

noting that this equation is based on the data available at the time of publishing Ref. [24] (1968) and it is defined for direct electron-impact ionization, not only for the inner shell ionization. For the K-shell, $a_K = 4.0 \times 10^{-14}$ cm^2 eV^2, $b_K = 0.75$ and $c_K = 0.5$. Lotz estimates the error on the calculated cross sections, using Eq. (2), to be smaller than 30%–40% [24]. The volumetric rate at which K-shell vacancies are produced inside the ECRIS plasma is given by the so-called balance equation [25,26]:

$$\frac{dN_{K\text{-vacancy}}}{dt} = \sum_{q=0}^{z} n_e n_q^0 \left[\langle \sigma^{q\to q}_{\text{exe},1s\to\sum_{n=2}^{\infty} np} v_e \rangle + \langle \sigma^{q\to q+1}_{\text{ion},1s} v_e \rangle \right] - \frac{n_q^i}{\tau_i} = 0 \quad (3)$$

where n_e is the electron density, n_q is the ion density of ions with charge state q, z is the number of electrons in the considered element and τ_i is the lifetime of the excited state i. The post scripts i and 0 in Eq. (3) indicate the excited state, generated as a result of a K-shell vacancy, and the ground state, respectively. In writing the balance equation in the above manner, the assumption is made that the system has reached steady-state conditions and the only loss process assumed for the K-shell vacancies is spontaneous transitions. The rate coefficients for inner shell excitation and ionization used in Eq. (3) are given by the expression [1]:

$$\langle \sigma v_e \rangle = \int f_e(E)\sigma(E)v_e(E)dE \quad (4)$$

where $f_e(E)$ is the prevailing EEDF in the ECRIS plasma, $\sigma(E)$ is the cross section for the process and $v_e(E)$ is the speed of the projectile electrons. From Eq. (4) the rate coefficient can be determined, as a function of the warm electron temperature, for each of the two processes. This result is shown in Fig. 1. To calculate the rate coefficients a Maxwellian distribution was used for the warm electrons and as a result of this relativistic effects were not taken into account. At 10 keV the electrons reach approximately 20% the speed of light, hence this assumption is deemed to be acceptable. The figure clearly shows that ionization plays the dominant role in the generation of K-shell vacancies. This is especially true for ECRIS plasmas in which the densities of high charge states possessing $2p$-vacancies are small in comparison to low charge state ions.

The observable $K\alpha$ volumetric emission rate (Φ_R) is given by the following expression:

$$\Phi_R = K\left[n_e n_n \left(\langle \sigma_{\text{ion}} v_e \rangle + \langle \sigma_{\text{exe}} v_e \rangle \right) + n_e n_i \left(\langle \sigma_{\text{ion}} v_e \rangle + \langle \sigma_{\text{exe}} v_e \rangle \right) \right] \quad (5)$$

where K is a constant that depends on the detector geometry and efficiency and n_i and n_n are the ion and neutral densities, respectively. This expression can be simplified by defining $\langle Q \rangle$ as the average charge state inside the ECRIS plasma and δ as the ionization degree of the plasma. By assuming charge neutrality and expressing n_i and n_n in terms of the ionization degree leads to the expressions:

$$n_i = \frac{n_e}{\langle Q \rangle} \quad (6)$$

$$n_i = \delta n_n. \quad (7)$$

Substituting these expressions into Eq. (5) leads to the simplified form of the observable $K\alpha$ emission rate:

$$\Phi_R = n_e^2 \left(\langle \sigma_{\text{ion}} v_e \rangle + \langle \sigma_{\text{exe}} v_e \rangle \right) \left[\frac{K}{\langle Q \rangle} \right] \left(1 + \frac{1}{\delta} \right). \quad (8)$$

This expression further simplifies to:

$$\Phi_R = n_e^2 \left(\langle \sigma_{\text{ion}} v_e \rangle \right) \left[\frac{K}{\langle Q \rangle} \right] \left(1 + \frac{1}{\delta} \right) \quad (9)$$

when the excitation reactions are neglected as justified above. In Eqs. (8) and (9) it is assumed that the total cross section for inner shell ionization and electron-impact excitation is independent of the charge state of the ion. The error in this assumption is mostly due to the excitation cross section which would be larger for very high charge states and smaller for lower charge states. The error in the ionization cross section is largely due to the increased binding energy of the $1s$ electrons, with increasing charge state. In the case of argon, the binding energy of the $1s$ electrons increases by 33% from neutral argon to Ar^{17+} [27]. With the given assumptions the observable $K\alpha$ emission rate depends on electron energy and density (through the rate coefficient), average charge state and ionization degree of the plasma.

The measured $K\alpha$ emission rate can be correlated with the inner shell ionization rate by taking into account the radiationless de-excitation processes. Once an inner shell vacancy has been produced as a result of the two processes mentioned above, it can be filled by one of three filling mechanisms, as described in Section 1. Each of these filling mechanisms has a defined probability of filling the vacancy, the sum of which equates to unity i.e. the vacancy must be filled for the atomic system to reach its lowest energy state.

$$\omega + f + a = 1 \quad (10)$$

ω, f and a in Eq. (10) are the fluorescence, Auger and Coster-Kronig yields as defined in Ref. [2]. To determine the total inner shell vacancies i.e. total inner shell ionization and excitation rate, from the measured radiative transitions, a correction needs to be applied for the radiationless transitions. This correction is performed in Eq. (11) below:

$$n_e n_q^0 \langle \sigma^{q\to q}_{\text{exe},1s\to\sum_{n=2}^{\infty} np} v_e \rangle + n_e n_q^0 \langle \sigma^{q\to q+1}_{\text{ion},1s} v_e \rangle = \frac{\Phi_R}{\omega_K} \quad (11)$$

when only inner shell ionization is considered. Here ω_K is the K-shell fluorescence yield. From the discussion in Ref. [2], the K-shell fluorescence yield can be defined as the ratio of the number of $K\alpha$ characteristic X-rays emitted to the total number of vacancies in the K-shell [2]. This concept was introduced by Barkla in 1918 [28]. The K-shell fluorescence yield for argon is 0.118, with an estimated uncertainty of 5%–10% [3].

The prime goal of an ECRIS is the production of multiply charged ions. To achieve this goal, both the number density and temperature of the warm electron population has to be optimized for the desired charge state. One of the major obstacles which opposes multiply charged ion production is charge exchange [1]. This process refers to an interaction between a multiply charged ion and a lower charged ion or atom, in which the multiply charged ion captures a bound electron from the other participant, and in so doing reducing its charge state. Charge exchange affects both the ion densities, and by implication, also the extracted ion beam currents. The influence of charge exchange on the production rate of multiply charged states, can be determined by calculating the mean time between two charge exchange events, τ_{cex}, and comparing it to the mean time between two multiply charged state ionization events, $\tau_{q\to q+1}$. The cross section for charge exchange is highest for interactions

with neutral atoms [29,30], so this process is strongly coupled to the number density of the neutral atoms. By increasing the neutral content of the plasma, the mean time between two charge exchange events decreases resulting in lower high charge state density. To maintain a certain high charge state density with increasing neutral content, the ionization rate should be increased in unison with the neutral content. Due to charge exchange and diffusive losses of high charge states the dependence of inner shell ionization and high charge state production i.e. extracted beam currents is expected to depend in a different manner on the source tune parameters. This underlines the importance of the $K\alpha$ emission as a diagnostic tool for benchmarking simulations.

3. Experimental setup and data analysis

3.1. Experimental setup

The volumetric emission rate of the $K\alpha$ X-rays of argon, was studied with the 14 GHz JYFL ECRIS and the 14.5 GHz GTS at iThemba LABS. The JYFL ECRIS has been extensively described in the literature [6] and here only the main features of the source are highlighted. The source is operated at a plasma heating frequency of 14.056 GHz, it has a plasma chamber length of 28 cm and a plasma chamber diameter of 7.8 cm. The biased disc of the JYFL ECRIS is made of stainless steel and it has a diameter of 21 mm. The extraction aperture for the JYFL ECRIS is 8 mm. The magnetic confinement field is provided by two solenoid coils and a permanent magnet hexapole, resulting in magnetic field strengths at injection and extraction of 2.2 T and 0.95 T, respectively. The nominal radial field strength on the magnetic pole is 1.07 T. The base pressure in the source is approximately 1×10^{-7} mbar. In the present configuration the source has one einzel lens to focus the extracted beam.

The GTS is equipped with two 2.3 kW RF amplifiers, operating at 14.5 and 18 GHz. The radial confinement field is provided by a permanent magnet hexapole with a magnetic field strength of 1.27 T at the plasma chamber wall. The longitudinal magnetic field is produced by three solenoidal coils (injection, extraction and center). The plasma chamber has an active length of 30 cm and a diameter of 7.8 cm. The GTS has a triode extraction system with aperture diameters of 12, 17 and 17 mm for the plasma electrode, intermediate electrode and ground electrode respectively [31]. The source has a tantalum biased disc with a surface area of 12 cm^2, though the disc is not circular. For all the measurements described in this paper, both sources were operated in continuous wave (CW) mode.

The main components of the experimental setup, at both JYFL and iThemba LABS, were the detector, the collimator and the digital pulse processor (DP5). In both cases the detector was positioned to measure the axially emitted X-rays from the ECRIS. At JYFL, the detector was positioned to view the plasma through the bending magnet in the transfer beamline, as shown in Fig. 2a. In the case of the GTS, the detector was positioned in one of the ports of the vacuum chamber of the analysing magnet, as shown in Fig. 2b. The distance (D) between the front face of the detector and the extraction electrode of the source is given in Table 1. For the measurements described in this work, we used the Amptek X-123SDD X-ray detector [9]. This compact device incorporates the detector, preamplifier, power supplies and DP5 all in one package. Between the detector and the source, the collimator was installed. As an example, the position of the collimator relative to the detector in the experimental arrangement on the GTS is shown in the expanded detailed view B in Fig. 2b. The collimator was used to eliminate pile-up events and therefore to avoid potential saturation of the measured count rate especially at high microwave power. Additionally the collimator also enabled us to view X-rays emanating from the plasma volume, thus reducing wall bremsstrahlung background. The aperture of the collimator used at JYFL had a diameter of 900 μm and the aperture used at iThemba LABS had a diameter of 500 μm. To protect the detector against charged particles, a permanent magnet filter was included in the experimental setup at JYFL.

Table 1
Geometric dimensions of the different experimental arrangements used at JYFL and iThemba LABS.

	D	L	A_d	A_e
JYFL 14 GHz A-ECR	2627 mm	280 mm	$\pi(0.45\ mm)^2$	$\pi(4\ mm)^2$
14.5 GHz GTS	4032 mm	300 mm	$\pi(0.25\ mm)^2$	$\pi(6\ mm)^2$

Assuming that the plasma volume visible to the detector can be described by a truncated slightly conical cylinder and the $K\alpha$ emission is uniformly distributed within the plasma chamber volume,[1] the volumetric emission rate $\left(d\Phi_t/dVdt\right)$ is given by the following expression [32]:

$$\frac{d\Phi_t}{dVdt} = \frac{4\pi\left(D+\frac{L}{2}\right)^2}{A_e A_d L\left(1+\frac{L}{D}+\frac{1}{3}\frac{L^2}{D^2}\right)}\Phi_e \tag{12}$$

where L is the length of the plasma chamber, D is the distance from the plasma electrode to the entrance of the collimator, A_d is the area of the collimator aperture in front of the detector and A_e is the area of plasma electrode aperture. These numbers are given in Table 1 for the two different experimental arrangements used at JYFL and iThemba LABS.

When an X-ray is emitted from the ECR heated plasma, it has a certain likelihood of entering the detector through its 12.5 μm (0.5 mil) beryllium window. Inside the detector, the X-rays create electron–hole pairs in the depletion region of the detector. These charges drift towards the electrodes as a result of the applied bias voltage. This creates a pulse which is proportional to the energy of the incoming X-ray. The anode of the silicon drift detector (SDD), used in this work, is very small and is surrounded by a series of annular drift electrodes. These electrodes guide the electrons through the detector, to be collected at the anode. As a result of the small area of the anode, the total input capacitance of the SDD is very small, which leads to improved energy resolution. The beryllium window of the SDD alters the transmission of the low energy X-rays incident onto the detector. A flux of 1 keV X-rays for example will be attenuated by 76% inside the beryllium window of the SDD [33]. Similarly the finite width of the active region of the detector, limits high energy X-rays from being detected. This effect refers to the efficiency of the X-ray detector. At the 2.96 keV energy of the $K\alpha$ of argon, approximately 86% of the $K\alpha$ X-rays is detected in the 450 μm thickness of the active region of the SDD [9]. Both these transmission and efficiency effects had to be taken into account in translating the measured $K\alpha$ emission rate into a volumetric emission rate and inner shell ionization rate.

3.2. Data processing

The DP5 digitizes the preamplifier output from the detector. Inside the DP5, pulse shaping is done with a digital shaping amplifier. The advantage of digital shaping amplifiers over analog shaping amplifiers are well documented [9]. In the case of our measurements, a digital trapezoidal shaper was used. With such a trapezoidal shaper the so-called 'peaking time' and 'flat top time' can be specified independently. In this way one can minimize the pile-up and maximize the count rate. The peaking time and flat top time was set to 4.8 μs and 100 ns, respectively for all the measurements performed in this work. Since the peaking time influences the energy resolution of the detector, this parameter had to be determined as a function of peaking time. At the peaking time used for our measurements, the energy resolution was determined to be 160 eV at the $K\alpha$ of Mn (5.9 keV). The data was acquired with custom software supplied by Amptek. The digitized output of the slow channel is stored in the FIFO (First-In First-Out) memory, along with its time-stamped information. This method of

[1] This assumption is discussed in further detail later in this paper.

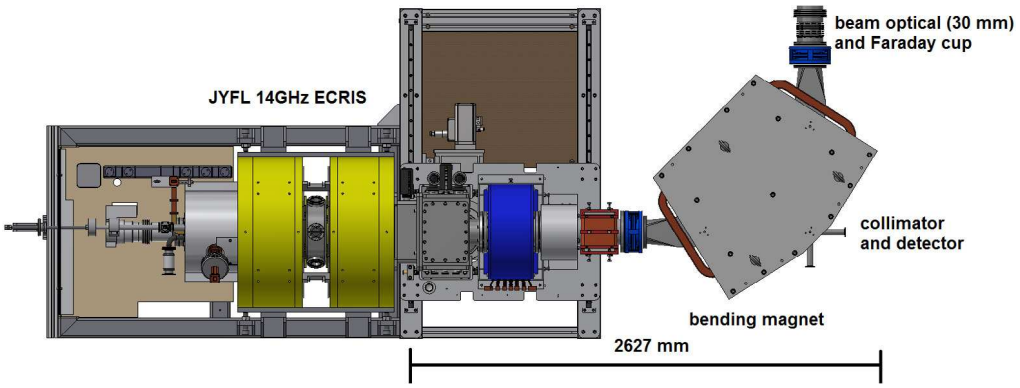

(a) Schematic of the JYFL ECRIS and connecting transfer beamline elements. The two ports of the bending magnet are also shown. The X-ray detector (not shown) was attached to the one port enabling it to view the ECR plasma axially through the bending magnet.

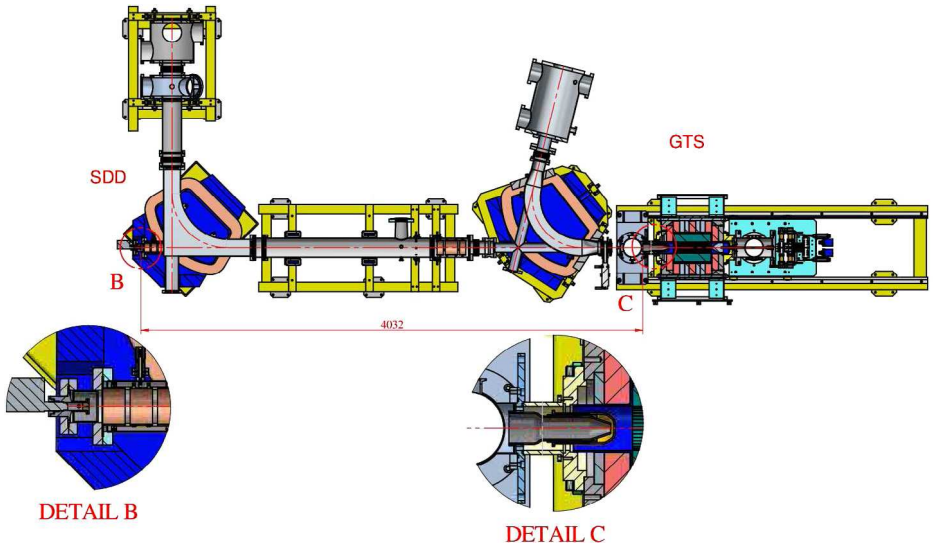

(b) Layout of the experimental arrangement at iThemba LABS showing the GTS and the position of the SDD.

Fig. 2. Schematic view of the experimental arrangements used at JYFL and iThemba LABS.

organizing data entails that the data first read into the memory will be lost first if the memory capacity is exceeded. This information is readout to a host computer via the USB port every 10 ms. As long as the readout rate exceeds the rate of writing data to the FIFO, the FIFO never overflows and no data is lost. With the acquisition software, piled-up events were tagged to be dealt with later during the analysis. The DP5 allows for piled-up events to be identified by determining the time difference between two incoming X-rays on the fast channel. If this time difference is less than the sum of the peaking time and flat top time, the event is tagged as pile-up. With the implementation of the collimator, pile-up was reduced to less than 0.001%.

To determine the volumetric emission rate of the $K\alpha$ of argon, the measured spectrum was firstly corrected for the X-ray losses in the beryllium window, as well as for the efficiency of the detector. Following this, the background spectrum generated by the combined effects of the plasma and wall bremsstrahlung was subtracted from the corrected spectrum. In the case of the work presented in this paper, the background was determined using a ROOT function [34]. This function is based on the so-called Sensitive Peak Clipping Algorithm (SNIP) [35,36] and allows for continuous background to be extracted from a measured spectrum. A Gaussian peak was then fitted to the $K\alpha$ of argon. The number of counts between the 10% threshold on either side of the peak of the Gaussian was then determined. By integrating between the two 10% thresholds, the number of counts in the integration

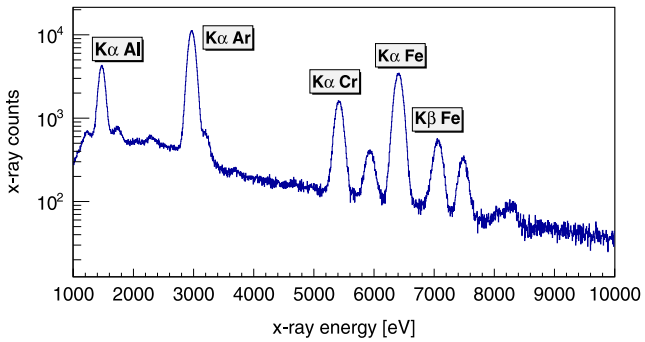

Fig. 3. A typical X-ray spectrum measured from the ECRIS plasma of the JYFL ECRIS with a few prominent lines being identified. The bremsstrahlung background has not been subtracted in this spectrum.

corresponds to roughly 2σ of a Gaussian distribution. The number of counts is then averaged over the measurement time to yield Φ_e. Figs. 3 and 4 show typical spectra recorded from the two ion sources.

Comparing Fig. 3 with Fig. 4, reveals the difference between the two sources from an X-ray spectral point of view. For both sources, the line-of-sight of the X-ray detector ends at the biased disc, which

Table 2
Most prominent characteristic lines observed in each of the X-ray spectra measured on the two ion sources. The measured number of counts in each of the lines was normalized with respect to the $K\alpha$ counts of argon. The symbol (–) implies that the lines could not be detected as their intensity is below the threshold of the detection system.

Characteristic line energy (Siegbahn notation)	iThemba LABS GTS (%)	JYFL A-ECR (%)
1.5 keV (Kα Al)	5.8	19.8
1.7 keV (Mα1 Ta)	24.8	–
3.0 keV (Kα Ar)	100	100
4.5 keV (Kα Ti)	15.4	–
4.9 keV (Kα V)	4.3	–
5.4 keV (Kα Cr)	3.5	25.9
5.9 keV (Kα Mn)	2.5	8.5
6.4 keV (Kα Fe)	4.7	58.9
7.1 keV (Kβ1 Fe)	2.8	10.9
7.5 keV (Kα Ni)	–	6.6
8.1 keV (Kα Cu)	6.4	–
9.4 keV (Lβ Ta)	8.7	–

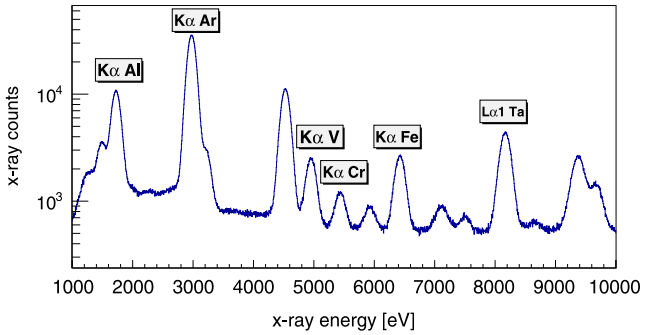

Fig. 4. A typical X-ray spectrum measured from the ECRIS plasma of the GTS with a few prominent lines being identified. The bremsstrahlung background has not been subtracted in this spectrum.

enables the detector to measure characteristic lines from the material of the biased disc. As discussed in Section 3.1, the material of the biased disc in the GTS and the JYFL ECRIS differ. Table 2 shows the most prominent lines observed in the X-ray spectra of the two sources, along with their intensity normalized with respect to the counts in the $K\alpha$ of argon. The measured GTS X-ray spectrum shown in Fig. 4, has various characteristic lines emanating from the tantalum biased disc. These lines are not observed in the case of the JYFL ECRIS, instead strong lines are observed from the composites of stainless steel coming from the stainless steel biased disc. The X-ray spectra taken from the JYFL ECRIS also reveals strong aluminium and chromium lines. The aluminium lines most probably emanate from backstreaming electrons which interact with the aluminium extraction system of the source. The extraction electrodes of the GTS are made of stainless steel which most likely accounts for the lines of the stainless steel composites observed in the case of the GTS. The chromium lines observed with the JYFL ECRIS most probably originates from residues accumulated on the plasma chamber surface from previous ion source operation, as well as from the biased disc. The fact that both plasma chambers are made of aluminium and weak aluminium lines are observed with the GTS spectra leads us to believe the contribution from the plasma chamber to the aluminium lines is insignificant. The $K\alpha$ of argon is the dominant peak in both spectra which implies that the contribution of the confined electrons is more prominent in comparison to lost electrons creating characteristic X-rays and bremsstrahlung on the surfaces.

3.3. Analysis of the sources of error

During the process of acquiring the data, a number of sources of error were identified. These will be briefly discussed in this section. The measurements were performed over many hours to accumulate sufficient statistics. Over such extended measurement periods, the source tune could change. These changes could alter the measured volumetric emission rate. To assess the influence of this uncertainty on the results, the volumetric emission rate was measured at three different times during the measurement campaign, at the same source setting. This comparison gave an indication of systematic error as well as the changing volumetric emission rate with time. This led us to conclude that the sum of these two effects results in an uncertainty of 12.5% in the measured emission rate. Another source of error is the difference between the measurement time and the acquisition time. The detector has a charge sensitive preamplifier, which produces a voltage proportional to the time integral of the current [9]. The integrator in the preamplifier saturates with time and needs to be reset. During reset, data acquisition is temporarily stopped. In determining the count rate, the measurement time was not corrected for these reset intervals. Since the reset interval was set to 102 μs and the measurement time extended for up to thirty minutes, the error in determining the count rate is deemed small.

An error was also incurred as a result of the alignment of the detector relative to the magnetic axis of the source. In the case of the measurements performed with the GTS, the detector was placed in a port on the vacuum chamber of the bending magnet. As the bending magnet had to be aligned with the magnetic axis of the source, the alignment in this case was deemed small. In the case of the measurements performed on the 14 GHz ECRIS at JYFL, the detector was also mounted in a port in the vacuum chamber of the bending magnet. The vacuum chamber of the magnet is however not firmly attached to anything which makes alignment of the detector rather tricky. The initial alignment was checked with a theodolite relative to a reference point on the transfer beamline. With the detector installed, the alignment was fine tuned by making minor adjustments and looking at the total count rate measured by the detector. At roughly maximum count rate, the detector position was fixed. The error on the alignment results in an error on the effective radius of the collimator as seen by the X-rays. Due to the uncertainty related to the alignment, the effective diameter of the collimator is estimated to 600–800 μm.

To determine the volumetric emission rate the initial assumption is made that the $K\alpha$ emission originates from a point source in the centre of the plasma volume. Given the large distance of the detector from the plasma volume, the emission closely resembles that of a point source. The error in this assumption is therefore deemed to be very small as described thoroughly in the literature [32]. To translate the point source like emission into a volumetric emission rate using Eq. (12), a further assumption is made that the emission from the volume visible to the detector is spatially uniform as well as isotropic. In reality, it is well-known that the electron, ion and neutral distributions are not uniform inside the plasma volume. The heated electron populations are strongly collisionless and therefore magnetically confined. The magnetic confinement field therefore dictates the electron distribution inside the

Table 3
Ion source settings for the microwave power sweep.

Calibrated pressure at injection (0 W)	4.3×10^{-7} mbar
B_{inj} (magnetic field strength at injection)	2.02 T
B_{min} (B minimum)	0.35 T
B_{ext} (magnetic field strength at extraction)	0.95 T A
biased disc voltage	−170 V
microwave power	100–600 W

ECRIS. Given the very short lifetime of a K-shell vacancy (typically nanoseconds), $K\alpha$ emission occurs almost instantaneously after the generation of a K-shell vacancy. This implies that the ions and neutrals do not move significant distances between a K-shell vacancy generation and $K\alpha$ emission. The neutrals and ions therefore form a background of targets, in the vicinity of the heated electrons, which collides with the heated electrons. It can therefore be argued that the $K\alpha$ emission distributions are dictated by the magnetic confinement field. From the results obtained from numerical simulations it is believed that the plasma density is higher inside the ECR zone [11]. The assumption of uniform $K\alpha$ emission therefore corresponds to the lower limit of the volumetric emission rate, in absolute terms. Since the plasma does not fill the entire volume described by Eq. (12), the true volumetric rate is higher than the result obtained. The upper limit for the volumetric emission rate can be calculated by assuming there is a dense plasma inside the ECR zone and using the volume of the ECR zone to calculate the volumetric emission rate in Eq. (12). In the case of the JYFL 14 GHz ECRIS, for example, the axial length of the ECR zone is 80–90 mm at typical magnetic field settings. This translates to the upper limit of the volumetric emission corresponding to concentrated emission profile to be 3.1–3.5 times the lower limit corresponding to a uniformly distributed emission. The real volumetric emission rate is most likely between these two limits.

4. Experimental results

4.1. Influence of the microwave power and neutral gas pressure on the absolute inner shell ionization rate

The influence of the microwave power and neutral gas pressure on the absolute inner shell ionization rate was studied with the JYFL 14 GHz ECRIS. With this investigation, the source was tuned for a high charge state (Ar^{13+}) and for the first part of the investigation the incident microwave power was varied between 100 W and 600 W, at a fixed neutral gas pressure. All other source parameters were kept at constant settings shown in Table 3.

It has been shown previously that the microwave power absorbed by the plasma changes as the incident microwave power changes [37]. To estimate the absorbed microwave power, the microwave power losses in the waveguide were estimated to be 20% of the incident microwave power. These power losses were subtracted from the incident microwave power to yield the power absorbed by the plasma. Due to an impedance mismatch between the klystron and the plasma load and transmission system, a fraction of the forward power gets reflected in the transmission system. In the case of measurements performed at JYFL, the reflected power was estimated to be less than 2% of the forward power. The absorbed power, as defined here, is however only an estimation of the maximum possible power that can be absorbed by the plasma. Besides power losses and reflection in the waveguide, various other possible power dissipation channels exist, for example losses in the plasma chamber, high voltage break and vacuum window. The variation of the absolute inner shell ionization rate with increasing absorbed microwave power, at different neutral gas pressures, is shown in Fig. 5. By propagating the uncertainties in the alignment, the systematic error and K-shell fluorescence yield, the uncertainty in the absolute inner shell ionization rate, as presented in Fig. 5, was determined to be ±32%. Additionally the presented absolute inner shell ionization rates were also

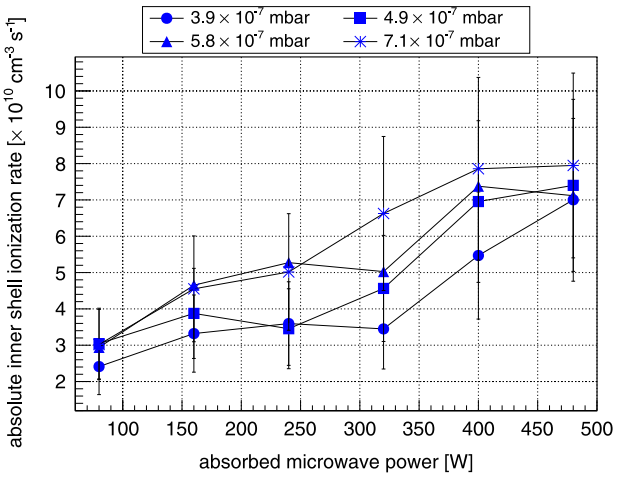

Fig. 5. Variation of the (minimum) absolute inner shell ionization rate as a function of absorbed microwave power, at different neutral gas pressures.

corrected for vacancies generated as a result of inner shell excitation, to take this process into consideration. Lastly it should be mentioned that the absolute inner shell ionization rates shown in Fig. 5 is the estimated lower limit due to the assumption of uniformly distributed and isotropic emission.

From the discussion in Section 2 it is known that the observable $K\alpha$ emission rate, and therefore also the absolute inner shell ionization rate, depends on the average charge state and ionization degree of the plasma, as well as on the electron energy and density. It is commonly assumed that the charge state distribution (CSD) of the plasma core differs from the extracted CSD [15], but the extracted CSD can be used to gain insight into the changing plasma core CSD during a parametric sweep. During a typical microwave power sweep, the variation of the average extracted charge state observed was from 7.98 to 10.45. These average extracted charge states were however calculated for argon only and it should be emphasized that any impurities present within the plasma will decrease the average charge state. Also, to determine the average extracted charge state, the low charge states had to be estimated as these cannot be measured due to limitations on the analysing magnet. To estimate the low charge state, a particle spectrum was formed and an envelope curve fitted over the particle currents. The low charge state particle currents determined from the envelope curve were most likely underestimated and additionally all charge states are subjected to losses in the transmission line. All these factors enhance the difference between the plasma core CSD and the extracted CSD. In comparison to the variance of the average extracted charge state, the typical variation in the absolute inner shell ionization rate during the same parameter sweep was determined to be between 8.80×10^9 cm^{-3} s^{-1} and 3.00×10^{10} cm^{-3} s^{-1}. The relative variation of the absolute inner shell ionization rate (during the parameter sweep) is at least three times more than the estimated variation in the average charge state of the plasma core. This implies that the average charge state of the plasma core probably plays a lesser role in comparison to the other plasma parameters which affect the inner shell ionization rate. Thus, the increase of inner shell ionization rate with microwave power is most likely due to increasing plasma energy content, $n_e kT_e$, as deduced from experiments on ECRIS plasma diamagnetism [38].

The influence of the ionization degree on the absolute inner shell ionization rate can be established by determining the efficiency of producing inner shell ionization per unit absorbed microwave power. Fig. 6 shows that the rate of producing inner shell ionization, per unit of absorbed microwave power, is highest at the lowest absorbed microwave power. This implies that inner shell ionization is most effectively produced at low degree of ionization of the plasma. The figure

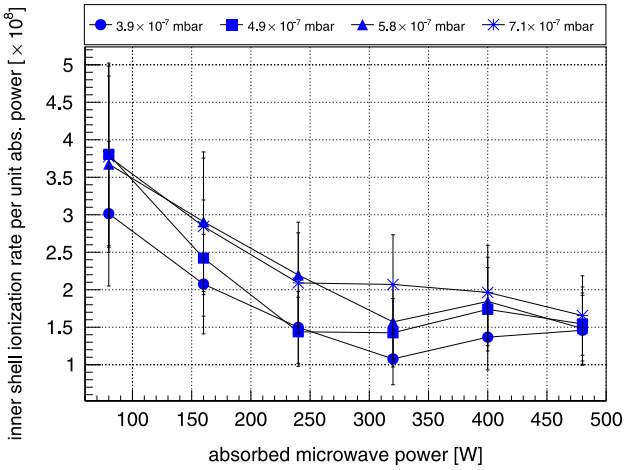

Fig. 6. Variation of the (minimum) absolute inner shell ionization rate per unit absorbed microwave power, at different neutral gas pressures.

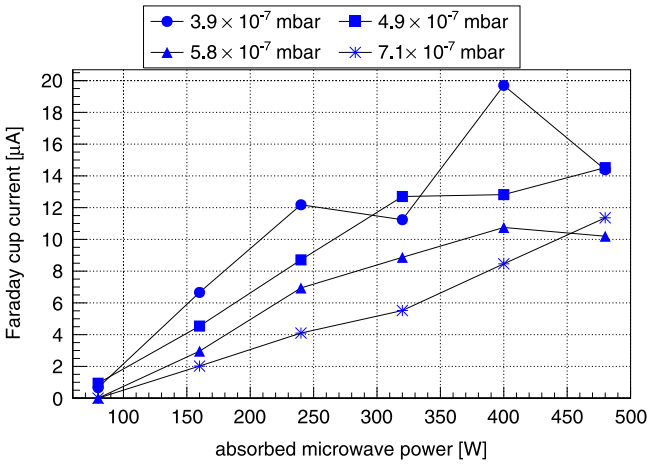

(a) Faraday cup current of Ar^{13+} as a function of the absorbed microwave power, at different neutral gas pressures.

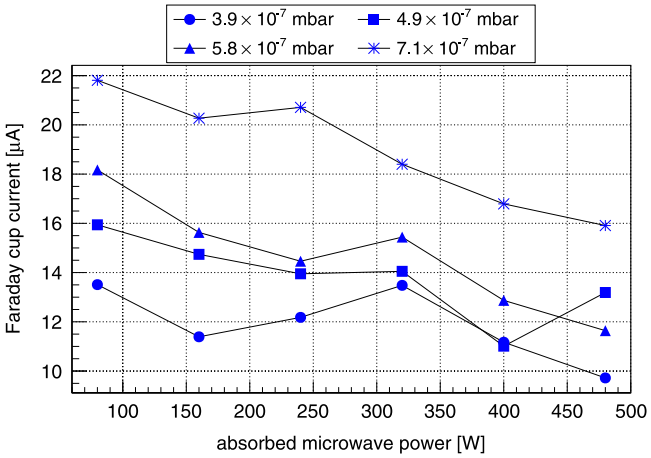

(b) Faraday cup current of Ar^{6+} as a function of the absorbed microwave power, at different neutral gas pressures.

Fig. 7. Faraday cup current of Ar^{13+} and Ar^{6+} as a function of the absorbed microwave power, at different neutral gas pressures.

also shows that the inner shell ionization rate, per unit absorbed power, saturates as the absorbed power is increased. Since the behaviour of the ionization rate and production efficiency (reported in Ref. [39]) with increasing microwave power is logarithmic, the curves in Fig. 6 illustrate the inverse behaviour of the $K\alpha$ emission rate and the ionization rate.

The observations from Fig. 6 can be explained by assuming that the ions and neutrals behave as an ideal gas. Neutral atoms are typically considered to be cold ($kT_{\text{neutral}} \approx 25$ meV at room temperature), while the ion temperature (kT_{ion}) is typically between 1 and 5 eV [26]. This implies that the total density of argon (atoms and ions) decreases with increasing ionization degree, which (along with the average charge state) could presumably explain the behaviour observed in Fig. 6. At low absorbed microwave power, the ionization degree and energy content of the plasma is still very low. The neutrals therefore make up a sizeable fraction of the plasma constituents. This larger neutral content presumably leads to the increased inner shell ionization rate, averaged over the absorbed microwave power, as observed in the experimental results. As the degree of ionization of the plasma increases, with increasing absorbed microwave power, the neutral content becomes less. This leads to the decreased inner shell ionization rate, averaged over the absorbed microwave power.

Based on the discussion above, it can be concluded that the absolute inner shell ionization rate is affected by the ionization degree of the plasma. The influence of the electron energy and density i.e. the plasma energy content on the absolute inner shell ionization rate becomes more pronounced as the absorbed microwave power increases as seen in Fig. 5. The saturation of the inner shell ionization rate per unit of absorbed microwave power is consistent with the saturation of the plasma energy content as a function of microwave power, reported in Ref. [38]. The relative large error bars of the absolute inner shell ionization rate do not affect these tendencies since the error is considered to be mostly systematic (due to the given assumptions) as described in Section 3.3.

To relate the absolute inner shell ionization rate to the extracted CSD, the faraday cup current of a high (Ar^{13+}) and low (Ar^{6+}) charge state were compared to the absolute inner shell ionization rate. Fig. 7 presents the faraday cup currents of the two different charge states during the microwave power sweep, at different neutral gas pressures. By comparing Fig. 7a with Fig. 5, it is observed that the absolute inner shell ionization rate and Ar^{13+} production shows some resemblance i.e. both quantities increase with increasing absorbed microwave power. The reason for the observed trend is most likely due to the increasing average charge state of the plasma, as well as the increasing plasma energy content. From the comparison of Fig. 7b and Fig. 5 it can also be remarked that the absolute inner shell ionization rate and the Ar^{6+} production appear to have opposing trends i.e. the absolute inner shell ionization rate increases while the Ar^{6+} production decreases. The Ar^{6+} current presumably decrease due to the CSD shifting towards higher charge states which is caused by the increasing plasma energy content.

For the second part of this investigation the variation of the absolute inner shell ionization rate, with neutral gas pressure, was probed. With this investigation the same source settings as given in Table 3 was used, with the incident microwave power fixed and the neutral gas pressure varied between 2.5×10^{-7} mbar to 1.1×10^{-6} mbar. The values of the neutral gas pressures were obtained without igniting the plasma. The results of this set of measurements is shown in Fig. 8. Previous studies investigating the X-ray power emitted by the confined electrons of an ECRIS proposed a saturation of the X-ray power with increasing neutral gas pressure [38]. These studies however focused on the X-ray emission from the plasma bremsstrahlung. With the current investigation it was found that the behaviour of the $K\alpha$ emission rate with increasing neutral gas pressure, and by implication also the absolute inner shell ionization rate with increasing gas pressure, behaves very similar to the results obtained in the cited reference. The inner shell ionization rate was found to initially increase rapidly with increasing neutral gas pressure. The rapid increase in absolute inner shell ionization rate is most likely due to the increase in the target densities (atoms and ions), as well as the electron density. The rapid increase in electron density with increasing

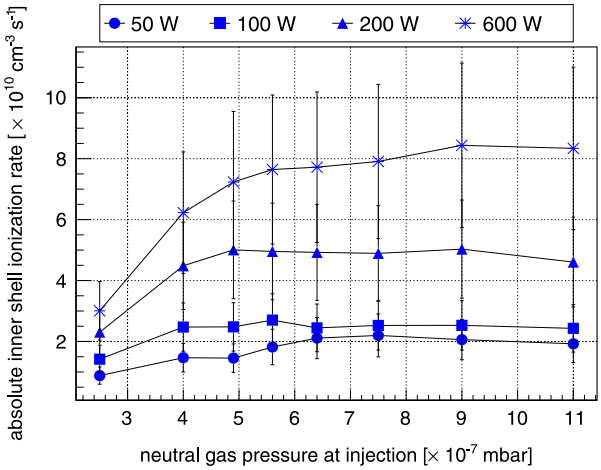

Fig. 8. Variation of the (minimum) absolute inner shell ionization rate as a function of gas pressure, at different incident microwave powers.

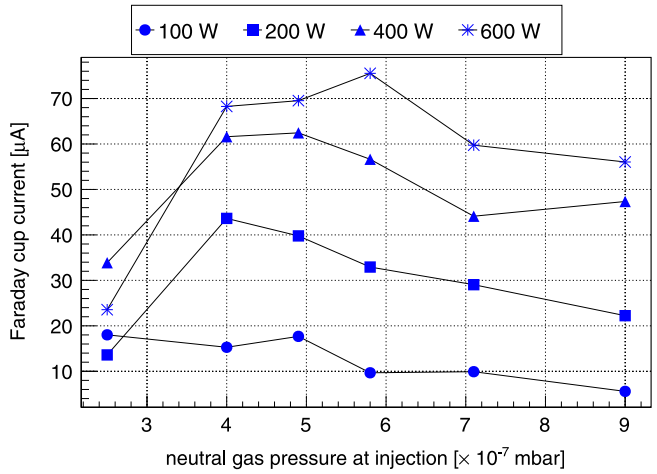

Fig. 9. Faraday cup current of Ar^{11+} as a function of the neutral gas pressures, at different incident microwave powers.

pressure is also simulated by some ECRIS codes [40]. The rate of increase becomes larger as the microwave power is increased. This most likely points to the increased contribution to inner shell ionization due to the increasing plasma energy content, with increasing microwave power. With further increase in pressure, the inner shell ionization rate reaches a saturation point. At this point the energy content of the plasma is considered insufficient to sustain any further growth in the ionization degree of the plasma. This assertion is supported by the saturation in the production rate of high charge states observed in the measured extracted charge state distribution as shown in Fig. 9. With even further increase in pressure, the charge exchange process becomes more dominant and results in a decrease in the extracted currents of high charge states. This is evident from the substantial decrease in Ar^{11+}, with increasing pressure, observed from the extracted CSD shown in Fig. 9.

To complete the investigation into the influence of the pressure sweep on the absolute inner shell ionization rate, the low and high charge state production as a function of the pressure sweep was also considered. From the discussion above it is known that the absolute inner shell ionization rate initially increases very sharply with pressure increase, at a fixed microwave power. This increase becomes more pronounced at higher microwave power. From the extracted charge state distribution, the general trend observed was for high charge state production to decrease as the pressure is increased, at a fixed incident microwave power as shown in Fig. 10a. This observation can be explained by referring to the discussion in Section 2. From the discussion there it is known that the charge exchange process dominates if the confinement time needed for high charge state production becomes greater than the time between two charge exchange events. By increasing the neutral pressure, this situation is realized resulting in the decreasing high charge state production. It was also observed that the optimum high charge state production occurs at low pressures and increases to higher pressure, as the microwave power is increased. From this observation it is concluded that the increasing inner shell ionization rate observed at low pressure results in increased high charge state production. As the pressure is further increased, at a fixed microwave power, the inner shell ionization rate increases but the high charge state production initially saturates and then decreases presumably due to increased rate of charge exchange reactions. As the microwave power is increased, the optimum high charge state production is reached at higher pressures. As an example, at 100 W of incident microwave power, the optimum Ar^{13+} production occurs at 2.5×10^{-7} mbar. At 600 W of incident microwave power, the optimum Ar^{13+} production occurs at 4.9×10^{-7} mbar. From the measured extracted CSD, the optimum pressure for Ar^{11+} production also increases monotonically with increasing absorbed microwave power. These observations suggest that the energy content of the plasma, for optimum high charge state production, is strongly influenced by the change in pressure.

4.2. Influence of the magnetic field configuration and biased disc voltage on the absolute inner shell ionization rate

The absolute inner shell ionization rate was also studied as a function of the magnetic field configuration and biased disc voltage. This investigation was again performed with the JYFL 14 GHz ECRIS, with the source tuned for optimum Ar^{13+} production. The corresponding source settings are given in Table 3. For the first part of the investigation the incident microwave power was fixed at 400 W, with only the solenoid coil currents being changed. In all measurements reported in this work, the injection and extraction coil currents were kept equal. As the source has a permanent magnet hexapole, the magnetic field contribution from this element remained constant during the investigation. When considering the influence of the magnetic field configuration, most literature only report on changes as a function of magnetic field parameters like the mirror ratio, B_{min}/B_{ECR}-ratio and the on-axis magnetic field gradients at injection and extraction. While these parameters certainly play an instrumental role during electron heating, it in a sense trivializes the heating process by considering only the magnetic field gradient at certain regions in the ECR zone, for example. It can be argued that the magnetic field gradient at these points do not alone influence the heating, but the heating is influenced by the gradient at all points over the ECR surface. The approach therefore employed in this work is to consider the average magnetic field gradient in the direction parallel to the field lines across the entire ECR surface, as was done in Ref. [41].

The variation of the absolute inner shell ionization rate as a function of average parallel magnetic field gradient and B_{min}/B_{ECR}-ratio is presented in Fig. 11a. The results of this investigation seems to indicate that the inner shell ionization rate is decoupled from changes to the magnetic field configuration. In changing the solenoid coil currents from 570 A to 490 A, the average parallel magnetic field gradient over the ECR surface changed from 4.03 T/m to 7.53 T/m, while the B_{min}/B_{ECR}-ratio changed from 0.825 to 0.683. The maximum change in inner shell ionization rate observed over the magnetic field sweep amounted to 29%, which is within the error bars of the measurement. This is in contrast with the microwave power and pressure sweeps, where changes in absolute inner shell ionization rate in excess of 400% were observed. This seems to indicate that the magnetic field changes have very little impact on the warm electron population of the ECRIS. Previous investigations determining the so-called spectral temperature also noted minimal changes of this parameter as a function

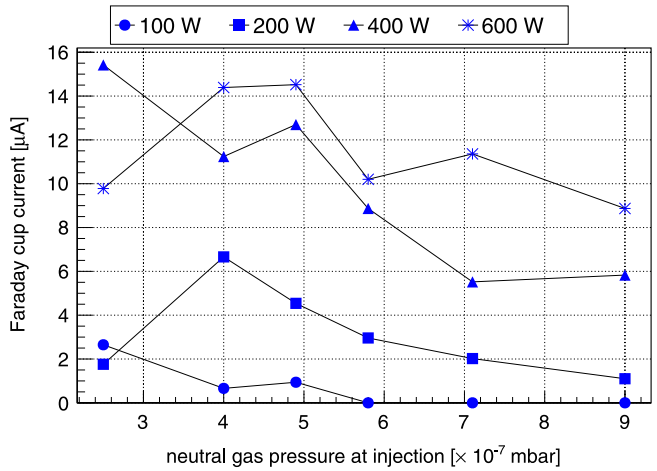

(a) Faraday cup current of Ar^{13+} as a function of neutral gas pressure, at different incident microwave powers.

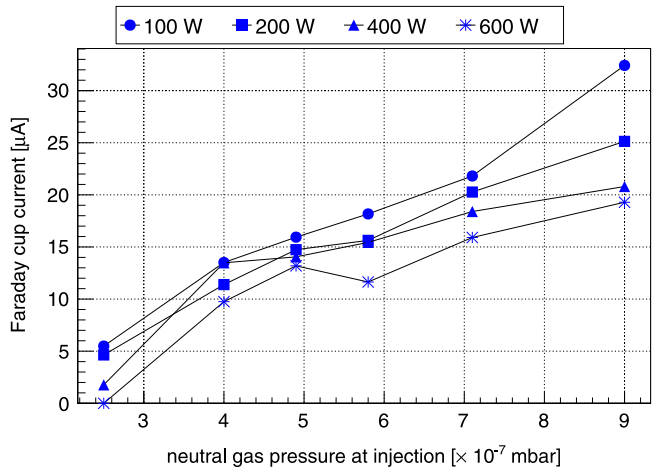

(b) Faraday cup current of Ar^{6+} as a function of neutral gas pressure, at different incident microwave powers.

Fig. 10. Faraday cup current of Ar^{13+} and Ar^{6+} as a function of neutral gas pressure, at different incident microwave powers.

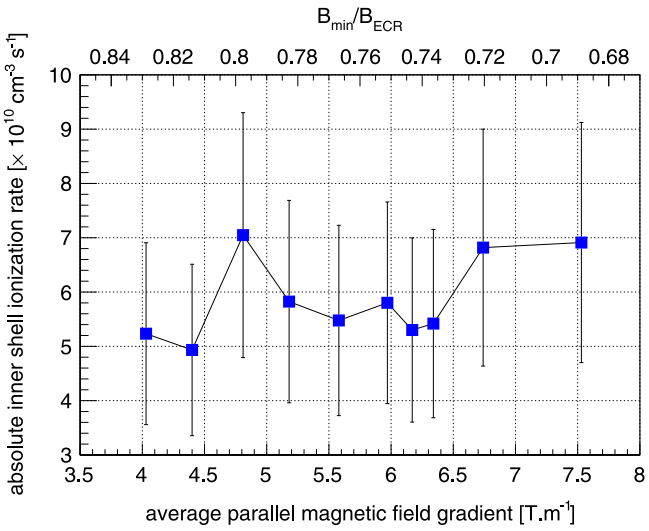

(a) Variation of the (minimum) absolute inner shell ionization rate as a function of average parallel magnetic field gradient and B_{min}/B_{ECR}-ratio.

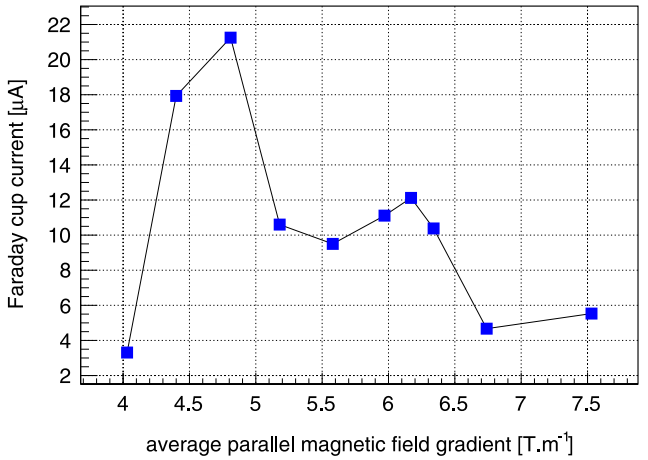

(b) Faraday cup current of Ar^{13+} as a function of average parallel magnetic field gradient.

Fig. 11. Variation of the (minimum) absolute inner shell ionization rate as a function of average parallel magnetic field gradient and B_{min}/B_{ECR}-ratio and Faraday cup current of Ar^{13+} as a function of average parallel magnetic field gradient.

of B_{min}/B_{ECR} [38]. The spectral temperature is equivalent to a mean electron temperature defined over a certain energy range. In the cited investigation, the spectral temperature was determined over a range (4–20 keV) very close to the binding energy of the $1s^2$ electrons of argon. From the spectral temperature results in Ref. [38], it appears as if the magnetic field sweep has a larger impact on the hot electron population.

To gauge the influence of the parameter sweep on high charge state production, the extracted Ar^{13+} beam current was used, as shown in Fig. 11b. The largest extracted Ar^{13+} intensity is achieved with the solenoid coil currents set to 550 A. Simultaneous optical emission measurements through the radial diagnostics port viewing the core plasma and probing the intensity of the $2s^22p^2\ P^{\circ}_{3/2} \longrightarrow 2s^22p^2\ P^{\circ}_{1/2}$ transition of Ar^{13+} confirmed that the Ar^{13+} density indeed is maximized at this coil current setting where the peak of the inner shell ionization is also achieved. At 550 A, the average parallel magnetic field gradient over the ECR surface was determined to be 4.81 T/m. As a result of this strong axial magnetic field, the average gradient is low which results in efficient heating of the plasma electrons. This results in an enhanced hot electron population trapping more ions through its ambipolar potential. These ions are confined for long times which ultimately leads to the higher Ar^{13+} beam intensity as shown in the figure above. At the same time the total ion current extracted from the source is decreased as the improved confinement affects the integrated flux of ions towards extraction i.e. the charge state distribution and dynamic equilibrium of charge particle losses are both affected by the strength of the magnetic field. As the coil current is further increased, the plasma becomes prone to plasma instabilities [41,42]. These instabilities manifest as beam instabilities, clearly observed in the extracted beam current at solenoid coil currents ≥ 560 A. The plasma instabilities were also observed with a microwave detector installed in the waveguide of the source. The plasma instabilities reduce the ion confinement time, as electrons are continuously expelled from the magnetic trap which decreases the ion confinement time and extracted current of highly charged ions [41].

The influence of the biased disc voltage on the absolute inner shell ionization rate was also studied with the JYFL 14 GHz ECRIS. From the literature it is proposed that by increasing the negative voltage applied to the biased disc, the confinement of low energy electrons is improved [43,44]. Previous investigations at JYFL have not observed any change of the bremsstrahlung emission as a result of the changes to the biased disc voltage. In the current investigation, the variation of

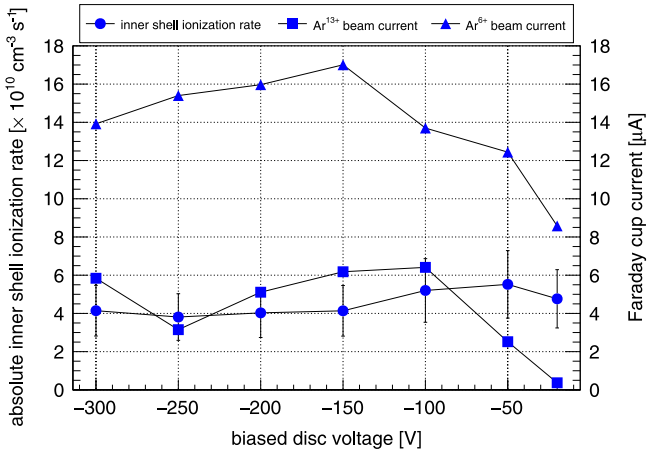

Fig. 12. Variation of the (minimum) absolute inner shell ionization rate as a function of biased disc voltage as well as the Faraday cup current of Ar^{13+} and Ar^{6+}.

the $K\alpha$ emission rate as a function of biased disc voltage was probed. As with the other parameter sweeps, the source was again tuned for optimum Ar^{13+} production. The source settings for this investigation are given in Table 3, with the incident microwave power fixed at 400 W, and only the biased disc voltage varied. Similar to the magnetic field sweep, the variation of the absolute inner shell ionization rate with biased disc voltage was minimal as shown in Fig. 12. Over the entire range of the voltage sweep, the maximum variation in absolute inner shell ionization rate measured was 31% which was again within the experimental uncertainty. This meagre variation leads to the conclusion that the biased disc voltage sweep has no direct impact on the warm electron population. From measurements performed on the JYFL 6.4 GHz ECRIS, it was concluded that the plasma potential decreases with increasing negative biased disc voltage [43]. This observation leads to the conclusion that the biased disc voltage repels electrons back into the plasma and enhances ion losses axially at the injection side of the source. Given the relatively small voltage applied to the biased disc (≤ -300 V), it is suggested that the biased disc only acts on cold electrons and, thus, the effect on the inner shell ionization caused by the warm electrons is insignificant.

To relate these observations to high charge state production, the inner shell ionization rate as a function of the voltage sweep was compared to the production rate of Ar^{13+} as shown in Fig. 12. Between −300 V and −100 V, the Ar^{13+} production remained largely constant, similar to the inner shell ionization rate. This leads to the conclusion that the bulk of the cold electrons is reflected with a biased disc voltage ≤ -100 V. By therefore increasing the negative bias voltage beyond −100 V, the electron reflection is not significantly enhanced which implies that the warm electron population remains largely constant. This results in both the Ar^{13+} production and the absolute inner shell ionization rate remaining largely unperturbed as observed with this investigation. From the literature it is known that the typical energy of the cold electron population is approximately 50 eV [26]. This further strengthens the argument that the cold electron reflection should saturate with negative biased disc voltage beyond ∼−50 V. The investigation also reveals that the inner shell ionization rate peaks at −50 V, while the maximum Ar^{13+} Faraday cup current is observed at −100 V. From −100 V to −20 V, the Ar^{13+} production decreases drastically from 6.4 eμA to 0.37 eμA. During the same voltage interval, the inner shell ionization rate only decreases by 14%. The fact that the absolute inner shell ionization rate does not directly follow the Ar^{13+} production leads to the suggestion that the ionization degree of the plasma decreases as the negative biased disc voltage is decreased from −100 V to −20 V. This is also evident from the mean extracted charge state as a function of the voltage sweep. As the biased disc voltage is decreased from −100 V to −20 V, the mean extracted charge state distribution decreases drastically. The fact that the biased disc voltage does not affect the volumetric emission rate, but affects the CSD implies that optimizing the biased disc voltage affects the confinement time of the ions. The last observation that can be drawn from the current investigation is that the secondary electron emission from the biased disc appears not to account for its performance. The results of this investigation clearly show that the thick-target counts from the biased disc remain largely unperturbed during the voltage sweep. This would result in constant secondary electron emission from the biased disc. The secondary electron emission, from the biased disc, therefore appears to be decoupled from high charge state production.

From the behaviour of the inner shell ionization rate as a function of the magnetic field strength and biased disc voltage it can be observed that the inner shell ionization rate remains largely constant, within the experimental uncertainty, during the parameter sweeps. In stark contrast to this, the beam currents of low and high charge states can change drastically over the course of the parameter sweeps. This highlights the fact that the changes in the plasma behaviour, induced during the parameter sweeps manifests differently in the $K\alpha$ emission rate and the extracted ion beam currents of the different charge states. This underlines the importance of using $K\alpha$ emission as a plasma diagnostic and benchmarking tool for ECRIS simulations.

4.3. Comparison of the JYFL 14 GHz ECRIS and GTS at iThemba LABS in terms of absolute inner shell ionization rate

To confirm that the absolute inner shell ionization rates measured with the JYFL 14 GHz ECRIS are valid, at least to within an order of magnitude, it was necessary to measure and compare the $K\alpha$ emission rates from two different sources. For this comparison, the volumetric $K\alpha$ emission rate of argon was measured from the two ion sources, as a function of the source tune parameters. Fig. 13a shows the total absolute inner shell ionization rate for the two ion sources, as a function of absorbed microwave power. The ion source settings for the GTS, during the parametric sweep, were very similar to those of the JYFL 14 GHz ECRIS and represent typical operating conditions used for ion beam production. From the results of the microwave power sweep it can be observed that the absolute inner shell ionization rate of the GTS is very similar to that of the JYFL 14 GHz ECRIS. The general trend is also the same for both sources, i.e. the ionization rate increases with increasing microwave power. The propagated error on the absolute inner shell ionization rate of the GTS is roughly half of that of the JYFL 14 GHz ECRIS, due to the smaller error in the alignment of the position of the X-ray detector in the case of the measurements performed on the GTS. With the pressure sweep, the order of magnitude of the inner shell ionization rate again matches well when the sources are compared. Fig. 13b presents the absolute inner shell ionization rate of the JYFL 14 GHz ECRIS as a function of neutral gas pressure, at 400 W of incident microwave power, at two different times during the measurement period. The absolute inner shell ionization rate measured with the GTS at roughly the same source settings varies between 1.50×10^{10} cm^{-3} s^{-1} and 1.27×10^{11} cm^{-3} s^{-1}. This comparison is however subject to some uncertainty. Due to the different locations of the pressure gauge and the different pumping speeds, it is difficult to estimate the pressure. The location of the pressure gauge is also different in the case of the GTS at iThemba LABS as oppose to the JYFL 14 GHz ECRIS. The actual pressures in the chamber are therefore probably different for the curves shown in Fig. 13b compared to the pressures used for the measurements on the GTS. Additionally in the case of the measurements performed with the GTS, the neutral pressure at injection were not determined without microwave power. With microwave power launched into the plasma chamber, the ECR volume acts as a neutral gas sink resulting in a pressure drop in the region of the pressure gauge. This therefore results in a pressure difference with and without microwave power. With the pressure sweep on the GTS, the valve controlling the amount of gas flow

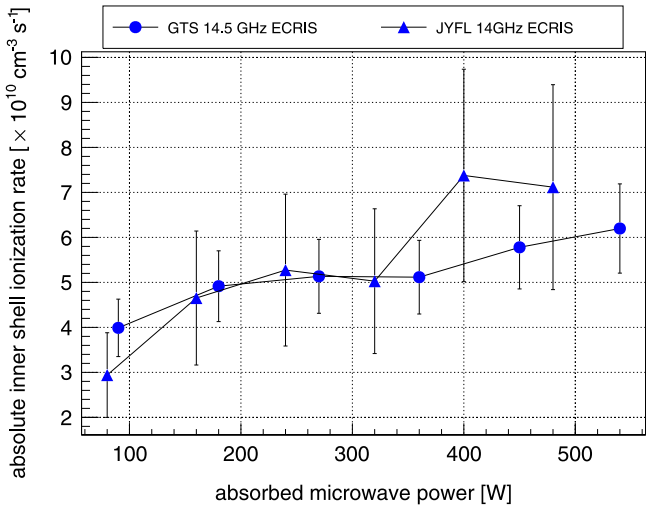

(a) Comparison of the (minimum) absolute inner shell ionization rates. Variation of the (minimum) absolute inner shell ionization rate as a function of absorbed microwave power for the two ECR ion sources.

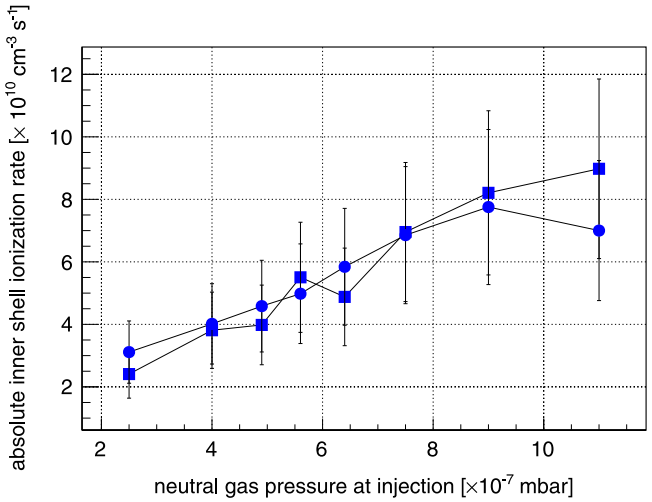

(b) Comparison of the (minimum) absolute inner shell ionization rates. Variation of the (minimum) absolute inner shell ionization rate of the JYFL 14 GHz ECRIS as a function of neutral gas pressure at 400 W of incident microwave power. The inner shell ionization rate was determine at two different times during the measurement period at the same source settings.

Fig. 13. Comparison of the (minimum) absolute inner shell ionization rates.

to the source injection region was adjusted to three different values, yielding high, medium and low flow rates. These were then compared to typical high, medium and low flow rates of the JYFL 14 GHz ECRIS. The general behaviour of the two sources during the pressure sweep were similar. The trend observed was for the inner shell ionization rate to increase with increasing neutral pressure. For the magnetic field configuration and the biased disc voltage the dependencies were very similar.

5. Conclusions

The influence of the ECRIS tune parameters on the absolute inner shell ionization rate was studied with two different ion sources. By combining the absolute inner shell ionization rate with the extracted charge state distribution, the study enabled a deeper understanding of high charge state production. Taking into consideration the propagated error as a result of the major uncertainties in the experimental arrangement and atomic processes, the absolute inner shell ionization rate determined from the two ion sources were very similar. The microwave power and neutral gas pressure were found to have the largest impact on the absolute inner shell ionization rate. The increase in inner shell ionization rate, with increasing microwave power, was found to most likely occur as a result of the increasing plasma energy content. The plasma energy content was also found to saturate as the absorbed microwave power is increased. This leads to the suggestion of a logarithmic increase of $K\alpha$ emission with increasing microwave power. The investigation also revealed that the inner shell ionization rate at low degree of ionization is largely controlled by the target (atom and ion) densities as oppose to the plasma energy content. The influence of the neutral gas pressure on the inner shell ionization rate was found to be larger than the microwave power sweep. This rapid increase was found to be driven by the target densities and the plasma energy content. It was also established that the plasma energy content beyond a certain neutral gas pressure becomes insufficient to sustain the growth in inner shell ionization rate. Above this critical point, the absolute inner shell ionization rate saturates. With further increase in neutral gas pressure, charge exchange processes became dominant resulting in decreased high charge state currents.

The results of the investigation also showed that the influence of the magnetic field and the biased disc voltage on the inner shell ionization rate was far less pronounced, when compared to the microwave power and neutral pressure sweeps. This led to the suggestion that the magnetic field and the bias disc voltage do not directly affect the warm electron population but influences inner shell ionization via indirect avenues. The influence of the bias disc voltage was attributed to the increasing cold electron reflection. The investigation also concluded that secondary electron emission plays a minimal role. The influence of the axial ion losses was not adequately investigated with this study and will perhaps be probed with a future investigation. The magnetic field configuration was studied using a novel parameter to characterize the influence of the magnetic field variation on the absolute inner shell ionization rate. Using the average parallel magnetic field gradient over the entire ECR surface, the inner shell ionization was found to be largely decoupled from this parameter. Combining the results of the current investigation with an investigation on the plasma bremsstrahlung, it was concluded that the magnetic field variation acts largely on the hot electron population [38]. It has been suggested that the magnetic field gradient results in heating of warm electrons to hot electrons [11]. The results of the current investigation indicates that the source performance is slightly improved, up to a certain point, by decreasing the average magnetic field gradient.

The plasma diagnostic developed with this work will be used in future experiments to gain a better understanding of the gas mixing effect and the double frequency heating mechanisms. The beneficial influence of both processes have been abundantly demonstrated with routine operation on various ion sources, yet the detailed understanding of these processes remains not well understood. By mixing two gases one could study the influence of the rate coefficient on the absolute inner shell ionization rate and exclude the influence of the electron density. By then varying any of the source tune parameters, one could study how this changes the absolute inner shell ionization rate. The latter effect as an example is said to alter the excited mode patterns over the ECR surface. By combining frequency tuning with the current diagnostic the current understanding wave-plasma energy transfer could be enhanced.

Acknowledgements

MS wishes to thank Prof. Paul Papka and the Department of Physics at the University of Stellenbosch for the use of their Silicon Drift Detector (X123-SDD) during the work described in this manuscript. The work of OT has been supported by the Väisälä Foundation of the Finnish Academy of Science and Letters (22-6865-18). This research was conducted at JYFL and iThemba LABS and MS wishes to thank all

those involved for their support. This work has been supported by the Academy of Finland under the Finnish Center of Excellence Program (Contract No. 213503) and mobility grant (No. 290390). The work is also based on the research supported in part by iThemba LABS and the National Research Foundation of South Africa (Grant No. 90741).

References

[1] R. Geller, Electron Cyclotron Resonance Ion Sources and ECR Plasmas, first ed., Institute of Physics Publishing, Bristol, 1996.
[2] W. Bambynek, B. Crasemann, R. Fink, et al., X-ray fluorescence yields, auger, and coster kronig transition probabilities, Rev. Modern Phys. 44 (4) (1972) 716–813. http://dx.doi.org/10.1103/RevModPhys.44.716.
[3] M. Krause, Atomic radiative and radiationless yields for k and l shells, J. Phys. Chem. Ref. Data 8 (2) (1979) 307–327. http://dx.doi.org/10.1063/1.555594.
[4] P. Auger, The compound photoelectric effect, J. Phys. Radium 6 (6) (1925) 205–208. http://dx.doi.org/10.1051/jphysrad:0192500606020500.
[5] D. Coster, R. Kronig, New type of auger effect and its influence on the x-ray spectrum, Physica 2 (1) (1935) 13–24. http://dx.doi.org/10.1016/S0031-8914(35)90060-X.
[6] H. Koivisto, P. Heikkinen, V. Hänninen, A. Lassila, H. Leinonen, V. Nieminen, J. Pakarinen, K. Ranttila, J. Ärje, E. Liukkonen, The first results with the new jyfl 14 ghz ecr ion source, Nucl. Instrum. Methods Phys. Res. 174 (3) (2001) 379–384. http://dx.doi.org/10.1016/S0168-583X(00)00615-7.
[7] D. Hitz, D. Cormer, J. Mathonnet, A new room temperature ecr ion source for accelerator facilities, Proc. EPAC (2002) 1718–1720.
[8] D. Hitz, A. Girard, K. Serebrennikov, G.G. Melin, D. Cormier, J. Mathonnet, J. Chartier, Production of highly charged ion beams with the grenoble test electron cyclotron resonance ion source, Rev. Sci. Instrum. 75 (5) (2004) 1403–1406. http://dx.doi.org/10.1063/1.1675930.
[9] Amptek website, [cited 21 December 2015]. URL http://www.amptek.com.
[10] J. Vámosi, S. Biri, Trapcad - a tool to design and study magnetic traps of ecr ion sources, Nucl. Instrum. Methods Phys. Res. 94 (3) (1994) 297–305. http://dx.doi.org/10.1016/0168-583X(94)95369-4.
[11] D. Mascali, A New Approach to the Study of the ECR Heating and Particle Dynamics in the Plasma of Electron Cyclotron Resonance ion Sources (Ph.D. thesis), Università Degli Studi Di Catania, 2008.
[12] V.V. Mironov, J. Beijers, Three-dimensional simulations of ion dynamics in the plasma of an electron cyclotron resonance ion source, Phys. Rev. Spec. Top.-Accel. Beams 12 (7) (2009). http://dx.doi.org/10.1103/PhysRevSTAB.12.073501. 073501-1 to 073501-10.
[13] G. Shirkov, T. Nakagawa, Numerical simulation of highly charged ion production in riken 18 ghz electron cyclotron resonance ion source, Rev. Sci. Instrum. 69 (2) (2009) 1141–1143. http://dx.doi.org/10.1063/1.1148649.
[14] Kobra3d-inp, inp, URL www.inp-dme.com.
[15] D. Edgell, J. Kim, I. Bogatu, R. Vondrasek, Modelling of electron cyclotron resonance ion source plasmas, in: Proceedings of the Particle Accelerator Conference, 2001, pp. 2135–2137.
[16] K. Bernhardi, K. Wiesemann, X-ray bremsstrahlung measurements on an ecr-discharge in a magnetic mirror, Plasma Phys. 24 (8) (1982) 867–884. http://dx.doi.org/10.1088/0032-1028/24/8/001.
[17] R. Friedlein, G. Zschornack, Angle dispersive de-convolution of bremsstrahlung spectra from plasma, Nucl. Instrum. Methods Phys. Res. A 349 (2–3) (1994) 554–557. http://dx.doi.org/10.1016/0168-9002(94)91226-2.
[18] M. Lamoreux, P. Charles, General deconvolution of thin-target and thick-target Bremsstrahlung spectra to determine electron energy distributions, Radiat. Phys. Chem. 75 (10) (2006) 1220–1231. http://dx.doi.org/10.1016/j.radphyschem.2006.06.006.
[19] K. Bernhardi, An improved deconvolution method for bremsstrahlung spectra from hot plasmas, Comput. Phys. Comm. 19 (1) (1980) 17–21. http://dx.doi.org/10.1016/0010-4655(80)90061-2.
[20] C. Barué, M. Lamoureux, P. Briand, A. Girard, G. Melin, Investigations of hot electrons in electron-cyclotron-resonance ion sources, J. Appl. Phys. 76 (5) (1994) 2662–2670. http://dx.doi.org/10.1063/1.357563.
[21] H. van Regemorter, Rate of collisional excitation in stellar atmospheres, Astrophys. J. 136 (1962) 906–915. http://dx.doi.org/10.1086/147445.
[22] D. Sampson, H. Zhang, Use of the van regemorter formula for collision strengths or cross sections, Phys. Rev. A 45 (1992) 1556–1560.
[23] V. Fisher, et al., Electron-impact excitation cross section of hydrogenlike ions, Phys. Rev. A 55 (1) (1997) 329–334. http://dx.doi.org/10.1103/PhysRevA.55.329.
[24] W. Lotz, Electron-impact ionization cross-sections and ionization rate coefficients for atoms and ions from hydrogen to calcium, Z. Phys. 216 (3) (1968) 241–247. http://dx.doi.org/10.1007/BF01392963.
[25] G. Shirkov, C. Mühle, G. Musiol, C. Zschornack, Ionization and charge dispersion in electron cyclotron resonance ion sources, Nucl. Instrum. Methods Phys. Res. A 302 (1) (1991) 1–5. http://dx.doi.org/10.1016/0168-9002(91)90485-9.
[26] G. Douysset, H. Khodja, A.G.J. Briand, Highly charged ion densities and ion confinement properties in an electron-cyclotron-resonance ion source, Phys. Rev. E 61 (3) (2000) 3015–3022. http://dx.doi.org/10.1103/PhysRevE.61.3015.
[27] G. Zschornack, Handbook of X-ray Data, second ed., Springer, Berlin, 2007.
[28] C. Barkla, X-rays and the theory of radiation, J. Röntgen Soc. 14 (55) (1918) 73. http://dx.doi.org/10.1259/jrs.1918.0039.
[29] Alfred Müller, Reinhard Frode, L-Shell Contributions to Multiple Ionization of Ar^{i+} Ion ($i = 1, 2, 3$) by Electron Impact, Phys. Rev. 44 (1980) 29.
[30] A. Müller, R. Frode, Scaling of cross sections for multiple electron transfer to highly charged ions colliding with atoms and molecules, Phys. Lett. 59 (1976) 19.
[31] R. Thomae, et al., Beam experiments with the Grenoble test electron cyclotron resonance ion source at ithemba labs, Rev. Sci. Instrum. 87 (2) (2016) 623–625. http://dx.doi.org/10.1063/1.4935630.
[32] J. Komppula, O. Tarvainen, T. Kalvas, H. Koivisto, R. Kronholm, J. Laulainen, J.J. Myllyrperkiö, Vuv irradiance measurement of a 2.45 ghz microwave-driven hydrogen discharge, J. Phys. D: Appl. Phys. 48 (36) (2015) 1–12. http://dx.doi.org/10.1088/0022-3727/48/36/365201.
[33] X-ray attenuation and absorption calculator, [cited 31 December 2016]. URL http://web-docs.gsi.de.
[34] ROOT: An object-orientated data analysis framework, [cited 15 March 2011]. URL http://root.cern.ch/drupal/.
[35] M. Morhac, Multidimensional peak searching algorithm for low-statistics nuclear spectra, Nucl. Instrum. Methods A 581 (2007) 821–830.
[36] C. Ryan, E. Clayton, W. Criffin, S.H., S.H. Sie, D. Cousens, A statistics-sensitive background treatment for the quantitative analysis of pixe spectra in geoscience applications, Nucl. Instrum. Methods B 34 (1998) 396.
[37] G. Melin, et al., Some particular aspects of the physics of ecr sources for multiplicharged ions, Rev. Sci. Instrum. 61 (1) (1990) 236–238. http://dx.doi.org/10.1063/1.1141305.
[38] J. Noland, O. Tarvainen, Benitez, D. Leitner, C. Lyneis, Verboncoeur, Studies of electron heating on a 6.4 GHz ECR ion source through measurement of diamagnetic current and plasma bremsstrahlung, Plasma Sources. Sci. Technol. 20 (3) (2011) 1–11. http://dx.doi.org/10.1088/0963-0252/20/3/035022.
[39] O. Tarvainen, Studies of Electron Cyclotron Resonance Ion Source Plasma Physics (Ph.D dissertation), University of Jyväskylä, 2005.
[40] A. Girard, C. Pernot, G. Melin, J. Lécot, Modeling of electron-cyclotron resonance-heated plasma, Phys. Rev. E 62 (1) (2000) 1182–1189. http://dx.doi.org/10.1103/PhysRevE.62.1182.
[41] O. Tarvainen, J. Laulainen, J. Komppula, R. Kronholm, T. Kalvas, H. Koivisto, I. Izovtov, D. Mansfeld, V. Skalyga, Limitations of electron cyclotron resonance ion source performance set by kinetic plasma instabilities, Rev. Sci. Instrum. 86 (2) (2015) 1–9. http://dx.doi.org/10.1063/1.4906804.
[42] T. Ropponen, O. Tarvainen, P. Jones, P. Peura, T. Kalvas, P. Suominen, H. Koivisto, J. Ärje, The effects of magnetic field strength on the time evolution of high energy bremsstrahlung radiation created by an electron cyclotron resonance ion source, Nucl. Instrum. Methods Phys. Res. A 600 (3) (2009) 525–533. http://dx.doi.org/10.1016/j.nima.2008.12.065.
[43] O. Tarvainen, P. Suominen, H. Koivisto, A new plasma potential measurement instrument for plasma ion sources, Rev. Sci. Instrum. 75 (10) (2004) 3138–3145. http://dx.doi.org/10.1063/1.1790559.
[44] A. Drentje, U. Wolters, A. Nadzeyka, D. Meyer, K. Wiesemann, Simon short circuit effect in ecris, Rev. Sci. Instrum. 73 (2) (2002) 623–625. http://dx.doi.org/10.1063/1.1429315.

PII

INVESTIGATION INTO THE GAS MIXING EFFECT IN ECRIS PLASMA USING Kα AND OPTICAL DIAGNOSTICS

by

Muneer Sakildien, Olli Tarvainen, Taneli Kalvas, Hannu Koivisto, Risto Kronholm, Rainer Thomae, Joele Mira, Fhumulani Nemulodi and Pete Jones

Accepted for publication in AIP Conference Proceedings (2018)

Investigation into the gas mixing effect in ECRIS plasma using Kα and optical diagnostics

Muneer Sakildien[1,3,a)], Olli Tarvainen[3], Taneli Kalvas[3], Hannu Koivisto[3], Risto Kronholm[3], Rainer Thomae[1], Joele Mira[1], Fhumulani Nemulodi[1] and Pete Jones[2]

[1]*Accelerator and Engineering Department, iThemba LABS, P.O. Box 722, Somerset West, 7131, South Africa.*
[2]*Department of Subatomic Physics, iThemba LABS, P.O. Box 722, Somerset West, 7131, South Africa.*
[3]*Department of Physics, University of Jyväskylä, Jyväskylä 40500, Finland.*

[a)]Corresponding author: muneer@tlabs.ac.za

Abstract. Mixing a lighter gas species into the plasma of an ECRIS is known to enhance high charge state production of the heavier gas species. With this investigation, Kα diagnostics, optical emission spectroscopy and the measured charge state distribution of the extracted beam were combined to shed more light on the physics governing this phenomenon. Kα diagnostics data from two ion sources, the JYFL 14 GHz ECRIS and the GTS at iThemba LABS, are presented to gain confidence on the observed trends. The results seem to favor ion cooling as the most likely mechanism responsible for the favorable influence of the gas mixing.

INTRODUCTION

Adding a lighter mixing gas into the plasma of an Electron Cyclotron Resonance Ion Source (ECRIS) is known to enhance the highly charged ion (HCI) production of the heavier component, especially with of the mixture ratio [1]. Various explanations have been proposed for the beneficial effect. It has been suggested that the average charge state in the plasma is reduced, which increases the energy lifetime of the ions finally resulting to enhanced ion confinement and increased HCI production of the heavier minority species [2]. Another, perhaps the prevailing, explanation is attributed to ion cooling, resulting from the collisional interaction between the two gas species, with the lighter ions being heated and the heavier ones being cooled, thus increasing the confinement time of the latter [3]. Other explanations credit the increase in electron density and ionization efficiency of the heavier gas resulting in increased HCI production [4]. Yet another proposed explanation is the improvement of the plasma stability [5]. To develop the current understanding of the underlying physics of the gas mixing, Kα diagnostics, optical emission spectroscopy and the measured charge state distribution of the extracted beam were combined to study this phenomenon. The Kα emission rate Φ_R is proportional to the electron density, gas density (neutrals and ions) and the rate coefficient for inner shell ionization i.e. $\Phi_R \propto n_e n_{Ar} \langle \sigma_{ion} v_e \rangle$. The optical diagnostics were focused on probing the emission intensity of low charge states presumably playing a key role in gas mixing. Combining the results of the different diagnostics methods enables gauging different mechanisms listed above.

EXPERIMENTAL SETUP AND PROCEDURE

The experimental data have been obtained on two different ECR ion sources i.e. the JYFL 14 GHz ECRIS[6] and the 14.5 GHz Grenoble Test Source (GTS)[7] at iThemba LABS. With both sources a silicon drift detector was mounted in one of the vacuum chamber ports of the bending magnet, to view the axially emitted Kα radiation. In order to minimize the contribution from wall bremsstrahlung, the emitted x-ray flux was collimated, by a ϕ =900 μm / ϕ =500 μm (JYFL / iThemba LABS), 20 mm long lead channel placed in front of the detector. The optical emission data was only measured on the JYFL 14 GHz ECRIS using a high throughput Fastie-Ebert monochromator coupled with a photomultiplier tube detector with a phase-sensitive lock-in detection setup, connected to the radial port of the ion source through an optical fiber. The beam currents were also recorded, simultaneously with the x-ray and the

optical emission spectra. At JYFL the m/q range was limited to ≤ 8 with 10 kV extraction voltage and at iThemba LABS the transport efficiency of the extracted beams was limited. In both cases argon was used as working gas. In the measurements performed on the JYFL 14 GHz ECRIS, helium, neon and krypton were used as mixing gases. With the GTS, data were taken additionally with oxygen and xenon. To gain information on the behavior of the low charge state ions, the optical emission from the transition $3s^2 3p^4(^3P)4p\ ^4D^\circ_{5/2} \rightarrow 3s^2 3p^4(^3P)4s\ ^4P^\circ_{3/2}$ of Ar^{1+} was measured. This transition has an observed wavelength of 442.60008 nm. From results presented earlier, it has been shown that the optical emission of a particular charge state correlates very well with the extracted ion beam current of that charge state implying that the optical emission signal is directly proportional to the density of the given charge state in the core plasma.

In the experiments presented here the flow rate of the working gas (Ar) was kept constant while the flow rate of the mixing gas was varied without optimizing the mixture ratio for any particular charge state. As the response of the pressure gauge strongly depends on the gas composition, and the actual neutral gas pressure in the plasma chamber is unknown due to complex arrangement of the vacuum pumps, the results in the following section will be presented as a function of the valve setting of the mixing gas. This choice is further supported by the fact that both, the bias disc current and the source drain current, were not observed to follow the gas flow rate monotonically which invalidates them from being a measure of the neutral gas pressure. On the contrary, relating the total pressure measured by the ionization gauge of the 14 GHz JYFL ECRIS, to the valve setting, it was found that the behavior is well described by a quadratic function.

RESULTS AND DISCUSSION

Fig. 1 shows the normalized Ar Kα emission rates measured on the two ECR ion sources as a function of mixing gas valve setting (flow rate). The normalized Ar Kα emission rate was obtained by removing the continuum bremsstrahlung background spectrum from the raw measured spectrum, fitting a Gaussian distribution over the Ar Kα line, integrating over the area of the fit and averaging over the measurement time interval to yield a count rate. The general trend observed from Fig. 1 is for the Kα emission rate of argon to increase with helium as a mixing gas and decrease with heavier mixing gases. Neon mixing gas produces different trends in the two sources, which remains unexplained. Given that the inner shell ionization rate and Kα emission rate depends on the electron density, argon density and rate coefficient, it is concluded that argon density decreases when the mass of the mixing gas exceeds that of argon. The increase of the Kα emission rate of argon with lighter mixing gases could be due to both the increasing electron density and argon density, the former resulting from increasing total gas density. This assessment is based on the assumption that the rate coefficient for inner shell ionization remains quasi-constant (supported by Ref. [8]) during the mixing gas sweep. Combining the results with heavier and lighter gases it is concluded that the most likely explanation fitting both observations is that the gas mixing affects the density of argon (at constant feed rate), thus favoring the ion cooling explanation. The result also underlines the fact that the diagnostics of the lighter gas could reveal more about the physics of the gas mixing than looking at the heavier gas component in isolation.

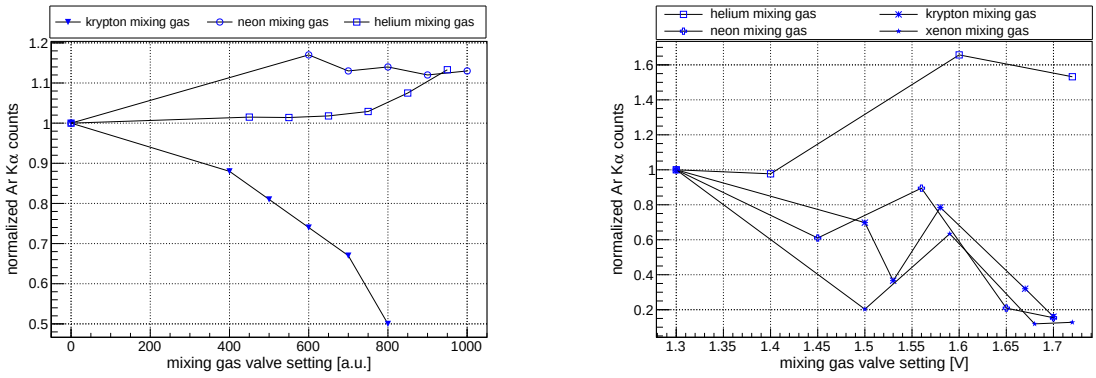

FIGURE 1: Normalized Ar Kα emission / inner shell ionization rates as a function of the mixing gas flow for the 14 GHz ECRIS at JYFL (left) and the GTS at iThemba LABS (right).

The results of the extracted current and the optical emission measurements showed that the inner shell ionization

rate and the optical emission intensity of the highest charge states, e.g. Ar^{13+} do not correlate very well. Nevertheless, it was observed that the optical data and beam currents have a better correlation in the case of the highest charge states. Since the inner shell ionization depends on the total argon density, it is reflecting the behavior of the whole population while the optical emission and beam current probe only the specific charge state in question. As an indicator of HCI production the Ar^{9+} beam current is used as this is the first ion produced with an electron removed from the L-shell resulting in a significant increase of the ionization potential in comparison to lower charge states. Furthermore, Ar^{9+} does not suffer from charge exchange reactions as much as the highest charge states, which enables probing the gas mixing effect in a wider range of total pressures. Fig. 2 presents the normalized Ar^{9+} beam current and the normalized Ar^{1+} optical emission, as a function of mixing gas flow rate. Ar^{1+} optical emission is used here as Ar^{1+} beam current can not be measured due to limitation of the bending magnet in the transfer beamline at JYFL. The result clearly demonstrates that the HCI production is accompanied by a modification in the density of the low charge state ions indicated by the decrease/increase of the optical emission signal with lighter/heavier mixing gas, respectively. The results of this investigation demonstrate a strong mass dependence, especially when a heavier gas is introduced into the plasma. This suggest that lowering of the average charge state and ion cooling are the key mechanisms responsible for the effectiveness of the gas mixing. Given that the ionization potential is lower for heavier gases, the increase in plasma density explaining the gas mixing effect can presumably be excluded.

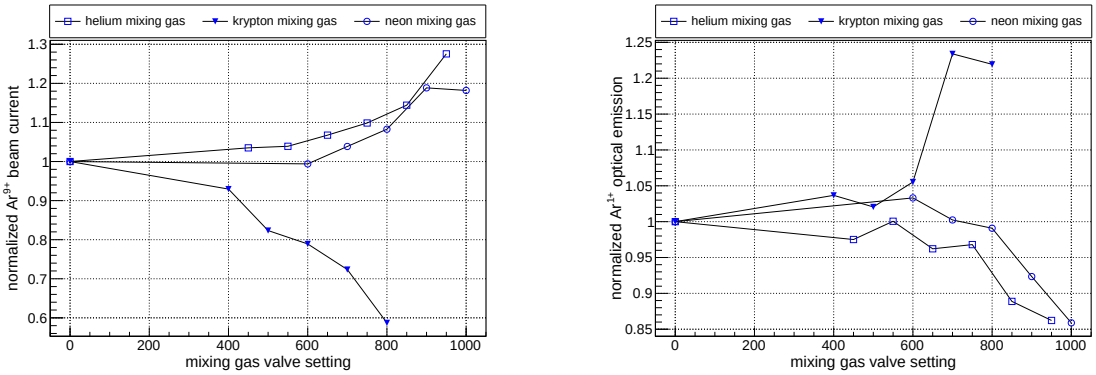

FIGURE 2: Normalized Ar^{9+} beam current (left) and the normalized Ar^{1+} optical emission (right) as a function of mixing gas flow.

ACKNOWLEDGMENTS

This work was supported by the Academy of Finland under the Finnish Centre of Excellence Programme 2012-2017 (Project No. 213503, Nuclear and Accelerator-Based Physics Research at JYFL). The work is also based on the research supported in part by iThemba LABS and the National Research Foundation of South Africa (Grant Reference No.: 109887 and 110072). The first author would also like to acknowledge the Department of Physics at the University of Stellenbosch for the loan of their x-ray detector.

REFERENCES

[1] A.G. Drentje and J. Sijbring *KVI Ann. Rep. 79*, (1983).
[2] R. Geller, *Electron Cyclotron Resonance Ion Sources and ECR Plasmas*, Institute of Physics, Bristol, 1996, ISBN 0 7503 0107 4
[3] T. Antaya, *Proc. Intl. Conference on ECR Ion Sources*, Grenoble, France, (1988).
[4] M. Delaunay, *Rev. Sci. Instrum. 63*, 2861 (1992).
[5] Z. Q. Xie and C. M. Lyneis, *Rev. Sci. Instrum. 65*, 2947 (1994).
[6] H. Koivisto, P. Heikkinen, V. Hänninen, A. Lassila, H. Leinonen, V. Nieminen, J. Pakarinen, K. Ranttila, J. Ärje and E. Liukkonen, *Nucl. Instrum. Meth. Phys. Res. B **174** (3)*, (2001) 379-384.
[7] D. Hitz, D. Cormer, J. Mathonnet, *Proc. of EPAC* 1718 (2002).
[8] A.M. Costa, M.C. Martins, F. Parente, *At. Data Nucl. Data Tables*, 79 (2001).

PIII

STUDYING THE DOUBLE-FREQUENCY HEATING MODE IN ECRIS PLASMA USING Kα DIAGNOSTICS

by

Muneer Sakildien, Olli Tarvainen, Risto Kronholm, Taneli Kalvas, Pete Jones and Hannu Koivisto

Accepted for publication in AIP Conference Proceedings (2018)

Studying the double-frequency heating mode in ECRIS plasma using Kα diagnostics

Muneer Sakildien[1,3,a)], Olli Tarvainen[3], Risto Kronholm[3], Taneli Kalvas[3], Pete Jones[2] and Hannu Koivisto[3]

[1]*Accelerator and Engineering Department, iThemba LABS, P.O. Box 722, Somerset West, 7131, South Africa.*
[2]*Subatomic Physics Department, iThemba LABS, P.O. Box 722, Somerset West, 7131, South Africa.*
[3]*Department of Physics, University of Jyväskylä, Jyväskylä 40500, Finland.*

[a)]Corresponding author: muneer@tlabs.ac.za

Abstract. Despite the success of double-heating frequency in enhancing high charge state production, the underlying physics remains poorly understood. By combining three different diagnostic techniques i.e. Kα emission, optical emission and the extracted charge state distribution, it is now possible to assess the proposed explanations for the effectiveness of double-frequency heating against the experimental results. These results seem to indicate that the increase of plasma density accounts largely for the favorable behavior of this operation mode compared to single-frequency mode.

INTRODUCTION

Heating the plasma of an Electron Cyclotron Resonance Ion Source (ECRIS) with multiple frequencies, as opposed to a single frequency, enhances the extracted ion beam current of high charge states [1]. Despite numerous investigations into multiple frequency heating, the exact reason for its favorable influence remains poorly understood. Some plausible explanations for its effectiveness include increasing the plasma density, improving plasma stability and modifying the plasma potential structure [2]. All these proposed explanations appear to be linked to a modification of the electron density and energy distribution resulting to an increase in the ionization rate and ion confinement time.

To gain understanding on the impact of double-frequency heating on high charge state production, the axially emitted characteristic Kα emission from the argon plasma of an ECRIS was measured, in conjunction with radial optical light emission ($2s^2 2p^2\ P^\circ_{3/2} \longrightarrow 2s^2 2p^2\ P^\circ_{1/2}$ for Ar^{13+} and $2s^2 2p^5\ P^\circ_{1/2} \longrightarrow 2s^2 2p^5\ P^\circ_{3/2}$ for Ar^{9+}) from ions, as well as their beam currents. The measured Kα emission rate is proportional to the electron density, argon density (neutrals and ions) and the rate coefficient for inner shell ionization. The Kα emission allows us to assess the relative influence of the electron density and rate coefficient on high charge state production, thus enabling us to gauge the different mechanisms proposed to explain the favorable effect of double-frequency heating against the Kα diagnostics supported by the optical emission data and beam currents. Furthermore, the Kα emission rate of argon was compared to the Kα emission rate of iron originating from the stainless steel biased disc, which enables probing the effect of double-frequency heating on electron confinement and losses.

EXPERIMENTAL SETUP AND PROCEDURE

The experimental setup used for this work has been extensively described previously [3] and only the main features will be mentioned here. To measure the Kα emission, the JYFL 14 GHz ECRIS [4] was utilized. This ECRIS, which is equipped with a klystron and a traveling wave tube amplifier (TWTA), was operated in double-frequency heating mode with the TWTA frequency varied between 11.100 GHz and 12.450 GHz and the klystron frequency fixed at 14.056 GHz. The x-ray detector used to measure the Kα emission was positioned to view the plasma volume and biased disc surface through a port on the vacuum chamber of the 90 degree bending magnet 2.6 m downstream in

the beamline. A ϕ = 0.90 mm collimator was installed in front of the detector to limit the solid angle, thus observing emission (mostly) from the plasma volume and thick target radiation from the biased disc.

The source was first operated in single-frequency mode. The Kα emission rate was measured at three microwave powers, with the frequency delivered from the TWTA varied at each of them. This allowed for probing the effect of the plasma heating frequency on the diagnostics signals. The axial magnetic field profile was scaled to maintain a constant injection mirror ratio $R_{\mathrm{inj}} = B_{\mathrm{inj}}/B_{\mathrm{ecr}} = 3.87$ at the different heating frequencies. Finally, the source was operated in double-frequency mode varying the power ratio of the klystron and the TWTA at constant total power. The source was optimized separately for Ar^{9+} and Ar^{13+} and the emission rates of the Kα and optical transitions of the afore-mentioned ions were recorded.

RESULTS AND DISCUSSION

An example of the results, namely the Ar and Fe Kα emission rates and their ratios (r), obtained in single frequency operation mode with 150 W power (< 2 W reflected) and constant injection mirror ratio is presented in Table 1. The table also lists the volumetric emission rate of Ar Kα, averaged over the plasma volume visible to the x-ray detector, and the corresponding beam current of Ar^{9+}. It is evident that both, the inner shell ionization rate of argon (indicated by the Kα count rate) and extracted beam current of Ar^{9+} (first charge state with empty M-shell) increase with the microwave frequency. The frequency trend of the inner shell ionization rate can most likely be explained by the electron density increasing with the frequency, which also favors the high charge state ion beam production. Simultaneously it was observed that the Fe-to-Ar Kα ratio (r) displays the opposite frequency trend. Here r can be used as an indication of the warm electron losses towards the biased disc (at the energies close to Kα). The result leads us to conclude that the electron losses of the afore-mentioned population toward the bias disk are not determined exclusively by the mirror ratio R_{inj}, which is often used to describe the magnetic field of ECRISs [5].

TABLE 1: Ar and Fe Kα counts, Fe-to-Ar Kα ratio (r) and extracted Ar^{9+} beam current as a function of the microwave frequency at constant 150 W power and $R_{\mathrm{inj}} = 3.87$. The volumetric rate is calculated for the plasma volume visible to the x-ray detector.

Frequency [GHz]	**Ar Kα counts [cps]**	**Fe Kα counts [cps]**	**Fe-to-Ar Kα-ratio (r)**	**Ar Kα volumetric rate [counts/ cm^3]**	**Ar^{9+} current [μA]**
11.100	110	720	6.4	9.9×10^9	17
11.560	200	1010	5.1	1.7×10^{10}	35
12.450	290	860	2.9	2.6×10^{10}	50
14.056	600	160	0.3	5.2×10^{10}	81

When comparing the single and double-frequency operation modes at constant total powers, i.e. 520 W (Ar^{13+} tune) or 320 W (Ar^{9+} tune) delivered from the klystron (14.05 GHz) and another 10 – 100 W from either the klystron or the TWTA (11.56 GHz), it was observed that the additional frequency only becomes effective if the source is tuned for high charge state production i.e. Ar^{13+} as opposed to Ar^{9+}. This is evident from the Kα emission, as well as the light emission signals of the given charge states and their extracted beam currents shown in Fig. 1. Furthermore, it is observed that the Fe-to-Ar Kα ratio decreases with added power in double-frequency mode with the source tuned for Ar^{13+} indicating that the relative electron losses towards the biased disc decrease in that case. With the source tuned for Ar^{9+} these trends revealing a clear difference between the single and double frequency heating modes are not visible as shown in Fig. 2. This strengthens the argument that the secondary frequency only becomes effective with the source tuned for high charge state production as discussed e.g. in Ref. [2].

Assessing the proposed explanations put forward for the effectiveness of double-heating frequency, the measured results seems to suggest that the increase in plasma density in comparison to single frequency operation accounts for the effect. Judging by the trends of the Fe-to-Ar Kα emission ratios (see Fig. 1), it seems clear that, in relative terms, less electrons are expelled from the magnetic confinement system if the source is operated in double-frequency mode. This appears to indicate that the division of the power between two frequencies, i.e. power deposition on two concentric resonance zones instead of one, affects the RF pitch angle scattering rate [6] and/or improves the stability of the plasma [7]. However, the detector used for this investigation is not able to measure quick bursts of bremsstrahlung,

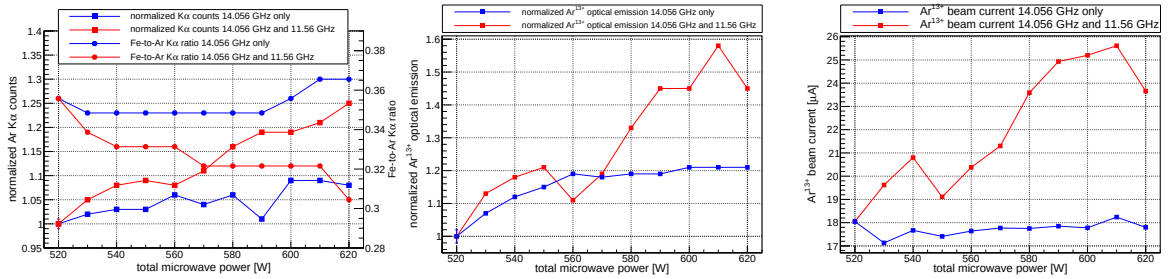

FIGURE 1: Normalized Ar Kα counts and the Fe-to-Ar Kα ratio (left), normalized optical emission for $2s^2 2p^2\ P^{\circ}_{3/2} \longrightarrow 2s^2 2p^2\ P^{\circ}_{1/2}$ transition of Ar^{13+} (middle) and the Ar^{13+} beam current (right), with the source optimized for Ar^{13+}.

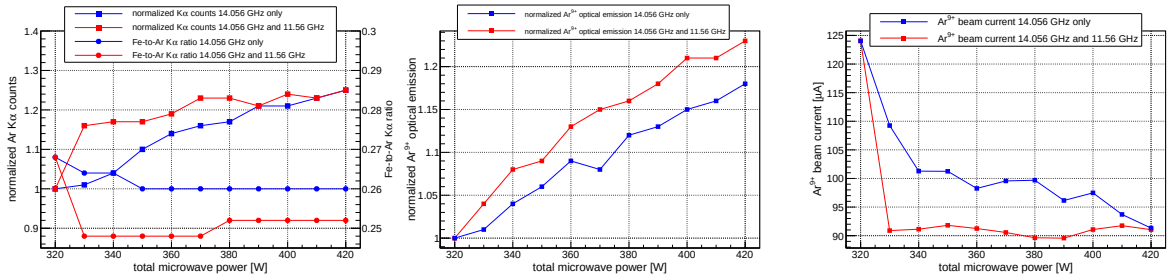

FIGURE 2: Normalized Ar Kα counts and the Fe-to-Ar Kα ratio (left), normalized optical emission for $2s^2 2p^5\ P^{\circ}_{1/2} \longrightarrow 2s^2 2p^5\ P^{\circ}_{3/2}$ transition of Ar^{9+} (middle) and the Ar^{9+} beam current (right), with the source optimized for Ar^{9+}.

as expected when the plasma experiences kinetic instabilities [8]. We can therefore not make any definitive statements concerning the stability of the plasma.

ACKNOWLEDGMENTS

This work was supported by the Academy of Finland under the Finnish Centre of Excellence Programme 2012-2017 (Project No. 213503, Nuclear and Accelerator-Based Physics Research at JYFL). The work is also based on the research supported in part by iThemba LABS and the National Research Foundation of South Africa (Grant Reference No.: 109887 and 110072). The first author would also like to acknowledge the Department of Physics at the University of Stellenbosch for the loan of their x-ray detector.

REFERENCES

[1] Z. Q. Xie and C. M. Lyneis *Proc. 12th Intl. Workshop on ECR Ion Sources*, Riken, Japan, (1995).
[2] R.C. Vondrasek, R. Scott and R.C. Pardo *Rev. Sci. Instrum.* ***77****, 03A337*, (2006).
[3] M. Sakildien, R Kronholm, O Tarvainen, T Kalvas, P Jones, R Thomae and H Koivisto, "Inner shell ionization of argon in ECRIS plasma", submitted to Nucl. Instrum. Meth. Phys. Res. A, (2017).
[4] H. Koivisto, P. Heikkinen, V. Hänninen, A. Lassila, H. Leinonen, V. Nieminen, J. Pakarinen, K. Ranttila, J. Ärje and E. Liukkonen, *Nucl. Instrum. Meth. Phys. Res. B* ***174*** *(3)*, (2001) 379-384.
[5] R. Geller, *Annu. Rev. Nucl. Part. Sci.* ***40***, (1990) 1543.
[6] B.P. Cluggish, L. Zhao and J.-S. Kim, *Nucl. Instrum. Meth. Phys. Res. A* ***631***, (2011).
[7] V. Skalyga, I. Izotov, T. Kalvas, H. Koivisto, J. Komppula, R. Kronholm, J. Laulainen, D. Mansfeld and O. Tarvainen, *Phys. Plasmas* ***22****, 083509*, (2015).
[8] O. Tarvainen, I. Izotov, D. Mansfeld, V. Skalyga, S. Golubev, T. Kalvas, H. Koivisto, J. Komppula, R. Kronholm, J. Laulainen and V. Toivanen, *Plasma Sources Sci. Technol. 23, 025020*, (2014).

PIV

EXPERIMENTAL EVIDENCE ON MICROWAVE INDUCED ELECTRON LOSSES FROM ECRIS PLASMA

by

Muneer Sakildien, Olli Tarvainen, Risto Kronholm, Ivan Izotov, Vadim Skalyga, Taneli Kalvas, Pete Jones and Hannu Koivisto

Physics of Plasmas **25**, 062502 (2018)

Experimental evidence on microwave induced electron losses from ECRIS plasma

M. Sakildien,[1,a)] O. Tarvainen,[2] R. Kronholm,[2] I. Izotov,[3] V. Skalyga,[3] T. Kalvas,[2] P. Jones,[4] and H. Koivisto[2]

[1]*Accelerator Department, iThemba LABS (Laboratory for Accelerator Based Sciences), PO Box 722, Somerset West 7192, South Africa*
[2]*Department of Physics, University of Jyväskylä, 40500 Jyväskylä, Finland*
[3]*Institute of Applied Physics, RAS, 46 Ul'yanova st., 603950 Nizhny Novgorod, Russian Federation*
[4]*Subatomic Physics Department, iThemba LABS (Laboratory for Accelerator Based Sciences), PO Box 722, Somerset West 7192, South Africa*

(Received 14 March 2018; accepted 18 May 2018; published online 5 June 2018)

The balance between warm and hot (>1 keV) electron density and their losses from the magnetic confinement system of an Electron Cyclotron Resonance Ion Source (ECRIS) plasma is considered to be one of the main factors determining the rate of the high charge state ion production. One of the key loss channels for heated electrons is thought to be induced by the injected microwaves. While this loss mechanism, referred to as rf-induced pitch angle scattering, has been studied theoretically and with computational tools, direct experimental evidence of its significance in minimum-B ECRIS plasmas remains limited. In this work, experimental evidence of microwave induced electron losses in the axial direction is presented in both continuous wave (CW) and pulsed operation of a 14 GHz ECRIS. In the CW mode, the experiment was carried out by comparing the characteristic X-ray emission from the plasma volume and from the surface of the biased disc located in the flux of the escaping electron at the axial magnetic mirror. Parametric sweeps of magnetic field, neutral gas pressure, and microwave power were conducted to determine their effect on electron losses. In the pulsed mode, the experiment was conducted by measuring the flux of escaping electrons through aluminum foils of different thicknesses providing some energy resolution. Both diagnostics support the view that rf-induced losses account for up to 70% of total hot electron losses and their importance depends on the source parameters, especially power and neutral gas pressure. *Published by AIP Publishing.* https://doi.org/10.1063/1.5029443

I. INTRODUCTION

The extractable charge state distribution (CSD) of ions from an Electron Cyclotron Resonance Ion Source (ECRIS),[1] as well as the plasma energy confinement time, is strongly dependent on the density of the different electron populations (see Barué *et al.*[2] and Shirkov[3]) present inside the ECRIS plasma.[4] The number of warm and hot electrons lost from the magnetic confinement system of an ECRIS is therefore a critical parameter affecting the volumetric production rate of high charge state ions. Additionally, the warm and hot electrons are thought to play a crucial role in the build-up of an electrostatic potential which is suggested to regulate ion confinement via a small potential dip in the core of the plasma. This confinement scheme, extensively discussed by Petty *et al.*,[5] enables ions to remain in the plasma for a sufficiently long time in order to reach the desired charge state through step-wise electron impact ionization.

Some of the first theoretical studies on electron cyclotron resonance heating (ECRH) in magnetic mirror devices were published in the 1970s,[6] with the relativistic theory of ECRH developed later.[7] In the 1980s, Mauel performed experimental measurements on ECRH of a highly ionized plasma in a pulsed magnetic mirror configuration.[8] The results obtained in this study demonstrated that the fractional densities of the warm and hot electron populations depend on the absorbed microwave power. The experiment revealed an enhanced electron end-loss current associated with the increase in microwave power and consequently it was concluded that the electromagnetic (EM)-field of the incident microwaves could enhance electron losses. Moreover, an investigation of helium plasma diamagnetism and electron end losses conducted by Perret *et al.*[4] suggested that the warm and hot electron losses from the magnetic confinement system of an ECRIS plasma can under certain conditions exceed those accounted for by Coulomb collisions only. This led to the suggestion of enhanced electron losses induced by the EM-field of the incident microwave power affecting the performance of modern ECR ion sources. The role of microwave induced pitch angle scattering in ECRIS was recently discussed for e.g., by Noland *et al.* comparing the emission power from the plasma bremsstrahlung to the wall bremsstrahlung[9] and by Cluggish *et al.* conducting a computational study on the topic.[10]

Although the concept of radiofrequency (rf)-induced pitch angle scattering is well-established, direct and systematic experimental evidence on its role in ECRIS plasmas is scarce. With the current investigation, three complementary plasma diagnostic methods are combined to study electron

a)Electronic mail: muneer@tlabs.ac.za

losses from the minimum-B confinement system of an ECRIS. The diagnostics study different electron populations of the electron energy distribution function (EEDF) allowing for a more complete understanding of the physics governing electron losses. For the first part of the investigation, Kα diagnostics obtained in the continuous wave (CW) mode are used to estimate the relative electron losses from the magnetic confinement system. The electron losses are estimated from the ratio of the thick target Kα (iron) emission from the axial wall of the plasma confinement vessel to the Kα emission of the confined ion species (argon). The measurement of this ratio as a function of the ion source parameters probes the electron loss rate against the inner shell ionization rate, which is affected by mostly the warm electron density, and thus can be used for identifying electron loss mechanisms in action. With the second part of the investigation, bremsstrahlung diagnostics and electron end-loss current are measured in pulsed mode operation. This allows a comparison of the electron losses between microwave power on and off periods and sheds new light on the influence of the plasma parameters on electron losses. The electron end-loss current is measured through different attenuators (aluminium foils) enabling a study of the electron losses as a function of electron energy with discrete steps. Altogether, the investigation demonstrates the feasibility of the Kα-diagnostics for probing the role of microwave induced electron losses in CW mode while the pulsed experiments provide direct evidence of such losses in ECRIS plasmas.

II. THEORETICAL BACKGROUND

A. Electron loss processes

The electrons inside an ECRIS are confined by a complex magnetic field. This magnetic field consists of a solenoid mirror field, for axial confinement, combined with a multipole field, for radial confinement, forming the so-called minimum-B field and magnetic bottle.[1] In the absence of collisions and interaction with electromagnetic waves, the confinement of an electron depends only on its parallel $(v_\parallel)$ and perpendicular $(v_\perp)$ velocity components defining the electron loss cone in velocity space.[1] Upon entering the loss cone, the electrons experience a force as a result of the gradient and curvature of the magnetic field and will leak out of the magnetic bottle as thoroughly discussed by Thuillier *et al.*[11] From the analysis performed, it appears that the electron losses through the weakest mirrors occur faster in comparison to the characteristic time of the diffusion into the loss cone[11] i.e., the loss cone can be assumed to be empty. Contrary to the plasma electrons, high charge state ions are confined electrostatically[5,12] and their losses are due to electron losses i.e., ions follow the electrons owing to the ambipolar field.[13]

The (electron) loss cone can be populated by a number of processes, as thoroughly discussed in the literature,[10,14] including Coulomb collisions, inelastic collisions, microwave induced pitch angle scattering, and non-linear effects.[15] The most important loss channels in stable operating conditions of high-performance ECRISs are considered to be collisional and microwave induced losses, the latter being discussed and studied extensively in this paper. Additional loss mechanisms include synchrotron radiation losses[7] and radial diffusion losses[16] but their contributions on the total flux of escaping electrons are considered to be insignificant.[10]

B. Microwave induced electron losses from the ECRIS plasma

In ECR plasmas, the electrons interact with the EM-field of the microwaves mainly at a surface where the resonance condition given by

$$\omega_{rf} = \omega_{ce}(B) - k_\parallel v_\parallel \tag{1}$$

is fulfilled. Here, ω_{rf} is the microwave (angular) frequency, $k_\parallel$ is its parallel wave number, and $\omega_{ce}(B)$ is the relativistic electron gyrofrequency at magnetic field B. For the purpose of this study, it is sufficient to consider only the interaction between the circulating electrons and the right-hand circularly polarized wave (RHCP) component. Considering energy conservation in the frame moving with the wave, it can be shown that the electrons interacting with the RHCP wave, of phase velocity v_p, move in the velocity space along a circle defined by

$$v_\perp^2 + (v_\parallel - v_p)^2 = a^2, \tag{2}$$

where $v_\perp$ and $v_\parallel$ are the electron velocity components perpendicular and parallel to the external magnetic field, respectively, and a is a constant.[17] It is convenient to express this in a spherical polar coordinate system (v, ψ, ϕ) in the velocity space, where v is the electron speed, $\arccos\psi$ is the pitch angle, i.e., $\psi = \frac{v_\parallel}{v}$, and ϕ is the angle about the axial magnetic field.[4] The equation defining the loss cone then becomes

$$v^2 - 2v\psi v_p = b^2, \tag{3}$$

where b is yet another constant. Differentiating Eq. (3) yields the increments $(\Delta v, \Delta\psi)$ in velocity and pitch angle during the interaction, i.e.,

$$\Delta v\left(\frac{v}{v_p} - \psi\right) - v\Delta\psi = 0. \tag{4}$$

In order to understand microwave induced loss processes, we need to consider two cases defined by the phase difference between the electron gyromotion and the electric field of the microwaves i.e., (a) $\Delta v > 0$ and (b) $\Delta v < 0$, corresponding to acceleration or deceleration of electrons at the resonance, respectively.

1. Electron energy gain ($\Delta v > 0$): it follows from Eq. (4) that if $\left(\frac{v}{v_p} - \psi\right) < 0$, then $\Delta\psi < 0$, similarly if $\left(\frac{v}{v_p} - \psi\right) > 0$, then $\Delta\psi > 0$. We may rewrite this condition as $\frac{v}{v_p} \lessgtr \frac{v_\parallel}{v}$. It is evident from $v^2 = v_\parallel^2 + v_\perp^2$ that $\frac{v_\parallel}{v} \leqslant 1$ and hence the condition for microwave heating improving electron confinement (decrease of ψ) becomes $\frac{v}{v_p} < 1$ i.e., $v < v_p$. On the contrary, microwave heating induces electron losses (increase of ψ) if $\frac{v}{v_p} > 1$ i.e., $v > v_p$. Since

electrons with velocities above the phase velocity are mainly pitch-angle scattered, the maximum mean velocity of the electron distribution function is the phase velocity at the resonance.

2. Electron energy loss ($\Delta v < 0$): applying similar reasoning as above, it follows from Eq. (4) that $\Delta\psi \lessgtr 0$ when $v \gtrless v_p$ i.e., for electron velocities less than the phase velocity of the EM-wave, the electron confinement is weakened by the interaction between electrons and the microwave electric field in the decelerating phase. On the other hand, electrons whose velocity exceeds the phase velocity become better confined as a result of interacting with the magnetic field of the EM-wave despite their energy loss.

All of the interaction mechanisms identified above play a role in ECRIS plasmas. However, the improvement of the electron confinement due to pitch angle scattering (Δv, $\Delta\psi < 0$) during electron deceleration is of negligible importance since, as explained above, the electrons exit the plasma through the weakest mirror very fast.

Following Girard *et al.*, the mean velocity kick parallel $\Delta v_\parallel$ and perpendicular $\Delta v_\perp$ to the magnetic field in a single resonance crossing can be expressed as[18]

$$\Delta v_\parallel = \frac{eE}{m_e}\frac{v_\perp}{v_p}\sqrt{\frac{\pi}{\omega' v_\parallel}}, \tag{5}$$

$$\Delta v_\perp = \frac{eE}{m_e}\left(1 - \frac{v_\perp}{v_p}\right)\sqrt{\frac{\pi}{\omega' v_\parallel}}, \tag{6}$$

where $-e$ and m_e is the charge and mass (relativistic if necessary) of an electron, respectively, E is the microwave electric field amplitude at resonance, and ω' is the derivative of the local electron cyclotron angular frequency along the magnetic field B.

According to this formulation, the electron confinement is improved, i.e., $\frac{\Delta v_\parallel}{\Delta v_\perp} \leq 1$ when $v_p \geq 2v_\perp$. This results to a stochastic diffusion coefficient $D_{\mu\mu}$ in the pitch angle which can be defined as[14]

$$D_{\mu\mu} = \pi\left(\frac{eE}{2m_e}\right)^2 \frac{d}{L\omega}\left(\frac{v}{v_p}\right)^2 = D_{vv}\left(\frac{v}{v_p}\right)^2, \tag{7}$$

where d is the characteristic length for the magnetic field gradient, L is the characteristic plasma length, and ω is the microwave (angular) frequency. D_{vv} corresponds to the velocity diffusion coefficient. It is emphasized that the rf-induced pitch angle diffusion coefficient in Eq. (7) is less than the velocity diffusion coefficient if $v < v_p$ and increases quadratically with increasing ratio of the electron velocity to phase velocity. Furthermore, the diffusion coefficient is sensitive to the microwave electric field i.e., it can be expected that the rate of pitch angle scattering depends predominantly on the microwave power and plasma density (neutral gas pressure).

Estimating the phase velocity $v_p = \frac{\omega}{k}$, where k is the wave number, in ECRIS plasmas, is challenging due to the inhomogeneous plasma density and the existence of the electron cyclotron resonance, which affect the dispersion relation of the EM-wave through the local plasma permittivity. According to Stix,[16] the phase velocity can be expressed as

$$\frac{v_p}{c} = \frac{1}{\pi^{\frac{1}{6}}}\left(\frac{\omega}{\omega_{pe}}\right)^{\frac{2}{3}}\left(\frac{\langle v\rangle}{c}\right)^{\frac{1}{3}}, \tag{8}$$

where ω_{pe} is the plasma oscillation frequency, c is the velocity of light in vacuum, and $\langle v\rangle$ is the mean velocity of the (non-Maxwellian) electron distribution. The electron density in ECRIS plasmas is considered to be below the critical density at which $\omega = \omega_{pe}$, which implies that only >260 keV electrons satisfy the condition $v > v_p$ for pitch angle scattering. However, the given expression does not take into account the reduction of the phase velocity in the resonance, which is thoroughly discussed by Ropponen *et al.*[20] and Williamson *et al.*[21] The actual phase velocity at the resonance depends for e.g., on the plasma density and is reduced at least by an order of magnitude[20] from the maximum value given by Eq. (8), which implies that the warm and hot electron populations of ECRIS plasmas with energies on the order of 10–100 keV are affected by microwave induced pitch angle scattering. These considerations demonstrate that although, due to stochasticity, on average ECR-heating improves the electron confinement, microwave EM-fields also cause electrons to populate the loss cone throughout their energy distribution especially at high plasma densities which implies that the pitch angle scattering can limit the densities of the warm and hot electron populations.[4]

III. EXPERIMENTAL SETUP AND PROCEDURE

The experimental data described in this work were taken with the JYFL 14 GHz ECRIS, presented in Fig. 1 and described in detail by Koivisto *et al.*[22] The source has a plasma chamber length and a diameter of 28 cm and 7.8 cm, respectively, and uses an Nd-Fe-B permanent magnet sextupole arrangement and solenoid coils forming a minimum-B structure for plasma confinement. The magnetic confinement field provided by the solenoid coils and sextupole, results in typical magnetic field strengths at injection and extraction of 2.0 T and 0.9 T, respectively. The strength of the sextupole field on the wall of the plasma chamber is 1.09 T on the magnetic poles and 0.71 T in between them when the solenoids are not energized. The (typical) strength of the B-field and sextupole, as a function of axial and radial distance, respectively, is shown in the inset of Fig. 1. The plasma is sustained by 50–800 W of microwave power at 14.1 GHz. Typical operating neutral pressures are in the 10^{-7} mbar range.

The experimental setup used for the Kα diagnostic measurement campaign was thoroughly described by Sakildien *et al.*[23] and only the most important features are mentioned here. The axially emitted Kα X-rays are measured with a silicon drift detector (SDD) mounted in one of the ports of the vacuum chamber of the analyzing magnet [see Fig. 1(a)] providing a direct line-of-sight into the ECRIS plasma through the $\phi = 8$ mm extraction aperture. In an attempt to limit the measured spectrum to mostly observe the plasma volume and biased disc, a collimator structure (ϕ 900 μm) was installed in front of the entrance of the detector. A permanent

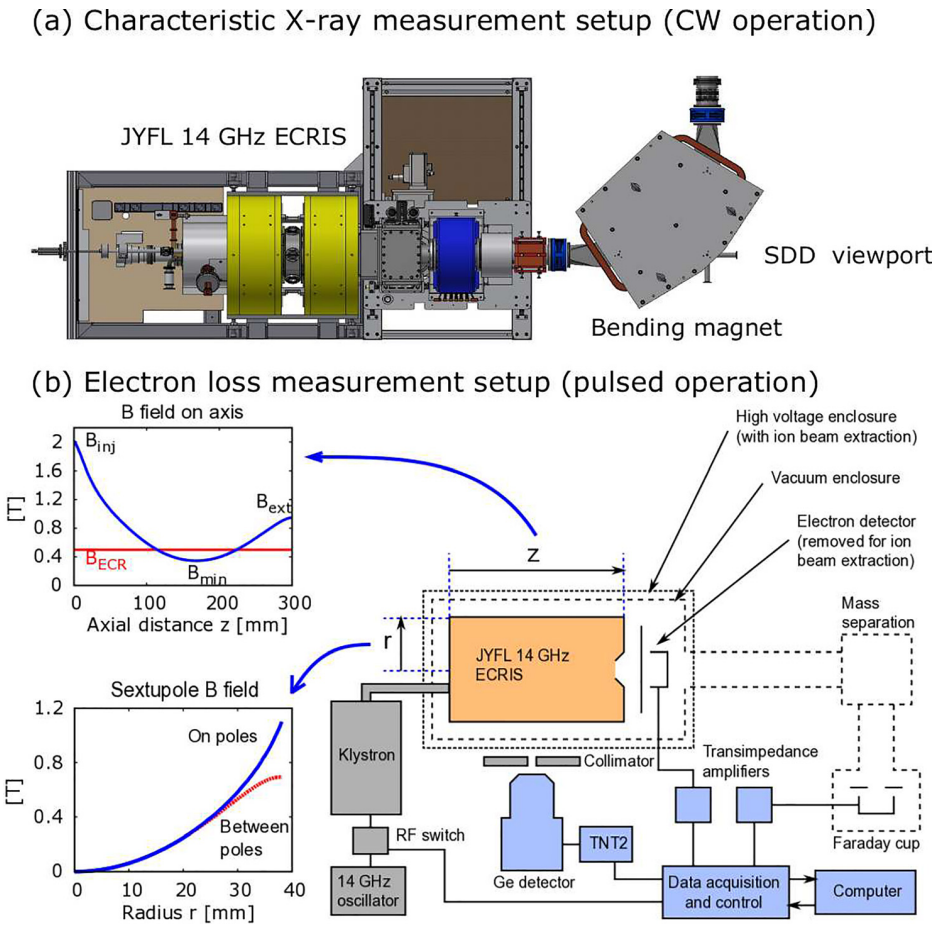

FIG. 1. Experimental setup used for measuring the relative electron losses in CW operation (a) and the setup used for measuring the escaping electrons in pulsed operation (b).

magnet filter was also included in the experimental setup to protect the detector against damage by charged particles in the event the analyzing magnet is not energized. The detector has an energy resolution of 120 eV at the Kα of Mn at 5.90 keV, which enables it to resolve many of the characteristic lines observed in a typical X-ray spectrum measured from the ECRIS plasma. To quantify the relative electron losses, the intensity of the Kα counts of the confined Ar ion species was compared to the intensity of the Kα counts of Fe. The latter signal results from warm and hot electrons escaping the magnetic confinement system and interacting with the stainless steel biased disc located at the tip of the iron plug at the injection side of the plasma chamber. The argon counts measured by the detector emanate from the plasma volume and therefore represents the confined warm and hot electrons. This assertion is based on the fact that argon, as a noble gas, does not accumulate on the walls of the plasma chamber and is therefore confined to the plasma volume. The density of iron sputtered from the biased disc in the plasma volume, on the other hand, is negligible. This claim is supported by the fact that the iron extracted beam intensity is below the detection threshold of the Faraday cup in the transfer beamline. The characteristic emission of iron is therefore dominated by thick target (characteristic) radiation from the surface of the biased disc and the count rate of Fe Kα is therefore proportional to the axial electron loss rate.

The schematic layout of the experimental setup used for measuring the electron losses in the pulsed mode is shown in Fig. 1(b). The incident microwave power into the source was controlled with a fast RF-switch. A dedicated detector recording the electron current escaping the magnetic confinement through the extraction aperture was used for the experiments. The detector, first described by Izotov *et al.*,[24] consists of an array of aluminium foils, a suppression electrode, and a Faraday cup. A transimpedance amplifier with 40 μs rise-time (0%–90%) was used to convert the electron current to a voltage signal. The aluminium foils were assembled on a movable cradle whose position could be adjusted through a vacuum feed-through. Foils of specific thickness were used for the experiments to provide a crude energy resolution for the detection of escaping electrons. The thicknesses and corresponding (approximate) energy thresholds[25] for the perpendicular angle of incidence are listed in Table I. The electron detector was positioned 205 mm downstream from the

TABLE I. Aluminium foil thickness and corresponding (approximate) energy threshold.

Foil number	Thickness (mg/cm^2)	Energy threshold (keV)
1	No foil	0
2	1.0	20
3	6.8	55
4	18.4	100
5	88.1	270
6	270 (1 mm plate)	570

extraction aperture (location of the foil) where the magnetic field strength has decreased to about 5% compared to the extraction mirror. The effect of the magnetic field on electron trajectories and velocity components has been neglected when calculating the threshold energies in Table I. In order to install the electron detector, the pumping speed of the ion source had to be reduced from the nominal value. Consequently, all the data in this particular experiment were recorded using only residual gas (mainly oxygen and nitrogen) whose pressure remained constant at 4×10^{-7} mbar throughout the experiments in the pulsed mode. Additionally, the high voltage was switched off (source potential was set to zero) during the pulsed mode measurements as this would have obstructed the escaping electron flux especially at low energies.

In order to understand the experimental conditions allowing the detection of pitch angle scattered electrons, some qualitative understanding of the sequence of events in the pulsed operation mode of an ECRIS is required. After switching off the microwaves, the electron density of the plasma decays exponentially due to collisional diffusion processes. Since the collision frequency of electrons scales with their temperature (energy) as $T_e^{-3/2}$, the hot electrons are the last ones to leak out from the magnetic bottle distorting the electron energy distribution during the afterglow plasma decays, which often results due to instabilities.[24] These hot electrons act as seed electrons for the following pulse reducing the plasma breakdown time.[15] The seed electron density naturally depends on the pulse pattern of the microwaves. At the very beginning of the microwave pulse, due to negligible plasma loading and high EM-fields,[26] electrons interact strongly with the microwaves. Therefore, we expect to observe a burst of pitch angle scattered electrons from the plasma immediately after turning on the microwave power. It is also possible to study the role of microwaves inducing pitch angle scattering by measuring the decay characteristics of electron signals after switching off the microwave power. The microwave induced pitch angle scattering should manifest itself by abrupt drop of electron flux from the plasma as soon as microwave EM-fields have decayed.

In addition to direct measurement of electrons escaping through the extraction aperture, two auxiliary diagnostics monitoring the radially emitted bremsstrahlung (>35 keV) and visible light emission were installed. The bremsstrahlung radiation was measured radially from one of the magnetic field poles of the ECR ion source simultaneously with the measurement of the escaping electron flux. The detector was located between the solenoids in the axial direction. Thus, the bremsstrahlung observed by the germanium detector is a mixture of thick target (wall) and plasma bremsstrahlung with the former dominating the spectrum. Because the focus of the experiments was to study the temporal evolution of the bremsstrahlung, no special attention was paid in optimizing the collimator structure. For this reason, only time-resolved (normalized) total count rates integrated over the energy range of the detected photons are presented. During the analysis, data from hundreds of rf pulses were combined to gain statistics. The counts caused by background radiation and pile-up events are subtracted from the data during the analysis with a dedicated code.[20] Visible light was collected from the radial port (between the magnet poles) viewing the plasma with a lens system connected to a photodiode (IRD Inc. AXUVPN100) with an optical fiber. The photodiode was reverse biased with 24 V and the collected signal was amplified with a current to voltage amplifier (400 μs rise-time).

IV. EXPERIMENTAL RESULTS

A. Relative electron losses in CW mode of operation

The relative electron losses from the magnetic confinement system of the ECRIS were studied in the CW mode by measuring the ratio of Fe-to-Ar Kα emission (denoted r hereafter). Figure 2 shows a typical X-ray spectrum measured with the JYFL 14 GHz ECRIS. The two dominant peaks i.e., Ar Kα and Fe Kα are identified in the figure. The remaining two prominent lines are Al Kα (1.5 keV) and Cr Kα (5.4 keV). The detector efficiencies at the relevant energies is 0.91 (Ar Kα) and 0.99 (Fe Kα). The main sources of error for the relative electron loss results presented are related to the repeatability of the plasma conditions during the measurement and the variation of the plasma parameters over long data acquisition times. The uncertainty related to the repeatability was estimated from a set of consecutive measurements under identical conditions while the effect of long-term parameter drifts was minimized by reducing the data acquisition time to twenty minutes. Altogether, the experimental uncertainty is estimated to be $\pm 18\%$. It is worth noting that the comparison of Ar and Fe Kα count rate eliminates the error related to the detector alignment, the energy dependent efficiency, and the assumption of a spatially uniform and isotropic plasma distribution, which influence the accuracy of absolute measurements as discussed in Ref. 23.

The experiments were started by conducting a parametric sweep of the four source tune parameters i.e., neutral gas pressure, microwave power, magnetic field configuration and biased disc voltage, and measuring r. These experiments revealed that the biased disc voltage had practically no influence on r and hence the discussion is limited to the influence of the magnetic field configuration, microwave power, and neutral gas pressure.

Figure 3 shows the behaviour of r as a function of the magnetic field strength, characterized by two figures; the B_{min}/B_{ECR}-ratio and the average field gradient parallel to

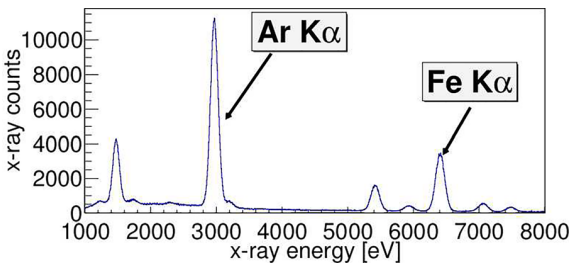

FIG. 2. A typical X-ray spectrum measured with the JYFL 14 GHz ECRIS. With this spectrum, pile-up events have been removed, however the bremsstrahlung background has not been removed and the detector efficiency correction has not been applied.

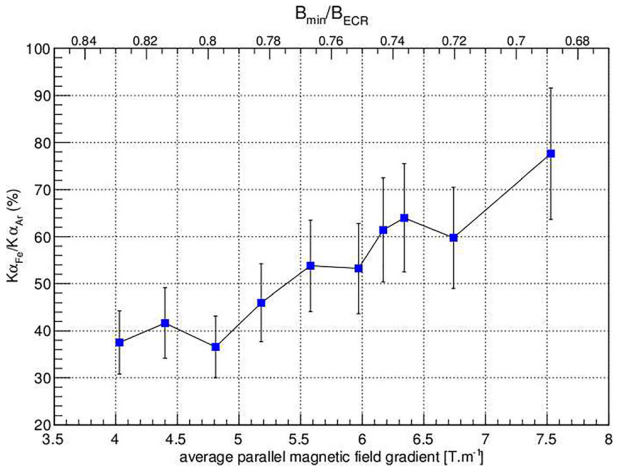

FIG. 3. Variation of r as a function of the magnetic field strength with 400 W microwave power and 4.3×10^{-7} mbar argon pressure.

the field, i.e., $\frac{\vec{B}}{|\vec{B}|} \cdot \nabla \vec{B}$. The magnetic field strength was altered by adjusting the currents of both coils simultaneously and hence preserving the relative strength of the axial magnetic mirrors. The fact that the JYFL 14 GHz ECRIS has only two solenoids makes it impossible to adjust the B_{min} independently from the axial mirror fields. However, the mirror ratio is defined here as B_{max}/B_{ECR} (where max is injection or extraction), not B_{max}/B_{min} which is often used for simple mirror traps. This definition is due to the fact that the magnetic confinement is based on the conservation of the magnetic moment which is violated each time the electron crosses the resonance where its velocity components are affected non-adiabatically. Hence, it is more meaningful to define the mirror ratio as B_{max}/B_{ECR}, which is a common practice of the ECRIS community. The definition then implies that the change of the axial mirror field (injection and extraction) is directly proportional to the change of the mirror ratio, independent of B_{min}. The general trend observed from Fig. 3 is for the electron losses to decrease, indicated by the monotonic decrease in r, as B_{min}/B_{ECR} increases or the average parallel magnetic field gradient decreases. It has been shown that the average electron energy, determined from bremsstrahlung diagnostics, is higher with increasing B_{min}/B_{ECR}.[19] Recent investigations performed by Izotov *et al.* also show directly that the local maxima of the EEDF of the escaping electrons shift towards higher energies with increasing B_{min}/B_{ECR}-ratio.[27] It is therefore argued that the average electron energy increases with the decreasing average parallel magnetic field gradient. This relation can also be understood on the basis of more efficient ECR heating due to the lower gradient at the resonance surface.[28,29] It is known that the inner shell ionization rate is a function of electron density, ion density, and rate coefficient for inner shell ionization. Accepting the fact that the ratio of the inner shell ionization rate of Fe-to-Ar should increase with increasing average electron energies[30] leads to two possibilities to explain the experimental observation: (1) the electron density in the plasma volume is visible to the detector increases and/or (2) the electron loss rate towards the injection region decreases with increasing magnetic field strength i.e., B_{inj} from 1.98 T to 2.13 T and B_{ext} from 0.90 T to 1.02 T. The first possibility would cause r to decrease as the Ar Kα emission rate within the probed plasma volume would increase. This result is in line with the fact that the source performance, in terms of high charge state production, tends to increase with the B-field as long as the instability threshold is not crossed.[15] However, this result of increasing electron density with increasing magnetic field strength is inconsistent with an earlier investigation which found that the electron density (responsible for inner shell ionization) remains virtually constant with the varying B-field in the range discussed here.[23] This strengthens the argument that the result presented in Fig. 3 is most probably being caused by the axial B-field affecting the electron loss rate, i.e., the electron flux towards the biased disc is reduced when the axial magnetic field strength is increased. This would be due to the increasing injection (and extraction) mirror ratio reducing the axial electron losses. Thus, the conclusion drawn from the experimental observation in Fig. 3 is that the combined effect of higher plasma density (which is suggested by Sakildien *et al.*[23] to play a lesser role) and reduced electron losses with increasing B-field results in the decrease in r. As remarked later again, the proposed reduced axial electron losses might affect the loss pattern of electrons and could most likely result in enhanced radial electron losses. Additionally, the variation of r with the B-field sweep should be interpreted with caution. The B-field sweep can also change the EEDF of the escaping electrons as discussed earlier.[27] However, the results presented in this work combined with an analysis of inner shell ionization rate coefficients indicate that the influence of the B-field strength on the axial flux of escaping electrons is greater than the influence of the shifting EEDF.[27] It should also be pointed out that the effect of the B-field is not directly probing pitch angle scattering. Nevertheless, the results presented here demonstrate that r is sensitive to particle losses and can therefore be used to probe the pitch angle scattering with different parametric sweeps. Furthermore, since it has now been established that r is sensitive to the magnetic field strength, this parameter needs to be kept constant (as was done for the remainder of this investigation) during any experiments trying to probe the significance of microwave induced pitch angle scattering.

Figure 4 shows the variation of r with neutral gas pressure at different microwave powers. The first observation made is that the neutral gas pressure has the most significant effect on the relative electron losses. This effect is especially pronounced at a low pressure. Based on auxiliary diagnostics signals (e.g., the biased disc current), it can be assumed that the electron density increases with increasing neutral pressure. The microwave power absorbed by the plasma at low neutral pressure/electron density results in an EEDF with high average electron energies. This is supported by the fact that the threshold magnetic field for the appearance of kinetic instabilities, driven by the anisotropy of the EEDF, is consistently lower at reduced neutral gas pressure. From an earlier investigation performed in the pulsed mode, it is known that the confinement time of high energy electrons can easily be of the order of seconds,[31] when collisional scattering is the only loss process. The fact that the experimental

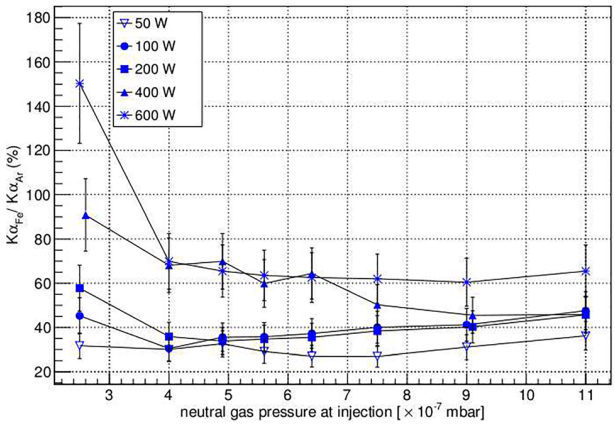

FIG. 4. Variation of r as a function of neutral gas pressure at injection, at different microwave powers.

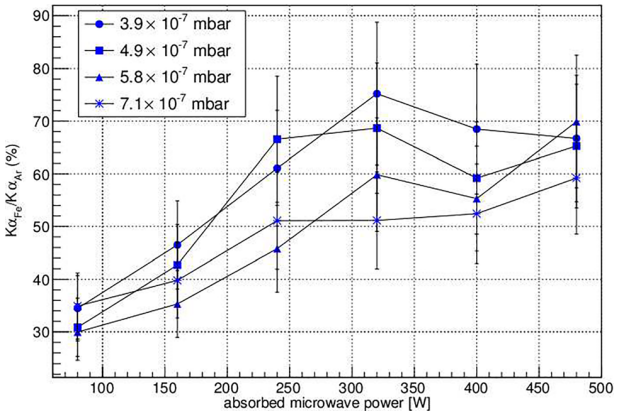

FIG. 5. Variation of r as a function of absorbed microwave power, at different neutral gas pressures.

results in Fig. 4 indicate enhanced (warm and hot) electron losses at a low pressure point to a different loss mechanism at work. At low pressure/low plasma density, the EM-field strength is higher due to reduced damping of the field. Therefore, rf-induced scattering becomes more prominent at these conditions. This result is presumably displayed by the low pressure part of Fig. 4. The electron losses, as estimated by r, increase substantially if the incident microwave power increases. As the neutral gas pressure is increased, both the electron density and argon density increase. This could impact r in two distinct ways: (1) the increasing argon density leads to increased argon inner shell ionization decreasing r and/or (2) the increasing electron density leads the average electron energy to decrease as the absorbed microwave power is now distributed between a larger electron population and the strength of the EM-field at the resonance is damped.[20] This results in a decrease in the mean velocity of the EEDF and reduced EM-field strength at the resonance due to increased damping of the EM-wave, reducing r due to the reduced rate of rf-induced electron losses. Since these effects cannot be separated unambiguously, the conclusion drawn from the parametric sweep is that the best way to probe rf-induced scattering is to conduct a power sweep at several different neutral pressures keeping the magnetic field constant.

Figure 5 presents the variation of r with absorbed microwave power, at different neutral gas pressures. The absorbed power is defined as the power available at the interface between the waveguide and the plasma (as discussed thoroughly in Ref. 23). The definition takes into consideration the power losses in the waveguide which are estimated to ∼20% as well as the reflected power which was measured to be less than ∼2%. It is assumed that all power which is not lost in transmission or reflected back to the WR-62 waveguide is absorbed by the plasma i.e., losses at the chamber wall are not taken into account. Initially, r increases with absorbed microwave power, which could be due to two instances: the changing EEDF favoring r or alternatively (or simultaneously) there could be a loss mechanism i.e., pitch angle scattering proportional to the microwave power. The second tendency observed from the figure is a saturation of r at powers higher than ∼300 W. To account for both tendencies, the influence of the EEDF, electron density, and electron loss mechanisms on r were considered. As a result of the increasing absorbed microwave power, the changing EEDF could result in both increased electron density as well as higher average electron energies. The increased electron density would result in both argon and iron Kα emission increase, under the assumption that the rates of the various electron loss mechanisms remain constant. This would not impact r and therefore could not influence the first tendency observed in Fig. 5. The changing EEDF could also result in a higher average electron energy. This could propel the average electron energy pass the optimum required for inner shell ionization of argon and closer to the optimum for inner shell ionization of iron. The increasing average electron energy could also lead to enhanced electron losses due to pitch angle scattering. From the discussion in Sec. II, it is known that the rf induced velocity space diffusion of the electrons and their subsequent losses are driven by the relation between the mean velocity of the EEDF and the phase velocity of the EM-field. Increasing the mean velocity in excess of the phase velocity of the EM-field (in the case of electron heating) would induce increased electron losses driven by the microwave heating. These effects resulting from increasing average energy of the electrons could account, either partially or wholly, for the first tendency observed in Fig. 5. The variation of the EEDF, as a function of power is, however, not supported by the recent experimental data reported by Izotov *et al.*[27] Thus, it seems fair to argue that purely based on elimination of the changing EEDF and increasing electron density, the measured result of increasing r with microwave power is most likely due to the increased rate of pitch angle scattering. It is worth noting that Perret *et al.* arrived at a similar conclusion by assessing the results of a power sweep obtained with diagnostics complementary to this work.[4] Assessing the second tendency, namely the saturation of r at microwave powers >300 W, against the three parameters that influence r leads to the conclusion that this tendency is dictated by the plasma energy content. The saturation of the plasma energy content with increasing microwave power has been observed e.g., by Noland *et al.* measuring the diamagnetic effect of the ECRIS plasma in the pulsed mode.[9] From

a previous investigation, it was observed that the argon Kα emission rate saturates with increasing absorbed microwave power.[23] The current investigation also indicates that r saturates with absorbed microwave power. Altogether, this leads to the conclusion that the iron Kα emission rate also saturates with the absorbed microwave power. It can be reasonably assumed that the increasing absorbed microwave power results in increasing electron density. Beyond a certain threshold, the absorbed microwave power becomes insufficient to heat the additional electrons resulting from ionization and causes the saturation of r observed in Fig. 5 and discussed by Perret *et al.*[4] Also, it can be argued that the EM-field of the microwave scales with the power (P) as the field is proportional to $\sqrt{P}$ and is also affected by the plasma density through damping effects. Thus it is expected that the pitch angle scattering rate which depends on the EM-field strength does not follow the injected power in a linear manner.

B. Electron losses in the pulsed operation mode

This experimental campaign was started by measuring the temporal evolution of escaping electron signals with different aluminum foils. Different pulse patterns were used in order to vary the density of the so-called seed electrons.[32] Figure 6 shows an example of the electron signals (in μA) measured with 25 ms/200 W microwave pulses at a repetition rate of 2 Hz (note different vertical scales). In the given example, the solenoid magnetic field (injection/minimum/extraction) was set to $B_{inj} = 2.11$ T/$B_{min} = 0.39$ T/$B_{ext} = 1.02$ T (later referred as the B-field profile #3).

The data in Fig. 6 reveal that turning on the microwave power leads to a burst of electrons from the trap. In this example, the duration of the transient is about 100 μs. The characteristics of the ignition peak, i.e., duration and magnitude, were observed to change with the ion source settings. The given example was selected for display because depending on the repetition rate, the peak either vanishes (lack of

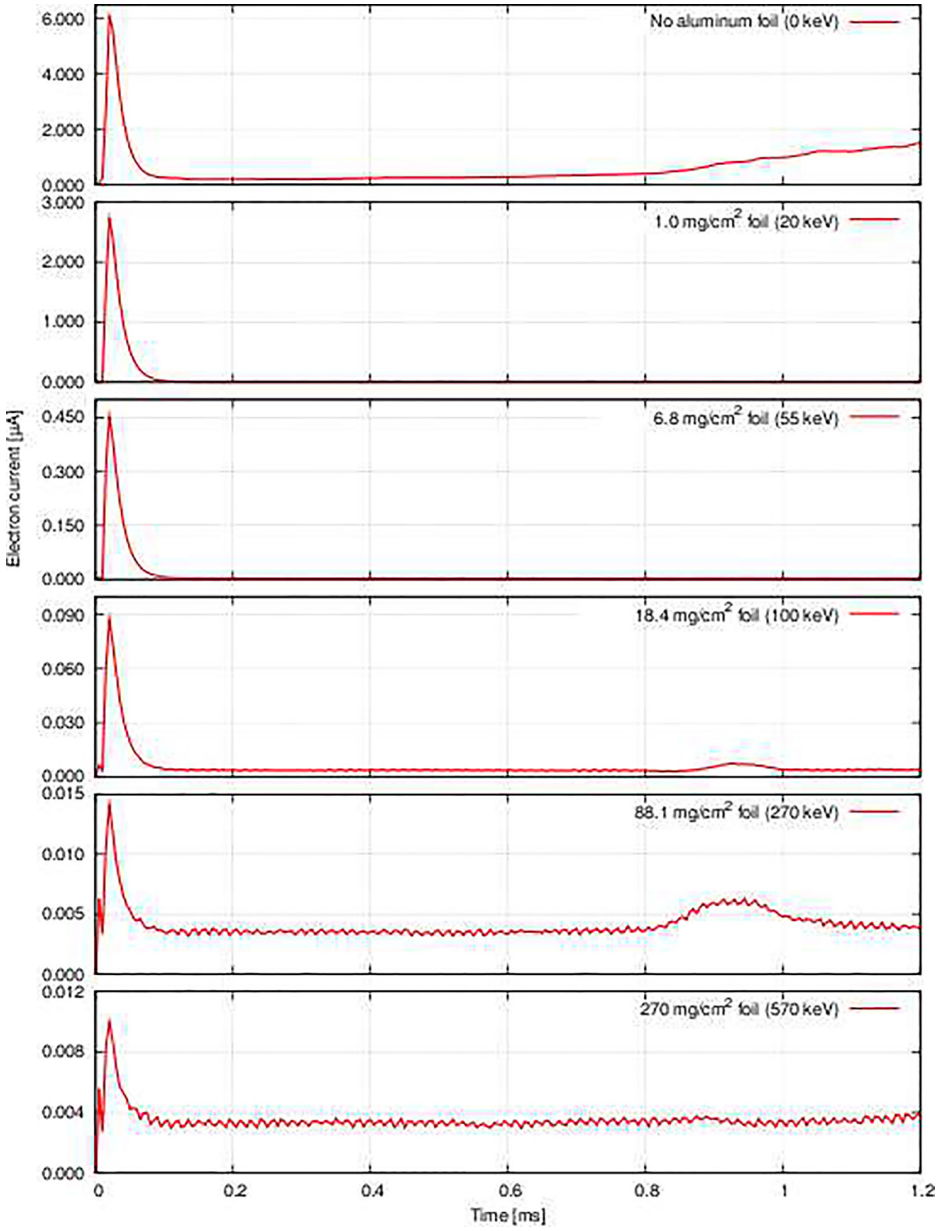

FIG. 6. Variation of the electron signal with a 25 ms/200 W microwave pulse at a repetition rate of 2 Hz at B-field profile #3.

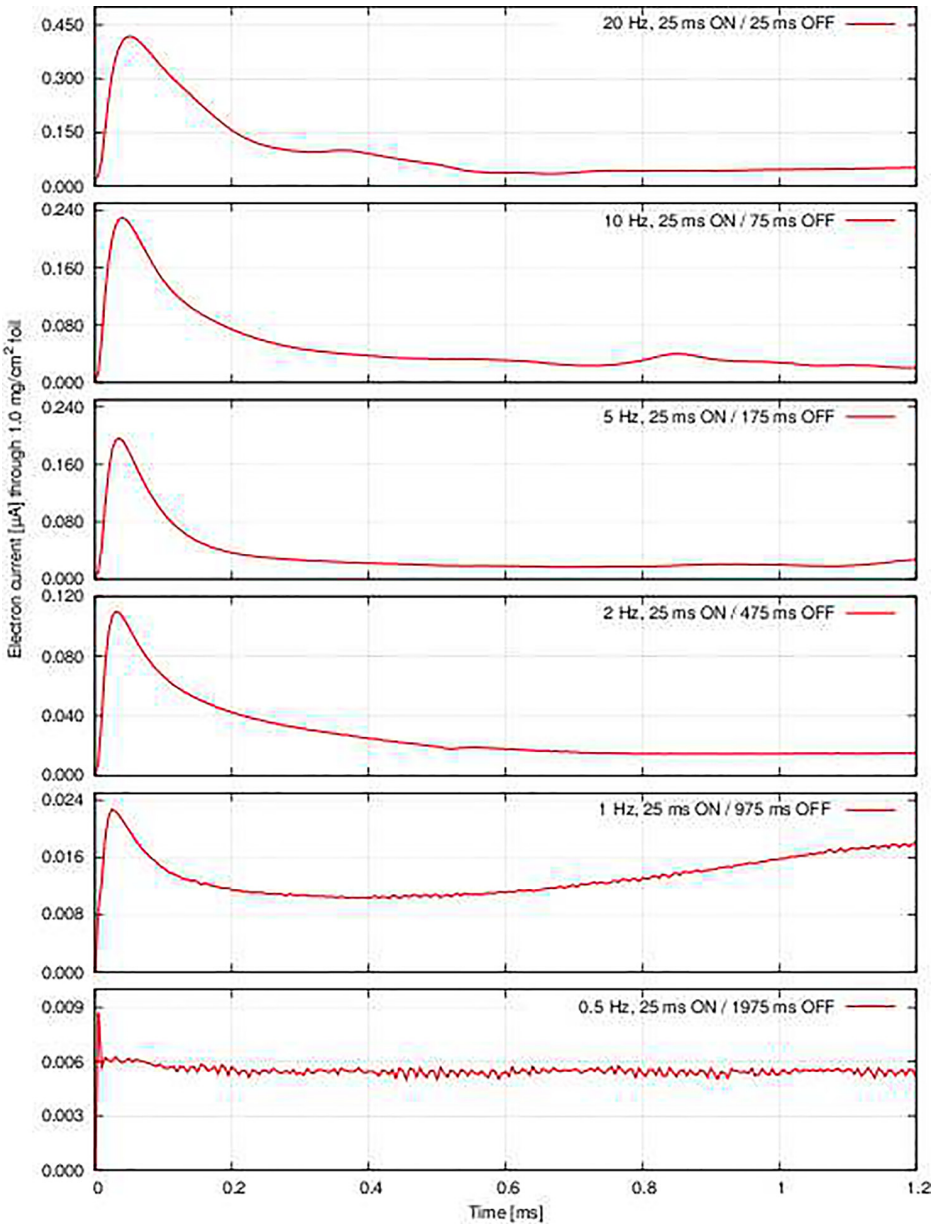

FIG. 7. Variation of the electron signal with a 25 ms/700 W microwave pulse at different repetition rates at B-field profile #2. The measured results were obtained with a 1 mg/cm^2 foil (E > 20 keV).

seed electrons) or overlaps with the effects caused by the ionization cascade (high seed electron density).

The effect of the pulse repetition rate on electron signals in the beginning of the microwave pulse is presented in Fig. 7 showing an example measured with a 1 mg/cm^2 foil (20 keV threshold) at 0.5–20 Hz/25 ms pulses (note different vertical scales). The data were obtained with 700 W incident power and a solenoid field profile of $B_{inj} = 2.01$ T/$B_{min} = 0.35$ T/$B_{ext} = 0.95$ T (B-field profile #2). The fact that the magnitude of the transient peak depends on the repetition rate suggests that the initial burst of electrons at the very beginning of the microwave pulse is indeed caused by the seed electrons that are expelled from the trap. A similar behavior depending on the pulse repetition rate was observed also with other aluminum foils.

In order to highlight the fact that the discussed burst of hot electrons is a transient, independent of the plasma breakdown, stepwise ionization, and gradual saturation of plasma density and temperature, Fig. 8 shows the electron signal measured with various foils, visible light signal recorded with the photodiode, and the total bremsstrahlung count rate for the full length (25 ms) of the microwave pulse. The presented data were measured with 200 W of incident power at 20 Hz repetition rate and a magnetic field configuration of $B_{inj} = 1.95$ T/$B_{min} = 0.32$ T/$B_{ext} = 0.90$ T (B-field profile #1).

The data show that with the given ion source settings, the initial transient peak is more pronounced with increasing electron energy, thus strengthening the claim that the rf-induced pitch angle scattering plays a significant role in determining the electron losses (as opposed to collisional scattering) of high energy electrons especially. Also, the bremsstrahlung count rate at energies >35 keV peaks immediately after microwave turn-on meaning that the burst of electrons is observed in both axial (electron detector) and radial (germanium detector) directions. The signals related to the existence of low energy electrons and their losses, i.e., electron flux measured without the aluminum foil and integrated light signal from the plasma, suggest that the EEDF in

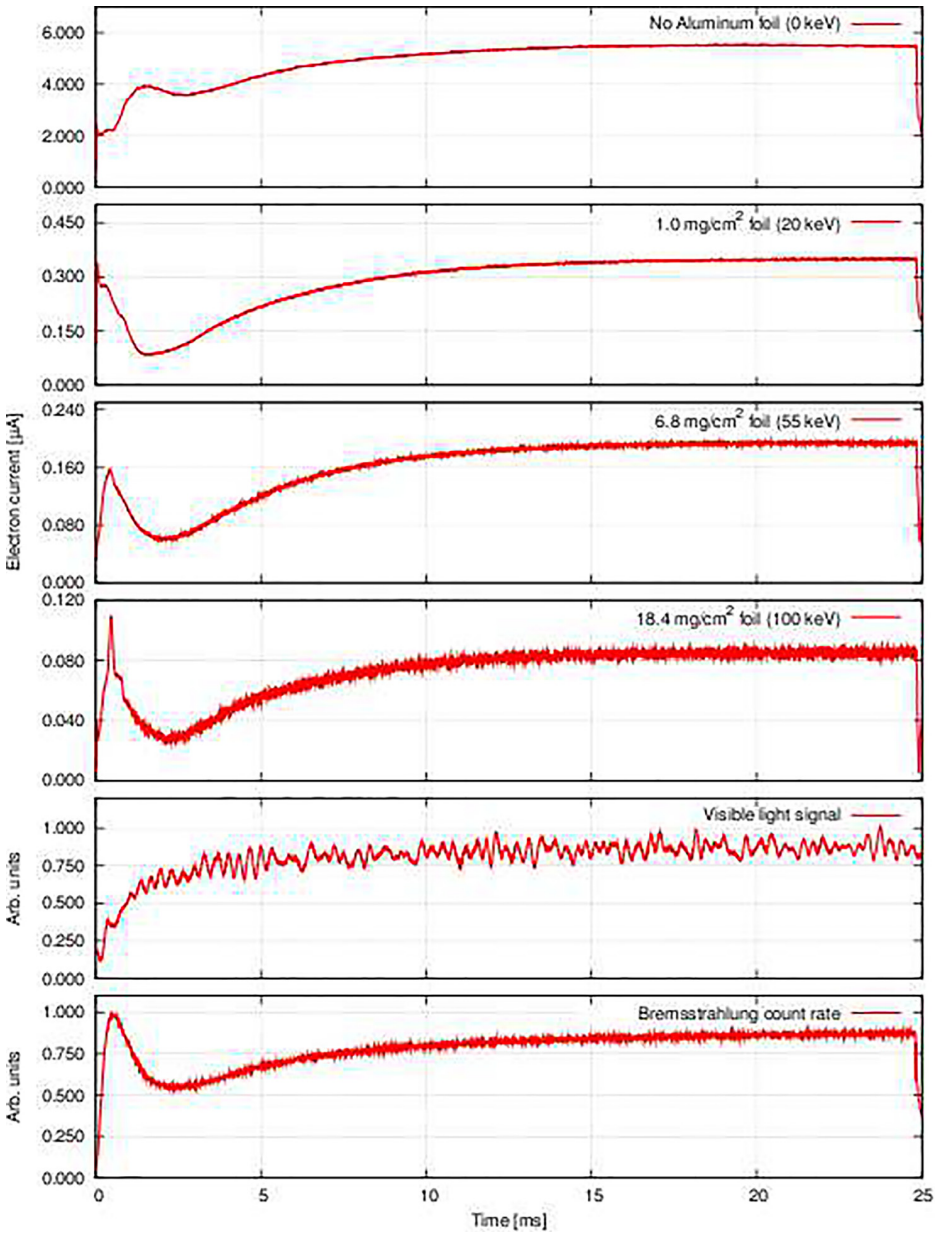

FIG. 8. Variation of the electron signal (μA), visible light signal, and the total bremsstrahlung count rate with 25 ms/200 W microwave pulse, at 20 Hz repetition rate, and B-field profile #1, with the various foils.

steady-state plasma differs greatly from the one observed during the burst. All these observations support the conclusion that at low plasma density in the beginning of the microwave pulse, the electric field and average electron energy are high, which enhances the microwave induced pitch angle scattering rate. As the ionization cascade proceeds, the electric field strength and average electron energy drop,[20,26] which finally leads to saturation of e.g., plasma density and loss rates of electrons.

Table II summarizes the effects of magnetic field configuration and microwave power on the detected electron flux and bremsstrahlung count rate during the initial transient. The presented values are the ratios of the transient to the value of the signal at the end of the pulse with various repetition rates. The length of the microwave pulse was set to 25 ms. With certain ion source settings, the signal to noise ratio was too low for the thickest two foils and, therefore, the corresponding data are omitted from the table.

The following is a summary of the qualitative tendencies observed with different ion source settings: (i) the electron flux during the transient burst increases with microwave power. This is probably due to increased plasma density during the microwave pulse, which in turn enhances the seed electron density in the beginning of the following pulse. Also, the transient could increase with power due to the fact that the RF-field strength scales with the power $\left(E \propto \sqrt{P}\right)$. (ii) The electron flux during the transient burst increases with the pulse repetition rate, which can be explained by the higher seed electron density as well. (iii) Increasing the solenoid magnetic field strength results in s stronger burst of electrons (flux in axial direction) in the beginning of the microwave pulse. From the earlier discussion, it is known that the axial mirror ratio (best defined by B_{max}/B_{ECR}) affects the hot electron confinement. During the microwave-off period, the electron loss rate depends on the strength of the mirror field and the rate of collisional scattering. The fact

TABLE II. Variation of the ratio of electron signal (μA) and total bremsstrahlung count rate at the initial transient to the value of the signal at the end of the microwave pulse, as a function of B-field configuration and microwave power, at different repetition rates.

B-field profile	1	2	3	2	2
μ-wave power	200 W	200 W	200 W	500 W	700 W
Rep. rate (Hz)	2/5/10	2/5/10	2/5/10	2/5/10	2/5/10
e^-, all E	0.12/0.20/0.26	0.12/0.28/0.53	3.16/2.28/1.87	0.07/0.17/0.36	0.07/0.12/0.22
e^-, E > 20 keV	0.16/0.25/0.45	1.04/1.79/7.24	41.2/51.4/80.4	0.76/2.08/3.98	0.64/1.32/1.81
e^-, E > 55 keV	0.07/0.20/0.37	1.00/1.09/3.81	40.1/45.4/42.9	0.53/0.96/1.14	0.51/0.57/0.78
e^-, E > 100 keV	0.08/0.26/0.53	1.28/1.42/2.11	4.71/4.49/3.40	0.55/1.01/1.67	0.40/0.63/0.97
X-ray rate (ratio/norm.)[34]	1.14/0.41	1.09/0.46	1.33/1	–/–	–/–

that a stronger burst of electrons is observed with increasing B-field during the microwave-on period is probably due to a combination of two effects. First, the electron confinement is enhanced as a result of the higher axial mirror ratio during the microwave-off period which leads to a higher seed electron density in the beginning of the subsequent microwave pulse. Second, the lower average magnetic field gradient over the resonance zone leads to higher average electron energies and, thus lower collision frequency, as shown from bremsstrahlung measurements[19] and direct measurement of the energy distribution of the escaping electrons.[27] The lower gradient also enhances the energy gain of the electrons as shown by Eqs. (5) and (6) and presumably increases the pitch angle scattering rate in the beginning of the microwave pulse. The result suggests that the process responsible for the initial burst expels electrons to all directions, which is indicative for microwave induced pitch angle scattering.[17] It is important to note that with this comparison, the initial electron burst was compared to the saturation electron flux at the same solenoid field setting and the behavior at different solenoid field settings was not compared. Furthermore, the observation of the transient peak in the beginning of the pulse, i.e., at low plasma density, across the given range of electron energies and ion source settings implies that the phase velocity of the microwave is significantly reduced, which highlights the importance of the resonant interaction inducing electron losses.

In addition to the initial electron burst, microwave induced electron losses presumably affect the decay of the electron flux following the trailing edge of the microwave pulse. Deviations from exponential afterglow decay (Coulomb collisions driving diffusion) could be interpreted as a signature of microwave induced pitch angle scattering actively increasing the electron loss rate during the microwave pulse. Figure 9 shows the electron signal measured with selected foils, visible light signal, total bremsstrahlung count rate, and microwave power signal associated with the trailing edge of the microwave pulse at 24.85 ms. The presented example was measured with 200 W of incident power at 20 Hz repetition rate and a magnetic field configuration of $B_{inj} = 1.95\,T/B_{min} = 0.32\,T/B_{ext} = 0.90\,T$ (B-field profile #1). The data were chosen for display because the signal levels are adequate and no instabilities affecting the electron losses are observed during the plasma decay, which is often the case.[33]

Independent of the foil thickness, the electron flux drops to less than 50% of its saturation value in <20 μs after the microwave power is switched off, followed by slower decay lasting tens of milliseconds. In the case of the two thickest foils (not shown here), the signal practically vanishes immediately after the microwave is switch off. Also the bremsstrahlung count rate initially decays very fast and then follows a smoother, exponential behavior. On the contrary, the decay of the visible light signal, representing the excitation and recombination rate of low charge state ions, exhibits much slower decay. The microwave power signal decays from its maximum value to zero in less than 20 μs. The measured decay of the signal shown in Fig. 9 is limited by the RC-constant of the klystron output channel—the switch-off time of the RF-switch being 40 ns (from 100% to 10%). Altogether, it is concluded that the escaping electron and bremsstrahlung signals decay faster than can be explained by Coulomb collisions alone. Thus, the data suggest that microwave induced pitch angle scattering contributes significantly (more than 50%) to the electron losses across the whole energy range during the microwave pulse. The fractional contribution to electron losses due to the three loss mechanisms discussed in Sec. II has been numerically investigated by Cluggish *et al.*[10] From the results of this simulation, it is concluded that Coulomb collision losses account for between 20% and 35% of the total electron losses under stable plasma conditions. The drop of the electron signal at the end of the microwave pulse to less than 50% of the rf ON signal suggests that the Coulomb collisions account for this fraction of the total losses, which is in good agreement with the numerical prediction.

The effect of ion source settings, i.e., microwave power and magnetic field configuration, on the decay characteristics of electron flux, bremsstrahlung count rate, and visible light signal is summarized in Table III, which shows each signal measured at 200 μs and at 2 ms after the microwave switch off and normalized with respect to the steady-state value. It was observed that the repetition rate and duty factor did not affect the decay characteristics and, therefore, only data recorded with 20 Hz/50% duty factor are displayed.

With all source settings, the qualitative decay characteristics of the electron, bremsstrahlung and visible light signals are similar to those illustrated in Fig. 9 i.e., the electron flux escaping the trap drops much faster than could be expected from diffusive decay. This corroborates the conclusion that during the microwave pulse, there is an active loss mechanism scattering electrons into the loss cone and contributing more than 50% to the total electron loss rate.

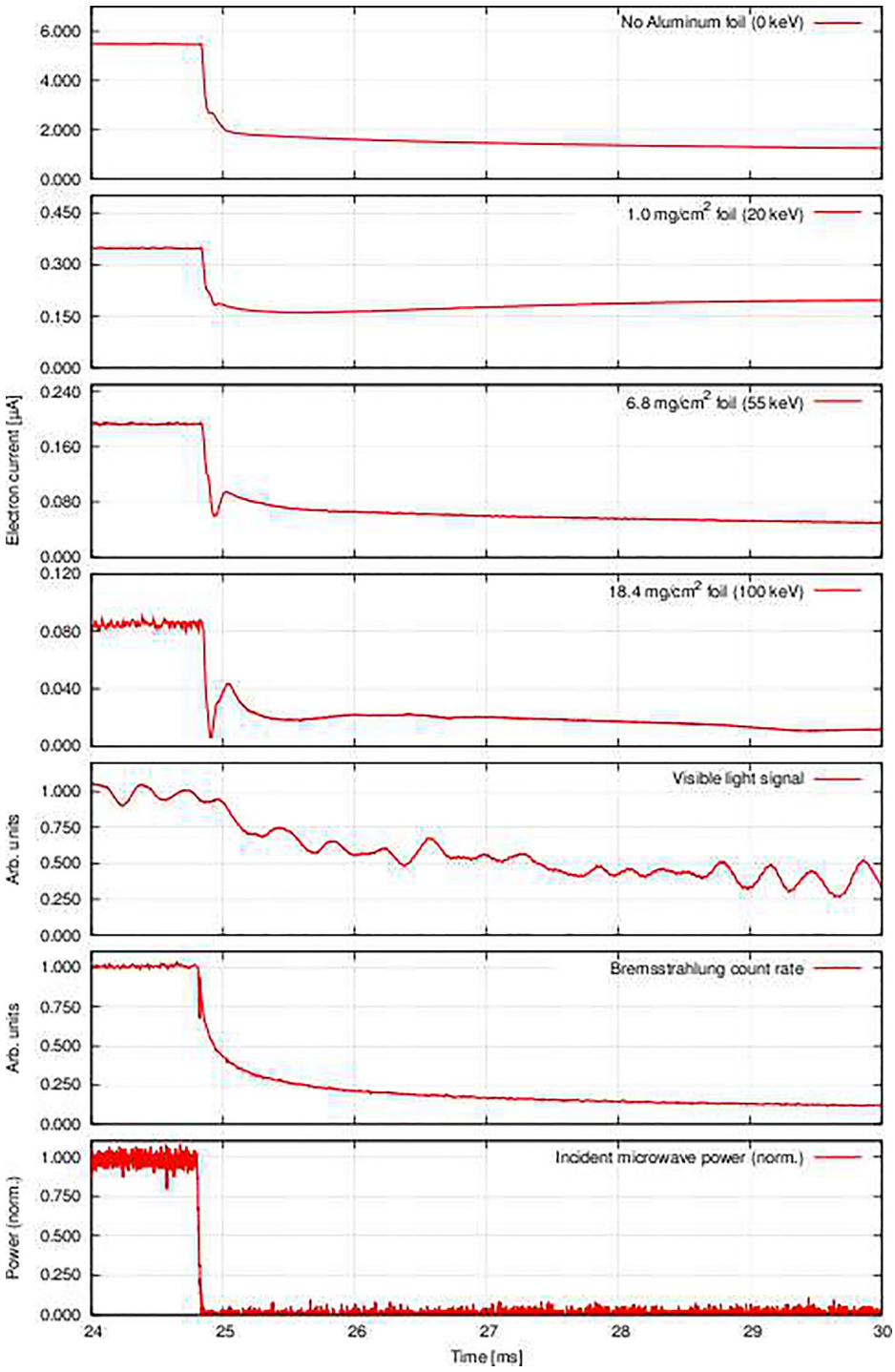

FIG. 9. Variation of the electron signal (μA) (with selected foils), visible light signal, the total bremsstrahlung count rate, and the microwave power signal associated with the trailing edge of the microwave pulse at 24.85 ms. The results displayed were taken with 200 W of incident power, at 20 Hz repetition rate, and B-field profile #1.

TABLE III. Variation of the electron signal (μA), total bremsstrahlung count rate, and the visible light signal measured at 200 μs and at 2 ms (after microwave switch off) and normalized with respect to the steady-state value, as a function of B-field configuration and microwave power.

B-field profile	#1	#2	#3	#2	#2
μ-wave power	200 W	200 W	200 W	500 W	700 W
e^-, all E	0.35/0.26	0.31/0.24	0.18/0.11	0.23/0.21	0.25/0.22
e^-, E > 20 keV	0.49/0.50	0.36/0.71	0.59/0.84	0.50/0.92	0.26/0.61
e^-, E > 55 keV	0.47/0.32	0.24/0.64	0.38/0.63	0.61/0.60	0.28/0.34
e^-, E > 100 keV	0.41/0.24	–/–	–/–	0.47/0.41	0.39/0.32
X-ray rate	0.41/0.18	0.37/0.21	0.55/0.33	–/–	–/–
Visible light[35]					

V. CONCLUSION

The relative electron losses in CW operation and the temporal behavior of the electron flux escaping through the extraction mirror of an ECRIS in pulsed operation have been shown to exhibit features that can be associated with microwave induced pitch angle scattering. In the former case, it was observed that r (defined above) increases with microwave power. An even more pronounced increase in r at low plasma density with increasing microwave power was also observed. Both these behaviors can be attributed to microwave induced pitch angle scattering in action. With the latter case, the initial burst of electrons in the very beginning of

the microwave pulse and the abrupt drop of electron flux at the trailing edge of the pulse is also suggested to be associated with microwave induced pitch angle scattering. Finally, it should be mentioned that the agreement between the experiment and simulations[10] is good.

ACKNOWLEDGMENTS

V. Toivanen and J. Komppula are acknowledged for the technical assistance and analysis of the bremsstrahlung data acquired in the pulsed mode. M.S. wishes to thank Professor Paul Papka and the Department of Physics at the University of Stellenbosch for the use of their Silicon Drift Detector (X123-SDD) during the CW measurements described in this manuscript. The work of OT has been supported by the Väisälä Foundation of the Finnish Academy of Science and Letters. This research was conducted at JYFL and M.S. wishes to thank all those involved for their support. This work has been supported by the Academy of Finland under the Finnish Center of Excellence Program (Contract No. 213503) and mobility grant (No. 290390). The work is also based on the research supported in part by iThemba LABS and the National Research Foundation of South Africa (Grant Nos. 90741 and 109887). The work of V. Skalyga and I. Izotov was carried out with the support of the Federal Agency for Scientific Organizations in the frame of state order No. 0035-2014-0026.

[1]R. Geller, *Electron Cyclotron Resonance Ion Sources and ECR Plasmas* (Institute of Physics Publishing, Bristol, 1996).
[2]C. Barué, M. Lamoureux, P. Briand, A. Girard, and G. Melin, "Investigation of hot electrons in electron-cyclotron resonance ion sources," J. Appl. Phys. **76**, 2662 (1994).
[3]G. Shirkov, "Multicomponent consideration of electron fraction of electron-cyclotron resonance source plasma," Rev. Sci. Instrum. **71**, 850 (2000).
[4]C. Perret, A. Girard, H. Khodja, and G. Melin, "Limitations to the plasma energy and density in electron cyclotron resonance ion sources," Phys. Plasmas **6**, 3408 (1999).
[5]C. C. Petty, D. L. Goodman, D. L. Smatlak, and D. K. Smith, "Confinement of multiply charged ions in an electron cyclotron resonance heated mirror plasma," Phys. Fluids B **3**, 705 (1991).
[6]F. Jaeger, A. J. Lichtenberg, and M. A. Lieberman, "Theory of electron cyclotron resonance heating - I. Short time and adiabatic effects," Phys. Plasmas **14**, 1073 (1972).
[7]I. B. Bernstein and D. C. Baxter, "Relativistic theory of electron cyclotron resonance heating," Phys. Fluids **24**, 108 (1981).
[8]M. E. Mauel, "Electron-cyclotron heating in a pulsed mirror experiment," Phys. Fluids **27**, 2899 (1984).
[9]J. Noland, O. Tarvainen, J. Benitez, D. Leitner, C. Lyneis, and J. Verboncoeur, "Studies of electron heating on a 6.4 GHz ECR ion source through measurement of diamagnetic current and plasma bremsstrahlung," Plasma Sources Sci. Technol. **20**, 035022 (2011).
[10]B. Cluggish, L. Zhao, and J. S. Kim, "Modeling of the stability of electron cyclotron resonance ion source plasmas," Nucl. Instrum. Methods Phys. Res., Sect. A **631**, 111 (2011).
[11]T. Thuillier, J. Angot, J. Y. Benitez, A. Hodgkinson, C. M. Lyneis, D. S. Todd, and D. Z. Xie, "Investigation on the electron flux to the wall in the VENUS ion source," Rev. Sci. Instrum. **87**, 02A736 (2016).
[12]G. D. Shirkov, "A classical model of ion confinement and losses in ECR ion sources," Plasma Sources Sci. Technol. **4**, 250 (1993).
[13]A. Girard, D. Hitz, G. Melin, and K. Serebrennikov, "Electron cyclotron resonance plasmas and electron cyclotron resonance ion sources: Physics and technology (invited)," Rev. Sci. Instrum. **75**, 1381 (2004).
[14]A. Girard, C. Pernot, G. Melin, and C. Lécot, "Modeling of electron-cyclotron-resonance-heated plasmas," Phys. Rev. E **62**, 1182 (2000).
[15]O. Tarvainen, J. Laulainen, J. Komppula, R. Kronholm, T. Kalvas, H. Koivisto, I. Izotov, D. Mansfeld, and V. Skalyga, "Limitations of electron cyclotron resonance ion source performances set by kinetic plasma instabilities," Rev. Sci. Instrum. **86**, 023301 (2015).
[16]T. H. Stix, *Waves in Plasmas* (Springer-Verlag, New York, 1992).
[17]C. F. Kennel and F. Engelmann, "Velocity space diffusion from weak plasma turbulence in a magnetic field," Phys. Fluids **9**, 2377 (1966).
[18]A. Girard, C. Perret, G. Melin, and C. Lécot, "Modeling of electron-cyclotron-resonance ion source and scaling laws," Rev. Sci. Instrum. **69**, 1100 (1998).
[19]T. Ropponen, P. Jones, T. Kalvas, H. Koivisto, P. Peura, O. Tarvainen, and P. Suominen, "Time evolution of endpoint energy of bremsstrahlung spectra and ion production from an electron cyclotron resonance ion source," in Proceeding of the 18th International Workshop on ECR Ion Sources TUCO-D01 (2008).
[20]T. Ropponen, O. Tarvainen, P. Suominen, T. K. Koponen, T. Kalvas, and H. Koivisto, "Hybrid simulation of electron cyclotron resonance heating," Nucl. Instrum. Methods Phys. Res., Sect. A **587**, 115 (2008).
[21]M. C. Williamson, A. J. Lichtenberg, and M. A. Lieberman, "Self consistent electron cyclotron resonance absorption in a plasma with varying parameters," J. Appl. Phys. **72**, 3924 (1992).
[22]H. Koivisto, P. Heikkinen, V. Hänninen, A. Lassila, H. Leinonen, V. Nieminen, J. Pakarinen, K. Ranttila, J. Ärje, and E. Liukkonen, "The first results with the new JYFL 14 GHz ECR ion source," Nucl. Instrum. Methods Phys. Res., Sect. A **174**, 379 (2001).
[23]M. Sakildien, R. Kronholm, O. Tarvainen, T. Kalvas, P. Jones, R. Thomae, and H. Koivisto, "Inner shell ionization of argon in ECRIS plasma," Nucl. Instrum. Methods Phys. Res., Sect. A (published online).
[24]I. Izotov, D. Mansfeld, V. Skalyga, V. Zorin, T. Grahn, T. Kalvas, H. Koivisto, J. Komppula, P. Peura, O. Tarvainen, and V. Toivanen, "Plasma instability in the afterglow of electron cyclotron resonance discharge sustained in a mirror trap," Phys. Plasmas **19**, 122501 (2012).
[25]See http://www.nist.gov/pml/data/star/index.cfm for more information regarding the calculation of the range for electrons in aluminium.
[26]V. Toivanen, O. Tarvainen, C. Lyneis, J. Kauppinen, J. Komppula, and H. Koivisto, "ECRIS plasma chamber studies using a network analyzer as a loaded cavity probe," Rev. Sci. Instrum. **83**, 02A306 (2012).
[27]I. Izotov, O. Tarvainen, V. Skalyga, D. Mansfeld, T. Kalvas, H. Koivisto, and R. Kronnholm, "Measurement of the energy distribution of electrons escaping minimum-B ECR plasmas," Phys. Plasmas **27**(2), 025012 (2018).
[28]S. Gammino, D. Mascali, L. Celona, F. Maimone, and G. Ciavola, "Considerations on the role of the magnetic field gradient in ECR ion sources and build-up of hot electron component," Plasma Sources Sci. Technol. **18**, 045016 (2009).
[29]H. Koivisto, "The effect of microwave frequency and grad B on the energy of electrons in an electron cyclotron resonance ion source," Rev. Sci. Instrum. **70**, 2979 (1999).
[30]W. Lotz, "Electron-impact ionization cross-section and ionization rate coefficients for atoms and ions from scandium to zinc," Z. Phys. **220**, 466 (1969).
[31]O. Tarvainen, P. Suominen, and H. Koivisto, "A new plasma potential measurement instrument for plasma ion sources," Rev. Sci. Instrum. **75**, 3138 (2004).
[32]O. Tarvainen, T. Ropponen, T. Thuillier, J. Noland, V. Toivanen, T. Kalvas, and H. Koivisto, "The role of seed electrons on the plasma breakdown and preglow of electron cyclotron resonance ion source," Rev. Sci. Instrum. **81**, 02A303 (2010).
[33]D. Mansfeld, I. Izotov, V. Skalyga, O. Tarvainen, T. Kalvas, H. Koivisto, J. Komppula, R. Kronholm, and J. Laulainen, "Dynamic regimes of cyclotron instability in the afterglow mode of minimum-B electron cyclotron resonance ion source plasma," Plasma Phys. Controlled Fusion **58**, 045019 (2016).
[34]Measured at 20 Hz repetition rate. Ratio = count rate during the initial transient/count rate at 25 ms. Norm. = count rate normalized to maximum at 25 ms with different B-field configurations.
[35]Due to some ripple, the visible light signals have (estimated) error bars of ±0.05